TOWARDS BIOPOLYMER PLATFORMS VIA SMALL MOLECULE CROSSLINKING, ORGANOCATALYTIC RING-OPENING POLYMERIZATION, AND ELECTROSPINNING

by

JI LI

A Dissertation submitted to the

Graduate School-New Brunswick

Rutgers, The State University of New Jersey

In partial fulfillment of the requirements

For the degree of

Doctor of Philosophy

Graduate Program in Food Science

Written under the direction of

Qingrong Huang, PhD

And approved by

_____

_____

_____

_____

New Brunswick, New Jersey

May, 2013

ABSTRACT OF THE DISSERTATION

Towards Biopolymer Platforms via Small Molecule Crosslinking, Organocatalytic Ring-opening Polymerization, and Electrospinning

By JI LI

Dissertation Director:

Qingrong Huang, PhD

The main objective of this research is to fabricate biopolymer platforms for nutraceutical delivery. Comprehensive physical and chemical tools have been utilized, and the engineered biopolymer platforms are promising to fulfill the demand of nutraceutical human transportation. However, single platform is not able to maintain the performance through varying administration routes. Under such circumstance, this work is driven by the premise to satisfy the multiple administrations of nutraceuticals. The work in this dissertation puts emphasis on the development and characterization of biopolymer-based platforms that enable food scientists better the design nutraceutical ingredients.

Multiple approaches, small molecule crosslinking, organocatalytic ring-opening polymerization, polymer blending and electrospinning are leveraged to target chitosan-tripolyphosphate nanoparticle, mPEG-*b*-PVL star polymer, zein/F127 blend film, and zein electrospun fiber mat. The characterization of engineered platforms shed light on the following aspects: (i) molecular self-assembly at nano scale; and (ii) property and functionality at macro scale. And the structure-property relationship is established based on those two aspects. With controllable performance, biopolymer platforms are convenient to be integrated into product matrix as novel ingredients. Through investigation, it is demonstrated that controllable properties such as particulate gel's tightness, particle aggregation, solid composite's flexibility, and fibril organization are achieved by manipulating the nanostructures of biopolymers. The proposed platforms are conventionally extended to a rich variety of disciplines based on the fact that numerous applications in novel food ingredient, medical synthesis, tissue engineering, and product scaling up require the various biopolymer platforms.

ACKNOWLEDGEMENTS

I, Ji Li, would like to express my deepest gratitude towards my Ph.D. dissertation advisor Dr. Qingrong Huang for his step-by-step supervision, guidance, and advice. Through 5-year Ph.D. training, Dr. Huang has guided me to grow from a scientific outsider to a well-trained scientist-to-be. He not only taught me to conduct experiments initially, but also provided me with tremendous opportunities, and cultivated me a capability of critical thinking. Those solid scientific training benefits me so much, and will exert its influence on my future career.

I feel fortunate to collaborate with scientists of different backgrounds, including Drs. Yunqi Li, Jianhui Song, and Songmiao Liang with chemistry background from Chinese Academy of Science, Timothy Nguyen, Dr. Robert Miller, and Dr. Joseph Sly from Nanomedicine group at IBM Almaden Research Center. Pavel Ivanoff Reyes and Ziqing Duan from Dr. Yicheng Lu's solid-state material lab in Department of Electrical and Computer Engineering, Fei Xu from Dr. Vikas Nanda's computational biology lab in Center for Advanced Biotechnology and Medicine (CABM). With those collaborations, I am able to touch, learn, and catch a command of characterization tools, theoretical explanation, polymer synthesis, and ways of phenomenon interpretation.

At last, I would like to acknowledge the funding agency United States Department of Agriculture for supporting my graduate work consistently, and United States Department of Energy for supporting 11th Neutron and X-ray Scattering School held at Oak Ridge National Lab, Tennessee, USA & Argonne National Lab, Illinois, USA.

List of Schemes

Scheme 4.1: Synthesis of mPEG-*b*-PVL star polymer by organocatalytic ring opening polymerization (OROP) method……88

Schematic diagram 6.1: Electrospinning facility equipped with the fiber collectors of aluminum foil and wired drum rotator……146

List of Tables

Table 1.1: Comparison of organo-, organometallic-, and enzymatic Ring-opening polymerization (ROP)……18

Table 3.1: Physical states of sodium tripolyphosphate (TPP)-crosslinked chitosan (CS) particles at different initial CS and TPP concentrations……69

Table 4.1: Molecular characteristics of mPEG-*b*-PVL, star polymer 1, and star polymer 2……..98

Table 4.2: Dimensions of mPEG-*b*-PVL micelle in water fitted from the solid sphere form factor, shell-core sphere form factor, and Guinier analysis……....103

Table 4.3: Aggregate dimensions of star polymer 1 (M_n=221 kD_a) in water fitted from the form factor fitting of cylinder and shell-core circular cylinder, and Guinier analysis…….104

Table 4.4: Hydrodynamic radius (R_h) of mPEG-*b*-PVL micelle and mPEG-*b*-PVL star polymer 2 (M_n=1423 kD_a) at 1 mg/mL concentration in aqueous medium…….108

Table 5.1: Thermal properties of zein/F127 composite films…….127

Table 5.2: Mechanical properties of zein/F127 composite films……130

Table 5.3: Hydrogen bonding profiles of zein/F127 composite films with low F127 loadings……...…….133

List of Figures

Figure 1.1: Chemical structures of small molecule crosslinkers including (A) glutaraldehyde, (B) genipin, (C) sodium tripolyphosphate (STPP), (D) sodium sulfate, and cationic polymer like (E) chitosan composed of glucosamine linked by β(1→4) glycosidic bond with degree of deacetylation of n/(n+m)……...3

Figure 1.2: Physical property, biomedical, and bioimaging applications of chitosan particle. (A) Model for the pig gastric mucin removal from negatively charged phospholipid monolayers caused by chitosan (Reproduced with kind permission from Ref. 45; © Elsevier); (B) Intravenous administration of transferrin-conjugated chitosan particle through mice; (C) Fluorescence imaging of H22 tumor-bearing mice 24 h after i.v. injection of CS-QD hybrid nanospheres. Right is the fluorescence imaging of dissected tumor from the mouse in the left (Reproduced with kind permission from Ref. 49; © Elsevier); (D) Release profiles of BB from CS-β-lactoglobulin nanoparticles in simulated gastric fluids for 0.5 h and in simulate intestinal fluids for another 6 h (without enzyme) (Reproduced with kind permission from Ref. 6; © American Chemical Society)……..10

Figure 1.3: Chemical structure, polymerization, and mechanisms of bicyclic guanidine catalyst. (A) Chemical structures of TBD, MTBD, TBO, and DBU; (B) Ring-opening polymerization of δ-valerolactone (left) and ε-caprolactone (right) using TBD and pyrenebutanol as initiator. For VL the targeted degrees of polymerization were 25 (squares), 50 (circles), and 100 (triangles); for CL they were 50 (squares), 100 (circles), and 200 (triangles). The open symbols represent the polydispersities. (Reproduced with kind permission from Ref. 56; © American Chemical Society); (C) Dual activation of

monomer and initiator by TBD; and (D) Dual activation by TBD strictly through hydrogen bonding (Reproduced with kind permission from Ref. 57; © American Chemical Society)……..14

Figure 1.4: Application of bicyclic guanidine catalysts (TBD, left and DBU, right) for polymer architectures, including (A) pendent group-functionalized polyester (Reproduced with kind permission from Ref. 59; © American Chemical Society), (B) poly(δ-valerolactone) star polymer (Reproduced with kind permission from Ref. 60; © American Chemical Society), (C) cyclic brush polymers (Reproduced with kind permission from Ref. 61; © American Chemical Society), (D) amphiphilic comb-block copolymers (Reproduced with kind permission from Ref. 62; © American Chemical Society), (E) poly(ethylene glycol) hydrogel (Reproduced with kind permission from Ref. 63; © American Chemical Society), and (F) dendrimer-like star polymer (Reproduced with kind permission from Ref. 64; © American Chemical Society)……17

Figure 1.5: Timeline of progress in the electrospinning research…….20

Figure 1.6: Schematic diagram of a standard laboratory electrospinning facility with the surface characterization of non-woven mat, including (A) photo of PVOH (61 kDa) electrospun fibrous mat, (B) optical microscopic image (×10) of PVOH (145 kDa) electrospun fibers, and (C) tapping mode-atomic force microscopy (TP-AFM) image of PVOH (61 kDa) electrospun fibers……23

Figure 1.7: The plot of zero shear viscosity (η_0) as a function of PVOH (61 kDa) concentration with power-law fitting. The two insets are 50 μm × 50 μm TP-AFM image of PVOH beaded fibers electrospun from 90 mg/mL PVOH solution (left), and 100 μm ×

100 μm TP-AFM image of PVOH bead-free fibers electrospun from 150 mg/mL PVOH solution (right)……...26

Figure 1.8: Behavior of the fluid droplet at the tip of the needle. (A) Applied electric field is below the lower threshold, (B) applied electric field is above the higher threshold (Reproduced with kind permission from Ref. 110; © IEEE Industry Applications Society), and (C) Schematic diagram of effect of applied voltage on the formation of the Taylor cone (Reproduced with kind permission from Ref. 111; © Elsevier)……...30

Figure 1.9: Applications of polymer electrospun fibrous mats. (A) Polyethylene terephthalate (PET) electrospun membrane before filtration and after apple juice filtration (Reproduced with kind permission from Ref. 143; © Elsevier); (B) Portable wound healing device based on electrospun nanofiber (www.electrosols.com)； (C) Photographs and SEM images of 10,12-pentacosadiynoic acid (PCDA)-derived electrospun fiber mats obtained before UV irradiation and after UV irradiation for 3 min, and after heating at 100 ^{o}C for 1 min (Reproduced with kind permission from Ref. 141; © Wiley); (D) Scaffold architecture affects cell binding and spreading. (Left and middle) Cells binding to scaffolds with microscale architectures flatten and spread as if cultured on flat surfaces. (Right) Scaffolds with nanoscale architectures have larger surface areas to adsorb proteins, presenting many more binding sites to cell membrane receptors (Reproduced with kind permission from Ref. 144; © The American Association for the Advancement of Science)…….34

Figure 1.10: Electrospun core-shell polymer fibers. (A) Schematic diagram of home-made dual syringe electrospinning platform, and the inset on the left is the photo of home-made coaxial nozzle; (B) Fourier transform infrared spectra of polyvinyl alcohol

(PVOH) electrospun fiber (black curve), polyvinyl alcohol/poly(ε-caprolactone) core/shell fiber (reddish curve), and the two insets are pendent water droplets on the fiber mat surfaces……...36

Figure 1.11: Fiber alignment by gap and rotational object techniques. (A) Fiber distribution on the gap of two metal electrodes after electrospinning; (B) Electrostatic force analysis of a charged nanofiber spanning across the gap; (C) Fiber distribution on the rotational drum collector……..38

Figure 1.12: Representative optical images of (A) random poly(ε-caprolactone) (PCL) electrospun fibers and (D) aligned PCL electrospun fibers; FFT output images of (B) random PCL electrospun fibers and (E) aligned PCL electrospun fibers; Normalized pixel intensity plots as a function of angle acquisition for (C) random fibers and (F) aligned fibers. The angle difference specifically refers to the angle difference between scattering lines and horizontal plane……..39

Figure 2.1: Schematic diagram of a conventional rotational rheometer; two plates of radius *R*, at gap height *H*. The top or the bottom plate rotates with an angular velocity Ω. a Ideal situation in a parallel-plate rheometer, the plates are perfectly parallel; b Sources of error during gap zeroing; a slight parallax (exaggerated in the figure) causes the plates to touch when not parallel, thus introducing a gap error of size ε; c Profile of the fluid sample when placed between nonparallel plates (Reproduced with kind permission from Ref. 180; © Springer)……47

Figure 2.2: (D1) Tapping mode AFM height image (2.5 μm × 2.5 μm), (D2) 3D images (625 nm × 625 nm), and (D3) corresponding section analysis on mica substrates prepared

with 20 mM DTAD concentrations for 15 min. (Reproduced with kind permission from Ref. 183; © American Chemical Society)…….……49

Figure 2.3: Schematic diagram of atomic force microscopy experimental setup…….52

Figure 2.4: Scattering triangle of wave vectors for incident beam $k_{0,}$ scattered beam k, and scattering vector q. θ: scattering angle……55

Figure 2.5: Schematics of a synchrotron radiation facility. The closed circuit on the left represents the storage ring. IS, injection system; RF, radiofrequency cavity; L, beamline; BM, bending magnets; FM, focusing magnets; ID, insertion device. (Reproduced with kind permission from Ref. 194; © Oxford University Press, USA)……..57

Figure 2.6: Schematic representation of the synchrotron X-ray scattering BioCAT-18ID beamline at the APS, Argonne National Laboratory, USA: (1) primary beam coming from the undulator, (2) and (3) flat and sagittaly focusing Si (111) crystal of the double-crystal monochromator, respectively, (4) vertically focusing mirror, (5) collimator slits, (6) ion chamber, (7) and (8) guard slits, (9) temperature-controlled sample-flow cell, (10) vacuum chamber, (11) beamstop with a photodiode, (12) CCD detector (Reproduced with kind permission from Ref 195; © Institue of Physics Publishing)……..…….58

Figure 3.1: Typical tapping mode-atomic force microscopy (AFM) height image (A), dynamic light scattering autocorrelation function and its fitting curve (B), as well as its particle size distribution obtained from Cumulant analysis (C) for chitosan–sodium tripolyphosphate (CS–TPP) particles prepared at initial CS/TPP mass ratio of 3.75. The chitosan concentration was fixed at 1.5 mg/mL and the AFM scan size is 1 μm × 1 μm……...68

Figure 3.2: Effect of initial chitosan/sodium tripolyphosphate (CS/TPP) mass ratios upon particle sizes of CS–TPP particles under different initial chitosan concentrations: 1 mg/mL (empty circles); 1.5 mg/mL (empty square); and 2 mg/mL (solid triangles)……70

Figure 3.3: FTIR spectra of (A) pure chitosan powder (M_w = 330 kDa, degree of deacetylation = 98%), (B) chitosan–sodium tripolyphosphate (CS–TPP) particle prepared at initial CS/TPP mass ratio of 3.75 under 4 min sonication with 3.75 W/mL energy input (the initial chitosan concentration was 10 mg/mL), and (C) sodium tripolyphosphate powder……..….71

Figure 3.4: (A) The curves of apparent viscosity versus shear rate for chitosan (CS) solutions and CS–TPP particle suspensions: (▲) 15 mg/mL chitosan solution; (▼) 10 mg/mL chitosan solution; (◆) 8 mg/mL chitosan solution; (△) 15 mg/mL CS–TPP suspension; (▽) 10 mg/mL CS–TPP suspension; (◇) 8 mg/mL CS–TPP suspension and (B) the plot of zero shear viscosity as a function of chitosan concentration for (●) pure chitosan solution, (▲) CS–TPP nanoparticle suspension, and the plot of particle size as a function of chitosan concentration for (◇) CS–TPP suspensions…….73

Figure 3.5: (A) Storage modulus (G') and loss modulus (G'') as a function of strain (%) for chitosan–sodium tripolyphosphate (CS–TPP) microgels prepared at initial chitosan concentration of 20 mg/mL under 6 min sonication with 3.75 W/mL energy input [•: storage modulus (G') and ○: loss modulus (G'')]. (B) Storage modulus (G', filled) and loss modulus (G'', empty) as a function of angular frequency (ω) at strain = 0.5% for CS–TPP microgels prepared with different particle sizes (circles, 470 nm; up triangles, 415 nm; down triangles, 370 nm; and stars, 340 nm). (C) Effect of particle sizes on the storage

modulus (G') and loss modulus (G'') of CS–TPP microgels [•: storage modulus (G'') and ○: loss modulus (G'')]. Here angular frequency (ω) and strain were fixed at 1 rad/s and 0.5%, respectively……..……75

Figure 3.6: The plot of water contents of chitosan–sodium tripolyphosphate (CS–TPP) microgels versus particle sizes……...76

Figure 3.7: (A) Schematic diagrams of interfacial tension (γ) between CS–TPP particles with different sizes during centrifugation processing. (B) Inter-particle interaction potential profiles of chitosan–sodium tripolyphosphate (CS–TPP) microgels which include van der Waals potential for small-sized CS–TPP particles (a), medium-sized CS–TPP particles (b), and large-sized CS–TPP particles (c); as well as electrostatic potential (d), total potential of small-sized CS–TPP particles (a′), medium-sized CS–TPP particles (b′), and large-sized CS–TPP particles (c′)……82

Figure 4.1: Encapsulation of curcumin by star polymer. Photo image of the solutions of curcumin-star in water, curcumin in water, and curcumin in acetone after filter through 0.2 μm PTFE microfilter (A), and their corresponding UV-Vis spectra (B)…….92

Figure 4.2: Synthesis trace of star polymer. (A) Gel permeation chromatography diagram of mPEG-*b*-PVL arm, star crude and star after purification; (B) ^{1}H NMR spectra of mPEG-*b*-PVL copolymer and star polymer 1……96

Figure 4.3: Surface morphology of star polymer. (A) Tapping-mode AFM height image of mPEG-*b*-PVL star polymer deposited on the mica surface; (B) Section analysis of single mPEG-*b*-PVL star polymer…….98

Figure 4.4: SAXS analysis of the mPEG-*b*-PVL copolymer and the nanogel star polymer 1 in non-selective solvent (THF), including (A) SAXS profiles with Gaussian chain

fitting and (B) Kratky plots (concentration, 11.7 mg/mL) of the mPEG-*b*-PVL copolymer in THF and the mPEG-*b*-PVL star polymer (concentration, 3.3 mg/mL) in THF. The SAXS profile of the mPEG-*b*-PVL copolymer in THF is best-fit by the Debye function. The intermediate and high Q regions for the nanogel star polymer in THF and the high Q region for the diblock copolymer are also fit by a power law. The inset is the Holtzer plot of mPEG-*b*-PVL star polymer (concentration, 3.3 mg/mL) in THF……...101

Figure 4.5: SAXS analysis of the mPEG-*b*-PVL micelle and the nanogel star polymer in a block selective solvent (water), including (A) SAXS profiles fit with a spherical model; (C) classical Guinier plot of the mPEG-*b*-PVL copolymer in water at various concentrations (1.82 mg/mL~6.3 mg/mL); (B) SAXS profiles fitted using a cylindrical model with cylinder-related fitting; (D) modified and (E) classical Guinier plot of the mPEG-*b*-PVL star polymer in water at various concentrations (1.52 mg/mL~5.26 mg/mL); and (F) effective structure factor of the mPEG-*b*-PVL star polymer in water at concentrations of 3.26 mg/mL and 5.26 mg/mL. The SAXS profile of the mPEG-*b*-PVL copolymer in water is best-fit by either a solid sphere form factor or a core-shell sphere form factor, while the SAXS profile of the mPEG-*b*-PVL star polymer is best-fit by either a cylinder form factor or a core-shell cylinder form factor. The Guinier fittings for a compact sphere and rod are performed at low Q region with $Q*R_g < 1.5$. ……..105

Figure 4.6: Loading capacity and encapsulation efficiency of (A) mPEG-*b*-PVL star polymer and (B) mPEG-*b*-PVL block copolymer for curcumin under different initial mass ratio of [curcumin]/[star polymer]…….…….110

Figure 5.1: Tapping mode atomic force microscopy (TPAFM) images of zein/F127 composite films with different F127 loadings. Height images: (A) 0% F127, (B) 10%

F127, (C) 20% F127, (D) 35% F127, (E) 50% F127, and (F) 100% F127; and phase images: (G) 50% F127, and (H) 100% F127. The scan size is fixed at 10 μm×10 μm……122

Figure 5.2: The plot of averaged root-mean-square (RMS) roughness of zein/F127 composite film surfaces versus F127 loadings. The insets are tapping mode atomic force microscopy height images of zein/F127 composite films with F127 loadings of 0%, 50%, and 100%, respectively……124

Figure 5.3: (A) Melting temperature (T_m) alternation of zein/F127 composite films with different F127 loadings (10%~75%); (B) Glass transition temperature (T_g) change of zein/F127 composite films with different F127 loadings (0%, 35%, and 50%); and (C) the plot of the crystalline melting enthalpy (ΔH) versus F127 loading. The solid line in (C) was used to guide the eyes……...126

Figure 5.4: Tensile stress-strain curves of zein/F127 composite films with F127 loadings of (a) 10%, (b) 20%, (c) 35%, and (d) 50%.....129

Figure 5.5: (A) Fourier transform infrared spectra of zein/F127 composite films with F127 loadings of (a) 0%, (b) 10%, (c) 20%, (d) 35%, (e) 50%, (f) 75%, (g) 100% within the wavenumber range of 4000~600 cm^{-1}; Best fit curves for the self-deconvoluted FTIR spectra using nonlinear regression analyses: (B) The overlapped –OH, $–NH_2$, and CH stretching bands (3600~3000 cm^{-1}) in pure zein film (0% F127 loading), and (C) zein/F127 blend film (35% F127 loading). The hydrogen bonding band was fitted with Gaussian functions using peak positions obtained from second derivative analysis.....132

Figure 5.6: (A) Small-angle X-ray scattering (SAXS) profiles of zein/F127 composite films with different F127 loadings (10%~100%); (B) wide-angle X-ray scattering (WAXS) profiles of zein/F127 composite films with F127 loadings of 20% (dash line) and 50% (solid line); (C) the plots of averaged long periodicity *d* (solid circles) and polar-apolar interfacial area α_p (solid triangles) versus F127 loading for the zein/F127 composite films……135

Figure 5.7: Mechanism of F127 crystallization in the zein/F127 composite films with different F127 loadings: (A) IF(n=0) and IF(n=1) crystal structures of PEO-PPO-PEO proposed by Zhang et al. (*1*), and zein domain in films; (B) crystallite formed at 20% F127; (C) branch-like (edge-on) lamellae formed at 50% F127 with eye perspective perpendicular (*c* axis) to the *a*-*b* plane; and (D) flat-on lamellae formed at 100% F127 with eye perspective perpendicular to the *a*-*c* plane. *a*-*b* plane is the film surface while *c* coordinate is perpendicular to the film surface…….……...139

Figure 6.1: Apparent viscosity of zein fluids and curcumin-zein complex fluids under concentrations from 40 w/v% to 55 w/v%. The curves of unfilled symbols represent pure zein solutions at different concentrations. The curves of solid symbols represent zein solutions with the addition of 5 w/v% curcumin…….150

Figure 6.2: Fluorescence images (10×) of curcumin-loaded zein fibers electrospun under solution concentrations from 40 w/v% to 55 w/v%. The insets are the fast Fourier transform (FFT) output images of the fluorescence images……....151

Figure 6.3: Curcumin loadings in zein fiber mats electrospun at 50 w/v%. The plot of curcumin loading in zein mat as a function of initial [curcumin]/[zein] mass ratio. The

insets are the corresponding photos (first row) and fluorescence images (second row) of zein mats loaded with different quantities of curcumin……...153

Figure 6.4: Tapping mode AFM height images of (A), (C), (F) zein fibers and (D), (G) curcumin-loaded zein fibers electrospun at concentrations from 40 w/v% to 55 w/v%; Fiber thickness distribution of (B) zein fibers electrospun at 40 w/v%, (E) curcumin-loaded/unloaded zein fibers electrospun at 50 w/v%, and (H) curcumin-loaded/unloaded zein fibers electrospun at 55 w/v%.....156

Figure 6.5: Tapping mode AFM images of zein/poly(caprolactone) (3:7 w/w) aligned fibers deposited by wired drum rotator operated at rotational rate of (A) 0 RPM, (B) 130 RPM, (C) 580 RPM, and (D) 850 RPM; Corresponding fast Fourier transform (FFT) output images (E~H); And normalized pixel intensity versus degree of angle plots (I~L). Note that the peaks generated by radial summation in the oval profile plug-in of Image-J containing information of fiber alignment……...158

Figure 6.6: Cytotoxicity of the blank zein and curcumin-loaded zein fiber mats to the HepG2 cells. Curcumin content in the fibers with respect to zein: 0% (pure zein), 2.8%, 6.5%, and 12%.....160

Figure 6.7: Fiber thickness (solid circle) and root-mean-square (RMS) roughness (solid square) of zein/poly(caprolactone) (3:7 w/w) aligned fibers as a function of v_c/v_f ratio. The insets are representative 50 μm×50 μm AFM height images of zein/PCL fibers electrospun at different v_c/v_f. The plot of fiber thickness~v_c/v_f is fitted by power-law equation $y=bx^a$, and the plot of RMS roughness~v_c/v_f is fitted by inverse second order polynomial equation: $y = a + \frac{b}{x} + \frac{c}{x^2}$ ……165

Figure S4.1: (A) Emission spectra of pyrene in mPEG-*b*-PVL solution with a concentration of 0.001 mg/mL. (B) Change of the intensity ratio (I_1/I_3) from excitation spectra of pyrene with various concentrations of mPEG-*b*-PVL……174

Figure S4.2: Cytotoxicity of mPEG-*b*-PVL copolymer and star polymer in HepG2 cells. Mean ± standard deviation (n =8)……....175

Figure S5.1: Photo image of zein/Pluronic F127 composite films containing 10%, 50%, and 75% of Pluronic F127……...176

Figure S5.2: DSC thermogram of pure Pluronic F127 film (pellet)……...176

Figure S6.1: Photo of a home-made copper wire-framed drum fiber collector……..177

Contents

ABSTRACT……...……...ii

ACKNOWLEDGMENTS……..iv

List of Schemes…….v

List of Tables……..……..vi

List of Figures……..vii

CHAPTER 1

MULTIPLATFORM DELIVERY SYSTEM…….1

1.1 DIVERSITY OF CONSUMER GOODS……...1

1.2 SMALL MOLECULE CROSSLINKING……..2

1.3 ORGANOCATALYTIC RING-OPENING POLYMERIZATION (OROP)…….11

1.4 ELECTROSPINNING PROCESS……19

CHAPTER 2

CHARACTERIZATION……43

2.1 RHEOLOGY……43

2.2 ATOMIC FORCE MICROSCOPY……...47

2.3 SMALL-ANGLE X-RAY SCATTERING…….……52

CHAPTER 3

RHEOLOGICAL PROPERTIES OF CHITOSAN–TRIPOLYPHOSPHATE COMPLEXES: FROM SUSPENSIONS TO MICROGELS……..59

3.1 INTRODUCTION……...……..59

3.2 MATERIALS AND METHODS……...……62

3.3 RESULTS……...…66

3.4 Discussion……...……...77

3.5 Conclusion…….82

CHAPTER 4

ASSEMBLY OF MPEG-*B*-PVL BLOCK COPOLYMER AND STAR POLYMER FOR CURCUMIN ENCAPSULATION……84

4.1 Introduction…….84

4.2 Experimental…….86

4.3 Results and discussion……95

4.4 Conclusions…….112

CHAPTER 5

STRUCTURE AND PHYSICAL PROPERTIES OF ZEIN/PLURONIC F127 COMPOSITE FILMS……...……113

5.1 Introduction……...……113

5.2 Materials and Methods……117

5.3 Results and Discussion……...……..121

CHAPTER 6

DEVELOPMENT OF HIGHLY-ALIGNED CURCUMIN-LOADED ZEIN FIBERS……...……141

6.1 Introduction……...……141

6.2 Experimental……...……144

6.3 Results and discussion……..149

CHAPTER 7……...……169

FUTURE WORK……...…167

SUPPLEMENTARY INFORMATION (SI) FOR CHAPTER 4……...…...170

S4.1 METHODS…….170

S4.2 RESULTS……...…172

SUPPLEMENTARY INFORMATION (SI) FOR CHAPTER 5……..176

SUPPLEMENTARY INFORMATION (SI) FOR CHAPTER 6……..……177

BIBLIOGRAPHY……..177

Chapter 1

Multiplatform Delivery System

1.1 Diversity of consumer goods

Health care is one of the dominant drivers of consumer markets in the 21st century. Upon progress of research and development, diversity of consumer goods explodes dramatically. The relevant benefits turn out to be the convenience of daily life, comprehensive nutrition, and long-term economic prosperity. The categories of personal care and health food have made a good performance in the sales and marketing during past half decades. According to Schaumburg, Ill.-based market research firm SPINS, natural products shoppers pent $295.3 million on natural and organic personal care in 2010, a 7.1% increase from 2009. Also, functional food market alone expanded at an annual growth rate of 5.7% between 2007 and 2012 (http://www.foodsciencecentral.com). The soaring sales numbers suggests not only the purchasing capability of consumer but also the products' diversity.

Behind the product diversification conceals varying biopolymer platforms to support the innovation of ingredient, packaging, and detection. On the contrary, fabrication of novel biopolymer platforms ensures the technical knowledge for product innovation, and consumers' complicated requirements. For instance, curcumin, one multi-functional

nutraceutical can be integrated into either beverage or band-aid for oral and transdermal administrations, respectively. Hence, the diversity of consumer goods is driving us to explore and fabricate advanced biopolymer platforms. In chapter 1, three approaches, small molecule crosslinking, organocatalytic ring-opening polymerization (OROP), and electrospinning have been generally introduced. The latter chapters 3, 4, 6 will put emphasis on each approach. Chapter 5 describes a conventional polymer blend technique to improve the solid zein material which is regarded as a reference for zein fiber material (Chapter 6).

1.2 Small molecule crosslinking

Basically, linear polymer chains behave as a random coil in good solvents (i.e. polystyrene in tetrahydrofuran). Charged polymer chains have stiffer backbones than neutral ones due to electrostatic repulsion along the chain. Such stiff conformation can be changed by small molecules (i.e. sodium tripolyphosphate), which further renders polymer chains collapse into condensed state. Specifically-speaking, polymers form particles, complexes, and aggregates in the condensed state. This molecular crosslinking method can be used to form polymer nanoparticle for nutraceutical delivery. The polymer candidates can be both synthetic polymers and natural biopolymers. For food-relevant application, we tend to use natural polymers such as proteins and polysaccharides.

1.2.1 Crosslinking mechanism

Different crosslinkers interact with biopolymers through distinct mechanisms. Figure 1.1 shows the chemical structures of 4 typically-used crosslinkers which are glutaraldehyde, genipin, sodium tripolyphosphate, and sodium sulfate. They are representative crosslinkers used in the particle formation, but other emerging crosslinkers like citric acid

(*1*), tartaric acid (*2*), Fe_3O_4 nanoparticles (*3*), and even CdSe/ZnS quantum dots (*4*) cannot be ignored by their contribution to functional particle formation.

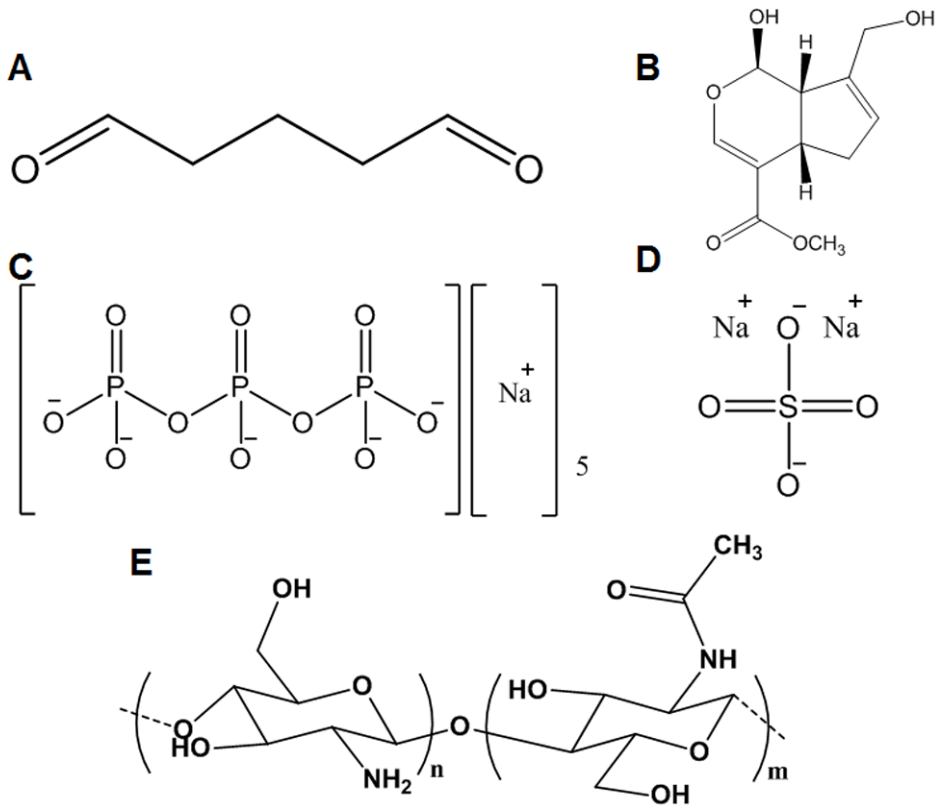

Figure 1.1: Chemical structures of small molecule crosslinkers including (A) glutaraldehyde, (B) genipin, (C) sodium tripolyphosphate (STPP), (D) sodium sulfate, and cationic polymer like (E) chitosan composed of glucosamine linked by β(1→4) glycosidic bond with degree of deacetylation of n/(n+m).

Glutaraldehyde is a common crosslinker which is widely used in the sampling of microscopy, enzyme immobilization, and stabilization of protein crystal (Figure 1.1A). The reaction between glutaraldehyde and biopolymer is complicated and different under different conditions. Glutaraldehyde can polymerize into long chain under alkaline condition (*5-7*). Hence, the crosslinking involves monomeric glutaraldehyde and polymeric glutaraldehyde. Generally, one proposed mechanism is that amino group attacks on the aldehyde group to form a non-conjugated Schiff base. The polymerization

of glutaraldehyde can affect the crosslinking which involve the formation of Schiff base and C-N bond. Genipin is a traditional chemical for dyeing in foods and fabrics in East Asia (Figure 1.1B) (*8-9*). It can be synthesized by hydrolysis of geniposide, an aglycone of geniposide isolated from the fruits of *Gardenia jasminoides (10)*. Its crosslinking mechanism of protein and polysaccharide lies in the nucleophilic attack by amino group on C-3 of heterocyclic genipin. Besides, the ester group of genipin can also participate in the reaction with amino group (*11*). Sodium tripolyphosphate (STPP) is a sodium salt of the polyphosphate penta-anion which can be produced by heating a mixture of disodium phosphate, Na_2HPO_4, and monosodium phosphate, NaH_2PO_4 (Figure 1.1C) (*12*). Famous for the capability of metal cations' chelation (i.e. Mg^{2+}, Ca^{2+}), STPP has been commercially used as a water softener in detergent and preservative in seafood, poultry, and animal feed (*13*). STPP has also been listed as "generally recognized as safe" (GRAS) by the United States Food and Drug Administration. Due to its dense anions, STPP can interact with cationic polymers (i.e. chitosan) through electrostatic interaction to form particles. Another crosslinker is sodium sulfate, which carries two negative charges (Figure 1.1D). This compound can be produced by the neutralization of sulfuric acid and sodium hydroxide, hence it is also a sodium salt of sulfuric acid. It is also a byproduct during the manufacture of other chemicals (i.e. sodium dichromate). Hence, sodium sulfate is among major commodity chemicals in the world. As a low-cost chemical, it has been used as a filler in powdered home laundry detergents, and also in the Kraft process for the manufacture of wood pulp. Sharing the similar structure with STPP, sodium sulfate can interact with cationic polymers through electrostatic interaction as well.

However, its crosslinking capability is expected to differ from STPP due to their charge difference.

1.2.2 Crosslinked particle applications

Those different biopolymer particles generated by small molecule crosslinking method have different applications. We take chitosan, a cationic biopolymer extracted from exoskeleton of crustaceans (i.e. crabs and shrimps), (Figure 1.1E) as an example for small molecule-crosslinked particle applications. Glutaraldehyde-crosslinked chitosan (GLA-CS) particles are relatively large, usually on the order of micron-meter. It is well-documented that chitosan has a high affinity to various strongly heavy and toxic metal ions (i.e. Cd^{2+}, Cr^{3+}, and Hg^{2+}) (*14*). Among different sorbent materials like clay, lignin, and solute, chitosan displays much better adsorption capacities (*15*). The maximum adsorption capacities of chitosan for Cd^{2+}, Cr^{3+}, and Hg^{2+} could reach 558, 92, 1123 mg/g chitosan, respectively (*15*). Based upon this feature, GLA-CS particles are micron-sized materials suitable for chromatography resin (*16*) and waste water cleaning agent (*17*). Ngah et al. compared the Cu(II) ions adsorbing capability from aqueous solution between chitosan and GLA-CS particle (*16*). Although chitosan has a higher adsorption capacity than crosslinked chitosan beads, GLA-CS particle displays a slow swelling behavior and low pH stability, two essential characteristics for a resin in ion-exchange chromatography columns. In addition to metal ion binding properties, GLA-CS particle also provides a cargo for loading drugs (*18-19*). Those GLA-crosslinked microparticles provide us with a sustainable release profile of the incorporated drug. The drug release rate can be controlled by GLA cross-linking density. Jameela et al. stated that CS micospheres of high crosslinking density may just release 25% of the inner drug over 36 days (*18*).

Differently, Nayak et al. argued that his formulation of GLA-CS microparticles crosslinked by 35% GLA with a 1:6 drug/chitosan ratio displayed a faster release profile and 75% drug could be released within 12 h (*19*). However, the glutaraldehyde is still a big concern for safety issue. As a strong disinfectant, glutaraldehyde is toxic and can cause severe irritation of several organs. When protein is loaded into GLA-CS microparticle, glutaraldehyde is very likely to penetrate the particle membrane, interact with the incorporated protein, and fix the protein. For comparison, genipin-crosslinked chitosan (GEP-CS) is less toxic, more environmentally-friendly, and ideal for clinical use. By using 3T3 fibroblasts through the MTT assay, Sung et al. compared the cytotoxicity of glutaraldehyde and genipin, and demonstrated that genipin was approximately 5000~10,000 times less cytotoxic than glutaraldehyde (*20*). In addition to its less cytotoxicity, GEP-CS particles show better swelling capability than GLA-CS particles. Compared with GEP-CS particles, GLA-CS particles display a wide range of swelling ratios from 100% to 225% upon different crosslinking periods (*21*). Also, the apparent viscosity of GEP-CS fluid is lower than that of GLA-CS fluid, and low viscosity can be kept within a long crosslinking period. With such processing convenience and structure flexibility, the controllable release of small molecular drugs (*21*), proteins (i.e. bovine serum albumin (*22-23*)), and essential oils (i.e. *Zanthoxylum limonella* oil (*24-25*)) can be achieved by GEP-CS particles. The structural flexibility of GEP-CS particles resulted in a wide releasing period of bovine serum albumin (BSA) ranging from 4 h to 31 days, and the total amount of released BSA (12%~27%) can be controlled by GEP concentration (*23*). By a simple rinsing method, the initial burst release of BSA from GEP-CS particle can also be effectively reduced (*22*). For GEP-CS particle-encapsulated small molecular

drug, not only crosslinking density but also chitosan-drug interaction plays an important role in tailoring the drug release kinetics. Mi et al. reported that the electrostatic interaction between chitosan and indomethacin at high pH eventually enhanced the dissolution of indomethacin (*21*). Other than release study, others focused upon the characterization of particulate membrane. Based upon the fluorescence of GEP-CS conjugate, Chen et al. established a noninvasive and *in situ* method to directly visualize the membrane composed of genipin cross-linked alginate-chitosan (GCAC) microcapsule, quantify the membrane thickness (37 μm) and its relative intensity by using confocal laser scanning microscopy (CLSM) (*26*). In addition to direct characterization, this fluorescence-based technique may be utilized to study the membrane elasticity at micro-level. Although genipin is safe to use, this crosslinker still has its own limitations like strong blue pigment, which retards its massive applications.

Milder crosslinking by sodium tripolyphosphate (STPP) and sodium sulphate (SS) has also been utilized in the fabrication of chitosan particulate systems. The main drive for the formation of STPP or SS crosslinked particles is electrostatic interaction, also named ionotropic gelation, which can be influenced by factors such as medium pH, ionic strength, molecular weight of chitosan, and initial mass ratios of [CS]/[crosslinker]. Hence, prior to applications, the optimization of STPP-CS particle is of essence to ensure the particular stability and the optimal performance (*27-32*). For particle optimization, particle size and zeta potential are viewed as two important parameters, which largely affect the particle arterial uptake (*33-34*) and storage stability (*35*), respectively. It is commonly reported that within appropriate chitosan concentration (*30*), the size of STPP-CS particle is in a linear relationship of chitosan concentration (*27-28, 31*). Another

important parameter is CS/STPP mass ratio. Although chitosan can be prepared under different molecular weights and concentration, the optimal particle size is empirically within certain range (3~7 (*27*) or 4~6 (*32*)). The STPP-CS particle platform was used to entrap a rich variety of molecules, which involve dye (*36*), protein (*32, 37-38*), drug (*31*), and DNA (*39*) or RNA (*40*). More or less, STPP-CS particle platforms are designed to ultimately aid the body delivery of those molecules, however, most of them are still lingering at the stage of physical characterization, and post-stage *in vivo* cell, animal study are further required. Instead of using active compounds, the initial trials for STPP-CS particles were entrapment of brilliant blue and FITC-dextran (*36*). The STPP-CS particle displayed a long-term release of hydrophobic dye (2 months) and a short-term release of hydrophilic dextran (2 days), which directs us to formulate food or medical ingredients with different release profiles. In addition to noticeable release functionality of cargo itself, surface structure of particles cannot be ignored, either. Due to positive charges on the chain backbone, chitosan is able interact with the negatively-charged components in the cell membrane like mucin (*41*) and phospholipid (*42-43*). The strong electrostatic, hydrophobic interactions support the chitosan-based mucoadhesive delivery system (*44*). Figure 1.2A exhibits a model for the pig gastric mucin removal from negatively charged phospholipid monolayers caused by chitosan. Mucin interacted with phospholipid through hydrophobic interaction, but the electrostatic interaction between mucin and chitosan was strong enough to remove the protein from interface (*41*). By monitoring glycemia through *in vivo* alloxan-induced diabetic rat model, Pan et al. demonstrated that CS-STPP cargo not only protected the insulin in the harsh gut environment, but also enhanced intestinal absorption of insulin (Figure 1.2B) (*30*). Mao

et al. further utilized surface chemistry to modify CS-SS particle with functional ligands, such as transferrin, KNOB protein, and PEG (*39*). The first two ligands improved the transfection performance of CS-STPP particle, while PEG enhanced the storage stability and made the formulation that could be lyophilized without loss of transfection. Besides, Chen et al. fabricated STPP-crosslinked chitosan/β-lactoglobulin core-shell nanoparticles for nutraceutical delivery, and the compound's slow release in stomach and quick release in small intestine suggest its potential for oral administration (Figure 1.2C) (*45*).

The above four crosslinkers are classic and representative, covering both covalent and non-covalent binding. Meanwhile, with the advanced approaches, fresh functional crosslinkers like negatively-charged CdSe/ZnS quantum dots (QD) are springing up as well. Those CS-QD hybrid nanospheres themselves acted as labeling agent in cell imaging which could be used in imaging of tumor in tumor-bearing mice via intratumoral administration (*4*). Figure 1.2D displays an *in vivo* fluorescence imaging of H22 tumor-bearing mice after intratumoral injection of CS-QD hybrid nanospheres under different time slots. The fluorescence signal was observed in the tumor region, while the solid H22 tumor was clearly distinguished from the normal tissues.

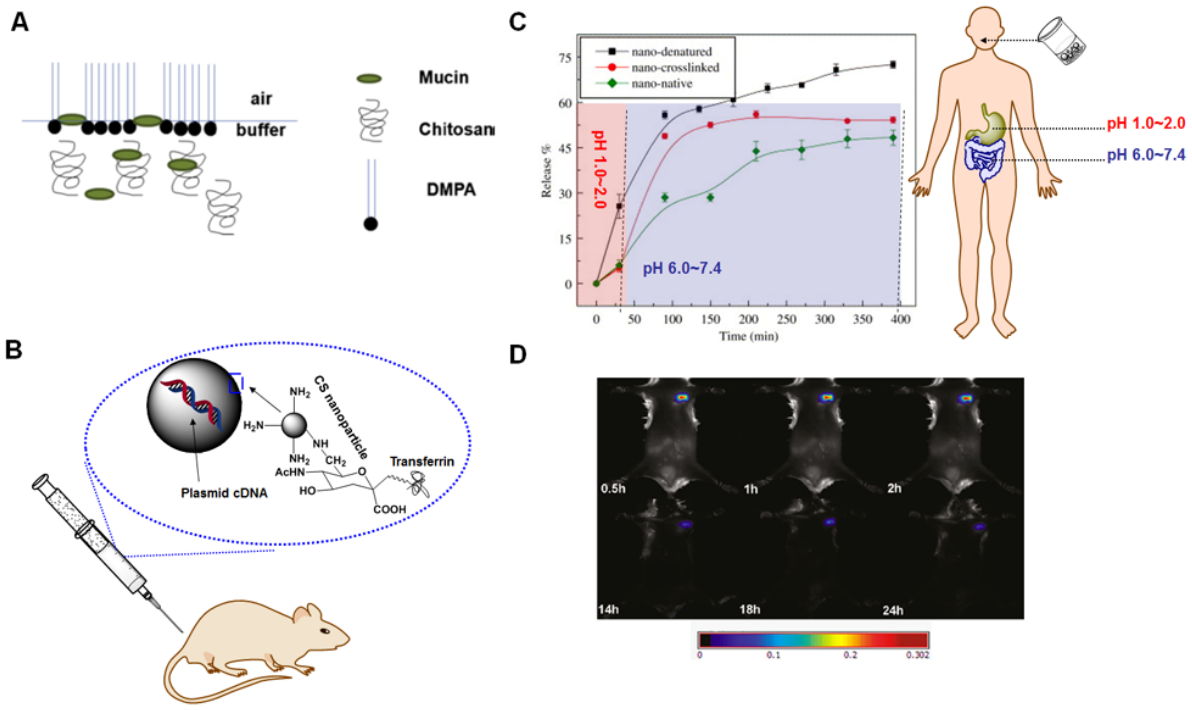

Figure 1.2: Physical property, biomedical, and bioimaging applications of chitosan particle. (A) Model for the pig gastric mucin removal from negatively charged phospholipid monolayers caused by chitosan (Reproduced with kind permission from Ref. 42; © Elsevier); (B) Intravenous administration of transferrin-conjugated chitosan particle through mice; (C) Release profiles of BB from CS-β-lactoglobulin nanoparticles in simulated gastric fluids for 0.5 h and in simulate intestinal fluids for another 6 h (without enzyme) (Reproduced with kind permission from Ref. 46; © American Chemical Society); (D) Fluorescence imaging of H22 tumor-bearing mice 24 h after i.v. injection of CS-QD hybrid nanospheres. Right is the fluorescence imaging of dissected tumor from the mouse in the left (Reproduced with kind permission from Ref. 5; © Elsevier).

1.2.3 Crosslinker comparison

Molecular crosslinking results in the nanoparticle formation by collapsing polymer chains into condensed format. Glutaraldehyde, genipin, sodium tripolyphosphate, and sodium sulphate can be categorized into two groups, covalent crosslinker and non-covalent crosslinker. Glutaraldehyde and genipin belong to covalent crosslinker, while sodium tripolyphosphate and sodium sulphate are classified into non-covalent crosslinker. However, appropriate use of those crosslinkers is important to design and fabricate ideal delivering vehicle. Each of those crosslinkers has its own advantages and disadvantages. Glutaraldehyde has strong crosslinking capability, but it is very toxic. Genipin, extracted

from natural herb, is much environment-friendly, however, the blue pigment also retards its application in food products. Both covalent crosslinkers generate micro-sized particles, usually on the order of μm or mm. Compared with two covalent crosslinkers, sodium tripolyphosphate and sodium sulphate generate more flexible release profiles of key compounds. Meanwhile, their crosslinking strength is much lower, and sometimes particle requires the combination of multiple crosslinkers (i.e. sodium sulfate and chloroquine diphosphate).

1.3 Organocatalytic ring-opening polymerization (OROP)

Ring-opening polymerization (ROP) is a polymerization method, in which cyclic monomers break their rings, and polymerize into macromolecule through ionic propagation. According to different catalysts, ROP can be categorized into three approaches, including organocatalytic, organometallic, and enzymatic ring-opening polymerization. Among them, organocatalytic ring-opening polymerization (OROP) is of particular interest due to its metal-free processing, which has a better affinity to biological systems. With the advanced catalytic chemistry, cyclic guanidine-based catalysts (i.e. triazabicyclodecene, TBD) improve the controllability and efficiency of ROP. And it is hard to imagine that the ring-opening polymerization of lactide with 0.1% TBD in THF can achieve yield 99 %, M_n = 23,000, PDI=1.09 in 20 sec (*46*). So far, it is among the most active catalysts for ring-opening polymerization (*47*).

1.3.1 Bicycled guanidine-based organocatalyst

Typical guanidine catalysts are 1,5,7-triazabicyclo[4.4.0]dec-5-ene (TBD) (*48*), *N*-methyl-TBD (MTBD), 1,4,6-triazabicyclo[3.3.0]oct-4-ene (TBO), and 1,8-diazabicyclo[5.4.0]-undec-7-ene (DBU) (Figure 1.3A). Those bicyclic compounds are

strong base with high pK_a in organic solvents (TBD, pK_a=26.0 in acetonitrile (*49*) or THF (*47*); MTBD, pK_a=25.0 in THF (*47*)). These basic compounds are used as catalysts for a various chemical reactions, including Wittig reactions (*50*), nitroaldol (Henry) reaction (*51*), Michael addition reaction (*52*), Strecker reaction (*53*), and transesterification reaction (*54*). Besides, they also serve as catalysts for polymerization of cyclic esters such as lactide, δ-valerolactone, and ε-caprolactone (*46*). Among four catalysts (Figure 1.3A), TBD is the most versatile and can ring open various monomers like lactic acid, β-butyro-, δ-valero-, and ε-caprolactone (*55*). By contrast, DBU and MTBD only show ring-opened products of lactic acid, but only starting materials of lactones. Thus, TBD is taken as a representative example for illustrating the functionality and mechanism of this type organocatalyst. With merely low loading of TBD (0.5%), the molecular weights of poly(δ-valerolactone) and poly(ε-caprolactone) increased linearly with conversion%, which was a feature of living polymerization (Figure 1.3B) (*55*). The living polymerization of lactone resulted in low polydispersity. Comparatively-speaking, TBD (blue circle in Figure 1.3A) displays better catalysis than MTBD, which is attributed to one more protonated nitrogen in TBD, which enables TBD to function as a bifunctional transesterification catalyst. Using computational chemistry, two pathways involving acetyl transfer (Figure 1.3C) and hydrogen bonding (Figure 1.3D) were investigated for the ring-opening polymerization of L-lactide using a guanidine-based catalyst (*56*). For acetyl transfer pathway, TBD first covalently binds to the ester group of the L-lactide, and then the adjacent nitrogen forms hydrogen bond with another alcohol to achieve one cycle of transesterification for polyester formation. For hydrogen bonding pathway, nucleophilic attack of the imine nitrogen at the carbonyl group of the L-lactide through

hydrogen bond, and the attraction of the incoming alcohol by adjacent nitrogen result in two pairs of hydrogen bonding. The activated alcohol facilitates esterification, and meanwhile the catalyst switches to bind to the ring oxygen neighboring the carbonyl group. Those two pairs of hydrogen bonds between catalyst and lactide facilitate the ring opening of lactide. The hydrogen bonding mechanism of bicyclic guanidine is analogous to that of thiourea-amine catalysts (*57*).

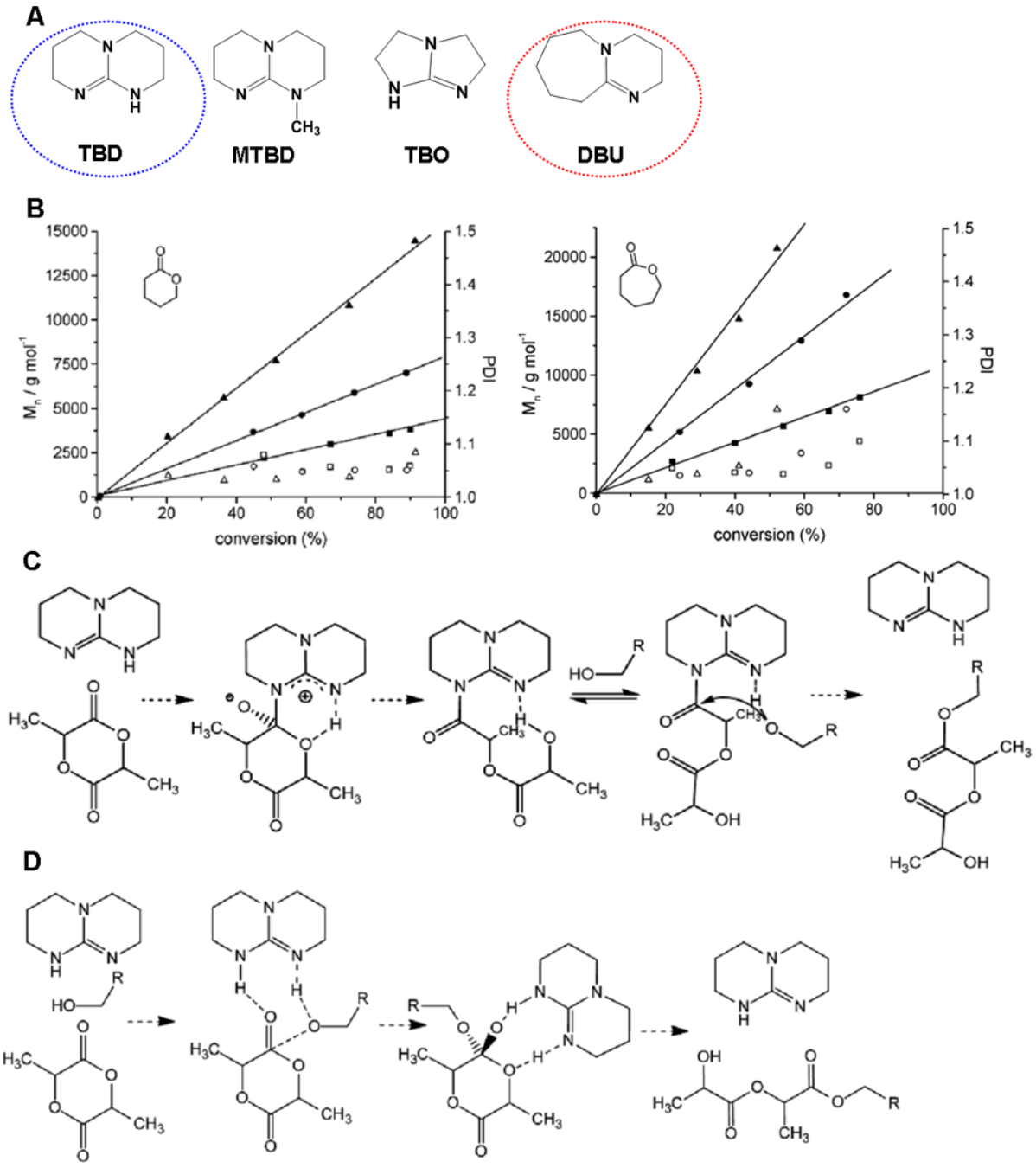

Figure 1.3: Chemical structure, polymerization, and mechanisms of bicyclic guanidine catalyst. (A) Chemical structures of TBD, MTBD, TBO, DBU, and two frequently-used catalysts are highlighted with dot circles; (B) Ring-opening polymerization of δ-valerolactone (left) and ε-caprolactone (right) using TBD and pyrenebutanol as initiator. For VL the targeted degrees of polymerization were 25 (squares), 50 (circles), and 100 (triangles); for CL they were 50 (squares), 100 (circles), and 200 (triangles). The open symbols represent the polydispersities. (Reproduced with kind permission from Ref. 56; © American Chemical Society); (C) Dual activation of monomer and initiator by TBD; and (D) Dual activation by TBD strictly through hydrogen bonding (Reproduced with kind permission from Ref. 57; © American Chemical Society)

1.3.2 Bicyclic guanidine-involved polymer synthesis

The bicyclic guanidine catalysts have been used to synthesize different macromolecular architectures. Recently, synthesis of different topologies has been proved-of-concept, which offers potential biomaterials, especially in the field of drug delivery. The polymer synthesis covers a broad range of architectures, involving group-functionalized polyester (*58*), polyester star polymer (*59*), cyclic brush polymer (*60*), amphiphilic comb-like copolymer (*61*), poly(ethylene glycol) hydrogel (*62*), and dendrimer-like star polymer (*63*) (Figure 1.4). In the category of TBD, different monomers and macroinitiators, unfunctionalized or functionalized can be combined with organocatalyst for synthesis of distinct molecular topologies. Kim et al. demonstrated a facile route to synthesize benzyl mercaptans functionalized co-polyester by one-step Michael addition reaction, which generally paved the way for hydrophilic or hydrophobic group functionalization of polyester (Figure 1.4A) (*58*). In addition to those functionalized or unfunctionalized linear copolymers, high-order macromolecules like unimolecular star polymer and cyclic brush polymer can also be benefited from TBD catalyst. Appel et al. used TBD in the "arm first living polymerization" for the synthesis of poly(δ-valerolactone) star polymer (Figure 1.4B) (*59*). His method provides us with a rapid, room temperature synthesis route which can be scaled up to 10 grams for controllable lactone star polymer. Very recently, Zhang et al. combined ring-expansion metathesis polymerization (REMP) and "grafting from" technique for the synthesis of cyclic brush polymer (Figure 1.4C) (*60*). Interestingly, they directly used cyclic macroinitiators for the TBD-catalyzed cyclic ester ring-opening polymerization (ROP) for side-chain brush, whose concept can be extended

to other controlled polymerization techniques like Atom transfer radical polymerization (ATRP) (*64*) or RAFT (*65*).

For less-base DBU, synthesis also covers multiple polymer architectures. Fukushima et al. synthesized amphiphilic comb-block copolymers composed of poly(ethylene glycol) (PEG), poly(methylcarboxytrimethylene carbonate) (PMTC), and poly(lactide) branches by using DBU-based ROP tool (Figure 1.4D) (*61*). The resulting comb polymer not only occupied improved mechanical- and thermal- properties, but also showed a low critical micelle concentration (CMC) which was a good sign of drug delivery agent for body injection. Nederberg et al. formed a PEG-network gel by ring-opening cyclic carbonate, a crosslinking monomer in the presence of DBU (Figure 1.4E) (*62*). The PEG-network gel with an open co-continuous (water-gel) porous structure swells significantly in aqueous environment, whose functionality can be fine-tuned by incorporating additional co-monomers. Coady et al. designed a facile synthesis route for dendrimer-mimic star polymer by using rapid chain extension polymerization, which negates the need of extra protection/deprotection steps for regular dendrimer (Figure 1.4F) (*63*). This synthesis provides high fidelity, fast kinetics, and easy catalyst removal, rendering it an ideal polymer delivering agent.

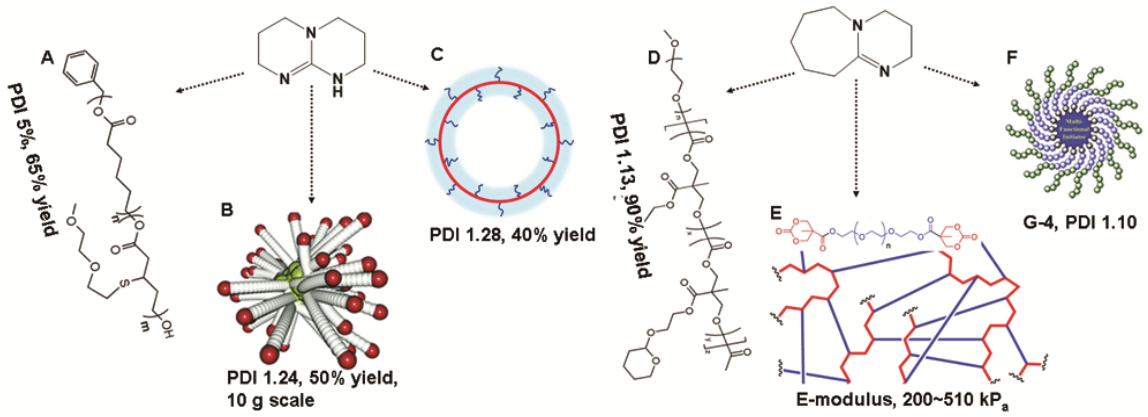

Figure 1.4: Application of bicyclic guanidine catalysts (TBD, left and DBU, right) for polymer architectures, including (A) pendent group-functionalized polyester (Reproduced with kind permission from Ref. 59; © American Chemical Society), (B) poly(δ-valerolactone) star polymer (Reproduced with kind permission from Ref. 60; © American Chemical Society), (C) cyclic brush polymers (Reproduced with kind permission from Ref. 61; © American Chemical Society), (D) amphiphilic comb-block copolymers (Reproduced with kind permission from Ref. 62; © American Chemical Society), (E) poly(ethylene glycol) hydrogel (Reproduced with kind permission from Ref. 63; © American Chemical Society), and (F) dendrimer-like star polymer (Reproduced with kind permission from Ref. 64; © American Chemical Society)

1.3.3 Comparison with organometallic and enzymatic ROP

Compared with conventional catalysts (organometallic catalyst and enzymatic catalyst), organocatalysts hold advantages that individual organometallic or enzymatic catalyst does not have. Enzymes like various lipases share the same biocompatibility as organocatalyst, however their reaction efficiency and molecular weight limit are the concerns. Uyama et al. synthesized poly(ε-caprolactone) by using *Pseudomonas fluorescens* lipase for 10 days, which afforded a polyester with mere average molecular weight of 7.0×10^3 (*66*). Higher polymerization temperatures (i.e. 75 ^{o}C) and different lipase species (i.e. *Candida cylindracea* lipase) can result in higher molecular weight poly(lactone) (*67*). By contrast, organometallic catalysts like Tin(II) 2-ethylhexanoate ($Sn(Oct)_2$) are known for efficient initiation of cyclic esters polymerization, including lactides (*68*) and lactones (*69*). However, those catalysts with metal ligands are notoriously difficult to remove, causing trouble to the application of resulting polymers. Due to high level of toxicity, the United States Food and Drug Administration (FDA) set

the limit for Tin(II) in commercially used biomedical polymer materials at 20 ppm (*59, 70*). But the reality is that many reactions of Tin(II)-catalyzed polymerization have left a high level of residue Tin, quite often on the order of hundred ppm (*71*). And sometimes, the level of Tin in finished polymers like poly(lactic acid) (*72*)) even increased by different extents during aging. Hence, when using those "biocompatible polymers", the clients are still facing a problem brought up by toxic residue metals and questioned chemists "How biocompatible are those synthesized polymers able to be?" To answer the clients' problem appropriately, chemists seek organocatalysts for solution, and their advantages through comparatively study are visible, highlighting non-toxicity and polymerization efficiency. Simultaneously, when claiming the above advantages of OROP approach, we are also trying different chemistries to functionalize the ring-shaped monomers, and eventually make OROP more diverse to applications, especially with specific functions.

Table 1.1: Comparison of organo-, organometallic-, and enzymatic Ring-opening polymerization (ROP)

	Reaction time	**Molecular weight**	**Cost**	**Biocompatibility**	**Ref**
Organo- ROP	Extremely short, i.e. 20 s	Wide range	Low	★★★	Ref 50
Organometallic-ROP	Reasonable, i.e. 24 hours	Wide range	Low	★	Ref 72, 73
Enzymatic ROP	Long, i.e. 10 days	low, i.e. 7×10^3	High	★★★	Ref 70

1.4 Electrospinning process

Electrospinning is a straightforward and versatile method to generate fibers from a rich variety of materials including polymer, ceramics, and composite. And this technique is not new to us that can be traced back to early 1930s, and has currently been rejuvenated in the era of nano- science. Electrospinning research, at both basic and application levels, is springing up. The research progress benefits the academy and industry in different aspects.

1.4.1 History

Overally, the historical events have been highlighted in the timeline of progress in the electrospinning research (Figure 5). The investigation of electrospinning can be traced back to early 1600s when William Gilbert observed the effect of electric charge on a solution, a general phenomenon that electrospinning is based on (*73*). This observation is electrospraying rather than electrospinning which popularized in the later years. However, the very first home-made device of electrospinning was assembled and described after more than 200 years, in 1887 (*74*). Afterwards, the progress of electrospinning towards commercialization was witnessed with early patents contributed by Cooley (1902) (*75*), Morton (1902) (*76*), and Formhals (1933, 1934) (*77-78*). Simultaneously, the mechanism study behind the phenomenon of electrospinning was initiated by Geoffrey Taylor who described and explained the “Taylor cone” phenomenon where polymer droplet elongates into a cone under an extra electric field (*79-80*). The stability of Taylor cone plays an important role in the stable electrospun fibers. In the recent 20 years, several research groups (notably that of Reneker in University of Akron, Xia in Georgia Tech, and Rutledge in Massachusetts Institute of Technology for their distinguished contributions to

the field) proved that a rich variety of organic polymers could be electrospun into fibers at nano- scale (*81-83*). Their research not only enriches the field, but also stimulates the peers' enthusiasm to devote to electrospinning. From the citation report with the keyword "electrospinning" in the web of science, we found that both published items and citations per year increased exponentially since 2000, and the total citation is soaring up to 120000.

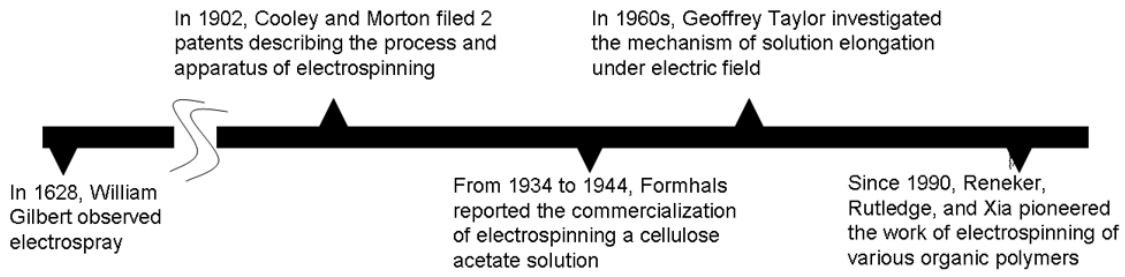

Figure 1.5: Timeline of progress in the electrospinning research.

1.4.2 Principle of electrospinning

As a high-voltage supplier is added to a polymer solution in a capillary, the droplet at the tip of capillary will be elongated, forming conical rather than hemispherical shape. This resulting conical shape is known as "Taylor cone" (*84*). When high voltage was applied, the electrostatic repulsion caused by the positive charges on the surface of polymer solution will overcome the surface tension which is the force to maintain the droplet shape. Maintenance of the stable Taylor cone is the key to generate sustainable, reproducible electrospun fibers. However, the stable Taylor cone is influenced by applied voltage, environmental condition, and process condition. Certain level of applied voltage is required to maintain the conical shape of droplet, while the polymer jet cannot be kept within a straight trajectory once the applied voltage surpasses high level, instead, it will be emitted in a skewed manner (*85*), maybe due to the inhomogeneous charge distribution on the solution interface. Other than that, the environmental factors such as

relative humidity and temperature should also be appropriate to initiate and maintain the Taylor cone, otherwise, the conical shape cannot be kept stable and is likely to break apart into droplets.

As the applied voltage enabled electrostatic repulsion to surpass surface tension, a polymer jet can be emitted from the tip of Taylor cone. Simultaneously, solvent evaporation causes a gradual polymer solidification, and eventually polymer fibers will be deposited onto the grounded collector (i.e. aluminum foil). The emitted polymer jet can be influenced by factors like solvent (*86*) and feeding rate (*87*). Eda et al. investigated the jet breakdown behavior of polystyrene electrospun fibers by using different solvents like tetrahydrofuran (THF), chloroform, *N*,*N*-dimethylformamide (DMF), and 1-methyl-2-pyrrolidinone (NMP) (*86*). The jet breakdown with THF and chloroform displayed a significant extensional flow followed by the onset of instabilities, while the solution jets from DMF and NMF showed extensive whipping producing a cloud of jets. The jet radius largely depends on the feeding rate of polymer solution, usually fiber thickness increase with the increase of feeding rate (*87*). Meanwhile, due to the uneven charge distribution on the polymer jet, bending instability or whipping is applied to the polymer jet (*88-89*). Jet whipping and bending instability are also accompanied with the mechanical stretching of as-spun fibers; as a result, we are able to collect electrospun fibers with a wide range of diameters (*90-91*), even below 100 nm. Besides, if using specific collectors like rotational object or gap, we are able to obtain electrospun fibers even thinner than those deposited on aluminum foil, because collector motion (i.e. rotation) exerts additional stretching on fibers. During the travel of polymer jet, in a short period of time, it still takes some time to let solidified fiber be deposited

onto the collector. Hence, the distance between capillary tip and collector should be long enough for solvent evaporation, otherwise, wet fibers will fuse together to form a 3D network of interconnected fibers rather than a dry non-woven fiber mat.

1.4.3 Facility of electrospinning

It is not complicated to build up a standard electrospinning facility which consists of a high-voltage power supply, a syringe equipped with a conductive needle which functions as nozzle and electrode, a syringe pump, and a grounded collector (Figure 1.6). During process, the polymer solution is pumped through a syringe that is connected with a power supply capable of producing voltage high up to 30 kV. Such high-voltage electric field affects polymer solution, and produces droplet projection, polymer jet, fibers deposited on grounded collector. Based on the standard facility, appropriate modifications can be made to improve the performance and functionality of electrospun fibers. Those modifications touch on coaxial needle for core-shell fiber architecture (*92*), heat jacket for temperature control during electrospinning (*93*), and rotational object-shaped collector for fiber alignment (*94*) and etc. In addition, fiber collection period determines the thickness of resulting non-woven mat. For instance, a PVOH (61 kD_a) non-woven mat with a thickness of approximately 0.05 cm can be obtained after 5-hour collection (Figure 6A). Typically, optical microscopy and electron microscopy are utilized to observe the fiber morphology at macro- and nano- level. Complimentarily, atomic force microscopy is used to record the 3-dimensional topography. PVOH (145, 61 kD_a) electrospun fibers are displayed in ×10 optical image (Figure 6B) and tapping mode-AFM image (Figure 6C).

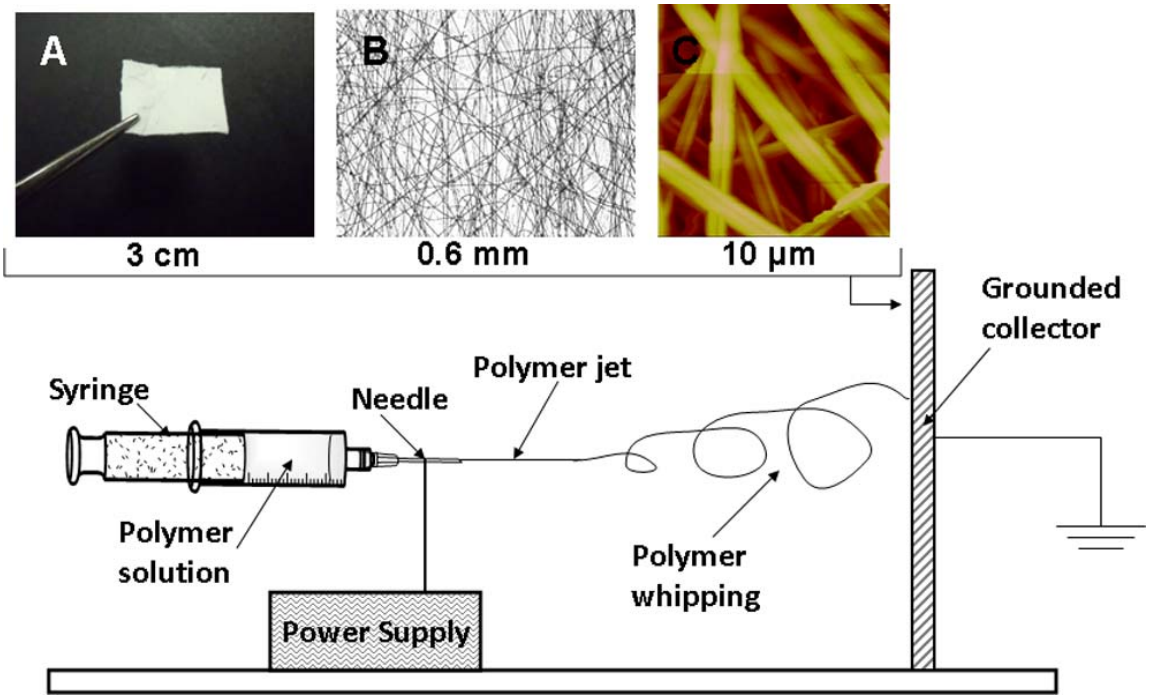

Figure 1.6: Schematic diagram of a standard laboratory electrospinning facility with the surface characterization of non-woven mat, including (A) photo of PVOH (61 kD_a) electrospun fibrous mat, (B) optical microscopic image (×10) of PVOH (145 kD_a) electrospun fibers, and (C) tapping mode-atomic force microscopy (TP-AFM) image of PVOH (61 kD_a) electrospun fibers.

1.4.4 Processing optimization

1.4.4.1 Viscosity

To produce fibers from polymer solutions by electrospinning process, various conditions involving polymer solution properties (polymer molecular weight, concentration, conductivity, surface tension, and solvent volatility), environmental conditions (temperature, relative humidity, and air velocity), and process conditions (voltage, feeding rate, and collecting format) should be carefully taken into consideration because tiny change of those conditions largely affect the fiber formation. Among those parameters, solution viscosity is of importance to electrospinning fibers because viscosity of polymer solution reflects the polymer chain entanglement which significantly influences the fiber formation (*95*). Solution rheological properties like viscosity, modulus, and polymer chain entanglement are clarified to predict the fiber formation, and

the correlation between rheology and fiber are used to map out the processing window of polymer solutions. However, the real situation of electrospun fibers is rather complicated, and most predictions are established based on some assumptions and limitations. On the other hand, appropriate application of those empirical results will promote the efficiency of finding working conditions for electrospinning unfamiliar polymers or other materials. Shenoy et al. established an empirical equation to predict fibers resulted from polymers in good solvents that were unlimited by non-specific polymer-polymer interaction (*95*). The specific equation is shown as follows.

$$(n_e)_{soln} = \frac{\phi_p M_w}{M_e} \tag{1.1}$$

where ϕ_p is the polymer volume fraction, Mw is the weight-average molecular weight of polymer, and M_e is the entanglement molecular weight of polymer. It is found that $(n_e)_{soln} = 2$ is the prerequisite for beaded fiber, and $(n_e)_{soln} = 3.5$ for bead-free fiber, which is a priori prediction of fiber/bead formation as a function of concentration and molecular weight for a rich variety of polymer/solvent systems including polyvinyl pyrrolidone (PVP) in water/ethanol mixture (*96*), polyvinyl alcohol (PVOH) in water (*97*), and polystyrene (PS) in THF (*98*). In addition to the above semi-empirical analysis, the viscosity scaling behavior of neutral polymers or polyelectrolytes can be linked with the electrospun fiber formation (*99-100*). For neutral linear polymers in good solvent, $\eta_{sp} \sim C^{1.25}$ ($\eta_{sp} = (\eta_0-\eta_s)/\eta_s$) in the semidilute unentangled regime, $\eta_{sp} \sim C^{4.8}$ in the semidilute entangled regime, and $\eta_{sp} \sim C^{3.6}$ in the concentrated regime (*101*). The entanglement concentration (C_e) can be determined from the crossing point of semidilute unentangled regime and semidilute entangled regime, and the detail is a method used by Colby et al. (*102*). For neutral copolyesters ($M_w >> M_e$), it has been found that C_e is the minimum

concentration for electrospinning of beaded fibers, and 2-2.5 C_e is the minimum concentration for electrospinning of bead-free fibers (*99*). From that, we can make full use of this empirical rule for predicting the morphologies of fibers electrospun from neutral polymers. In the case of polyvinyl alcohol (PVOH), the apparent viscosity (η_{app}) of PVOH in water at different concentrations is determined by static rheological measurement, and zero shear viscosities (η_0), the viscosities at vanishing shear rate, are determined by extrapolating the Newtonian plateau to zero shear rate. Thus, the two rheological regimes, (semidilute unentangled and semidilute entangled), can be clearly observed by plotting zero shear viscosity as a function of shear rate (Figure 1.7). Based on that, the entanglement concentration of PVOH (61 kD_a) (C_e), also a boundary between semidilute unentangled region and semidilute entangled region is determined to be 60 mg/mL. Afterwards, we re-divided the plot of zero shear viscosity ~ PVOH concentration into three regimes which include bead, beaded fiber, and bead-free fiber based on the rule of Mckee et al. Finally, the TP-AFM images of beaded fiber electrospun from 90 mg/mL PVOH solution and bead-free fiber from 150 mg/mL PVOH solution match our prior prediction quite well. This connection between rheological data and fiber morphology is helpful, and the observation bead-to-fiber transition is general to almost all of the electrospinnable polymers, no matter natural or synthetic. But the problem lies in that the correlation of rheological data and fiber formation is reasonably different due to various polymer architectures, solvent environments, and process conditions. Hence, efforts are being made to establish the different viscosity-fiber relationship, expanding the current law and better understanding the fiber formation of not ready-to-spun polymers like polyelectrolytes and other natural polymers.

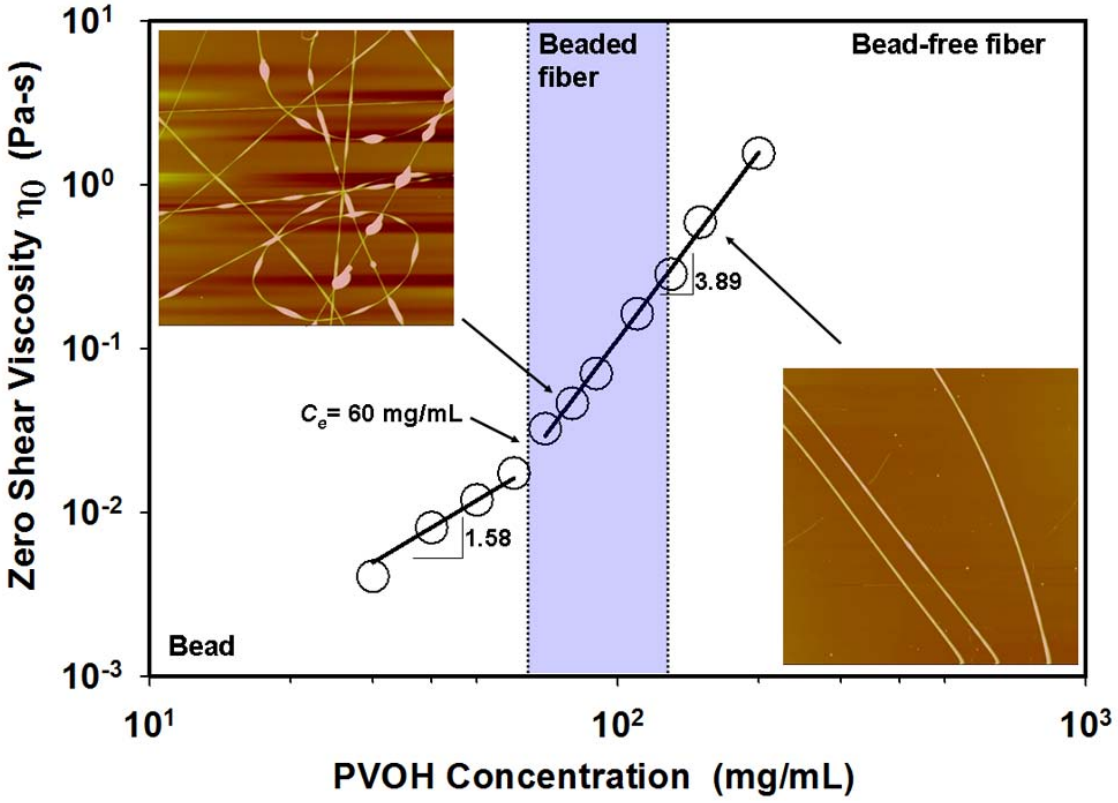

Figure 1.7: The plot of zero shear viscosity (η_0) as a function of PVOH (61 kD_a) concentration with power-law fitting. The two insets are 50 μm × 50 μm TP-AFM image of PVOH beaded fibers electrospun from 90 mg/mL PVOH solution (left), and 100 μm × 100 μm TP-AFM image of PVOH bead-free fibers electrospun from 150 mg/mL PVOH solution (right).

For polyelectrolyte, due to polymer chains' carrying positive or negative charges, the situation of chain entanglement is different from neutral polymer, which has distinct viscosity scaling relationship in the semidilute unentangled, semidilute entangled, and concentrated regimes. The viscosity scaling law of polyelectrolyte follows the relationship of $\eta_{sp} \sim C^{0.5}$ in the semidilute unentangled regime and $\eta_{sp} \sim C^{1.5}$ in the semidilute entangled regime. The solution behaviors result in the different thresholds of electrospun fibers. The threshold of polyelectrolyte fibers is much higher, and also salt-dependent. It is reported that poly(2-(dimethylamino)ethyl methacrylate hydrochloride)

(PDMAEMA•HCl), a cationic polymer, cannot form fibers without salt at concentrations less than $8C_e$ (*100*). The electrostatic repulsion on the chain of polyelectrolyte actually becomes a hurdle for its electrospinnability. Applying salt (i.e. NaCl) helps, because high salt screens the pendant charged groups, softens the backbone of polyelectrolyte, shifts the overall conformation towards a flexible, random coil, and eventually improves the electrospinnability of polyelectrolytes.

The rule of "nC_e" threshold for electrospun fiber can be applied to the electrospinning of natural polymers as well. Kong et al. studied the static rheological behavior of starches with different amounts of amylose prior to electrospinning (*93*). They found that the concentration threshold for effective electrospun fiber was dependent on the content of amylose. High amylose starch containing 80% amylose required 1.2-2.7 times the entanglement concentration (C_e), while low amylose starch containing 50% amylose required 3.7 times the C_e. The mung bean starches containing 35% amylose can only produce poor fibers, and starches with even lower amylose cannot be electrospun at all. In addition to neutral biopolymers, natural polyelectrolytes like chitosan are also investigated for the fabrication of electrospun fibers. Like synthetic polyelectrolyte, chitosan also poses a challenge for electrospinning process due to the highly-positive charged status. The success of chitosan electrospun fibers is only reported with the unusual and problematic solvents such as trifluoroacetic acid (TFA) (*103-105*) and trifluoroacetic acid-based co-solvent systems (*106-107*). Ohkawa et al. reported a viscosity-fiber phase diagram of chitosan in TFA with different molecular weights (M_v= 210, 1310, 1580, and 1800 kD_a) (*104*), which facilitated us to find the processing window

of chitosans in TFA. The critical concentrations for effective fiber of chitosans with different M_w in TFA can be determined from that phase diagram.

1.4.4.2 Process parameters

In addition to solution behavior, processing parameters such as applied voltage, feeding rate, and tip-to-collector distance also play roles in the electrospinnability of polymer solutions. Among those parameters, voltage is of priority because polymer jet can be emitted only when the applied voltage is high enough to allow electrostatic forces to overcome the surface tension (*108*). The applied voltage is usually set within the range of 6~20 kV which is necessary to induce a Taylor cone on the tip of polymer solution, and it is also reported that either positive or a negative dc voltage of more than 6 kV is required to cause the polymer jet emitted from the Taylor cone (*79*). The applied voltage has a large impact on the geometry of Taylor cone. As the voltage is low, it forms a large droplet at the tip of capillary (Figure 1.8A). On the contrary, if the voltage is too high, the rate of solution removal from the capillary tip maybe exceeds the feeding rate of solution, and eventually breakdowns the Taylor cone (Figure 1.8B) (*109*). The gradual change of Taylor cone corresponding to the increase of applied voltage is shown in detail (Figure 1.8C) (*110*). Under extreme condition, the unstable Taylor cone results in the bead defects in the fibrous mats (*111-112*). For instance, it is reported that the area density of bead defects in polyethylene oxide (PEO, 400 kD_a) electrospun fibrous mat dramatically increased from 1×10^6 #nodules/cm^2 to 1.2×10^7 #nodules/cm^2 once the applied voltage increased from 7 kV to 9 kV (*111*). The appropriate voltage can ensure a stable process for fiber production. In many cases, the increase of the applied voltage also affects the morphology of electrospun fibers. Higher magnitude of the applied voltage causes

polymer jet to speed up, transfers polymer mass more efficiently, and stretches fibers more. Based on those effects, we can observe fibers with smaller diameters when the applied voltage is increased (*109, 111, 113*). In some rare cases, an increase in fiber diameter with increasing voltage can be observed as well (*114*). And interestingly, for most electrospun polymer fibers, positive voltage supply is utilized to provide external electric field. Meanwhile, negatively-charged fibrous mat can be electrospun as an alternative by using negative voltage supply (*115*), which renders a wider range of functionalization opportunities like deposition of positive polyelectrolytes by using "layer-by-layer" technique (*116-117*).

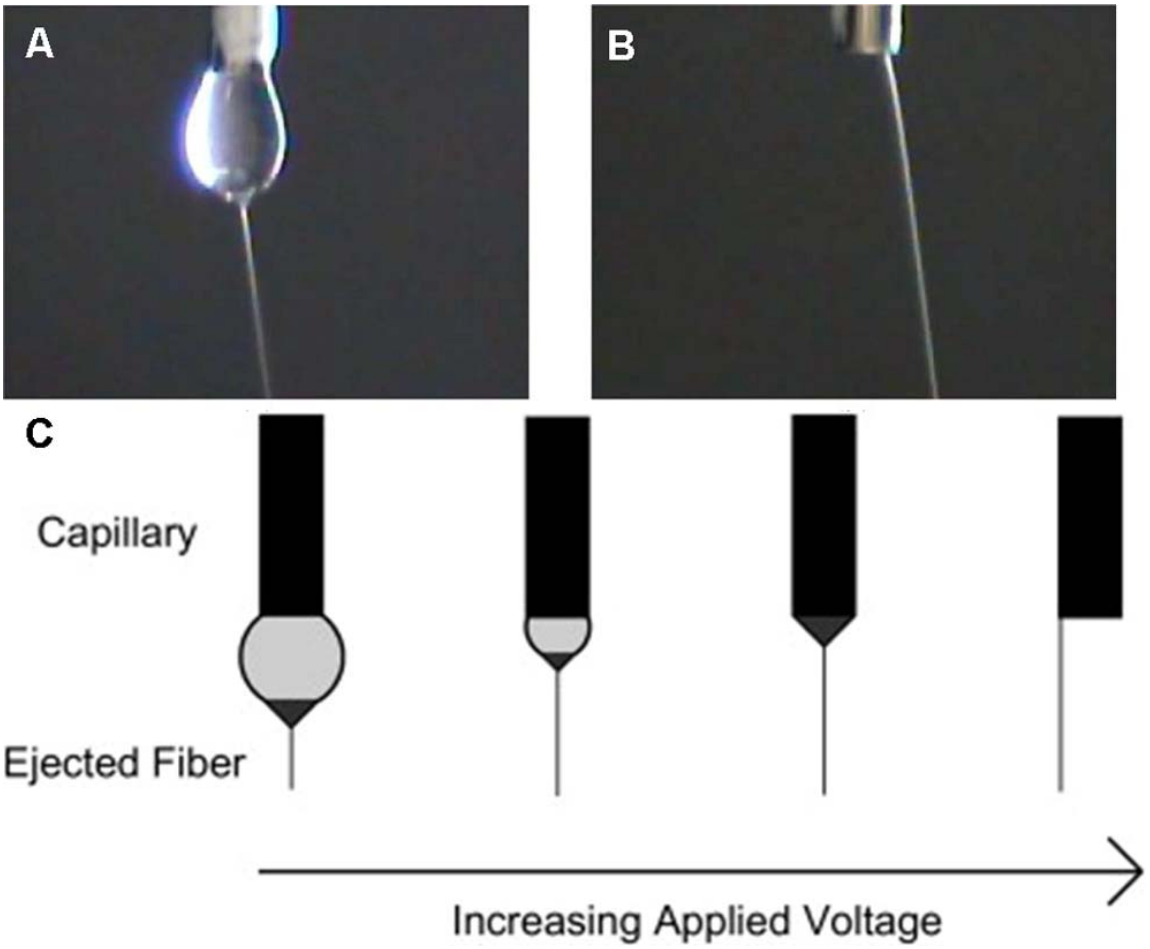

Figure 1.8: Behavior of the fluid droplet at the tip of the needle. (A) Applied electric field is below the lower threshold, (B) applied electric field is above the higher threshold (Reproduced with kind permission from Ref. 110; © IEEE Industry Applications Society), and (C) Schematic diagram of effect of applied voltage on the formation of the Taylor cone (Reproduced with kind permission from Ref. 111; © Elsevier).

Another important process parameter is the feeding rate of polymer solution. In single fluid electrospinning, an increase in feeding rate of polymer solution usually leads to electrospun fibers of larger diameters (*118-124*)，while in coaxial electrospinning, the feeding rates of inner fluid and outer fluid are critical for both stable polymer jet and inner-, outer fiber thickness (*125-127*). In order to maintain stable Taylor cone and high loading of encapsulated active component, sheath flow rate and core flow rate should be fixed within the reasonable working window, and the core flow rate should generally be lower than that of the sheath (*128*). Manipulating the feeding rate of inner fluid also

benefits the controllable release profile of the active component (i.e. bovine serum albumin) from the electrospun fiber core (*125*). Jiang et al. observed a delayed release profile of bovine serum albumin (BSA) from dextran/poly(ε-caprolactone) core-shell electrospun fiber when the feeding rate of the inner dope increased from 0.1 to 0.8 mL/h (*125*). Simultaneously, Zhang et al. demonstrated that various fitcBSA loadings (0.85-2.17 mg fitcBSA/g fibrous mat) can be achieved by varying the inner feeding rate from 0.2 to 0.6 mL/h (*129*). Such variation of inner dope feeding rate results in little fiber size fluctuation. Besides, the core-shell nanofibers fitcBSA/PEG-PCL significantly alleviated the initial burst release for higher protein loading and offered sustainable release profile.

1.4.4.3 Environment

Environmental conditions such as temperature and relative humidity also affect the polymer electrospinning. The preparation of polymer solution sometimes requires additional heat treatment. The typical example is polyvinyl alcohol (PVOH, M_w=146-186 kD_a), which is an electrospinnable model polymer. Due to the intense hydrogen bonding between chains, the fully dissolution of PVOH in water usually requires heating at 80 ^oC (*130*). Secondly, using heat jacket reduces the viscosity of concentrated polymer solution or polymer melt, and thus facilitates the electrospinning process (*131*). Compared with solution electrospinning, melt electrospinning avoids accumulation of residue solvent and its toxicity (*132*). The elevated temperature influenced the fiber morphology as well. Wang et al. investigated the temperature effect on the cone/jet/fiber morphologies that developed (*133*). It was found that the viscosity (η) and surface tension (γ) of polyacrylonitrile (PAN) in DMF were decreased, and the solution conductivity (κ) was increased. The change of those parameters favored the formation of thinner electrospun

PAN fibers (diameter below 100 nm) at high processing temperature, and the PAN fibers electrospun at high temperature were with less crystallinity. Overally speaking, Wang et al. demonstrated that high-temperature electrospinning was an effective method to fabricate ultrathin fibers. Interestingly, Simonet et al. demonstrated a low-temperature fiber collection device in air with controlled humidity, allowing the deposition of polymer fibers and ice particles from condensing humidity (*134*). The deposited ice crystals served as void templates which gives access to the preparation of biodegradable tissue scaffolds with an up to 4 times higher porosity compared to traditional fiber electrospinning.

Another environmental factor is relative humidity. Generally-speaking, high relative humidity generates a large amount of moisture which inhibits solvent evaporation. Hence, at high relative humidity, it is more likely to accumulate residue solvent in the electrospun fibrous mat. Under such circumstances, a certain amount of dried polymer droplets are obtained and require peeling off afterwards. In addition, when high-volatility solvent is used during electrospinning, those solvents' evaporation results in a highly viscous semi-solid at the spinneret, causing the clogging problem during electrospinning process (*135-136*). Simple method like using ethanol to re-wet the Taylor cone prevents the clogging of spinneret tip (*137*).

1.4.5 Functional electrospun fibers

1.4.5.1 General application

As a versatile method, electrospinning endows non-woven mats with a rich variety of functionalities. Those functional mats served as materials in various applications, touching areas of tissue scaffold (*138*), filter (*139*), sensor (*140*), wound healing (*141*),

etc., and shedding light on the solutions to key problems in biomedical, pharmaceutical, cosmetic, and functional food. Figure 1.9 showcases a big picture of electrospun fibers' applications, and four major categories are mentioned, including filter for juice clarification, portable wound healing device, temperature-response biosensor, and tissue scaffold. Many research groups world-widely attempt to make full use of this versatile technology for different research purposes. Veleirinho and Lopes-da-Silva demonstrated a high flux method for apple juice clarification by using polyethylene terephthalate (PET) electrospun fiber mat, and its physico-chemical characteristics were comparable to those conventional members for juice clarification (*142*) (Figure 1.9A). A portable wound healing device based on electrospun fibers was designed and commercialized (Figure 1.9B). Yoon and Kim utilized UV-induced *in situ* polymerization during electrospinning to fabricate polydiacetylene (PDA)-embedded fibers in one step (*140*) (Figure 1.9C). The *in situ* UV-induced polymerization lead to homogenous PDA fiber matrix, and was used as temperature sensor. Due to the diversity of DA monomer, those PDA-embedded fibers display great potential in the field of PDA-based chemosensor devices. For tissue regeneration, engineered scaffolds serve as host to cells harvested from natural tissue. Compared with other architectures, electrospun nanofibrous mat with high surface-to-volume ratio provides many more binding sites to cell membrane receptors (*143*) (Figure 1.9D).

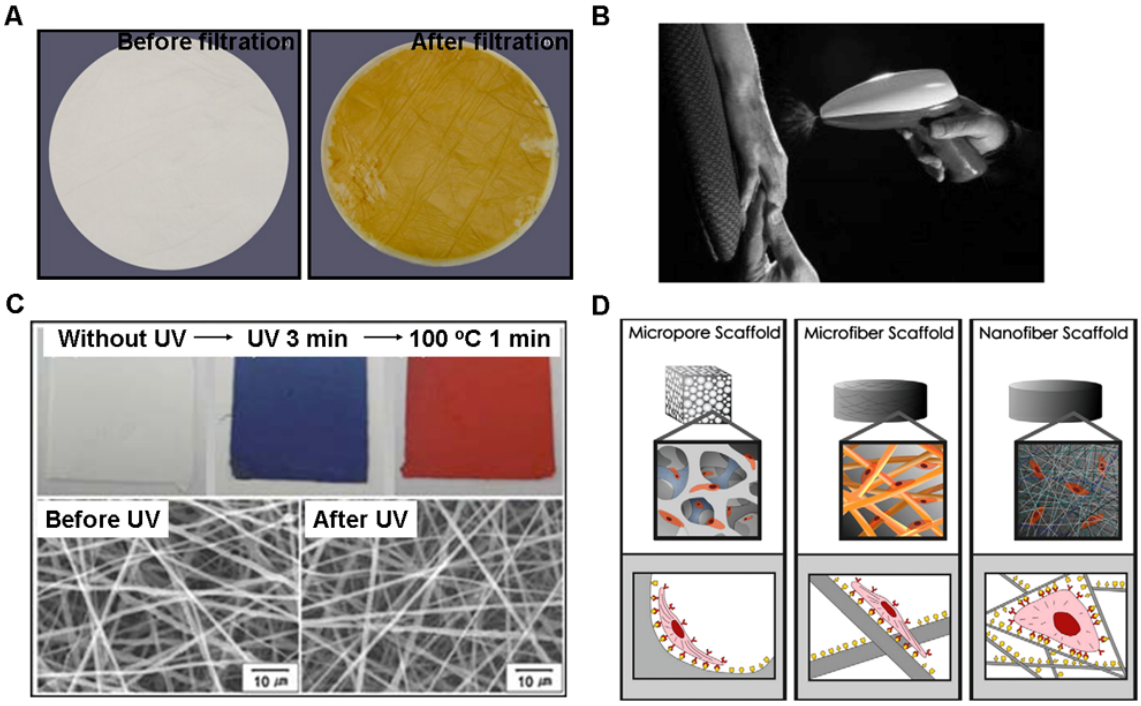

Figure 1.9: Applications of polymer electrospun fibrous mats. (A) Polyethylene terephthalate (PET) electrospun membrane before filtration and after apple juice filtration (Reproduced with kind permission from Ref. 143; © Elsevier); (B) Portable wound healing device based on electrospun nanofiber (www.electrosols.com)； (C) Photographs and SEM images of 10,12-pentacosadiynoic acid (PCDA)-derived electrospun fiber mats obtained before UV irradiation and after UV irradiation for 3 min, and after heating at 100 ^{o}C for 1 min (Reproduced with kind permission from Ref. 141; © Wiley); (D) Scaffold architecture affects cell binding and spreading. (Left and middle) Cells binding to scaffolds with microscale architectures flatten and spread as if cultured on flat surfaces. (Right) Scaffolds with nanoscale architectures have larger surface areas to adsorb proteins, presenting many more binding sites to cell membrane receptors (Reproduced with kind permission from Ref. 154; © The American Association for the Advancement of Science).

Based on those applications, electrospun fiber mats are making contribution to the human healthcare in different aspects. Behind those applications, two functionalities, compound encapsulation and fiber alignment, catch our eye particularly for chemo-functionality and structure re-organization, respectively. Basically, compound encapsulation directly implants chemical functionality into fibrous mat, while fiber re-organization (i.e. alignment in uniaxial direction) targets mimicking the extracellular matrix (ECM), providing suitable supporting for tissue growth. With those two functionalities, electrospun fiber mats will give better performance of its healthcare products.

1.4.5.2 Compound encapsulation

Compound encapsulation refers to the entrapment of active components into the electrospun fibrous mats. Those components stay either in the fibers or in the interstice regions. The majority of the entrapped components are model compounds (i.e. bovine serum albumin (*144*)), drug molecules (*145*), and nutraceuticals (*146*). So far, Single fluid and coaxial electrospinning are two majorly-used methods for compound encapsulation of electrospun fiber mats. Both facilities are almost identical, and most components in coaxial electrospinning keep the same as those in single fluid electrospinning. The key difference between single fluid and coaxial electrospinning lies in the utilization of coaxial nozzle. The standard laboratory electrospinning facility of single fluid electrospinning has been shown in Figure 1.6, while the equipment of coaxial electrospinning is displayed in Figure 1.10. The home-made coaxial nozzle is made of three needle pieces which are shown in the inset of Figure 1.10A. A quick example here is polyvinyl alcohol (PVOH, 61 kD_a)/polycaprolactone (PCL, 80 kD_a) core/shell electrospun fiber. For characterization, Fourier transform infrared spectroscopy (FTIR) and water contact angle of PVOH and PVOH/PCL core-shell fiber mats are measured (Figure 1.10B). By using co-axial electrospinning, we found that the –OH peak (3309 cm^{-1}) disappeared and the -COOR- group peak (1724 cm^{-1}) appeared. The water contact angle also suggested the surface transferred from a hydrophilic surface into a hydrophobic surface covered by PCL.

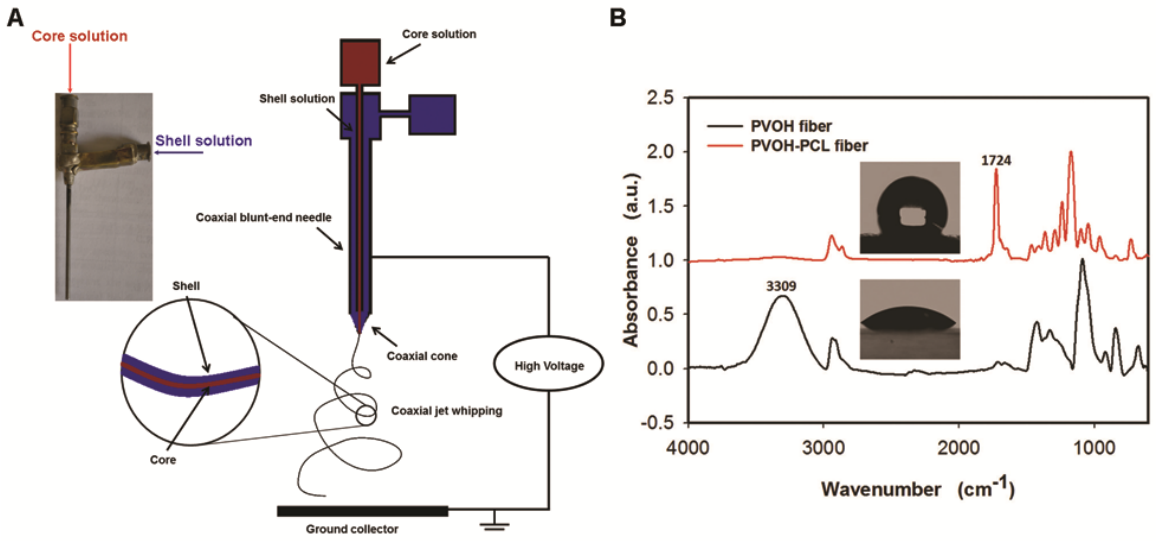

Figure 1.10: Electrospun core-shell polymer fibers. (A) Schematic diagram of home-made dual syringe electrospinning platform, and the inset on the left is the photo of home-made coaxial nozzle; (B) Fourier transform infrared spectra of polyvinyl alcohol (PVOH) electrospun fiber (black curve), polyvinyl alcohol/poly(ε-caprolactone) core/shell fiber (reddish curve), and the two insets are pendent water droplets on the fiber mat surfaces.

Compared with single fluid electrospinning, coaxial electrospinning enjoys several advantages, including strong protection against environmental invasion, sustainable release profile of active component, template for non-electrospinnable materials and tubular structure, and enhancement of physico-chemical properties. Those advantages of coaxial electrospinning drive us to shape core-shell fibrous mats into devices and systems, and the resultant core-shell fibrous mats serve as supporting materials for drug delivery (*144*), energy storage (*147*), and controllable surface wettability (*148*). For drug delivery, investigations demonstrated that core-shell fiber can effectively suppress the "burst release" phenomenon (*144, 149*), and provide sustainable drug release (*150*), usually on the order of months. For energy storage, Kurban et al. demonstrated the fabrication of composite polystyrene-ammonia borane fibers with controllable porosity through the solution selection protocol (*147*). This method is a scalable, one-step process for low weight hydrogen-storage device, and with appropriate selection of hydride, this

composite storage material can be made reversible by repressurizing H_2. For control of surface wettability, by using coaxial electrospinning, Teflon AF, a nonelectrospinnable and hydrophobic polymer due to its low dielectric constant succeeds to form electrospun fiber with the aid of poly(ε-caprolactone) sheath (*148*). The combination of Teflon AF core and poly(ε-caprolactone) sheath bettered the overall performance of the resulting electrospun fiber mat, and the fabricated Teflon AF/PCL core-shell fibers are integrated with properties of superhydrophobicity, oleophobicity, and improved mechanical property.

1.4.5.3 Fiber alignment

Normally, randomly-oriented fibers are obtained by using aluminum foil as fiber collector, while fiber alignment allows the re-arrangement of fibers in uniaxial direction. Although it is extremely difficult to render every single fiber align in one direction, highly-aligned fibers can be achieved through appropriate process.

Gap technique (*151*) and rotational object technique (*94*) are two common methods adopted to generate highly aligned fibers. In gap method, two pieces of conductive electrodes serve as fiber collector, and majority of the fibers are collected on the gap between those two electrodes (Figure 1.11A). By contrast, a rotational object is used to collect fibers that are formed during electrospinning. The mechanism of gap and rotational object is different due to their distinct features. In the case of gap collector, electrospun fibers experienced two set of electrostatic forces: the forces exerted by the two splitting electric field and the other electrostatic attraction between charged fibers and two electrodes (Figure 1.11B). Under the influence of those two force sets, the coming fibers can be suspended between two electrodes in uniaxial alignment. Different

from gap collector, rotational drum exerts strong stretching force at high rates, which guides the coming fibers to grow in uniaxial direction and thins the deposited fibers simultaneously (Figure 1.11C).

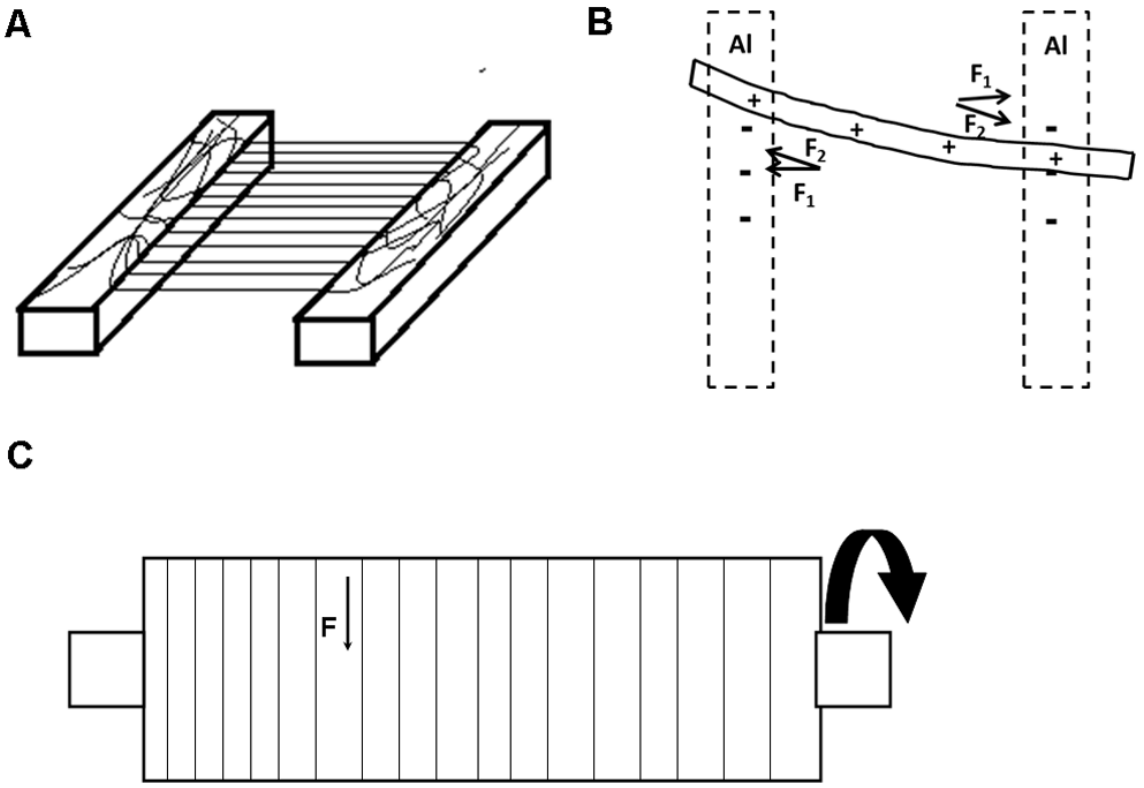

Figure 1.11: Fiber alignment by gap and rotational object techniques. (A) Fiber distribution on the gap of two metal electrodes after electrospinning; (B) Electrostatic force analysis of a charged nanofiber spanning across the gap; (C) Fiber distribution on the rotational drum collector.

The degree of fiber alignment can be quantified by the fast Fourier transform method (FFT). Through FFT process, the original image can be transferred into a grayscale pixel pattern that reflects the degree of fiber alignment from the original image. The detailed protocol can be found in the method established by Ayres et al (*152*). The following displays a typical example of FFT process on the morphology of poly(ε-caprolactone) fibers (Figure 1.12). The representative optical image of randomly-oriented fibers is presented in Figure 1.12A. FFT of randomly-oriented fiber image (Figure 1.12A)

produces an output image displaying pixel distribution in a symmetrical, and circular shape (Figure 1.12B). The white pixel lines scattering at almost all angles (0-360^{o}) reflect the non-specific fiber alignment. By contrast, FFT of aligned PCL fiber image (Figure 1.12D) results in an output image (Figure 1.12E) containing pixels distributed in two specific angles, suggesting a preference of fiber alignment.

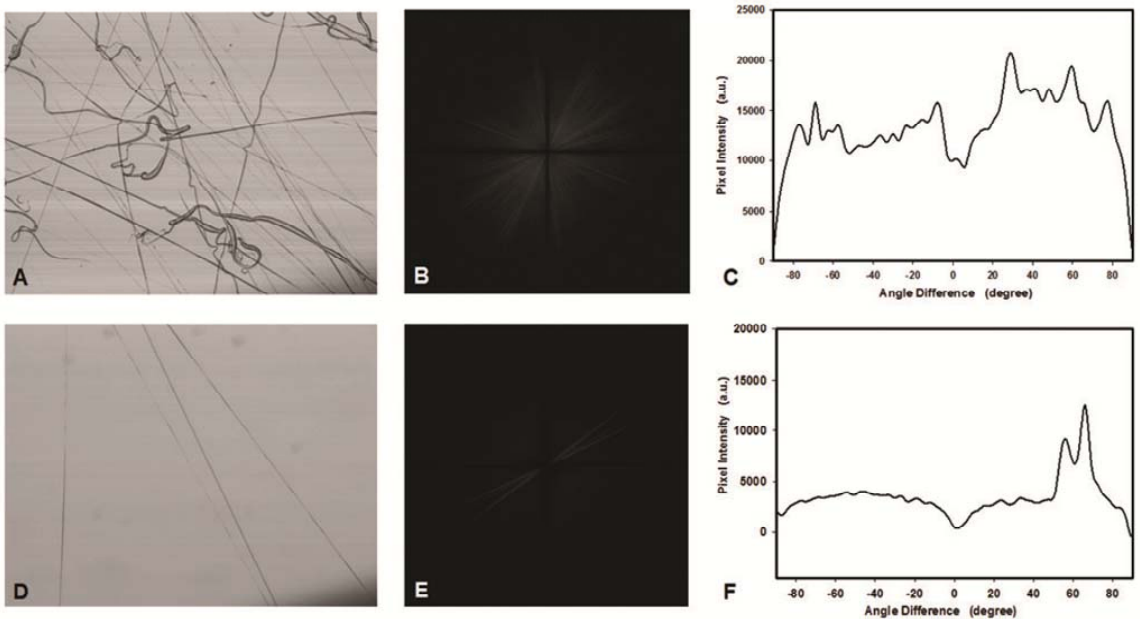

Figure 1.12: Representative optical images of (A) random poly(ε-caprolactone) (PCL) electrospun fibers and (D) aligned PCL electrospun fibers; FFT output images of (B) random PCL electrospun fibers and (E) aligned PCL electrospun fibers; Normalized pixel intensity plots as a function of angle acquisition for (C) random fibers and (F) aligned fibers. The angle difference specifically refers to the angle difference between scattering lines and horizontal plane.

The plot description of FFT results can be generated by putting a circular projection on the FFT output images and conducting a radial summation of the pixel intensities for each degree from 0^{o} to 360^{o}. The final plot shows normalized pixel intensity as a function of angle difference, and the pixel value of each point is summed from white line scattering at each angle. Since the FFT is symmetric about the horizontal axis, there is no necessity

for summation of 360^{o}. Due to the mathematical transformation, the FFT data is about 90^{o} different from the fiber alignment in real space. After conducting the process mentioned-above, we obtained the pixel intensity versus angle difference plot of randomly-oriented fibers (Figure 1.12C) and aligned fibers (Figure 1.12F).

Highly-aligned electrospun biopolymer fibers are frequently studied for biomedical applications, especially in the field of tissue engineering (*153-155*). Firstly, those fibers electrospun from solutions of poly (ε-caprolactone) (*156*) and poly (lactic acid) (*157*) are biocompatible with cells, tissues, and stay comfortably within environment. Secondly, uniaxially-aligned nanofibers can provide contact guidance cues for a rich variety of cells, including neurons (*158*), fibroblasts (*159*), endothelial cells (*160*), cardiomyocytes (*161*), skeletalmuscle cells (*162*), and Schwann cells (*163*). Thirdly, when supporting the cell growth, the electrospun fiber mats greatly affect the cell conformation, proliferation, and migration. And different combinations of polymers and cells studied by distinct groups enrich the diversity and fitness of polymer electrospun fibers applicable to the engineered tissues. By investigating the growth of adult human dermal fibroblasts on the poly(methyl methacrylate) (PMMA) fibrous scaffold, Liu et al. found a critical diameter (D_0=0.97 μm) below which no big difference in aspect ratio of was observed compared with PMMA film (*164*). Yang et al. studied the suitability of poly(L-lactic acid) (PLLA) scaffold for neural tissue engineering by using neural stem cells (NSCs) (*155*). From their results, fiber diameter influenced the rate of NSC differentiation rather than the cell orientation, and the rate of NSC differentiation was higher for PLLA nanofibers than that of micro fibers. Besides, Chew et al. also demonstrated a synergistic effect of growth factor encapsulation and fiber alignment by fabrication of a copolymer of caprolactone and

ethyl ethylene phosphate (PCLEEP) with human glial cell-derived neurotrophic factor (GDNF) (*155*). Their rat model study showed that a highest nerve electrophysiological recovery of the rats in the aligned GDNF-PCLEEP fibers compared with groups subject to other fiber formulations like plain PCLEEP fibers. Also, some portions of human tissues such as the transition of tendon to bone posted a challenge for scaffold engineering due to their complicated compositions and structures. Very recently, Xie et al. demonstrated the construction of tendon-to-bone mimicking scaffold by using "aligned-to-bone" poly(lactic-co-glycolic acid) (PLGA) nanofiber scaffolds (*165*). The tendon fibroblasts cultured on such scaffold displayed highly-aligned and haphazardly orientations, respectively, on the aligned and random portions. For better mimicking the texture of bone tissues, bonelike mineral (calcium phosphate or hydroxyapatite) were coated onto the surface of PLGA fibers (*166-167*). A gradient of calcium phosphate was coated on the surface of PLGA fibers by immersing the nanofiber scaffolds into a 10-fold-concentrated simulated body fluid, consequencing a gradient in the stiffness of the scaffold and activity of mouse preoteoblast MC3T3 cells (*166*). Furthermore, Liu et al. demonstrated a "pre-coating" method for the biomineralization of PLGA electrospun fibers (*167*). With a buffering layer of chitosan and heparin on the surface of nanofibers, experimenters were able to eliminate the mineral gradient on the fiber surface, enhance the mineral density by depositing thicker mineral layer, and eventually strengthen the fiber stiffness. The efforts put in surface functionalization result in a better performance of mimicking structure, composition, and functionality of mineralized tissues.

1.4.6 Future direction

According to the citation report on the topic of electropinning generated within the online data bank of Web of Science, the research of electrospinning is increasing exponentially since 2000 viewed by published items in each year, and the index of published items reached 1200 in 2011. Simultaneously, there is still large room for the innovation of electrospinning based on facility, resource, and application. Nowadays, the research focus is put on the fibers electrospun from various synthetic polymers to natural polymers, however, compared with electrospun fibers, the electrosprayed polymer beads are seldom put efforts in. Although in its infancy, the electrospraying technique is also of importance to the steady fabrication of biopolymer vehicles for large bioactive components like living cells (*168*). In terms of resource, freshly-synthesized polymers are always being tested for electrospinning, but we cannot ignore a large pool of polymer candidates from nature, especially polysccharides. Although challenges exist for some natural, stiff polymers like chitosan (*169*), novel methods like coaxial electrospinning are probably required to improve the performance of electrospun polysaccharide fibers. Finally, strengthening the application of electrospun polymer fibers, in other words, matching the basic research of electrospinning with applications will generate a harmonious atmosphere of theoretical study and device making.

Chapter 2

Characterization

2.1 Rheology

2.1.1 General information

Rheology aims at knowing the fluid behavior by observing the response of fluid to an applied force. A wide range of fluids such as polymer solution, particulate suspension, and concentrated gel are applicable to the rheological investigation. The rheological properties are directly relevant to the inner- structures of those fluids. For instance, the phase difference tan δ in dynamic oscillatory mode is a measure of the viscous/elastic ratio for the material at frequency ω, displaying the viscoelastic property. For measurement, static and dynamic modes are utilized to obtain the viscosity and modulus of materials.

In static mode, the apparent viscosity (η_{app}) of a fluid is directly measured as a function of shear rate (γ). According to flow behavior, fluids are categorized into three sorts, including Newtonian, pseudoplastic, and dilatant fluids. For Newtonian fluid like water, a plateau is observed; for pseudoplastic fluid like paint, viscosity decreases as a function of shear rate; for dilatant fluid like mixture of cornstarch and water, viscosity increases as a function of shear rate. Zero shear viscosity (η_0), the viscosity at vanishing shear rate, can

be determined by extrapolating the Newtonian plateau to zero shear rate. Pseudoplastic fluids, commonly in the soft materials (yoghurt, edible oil, salad dressing and etc.), can be fit into various empirical models including Power-law (*170*), Ostwald de-Waele (*171*), Cross (*172*), Carreau (*173*), and Herschel–Bulkley (*174*). Following are the equations of the models:

$$\eta = K\gamma^{n-1} \tag{2.1}$$

$$\sigma = K\gamma^{n} \tag{2.2}$$

where η is apparent viscosity (Pa*S), σ is shear stress (Pa), K is flow consistency index (Pa*S^n), and n is flow behavior index.

$$\eta = \eta_{\infty,\gamma} + \frac{\eta_{0,\gamma} - \eta_{\infty,\gamma}}{1 + (\alpha_c \gamma)^m} \tag{2.3}$$

$$\eta = \eta_{\infty,\gamma} + \frac{\eta_{0,\gamma} - \eta_{\infty,\gamma}}{[1 + (\lambda_c \gamma)^2]^N} \tag{2.4}$$

where $\eta_{\infty,\gamma}$ is infinite shear rate viscosity (Pa*S), $\eta_{0,\gamma}$ is zero shear rate viscosity (Pa*S), m and N are constant, α_c and λ_c are characteristic relaxation time (s),

$$\eta = K_H \gamma^{n_H - 1} + \eta_{\infty,\gamma} \tag{2.5}$$

where K_H is consistency index (Pa*S^n), n_H is flow behavior index, and $\eta_{\infty,\gamma}$ is infinite shear rate viscosity (Pa*S).

The fitting parameters resulted from different models need to be compared to increase the precision and accuracy of the non-linear regression and to avoid wrong prediction. For example, when the flow behavior of the fluid is only composed of initial Power law and final plateau, the estimation of zero shear viscosity ($\eta_{0,\gamma}$) from Cross and Carreau models is very likely unacceptable due to large variation.

In dynamic mode, the oscillatory frequency sweep test measures storage modulus (G'), loss modulus (G''), complex viscosity (η^*), and phase change tan δ. Prior to frequency sweep test, strain sweep measurement should be performed to find the viscoelastic linear region of G' and G''. During experiment, a sinusoidal strain wave of maximum strain γ_m and oscillatory frequency ω is applied to fluid sample using a specific geometry (i.e. parallel plate). If the fluid has a mixed feature of viscosity and elasticity, the corresponding stress wave usually has a phase difference δ ($0^o<\delta<90^o$). As mentioned previously, the parameter tan δ measures viscous/elastic ratio of the fluid. The elastic (in phase) and viscous (out of phase) portions of the stress wave are measured separately by software. The storage modulus G' in phase and loss modulus G'' out of phase are defined by: $G^*=\tau^*/\gamma_m=(G'^2+G''^2)^{1/2}$, where G^* is the complex shear modulus, τ^* the complex stress. The complex viscosity η^* is equal to G^*/ω, while the tan δ is the ratio of G''/G'. With dynamic oscillatory tool, we can distinguish the solid/liquid properties of a given fluid, especially semisolid gel. To some point, the dynamic oscillatory method gives a definition of gel. Various gels, including microgel (*175*), coacervate gel (*176*), clay gel (*177*) and etc. should show a value of G' which exhibits a pronounced plateau extending to times of the order of seconds, and a G'' which is considerably smaller than the storage modulus in this region (*178*).

2.1.2 Experiment setup

The ARES Rheometer (Rheometrics Scientific, NJ) is used to collect the data of fluid viscosity and modulus. The whole rheometer is composed of motor, transducer, sample holder, heating oven, pc control panel, and other accessories. The motor is used to rotate the sample chamber, and to provide shear force to the sample fluid. Transducer is utilized

to convert force signal into rheological signal (i.e. apparent viscosity η_{app}). Transducer 200G FRT has a small torque range (0.02-200 g·cm), while transducer 2K FRT has a larger torque range (2-2000 g·cm). The sensitivity of transducer should be taken into consideration, and less viscous samples should be subject to 200G FRT transducer. For sample holder, different geometries such as cone-and-plate, parallel plate, and concentric cylinder are used to hold samples. Among those fixtures, the cone-and-plate (diameter 50 mm, 0.04 rad or diameter 25 mm, 0.1 rad) and parallel plate (diameter 50 mm or 25 mm) are suitable for polymer solutions under a wide range of concentrations. The gap between cone or plate and plate largely affects the data collection. For parallel plate (diameter 50 mm), a slight parallax can cause the plates to touch due to sources of errors during gap zeroing when not parallel, thus introducing a gap error of size ε (Figure 2.1). Pipe et al. reported a relationship of estimating the relative error in η_{app} with respect to its stated value η_{true} given by (*179*):

$$\frac{\eta_{true} - \eta_{app}}{\eta_{app}} = \frac{\varepsilon}{H} \tag{2.6}$$

where η_{true} is the true viscosity (Pa*S), η_{app} is the measured apparent viscosity (Pa*S), ε is the magnitude of the gap error intrinsic to the instrument. Based on the equation 6, the relative percent error in apparent viscosity and true viscosity is estimated, assuming a representative gap error ε=30 μm. As the gap is set at 0.05 mm, the relative error% goes up to 60%, while the relative error% lowers back to 1.5% once the gap is 2 mm. Hence, according to the theoretical estimation and empirical protocol, the gap between parallel plates should be within the range of 0.5-2 mm.

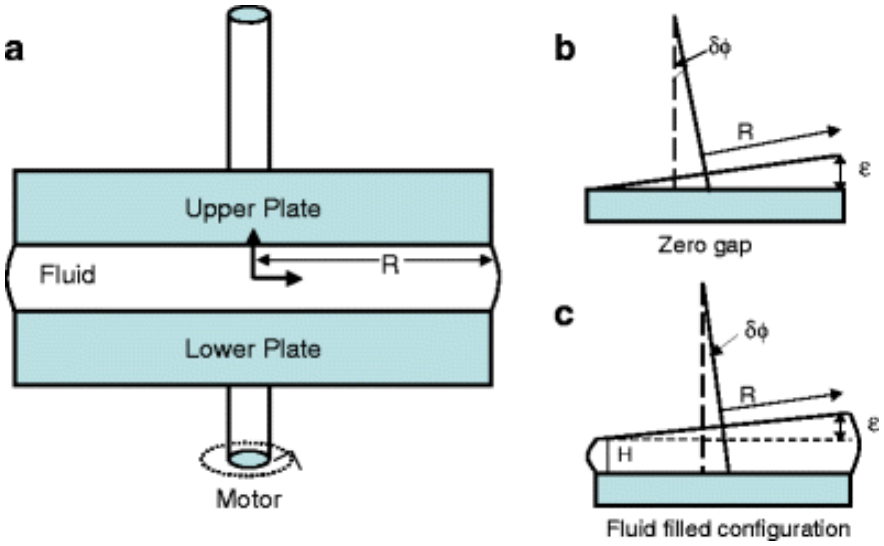

Figure 2.1: Schematic diagram of a conventional rotational rheometer; two plates of radius *R*, at gap height *H*. The top or the bottom plate rotates with an angular velocity Ω. a Ideal situation in a parallel-plate rheometer, the plates are perfectly parallel; b Sources of error during gap zeroing; a slight parallax (exaggerated in the figure) causes the plates to touch when not parallel, thus introducing a gap error of size ε; c Profile of the fluid sample when placed between nonparallel plates (Reproduced with kind permission from Ref. 180; © Springer)

In terms of temperature control, an air/N_2 gas convection oven is designed and equipped for optimizing temperature stability, rapid heating or cooling, and convenience of use over the temperature range of -150 to 600 ^{o}C. Also, the recirculating fluid bath is used together with concentric cylinders for a temperature range of -10 to 150 ^{o}C. This geometry is helpful especially for very low viscous fluids, dispersion of limited stability, and fluids where solvent evaporation may be a concern. Other accessories are used for calibration in static and dynamic mode. Viscosity standard 1000 cP nominal is used for calibration in static-state viscosity measurement, while polydimethylsiloxane (PDMS) gel is utilized for calibration in dynamic modulus test. For PDMS gel, a gel-to-liquid transition can be observed at frequency 5.46$\pm$5% rad (W_c, critical frequency) under 15% strain.

2.2 Atomic Force Microscopy

2.2.1 General information

A commercial Nanoscope IIIa multi-mode atomic force microscopy (AFM) (Veeco Instruments, CA) is an imaging instrument which is designed and assembled based on the phenomenon of piezoelectricity. The piezoelectricity refers to charge accumulation in solid materials such as crystals, ceramics, and biomaterials in response to mechanical stress. Simply-speaking, this feature enables AFM to convert mechanical signal into electric signal.

Compared with conventional electron microscopy (EM), AFM enjoys the advantages of ease of sampling, three dimensional topology, and accessories such as heat stage or liquid cell. When scanning electron microscopy (SEM) is in use, metal sputtering (i.e. gold) is commonly required for non-conductive biomaterials prior to imaging (*180*). Also, transmission electron microscopy (TEM) requires specially-treated copper grid for sample deposition. By contrast, sampling of AFM is straightforward and of multiple choices. Basically, any method that can fix the polymer samples (i.e. chitosan nanoparticles) onto the substrate can be applied. In detail, solution immersing (*29*) or spin coating (*181*) can be choice, and meanwhile samples should be fully dried before imaging in solid state. Secondly, only surface morphology is observed by using TEM, while SEM can capture both surface and cross-section morphologies. In addition to surface morphology in *x*-*y* plane, AFM also records the topological information in *z* axle, and hence can provide us with a re-construction of 3D topography. For instance, Hou et al. investigated the self-assembly of tri(dodecyldimethylammonioacetoxy)diethyltriamine trichloride (DTAD) under concentrations beyond critical micellization concentration

(CMC) by using tapping-mode AFM (*182*). The representative AFM height image, 3D image, and section analysis of 20 mM DTAD deposited on mica are shown in Figure 2.2. Many stripes with large width (>100 nm) of DTAD aggregates were observed at a much higher concentration of 20 mM.

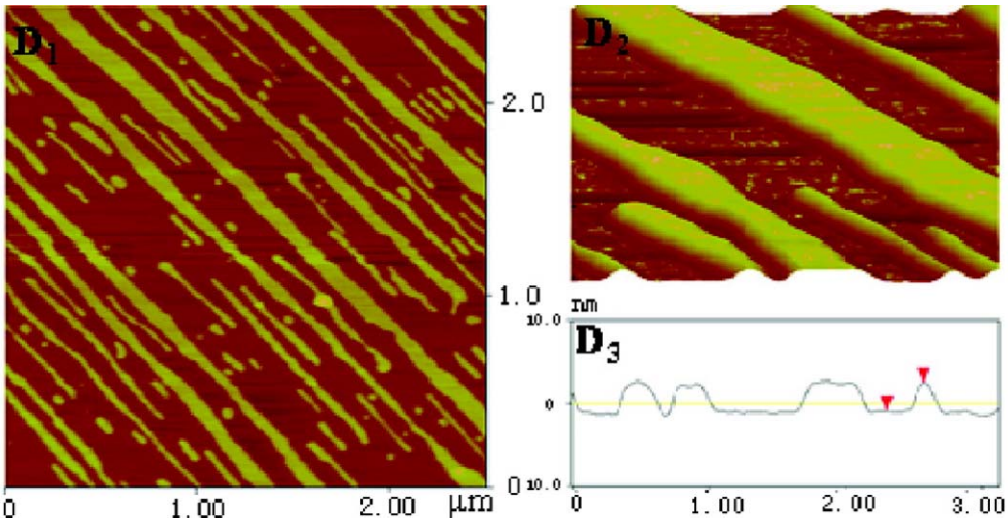

Figure 2.2: (D1) Tapping mode AFM height image (2.5 µm × 2.5 µm), (D2) 3D images (625 nm × 625 nm), and (D3) corresponding section analysis on mica substrates prepared with 20 mM DTAD concentrations for 15 min. (Reproduced with kind permission from Ref. 183; © American Chemical Society).

Other accessories such as liquid cell and hot stage enhance the functionality of atomic force microscopy. The liquid cell is used to monitor the aggregation-dissociation cycle of protein like β-lactoglobulin which is dependent on the solvent used. Wang et al. found that β-lactoglobulin molecules formed large aggregates in 0.8 M NaCl solution and these large aggregates disappeared as the 0.8 M NaCl solution was replaced with water, which proved to be a reversible process (*183*). The hot stage, temperature controlled microstage, can be built for a commercial tapping mode-AFM using resistive heater and a simple temperature controller (*184*). The hot stage has been applied to *in situ* investigate the isothermal crystallization of semicrystalline polymers on silicon substrate. Holger et al. quantified the lamellar growth rates of polypropylene ($<3\times10^{-3}$ µm/min) and obtained a

maximum temperature condition (40~45 ^{o}C) based on *in situ* hot stage AFM images. By using this hot stage accessory, Holger et al. also observed "edge-on" lamellae of poly(ethylene oxide) spin-cast on silicon wafer with thick layer (2.5 μm), and exclusively "flat-on" lamellae in the 200 nm film (*185*). Based on that phenomenon, the orientation of poly(ethylene oxide) can be tuned by spin-casting films of different thicknesses.

Embedded with those advantages, tapping mode-AFM instrument is suitable for imaging biopolymers such as proteins and polysaccharides. The self-assembly behavior of proteins and polysaccharides can be unveiled with the aid of AFM instrument. The shape and size of individual protein can be quantified by imaging diluted OPI particles deposited on the silicon wafer surface. Liu et al. found that the overall contour of OPI particle is ellipsoidal or disc-like, and the individual OPI particle is ~17.3 nm which is reported reasonably as dry size of OPI particle (*186*). The conformation and dimension of OPI particle in solution are determined and quantified by synchrotron small-angle X-ray scattering (SAXS) tool, whose manuscript is being generated (*187*). The structure information including radius of gyration (R_g), aspect ratio, and pair distribution function (PDF) are extracted from SAXS profiles, and an *Ab initio* model is roughly proposed for prediction. The solvent-induced orientation of zein tetramers spin-cast on silicon wafer surface was visualized by TP-AFM, and the rough surface cast from 95% EtOH and smooth surface cast from acetic acid maybe resulted from the polarity difference of solvent (*181*). In terms of polysaccharide self-assembly, typical example is pectin, a gelling and thickening agent. For instance, TP-AFM can be used to monitor the gelling behavior of high-methoxyl pectin, and to quantify the dimensions of strands and pores that appear within the pectin gel (*188*). Thus, the gel strength can be correlated not only

to the density of pectin strands, but also to the uniformity of pectin distribution within gels.

2.2.2 Experimental setup

From top to bottom, the whole AFM instrument is composed of CCD camera with ×10 optical microscopy, sample chamber, and scanner. The sample chamber is the key component, inside of which is shown in Figure 2.3. In sample chamber, AFM tip fixed on the cantilever scans back and forth continuously on the sample surface. Simultaneously, a laser producer generates an incident laser beam which hits the cantilever, and the cantilever reflects the laser beam (beam 1) toward a mirror. Through second reflection from the mirror, the laser beam (beam 2) reaches the position-sensitive photodetector which recognizes the physical position of the tip. Also, a feedback loop between photodetector and cantilever is used to adjust the tip-to-sample distance for a constant force between the tip and sample, avoiding tip damage.

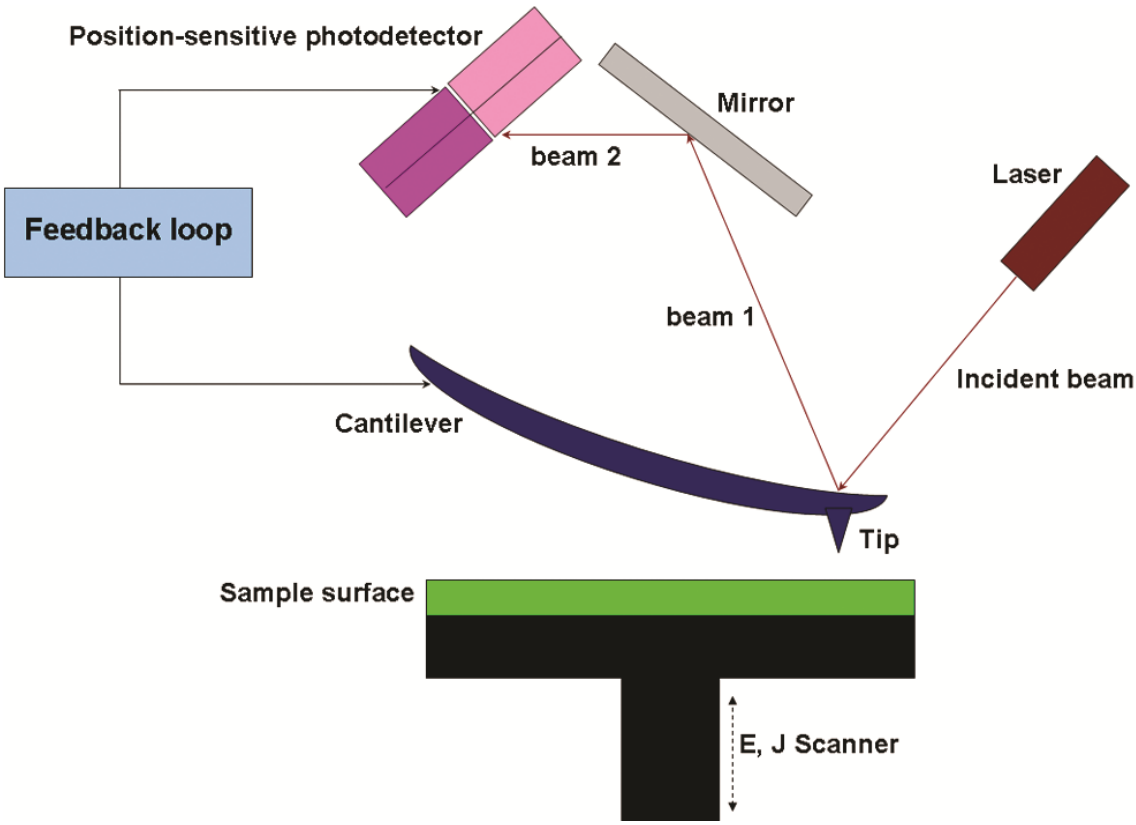

Figure 2.3: Schematic diagram of atomic force microscopy experimental setup.

2.3 Small-angle X-ray scattering

2.3.1 General information

Food systems are among the most complex soft materials studied by theoretical and experimental scientists (*189*). Although food systems are complex, they still follow the rules of modern physics of soft condensed matter. Modern technologies, including atomic force microscopy (AFM), dynamic light scattering (DLS), quartz crystal microbalance with dissipation monitoring (QCM-D), rheology, differential scanning calorimetry (DSC) etc. have been developed to better understand the structures and properties of food materials and interactions within them. Among those modern technologies, small-angle X-ray scattering (SAXS) with third-generation synchrotron radiation provides us with a

strong and convenient tool for probing the internal structures of those everyday soft materials. The X-ray scattering technique relies on the interactions of radiation with matter, like laser light scattering and neutron scattering. The differences between X-rays and other sources lie in their intrinsic properties (i.e., wavelength) and observation contrast (i.e., refractive index for laser and electron density for X-ray). The scientific use of X-rays began in the 1890s. As gradual understanding of the basic theory of X-ray scattering developed over the last 100 years, X-ray methods became more mature. During this period more than 16 Nobel Prizes have been awarded for research into the interaction of X-rays with matter and their applications (*190*). Nowadays, X-ray related methods are used for a wide range of applications, including powder diffraction to determine crystal structure, circular dichroism to determine protein secondary structure, and X-ray imaging for medical applications.

The new generation of intensive X-ray synchrotron sources has accelerated the study of X-rays. Traditional X-ray facilities are usually limited to one wavelength and x-rays of low intensity, which make it time-consuming to conduct small angle X-ray scattering experiments. Compared to traditional X-ray sources, synchrotron sources which generate X-rays through the acceleration of charged particles radially have the advantages of high flux, small beam size, high stability, convenience, and fast measurement. Among different X-ray technologies, small-angle X-ray scattering (SAXS) has been applied to study structures with sizes from roughly 10 Å to several hundred Å. Most food biopolymers like food proteins and polysaccharides are within this size region. Laser light scattering in diluted systems provides information on hydrodynamic radius and size distribution. X-ray scattering serves as an excellent complementary tool to provide a

systematic structural analysis involving overall shape, aggregation number, and surface roughness etc. for a rich variety of objects. SAXS will greatly help to provide insight into the structures of food components and link this structural information with the macro scale mechanical, thermal, and release properties of food components.

2.3.2 Basic Principles of X-ray Scattering

Unlike normal light, X-rays can only provide us with a scattering pattern instead of direct information of the observed objects. The real information (i.e., particle size distribution) and scattering pattern follow the real-and-reciprocal rules, which give us the basic knowledge required to interpret the SAXS data. If *R* represents the real length of an object, then *q*, the scattering vector is in its reciprocal format. They satisfy *R*q*= constant, which can be 2π or 6/π (*191*). Since the development of scattering theory is based upon Bragg's Law, let us take a quick look at the classical equation of Bragg's Law, which is as follows:

$$Sin\frac{\theta}{2} = \frac{\lambda}{2d} \tag{2.7}$$

Distance *d* represents the repeated-order distance in the structure; λ, wavelength of the incident beam, is approximately 1 Å for X-ray beam; θ is the scattering angle. Small-angle scattering is very suitable for detecting biopolymers' scattering patterns and structures. For instance, Pluronic PEO-PPO-PEO copolymer can form micelles with average sizes of approximately 10 Å. If you intend to view the repeated distance *d* with a value of 10 Å for micelle size calculation, the scattering angle θ should be lowered to less than 3°. For even larger biopolymers such as proteins and polysaccharides, it will need to be even lower scattering angle. Therefore, small-angle scattering technology needs to be used to characterize those biomaterials with large sized components.

Before going further, we need to understand the scattering vector q. The wave vector k of a monochromatic plane wave is defined as $2\pi/\lambda$. Figure 2.4 shows the scattering triangle in which k_0 is the wave vector of the incident beam, and k the wave vector of the scattered beam. The change between k_0 and k is defined as scattering vector q. Here we only discuss the elastic scattering, i.e., the energy of the beam does not change during scattering.

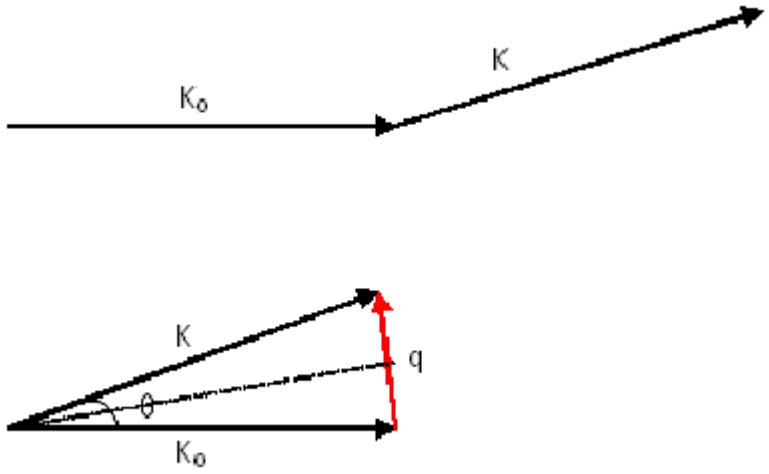

Figure 2.4: Scattering triangle of wave vectors for incident beam k_0, scattered beam k, and scattering vector q. θ: scattering angle.

Therefore, the wavelength λ of k_0 is equal to that of k. Then we can easily get another basic equation for describing scattering vector q.

$$q = \frac{4\pi}{\lambda} Sin(\frac{\theta}{2}) \tag{2.8}$$

Substitute eq. 1 into eq. 2, we can obtain the following reciprocal relationship:

$$d = \frac{2\pi}{q} \tag{2.9}$$

Equation 3 once again displays the real-and-reciprocal rule embedded in SAS technology. From eq. 3 it is once again demonstrated clearly that the small-angle method is suitable for viewing large-scale objects, especially food ingredients such as proteins and polysaccharides.

2.3.3 Modern Synchrotron X-ray Facilities

It is usually difficult for conventional X-ray facilities to undertake SAXS experiments due to beam divergence and wavelength limitations. With the development of modern synchrotron radiation, SAXS has been rejuvenated as a very powerful tool for applications in physics, biology, chemistry, and materials science. Currently, there are more than 35 synchrotron SAXS beamlines worldwide, including those located in the Photon Factory at High Energy Accelerator Research Organization in Tsukuba, Japan; Advanced Photon Source (APS) at Argonne National Lab in Illinois, USA; Laboratoire pour l'Utilisation du Rayonnement Electromagnétique (Lure) in France; and National Synchrotron Light Source (NSLS) at Brookhaven National Laboratory in New York, USA (*192*). With the increasing demand for structure analysis in different scientific disciplines, new synchrotron facilities have recently opened, such as the Shanghai Synchrotron Radiation Facility (SSRF) in China, which was opened to general users in May 2009, and the ALBA synchrotron facilities in Cerdanyola del Vallès, Spain, which was put in use in 2010.

Modern X-rays are generated from a highly vacuum-circulated electron beam accelerator. The bending trajectory along which the charged particles travel helps with the emission of X-rays. This modern X-ray is much more intensive than that provided by traditional X-ray tubes, usually with many orders higher intensity. Such a high flux beam greatly

shortens the period of experimental measurement. Figure 2.5 displays the schematic diagram of a synchrotron radiation circular accelerator (*193*). There are several major components installed in the storage ring, including an injection system, a vacuum chamber, bending magnets, focusing magnets and undulators. The injection system generates electrons prior to particle acceleration. Both bending magnets and focusing magnets are utilized to bend the trajectory of the generated electrons. Compared with bending magnets, focusing magnets are applied to tune the electron beam path in a more refined manner. Long vacuum chambers are utilized to transport the electron beam with very limited energy loss. Undulators keep the X-ray beam's high intensity with narrow energy bands in the spectrum along the beamline. Afterwards the generated X-ray beams are transported to different sites around the large acceleration ring for different applications.

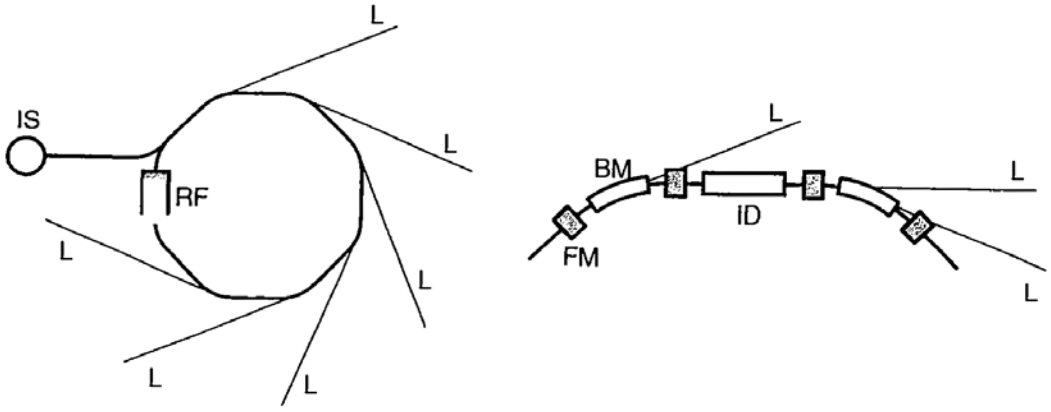

Figure 2.5 Schematics of a synchrotron radiation facility. The closed circuit on the left represents the storage ring. IS, injection system; RF, radiofrequency cavity; L, beamline; BM, bending magnets; FM, focusing magnets; ID, insertion device. (Reproduced with kind permission from Ref. 194; © Oxford University Press, USA)

Small-angle X-ray scattering is usually among those different synchrotron X-ray technique tools. Figure 2.6 shows the representative scheme of SAXS at BioCAT-18ID beamline at the Advanced Photon Sources (APS), Argonne National Laboratory, USA.

Different accessories are attached along the beamline to ensure the high quality of beamline output for SAXS experiments (*194*). Long adjustable vacuum chambers guarantee sample-to-detector distances from 100 to almost 6000nm, which covers the q range from ~0.001 to ~30nm^{-1}. The guard slits are applied to reduce parasitic scattering. Double focusing optics decrease focal spot sizes to approximately 150×40μm^2. The 18ID beamline is equipped with a high-sensitivity charge coupled device (CCD) detector with large working area and high spatial resolution. SAXS is often applied to test biological macromolecules such as a dilute protein solution. In order to avoid the sample damage caused by a high flux of beamline, a temperature-controlled water-jacketed flow cell has been designed for the bio-sample chamber.

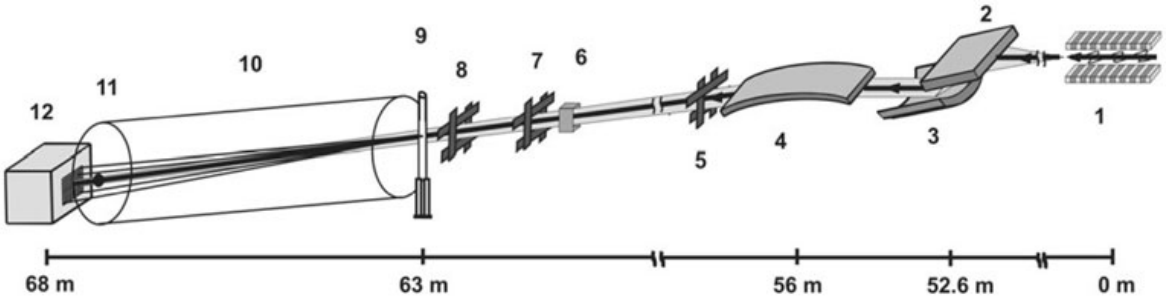

Figure 2.6 Schematic representation of the synchrotron X-ray scattering BioCAT-18ID beamline at the APS, Argonne National Laboratory, USA: (1) primary beam coming from the undulator, (2) and (3) flat and sagittaly focusing Si (111) crystal of the double-crystal monochromator, respectively, (4) vertically focusing mirror, (5) collimator slits, (6) ion chamber, (7) and (8) guard slits, (9) temperature-controlled sample-flow cell, (10) vacuum chamber, (11) beamstop with a photodiode, (12) CCD detector (Reproduced with kind permission from Ref 195; © Institue of Physics Publishing)

Chapter 3

Rheological properties of chitosan–tripolyphosphate complexes: From suspensions to microgels

3.1 Introduction

Chitosan (CS), the second most abundant biopolymer in nature next to cellulose, is one of the very few positively charged natural biopolymers existing in the world. It is derived from the exoskeleton of shrimps and other crustaceans, and has a linear structure composed of glucosamine unit and N-deacetylated glucosamine unit, also known as 2-amino-2-deoxy-(1 → 4)-β-d-glucopyranan. Chitosan has received broad attention from researchers of different backgrounds due to its unique structure and natural abundance (*195*). Previous literatures show that chitosan has been used to form complex coacervates (*196*), biocomposites (*197*), bio-carbon nanotubes (*198*), and scaffolds for tissue engineering (*199*). Other applications of chitosan include drug delivery systems, nanofibers, biosensors, and edible films (*200-202*). Among the above research areas, chitosan-based delivery system is one of the most important applications due to its biodegradability, biocompatibility, bioadhesion and non-toxicity (*44, 203-204*). Many investigations of chitosan-based delivery systems have been carried out previously. For example, Jang and Lee succeeded in improving the heat stability of l-ascorbic acid during

processing by utilizing chitosan–TPP nanoparticles (*205*). Richardson, Kolbe, and Duncan conjugated chitosan to DNA backbone for protecting DNA from endonuclease degradation and promoting DNA's cell targeting (*206*). Wu, Yang, Wang, Hu, and Fu applied CS–TPP nanoparticles for loading the drug ammonium glycyrrhizinate. The release profile of their CS–TPP nanoparticles followed the rule of first burst release and then steady release, suggesting that CS–TPP nanoparticle was a suitable oral delivery agent (*31*).

In order to meet different demands, distinct methods were used to produce chitosan nanoparticles. Chemical modification provides us with series of methods for producing stable chitosan nanoparticles. For instance, amphiphilic micellar structure of linolenic acid-modified chitosan could be immobilized with trypsin by using glutaraldehyde as the crosslinker, which greatly improved trypsin's thermal stability and enzymatic activity (*207*). Other researchers functionalized chitosan with multiple functional groups, such as octyl, sulfate and polyethylene glycol monomethyl ether (mPEG) groups to target both polymeric micelle structure and brain-targeting function, and the resulted chitosan nanoparticles could improve the water solubility of hydrophobic drug paclitaxel by 4000 times (*208*). Recently, a novel chitosan-based amphiphile, octanoylchitosan–polyethylene glycol monomethyl ether (acylChitoMPEG), has been synthesized using both hydrophobic octanoyl and hydrophilic polyethylene glycol monomethyl ether (MPEG) substitutions (*209*). The synthesized acylChitoMPEG exhibited good solubility in either aqueous solution or common organic solvents such as ethanol, acetone, and $CHCl_3$. Cytotoxicity results showed that acylChitoMPEG exhibited negligible cytotoxicity even at the concentration as high as 1 mg/mL (*209*).

In addition to chemical synthesis, physical methods were also used to create chitosan complexes or nanoparticles with milder processing conditions. Since chitosan has hydroxyl and amino groups on the backbone, chitosan can interact with other negatively charged hydrocolloids or small molecular weight compounds to form complexes. These complexes could potentially be used for mouth-feel improvement in food industry (*210*) and drug delivery in pharmaceutical industry (*211*). Gum arabic is a thickening agent commonly used in food product development, such as flavor encapsulation. Espinosa-Andrews et al. investigated the interactions between gum arabic and chitosan by examining the influence of gum arabic/chitosan ratio, total polymer concentration, pH and ionic strength upon the electrostatic complexes formation. Their turbidity and electrophoretic mobility results showed that the optimized gum arabic/chitosan mass ratio was 5 for coacervate formation. The maximized gum arabic–chitosan interaction could be obtained within the pH range between 3.5 and 5 (*196*). Another negatively charged compound worth noting is sodium tripolyphosphate (TPP), a small molecular weight crosslinker carrying five negative charges in each molecule. TPP has been approved as a GRAS ("generally recognized as safe") reagent by FDA. Chitosan (CS) and TPP can form nanoparticles through electrostatic interaction, which has previously been investigated for different delivery applications (*28, 31, 212-213*). One interesting formulation among them is CS–TPP nanoparticles developed through an O/W emulsion route for entrapping hydrophobic felodipine (*213*). After felodipine was entrapped into CS–TPP nanoparticles, the control release of felodipine could be achieved by tuning pH, initial concentration, and molecular weight during nanoparticles preparation.

Previous studies suggest that CS–TPP nanoparticles are very useful carriers for drug and nutraceutical delivery. It is known that the CS–TPP particles were formed mainly through the electrostatic interaction between positively charged chitosan and negatively charged TPP molecules. However, how the CS–TPP particle sizes affect their packing, as well as the rheological properties of the resulted complex fluids (either chitosan–TPP particle suspensions or microgels) have been scarcely reported. In this paper, chitosan particles of different sizes were prepared through the use of TPP and ultrasonication. Depending on particle sizes, either CS–TPP particle suspensions or microgels were obtained after centrifugation at $11{,}000 \times g$, and their corresponding rheological properties were investigated by both static and dynamic rheological measurements. The static rheological technique measured the apparent viscosity (η) of polymer solution as a function of shear rate, while dynamic frequency test determined the storage modulus (G') and loss modulus (G'') as a function of angular frequency (ω). The correlation between particle sizes and particle packing profiles was also explored through rheological measurements.

3.2 Materials and methods

3.2.1 Materials

Chitosan with deacetylation degree (DD) of 98.0% and molecular weight (M_w) of 330 kDa was purchased from Kunpoong Bio. Co., Ltd. (South Korea). Sodium tripolyphosphate (TPP, 85%, technical grade) was purchased from Acros Organics (Morris Plains, NJ). Acetic acid, glacial (ACS grade) was purchased from Fisher Scientific (Fair Lawn, NJ). All of these reagents were used as received. Milli-Q (18.3 MΩ) water was used in all experiments.

3.2.2 Methods

3.2.2.1 Preparation of chitosan–sodium tripolyphosphate (CS–TPP) nanoparticles

Different amounts of chitosan (CS, 330 kDa) were dissolved in 2 wt% acetic acid solution to form chitosan solutions with concentrations ranging from 1 mg/mL to 30 mg/mL. Sodium tripolyphosphate (TPP) was dissolved in Milli-Q water to form a 200 mg/mL solution. CS–TPP nanoparticles were formed by drop-wise addition of TPP solution into chitosan stock solution at different CS/TPP mass ratios under severe magnetic stirring. The change of solution volume caused by the addition of TPP solution was negligible due to the large CS/TPP volume ratio. After vortexing for 5 min, 40 mL of each CS–TPP particle suspension was processed under ultrasonication (Sonifier Cell Disruptor, Model W-350, Branson Sonic Power Co.) with 3.75 W/mL energy output and the duration varying from 3 to 9 min to obtain chitosan particles with controlled particle sizes. High speed centrifugation at ambient condition was set at 11,000 × *g* for 50 min to separate the microgel and supernatant. The supernatant was then removed, and the remaining microgels were washed with 2 wt% acetic acid buffer for three times prior to the rheological study.

3.2.2.2 Particle size measurements

Photon correlation spectroscopy (PCS)-based BIC 90 plus particle size analyzer equipped with a Brookhaven BI-9000AT digital correlator (Brookhaven Instrument Corporation, New York, USA) was used to measure hydrodynamic diameters (*d*) and size distribution of CS–TPP nanoparticles. The light source is a solid state laser operating at the wavelength of 658 nm with 30 mW power, and the signals were detected by a high sensitivity avalanche photodiode detector. All measurements were conducted at 25 ± 1 °C

with the detection angle of 90°. CS–TPP nanoparticle suspensions were diluted with buffer until their viscosities were close to that of water (i.e., 0.89 cp at 25 °C). The normalized field–field autocorrelation functions $g(q,t)$ were obtained from the intensity–intensity autocorrelation functions, $G(q,t)$, via the Sigert relation (*214*). Both single stretched exponential fit and Cumulant analysis method were used in our particle size measurements (*215*).

3.2.2.3 Rheological measurements

Rheological measurements of the CS–TPP nanoparticle suspensions were performed by using ARES Rheometer (Rheometrics Scientific, NJ) with either cone and plate geometry (diameter 50 mm, cone angle 0.04 rad) or parallel plate geometry (diameter 25 mm) at ambient temperature (approximately 25 °C). Steady sweep measurements were carried out by applying shear rate from 1 to 1000 s^{-1} with 20 data points per decade. Zero shear viscosities, the viscosities at vanishing shear rates, were determined by extrapolating the Newtonian plateau to zero shear rate. Prior to a dynamic frequency sweep test, dynamic strain sweep test ranging from 0 to 100% was performed at 2 rad/s angular frequency. In this paper, the strain was fixed at 0.5% and the angular frequency ω was ranged from 0.1 to 100 rad/s. Small amount of mineral oil was utilized to seal the sample edge to prevent solvent evaporation. The gap between one plate or cone and the other plate was properly selected to avoid sample slip.

3.2.2.4 Atomic force microscopy (AFM) measurements

Images of CS–TPP nanoparticles were collected by a commercial Nanoscope IIIa Multi-Mode AFM (Veeco Instruments, CA) equipped with a J scanner, which was operated in tapping mode using silicon cantilever. The scanned images were obtained at the scan size

of 2.0 μm × 2.0 μm and the scan frequency of 0.75 Hz. The CS–TPP nanoparticle suspensions for AFM imaging were prepared by solution immersion on silicon wafers. Those silicon wafers were immersed in the CS–TPP nanoparticle suspension for 1 h, washed by Milli-Q water and dried by nitrogen gas prior to morphological measurements.

3.2.2.5 Attenuated total reflection Fourier transformed infrared spectroscopy (ATR-FTIR)

The ATR-FTIR spectra were collected at ambient temperature using a Thermo Nicolet 670 FT-IR Spectrometer (Thermo Electron Corp, Madison, WI) with a Smart MIRacle horizontal attenuated total reflectance Ge crystal accessory. Each spectrum was averaged over 512 scans with 4 cm^{-1} resolution in the wavenumber range of 600–4000 cm^{-1}.

3.2.2.6 Water content measurement

The water contents of the CS–TPP microgels were determined by dry-weighing method. The CS–TPP microgel samples were weighed before and after fully drying by a balance with four digits after decimal point. The weighing process was duplicated for three times.

3.2.2.7 Theory for particle–particle interaction

The stabilization of CS–TPP nanoparticle suspensions or microgels depends upon particle–particle interaction which involves electrostatic repulsion and van der Waals attraction. For suspensions, electrostatic interaction between positively charged CS–TPP nanoparticles maintained particle stability. For microgels, the collective effect of van der Waals force and electrostatic interaction played a dominant role in the microgel formation. To qualitatively understand the effect of particle sizes on the rheological properties of microgels, Lennard–Jones potential was applied to determine van der Waals interaction between a pair of CS–TPP particles while Debye–Hückle theory was adopted

here for the electrostatic potential (*216*). For van der Waals potential, the Lennard–Jones equation was shown as follows:

$$U_{vdw}(r) = U_{0v}[(\frac{r_0}{r})^{12} - 2(\frac{r_0}{r})^6] \quad (3.1)$$

where r_0 was the van der Waals radii of CS–TPP particle, r was the particle–particle interaction range, and U_{0v} was the depth of the interaction well.

For electrostatic potential, the Debye–Hückle equation was displayed as follows:

$$U_{ele}(r) = \frac{\Delta S^2 \rho_1 \rho_2}{4\pi\varepsilon r} e^{r/\lambda_D} \quad (3.2)$$

where r is the particle–particle interaction range; ε, which equaled 0.18 e^2/pN nm^2 at room temperature in water, was the dielectric constant of 2% (v/v) acetic acid buffer; ρ_1 and ρ_2 were the surface charge densities of CS–TPP nanoparticle 1 and nanoparticle 2; ΔS was the projection area of a CS–TPP nanoparticle; λ_D, which was approximately equal to $0.304\varphi^{-1/2}$ (nm) for monovalent salts, where φ (mol/L) was the monovalent salt concentration, was the Debye screening length (*217*). The above two equations combined were used to obtain the total potential of CS–TPP particles in the microgel state.

3.3 Results

3.3.1 Morphology and sizes of CS–TPP nanoparticles

Figure 3.1A displays the tapping mode AFM height image of CS–TPP nanoparticles in dry state on the silicon wafer, which indicates the pseudo-spherical morphology of CS–TPP nanoparticles. Some particles were overlapped with each other. Section analysis embedded in the software Nanoscope5.30 was applied to calculate the particle size on the wafer surface. The vertical distance from the upper edge of the particle to the bottom of the silicon wafer was taken as particle size, which was previously utilized to calculate

size of oat protein isolate in dry state (*218*). The individual particle sizes of those CS–TPP nanoparticles (prepared at initial chitosan concentration of 1.5 mg/mL) from section analysis are approximately 20–30 nm. Figure 3.1B and 3.1C shows the autocorrelation function curve of dynamic light scattering (DLS) and its corresponding size distribution, respectively. The minimum particle size calculated from curve fitting through Stocks–Einstein's equation turns out to be 170 nm. The particle sizes calculated from AFM were smaller than those from DLS, which was mainly due to difference in sample states. AFM gave the particle images in dry state while DLS provided average particle size in solution. The particle size calculated from DLS contained hydrated layers surrounding the nanoparticles which disappeared for dried nanoparticles in AFM measurement. Besides, the existence of CS–TPP particle aggregates also contributed to the larger DLS value. Similarly, Wu et al. found that the sizes of chitosan nanoparticles (20–80 nm) determined by TEM were smaller than those determined by DLS (>120 nm) in water (*31*).

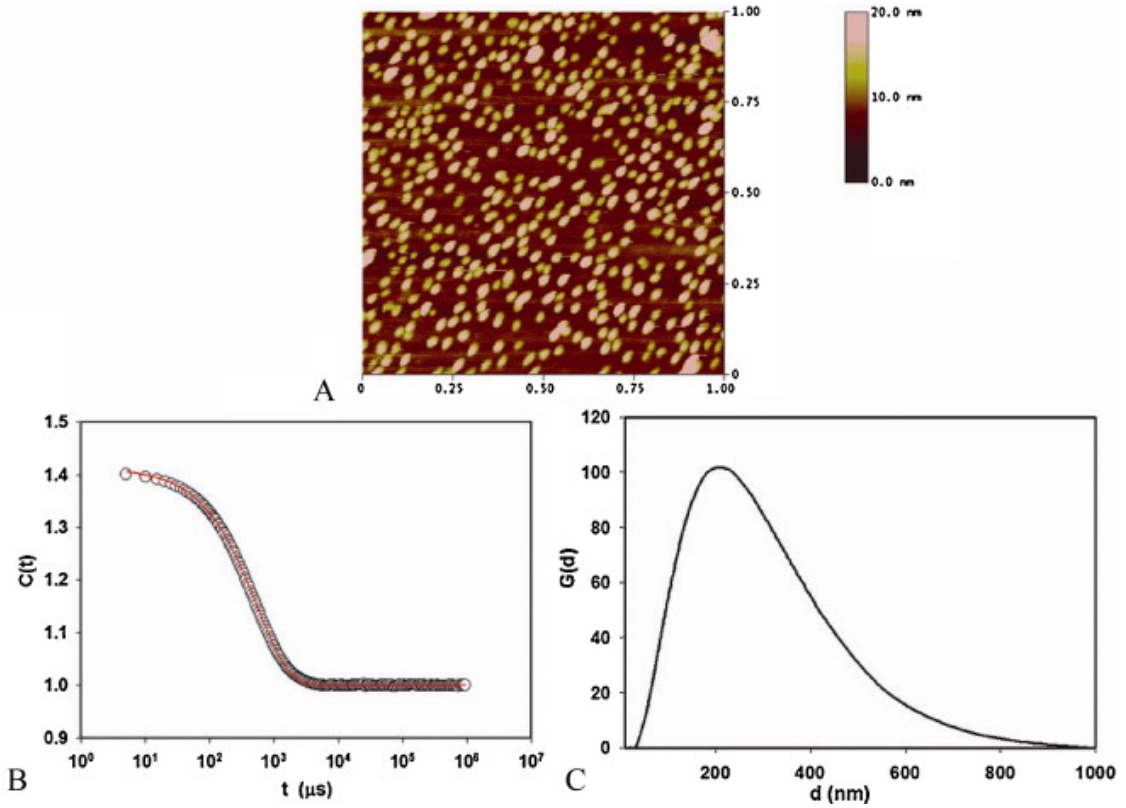

Figure 3.1: Typical tapping mode-atomic force microscopy (AFM) height image (A), dynamic light scattering autocorrelation function and its fitting curve (B), as well as its particle size distribution obtained from Cumulant analysis (C) for chitosan–sodium tripolyphosphate (CS–TPP) particles prepared at initial CS/TPP mass ratio of 3.75. The chitosan concentration was fixed at 1.5 mg/mL and the AFM scan size is 1 μm × 1 μm.

3.3.2 Effect of CS/TPP mass ratio

Table 3.1 shows the physical states of CS–TPP complexes at different initial TPP and CS concentrations. At low TPP concentrations (i.e., lower than 0.5 mg/mL), the amount of TPP was not enough to fully crosslink chitosan chains, and the solutions remained transparent. Further increase of TPP concentration (i.e., higher than 1 mg/mL) led to an increase in particle sizes, resulting in either suspension or precipitation.

Table 3.1: Physical states of sodium tripolyphosphate (TPP)-crosslinked chitosan (CS) particles at different initial CS and TPP concentrations

	TPP 0.1 mg/mL	TPP 0.5 mg/mL	TPP 1.0 mg/mL	TPP 1.5 mg/mL	TPP 2.0 mg/mL
CS 1.0 mg/mL	○	○	◇	□	□
CS 1.5 mg/mL	○	○	◇	◇	□
CS 2.0 mg/mL	○	○	◇	◇	◇

Figure 3.2 shows the hydrodynamic diameters of CS–TPP complexes under different CS and TPP concentrations. Chitosan concentrations between 1 mg/mL and 2 mg/mL were chosen because higher concentrations (i.e., 10 mg/mL chitosan solution) could significantly alter the rheological properties of CS–TPP complexes. The formation of CS–TPP nanoparticles mainly depends upon CS/TPP mass ratio when chitosan concentration is relatively low. The optimum CS/TPP mass ratio condition at low chitosan concentration could also be determined, and Figure 3.2 shows that the optimum CS/TPP mass ratio for the minimum particle sizes is 3.75, which is in agreement with previous results (*28, 31, 205*). To obtain chitosan particles of different sizes, ultrasonication (energy output of 3.75 W/mL) was also used as a complementary tool to break down the particle aggregates. Previously, Wu et al. reported that low chitosan concentration could increase the drug encapsulation capability. They recommended that for 1 mg/mL TPP crosslinker solution, chitosan concentration should be kept within the range of 0.5–4 mg/mL (*31*). Jang and Lee suggested that low molecular weight chitosan and TPP formed nanoparticles of minimum sizes at the CS/TPP mass ratio of 2.5. Combining the results of zeta-potential with dynamic light scattering, Hu et al. concluded

that the optimized CS/TPP mass ratio was 5 (*28*). In this paper, the CS/TPP mass ratio of 3.75 was used in our following AFM, FTIR, and rheological experiments.

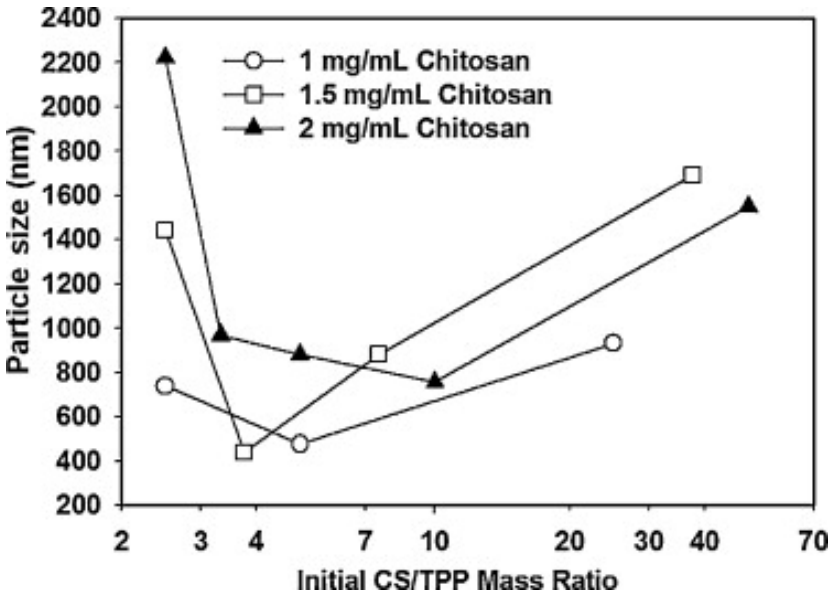

Figure 3.2: Effect of initial chitosan/sodium tripolyphosphate (CS/TPP) mass ratios upon particle sizes of CS–TPP particles under different initial chitosan concentrations: 1 mg/mL (empty circles); 1.5 mg/mL (empty square); and 2 mg/mL (solid triangles).

3.3.3 FTIR analysis of CS–TPP nanoparticles

Figure 3.3 shows the ATR-FTIR spectra of (A) pure chitosan (CS), (B) CS–TPP nanoparticle, and (C) pure TPP in the wavenumber range of 4000–600 cm^{-1}. For pure chitosan (Figure 3.3A), the characteristic bands due to the stretching vibration of $–NH_2$ and –OH groups were observed at 3356 cm^{-1}. The feature peak at 1547 cm^{-1} for amide II (N–H bending vibration) and the small shoulder peak at 1647 cm^{-1} for amide I (–CO stretching vibration) indicate the high degree of deacetylation of chitosan. The flattening of the amine peak at 3356 cm^{-1} in Figure 3.3B indicates that majority of amino group of chitosan participated in the electrostatic interaction with TPP. The characteristic peak located at 1206 cm^{-1} is assigned to P = O groups of TPP (Figure 3C). The disappearance

of that peak in the IR spectra of CS/TPP particle is another evidence of electrostatic interaction between the negatively charged phosphate group in TPP and positively charged amino group in chitosan.

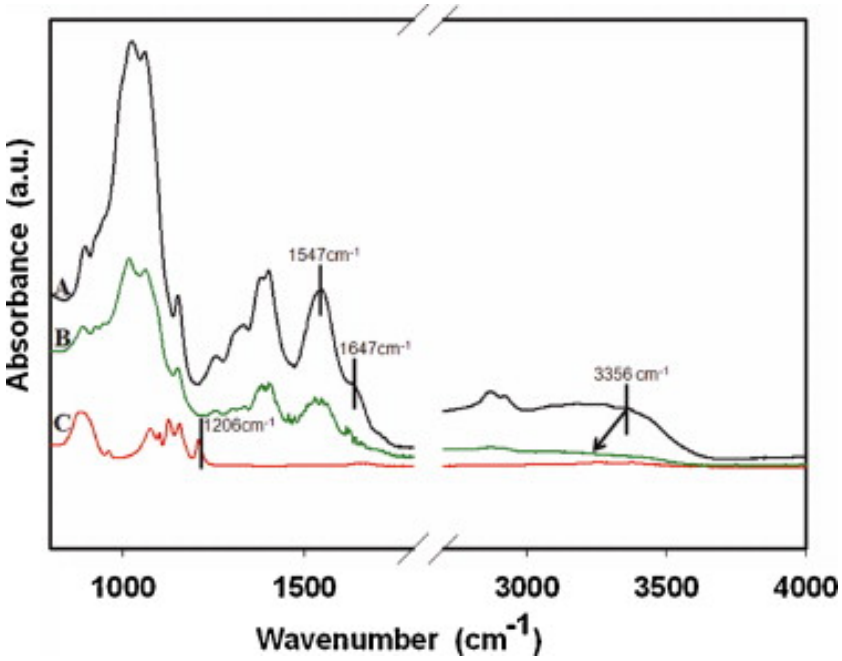

Figure 3.3: FTIR spectra of (A) pure chitosan powder (M_w = 330 kDa, degree of deacetylation = 98%), (B) chitosan–sodium tripolyphosphate (CS–TPP) particle prepared at initial CS/TPP mass ratio of 3.75 under 4 min sonication with 3.75 W/mL energy input (the initial chitosan concentration was 10 mg/mL), and (C) sodium tripolyphosphate powder.

3.3.4 Rheological properties

Figure 3.4A displays the plot of apparent viscosities versus shear rate for chitosan (CS) solutions and corresponding CS–TPP particle suspensions of three different initial chitosan concentrations (i.e., 15 mg/mL, 10 mg/mL, and 8 mg/mL). All of the CS solutions and CS–TPP suspensions exhibited Newtonian flow behavior. The apparent viscosities of 8 mg/mL, 10 mg/mL, and 15 mg/mL chitosan (CS) solutions were 0.012 Pa s, 0.015 Pa s, and 0.029 Pa s, respectively. In contrast, the apparent viscosities of 8 mg/mL, 10 mg/mL, and 15 mg/mL CS–TPP particle suspensions decreased to

0.003 Pa s, 0.004 Pa s, and 0.006 Pa s, respectively. Chitosan chains carried positive charges at pH below 6.4 while TPP was negatively charged from pH 2 to pH 6.4. The formation of compact chitosan particles reduced the affinity of chitosan molecules with water, leading to the reduced viscosities.

Figure 3.4B shows the plot of zero shear viscosities versus initial chitosan concentrations for CS solutions and CS–TPP suspensions (partially obtained from Figure 3.4A). The particle sizes of CS–TPP particles ranged from 180 nm to 360 nm. One notes that the increase of initial chitosan concentration results in bigger particle sizes. Similar results were also reported by Hu et al., who showed that the particle size increased linearly with the increase of chitosan concentration. The lower dependency of the apparent viscosities of TPP-crosslinked chitosan nanoparticles on the initial chitosan concentration is probably due to the compact nature of chitosan nanoparticles.

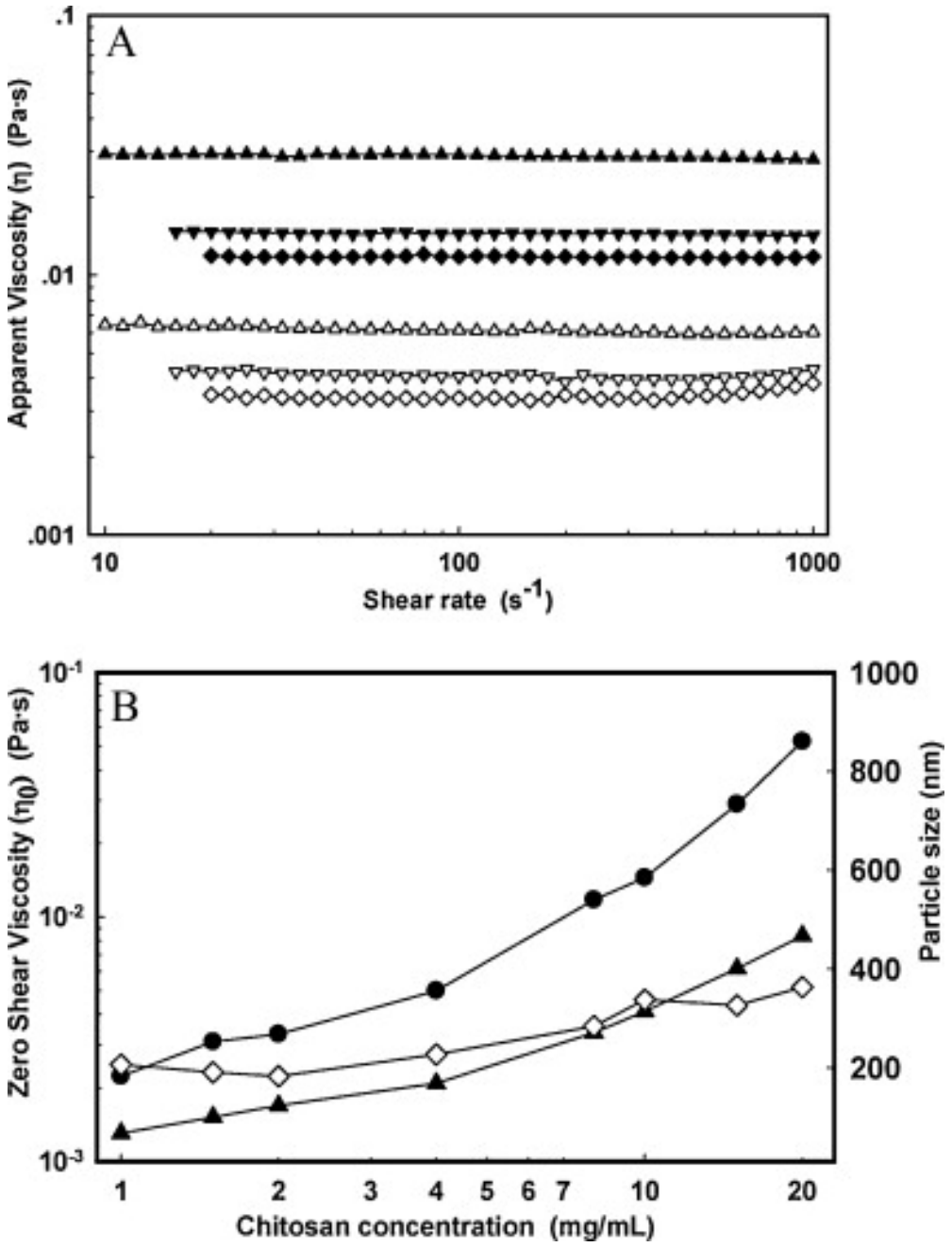

Figure 3.4: (A) The curves of apparent viscosity versus shear rate for chitosan (CS) solutions and CS–TPP particle suspensions: (▲) 15 mg/mL chitosan solution; (▼) 10 mg/mL chitosan solution; (◆) 8 mg/mL chitosan solution; (△) 15 mg/mL CS–TPP suspension; (▽) 10 mg/mL CS–TPP suspension; (◇) 8 mg/mL CS–TPP suspension and (B) the plot of zero shear viscosity as a function of chitosan concentration for (●) pure chitosan solution, (▲) CS–TPP nanoparticle suspension, and the plot of particle size as a function of chitosan concentration for (◇) CS–TPP suspensions.

Figure 3.5A shows the applied strain dependence for storage modulus (G') and loss modulus (G'') at the angular frequency of 2 rad/s. CS–TPP microgels, which were prepared through the centrifugation of chitosan sub-micrometer particles, displayed strain-softening behavior which was also found in chitosan-modified nanoclay at highly hydrated state (*177*). Here, the strain was fixed at 0.5% for dynamic oscillatory shear analysis, which was within the linear viscoelastic region. In Figure 3.5B, G' of all the microgels consistently showed higher values than G'' over the frequency range studied (i.e., 0.1–100 rad/s), suggesting the elastic behavior for these CS–TPP complexes. And the large difference between G' and G'' indicates a strong microgel. As oscillatory frequency increased, the G' slightly increased before reaching a plateau at high frequency region. In contrast, the G'' increased to a larger degree as with the increase of frequency, suggesting that a high oscillatory shear may weaken the original microgel structure and turn a tight gel into a loose structure.

The plots of G' and G'' as a function of particle sizes at $\omega = 1$ rad/s and shear strain = 0.5% are presented in Figure 3.5C. One notes that G' is always larger than G'' over the entire particle size range (i.e., 336–868 nm), indicating gel-like structure of CS–TPP microgels. There were two regions in Figure 3.5C: In the first particle size region (336–546 nm), G' increased significantly from 1000 Pa (particle size of 336 nm) to 10,568 Pa (particle size of 546 nm); further increase of particle sizes from 546 nm to 868 nm led to a smaller increase in G', which reached an ultimate value of 20,404 Pa. This phenomenon illustrates that larger particles tend to form stronger microgels.

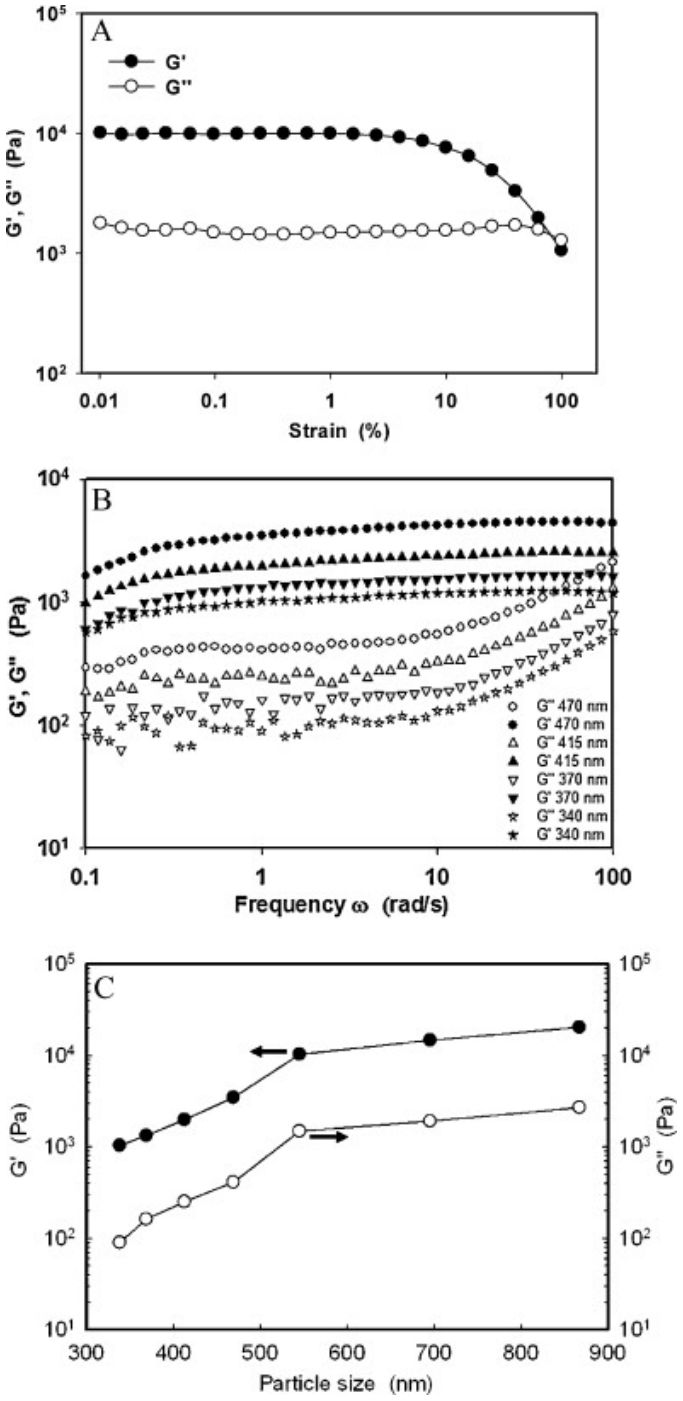

Figure 3.5: (A) Storage modulus (G') and loss modulus (G'') as a function of strain (%) for chitosan–sodium tripolyphosphate (CS–TPP) microgels prepared at initial chitosan concentration of 20 mg/mL under 6 min sonication with 3.75 W/mL energy input [•: storage modulus (G') and ○: loss modulus (G'')]. (B) Storage modulus (G', filled) and loss modulus (G'', empty) as a function of angular frequency (ω) at strain = 0.5% for CS–TPP microgels prepared with different particle sizes (circles, 470 nm; up triangles, 415 nm; down triangles, 370 nm; and stars, 340 nm). (C) Effect of particle sizes on the storage modulus (G') and loss modulus (G'') of CS–TPP microgels [•: storage modulus (G'') and ○: loss modulus (G'')]. Here angular frequency (ω) and strain were fixed at 1 rad/s and 0.5%, respectively.

3.3.5 Water content of CS–TPP microgels

In order to further analyze the composition of CS–TPP microgels, the water content within the microgels was determined by weight-loss analysis technique. Figure 6 exhibits the water content of CS–TPP microgels prepared from CS–TPP complexes of different particle sizes. All CS–TPP microgels had a water content of about 87%. No obvious change in the water content with the sizes of the CS–TPP particles was observed. We interpret this as due to the relatively homogeneous packaging of CS–TPP particles, in which each particle behaved like a hard sphere, and its free volume (interspace between particles) depended upon the packing pattern rather than the particle sizes.

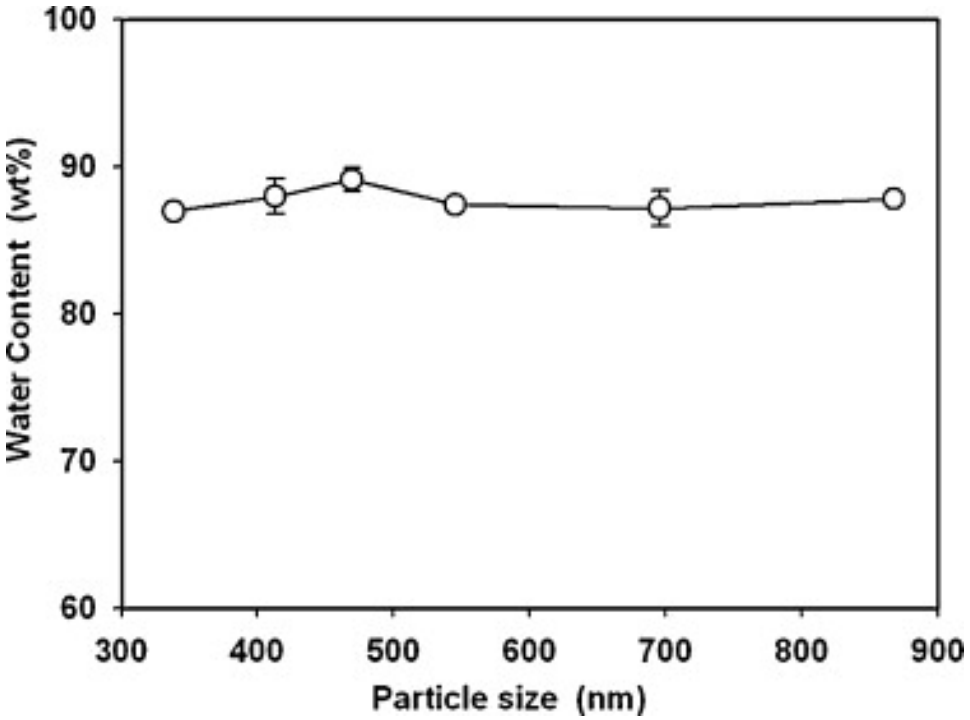

Figure 3.6: The plot of water contents of chitosan–sodium tripolyphosphate (CS–TPP) microgels versus particle sizes.

3.4 Discussion

Chitosan formed complexes/particles after being crosslinked by TPP. Calvo's classical procedure was commonly adopted by many researchers to directly prepare CS–TPP nanoparticles (*219-220*). Due to electrostatic interaction between chitosan and TPP, many physicochemical factors, including pH, ionic strength, CS/TPP mass ratio, initial chitosan concentration and processing methods can affect the stability of CS–TPP particle suspensions. Here we optimized the condition for CS–TPP nanoparticle formation by varying CS/TPP mass ratio, chitosan concentration, and ultrasonication conditions prior to rheological measurement. The CS/TPP mass ratio affected TPP's crosslinking efficiency, while the chitosan concentration influenced fluid viscosity, particle–particle distance, and surface charges of the particles directly. It was also reported that chitosan concentration could affect the zeta-potential of CS–TPP nanoparticles. Higher chitosan concentration caused more unneutralized $–NH_3^+$ on the surface of nanoparticles, which further led to much stronger electrostatic repulsion between particles (*28*). Unlike the conventional CS–TPP complex formulation, ultrasound processing used in the current research further decreased the particle size by breaking down the aggregates, and simultaneously enhanced their storage stability. In addition to our variables for optimization, the effect of chitosan molecular weight on particle size could not be ignored either. Janes et al. confirmed that chitosan of lower molecular weight tended to form smaller nanoparticles because shorter chitosan chains were easier to penetrate into the CS–TPP complexes, resulting in a denser pattern. CS/TPP mass ratio, one of the most important processing parameters, was optimized without sonication so that we could determine the crosslinking efficiency under natural condition. After fixing the CS/TPP

mass ratio, both chitosan concentration and sonication time were selected as adjustable parameters to control the particle sizes of CS–TPP nanoparticles during rheological measurement.

At the concentration range studied, both chitosan solutions and CS–TPP nanoparticle suspensions show Newtonian flow behavior within the major shear rate range, which is good for scale-up processing. Compared with chitosan solutions, CS–TPP nanoparticle suspensions were of much lower viscosity at the same chitosan concentration. This is because TPP-crosslinked chitosan molecules turned into more dense particles whose hydrodynamic volumes were smaller than pure chitosan chains. Fewer free chitosan chains and more crosslinked chains result in a decrease of total hydrodynamic volumes of chitosan. When the total hydrodynamic volume of chitosan is smaller than the solution volume, chitosan chains do not entangle with each other.

For CS–TPP microgels prepared from centrifugation of CS–TPP particle suspensions with initial particle sizes larger than 300 nm, two regions of G' and G'' were observed, as shown in Figure 3.5C. Here, different particle sizes were achieved by adjusting initial chitosan concentration and sonication time. The microgels with particle sizes ranging from 340 nm to 470 nm were prepared from 10 mg/mL chitosan solution, while the rest of the microgels were prepared from chitosan solution of higher concentration (i.e., 20 mg/mL). In the first region, the ultrasonication processing time was utilized to tune the particle size. Compared with sonication time, chitosan concentration exhibited a higher impact upon the storage and loss modulus, hence the particle packing density of CS–TPP microgels. At the same chitosan concentration, elastic modulus and loss modulus maintained a linear increase relationship on the semi-log scale with sonication period.

The particle sizes of CS–TPP microgels ranging from 340 nm to 870 nm were suitable for high speed centrifugation. Consistently larger G' than G'' over the entire frequency range studied suggested the elastic behavior of CS–TPP microgels, as shown in Figure 3.5B. The impact of particle sizes on the rheological properties of CS–TPP microgels may be related to the difference in particle packing profiles within the microgels. The higher G' of CS–TPP microgels at larger particle sizes indicated that larger particles tended to form tighter particle packing in microgels. The centrifugal force had a bigger influence on large particles than small particles, resulting in higher particle packing density and stronger interparticle interactions within the microgels.

For TPP-crosslinked chitosan particle suspension, electrostatic interaction plays an important role in preventing particle aggregation which can be verified by high value of CS–TPP nanoparticles' zeta-potential (averaged ~65 mV). For chitosan-based gels, the stabilization of gel structure is complicated. Different gel formations result from different gelation mechanisms. By proper manipulation, pH-induced chitosan hydrogel can be achieved. Ta et al. prepared a thermo sensitive orthophosphate–chitosan hydrogel which can be used for drug delivery (*221*). They prepared the gel by mixing dipotassium hydrogen orthophosphate and chitosan solutions at low temperature and obtained the gel through elevating temperature. Similar protocol has also been adopted by Chenite et al. for β-glycerol phosphate/chitosan hydrogel preparation (*222-223*). The preparation involved a sol–gel transition, and several interactions, including hydrogen bonding, electrostatic attraction and hydrophobic interaction are responsible for this transition. In their systems, the addition of glycerol phosphate can increase pH while prevent precipitation of chitosan through electrostatic interaction, and promote gel formation

upon elevating temperature through enhancing hydrophobic interactions among chitosan chains. The increase of temperature strengthened the dehydration of chitosan chains by glycerol moiety, hence the hydrophobic interaction among chitosans, which led to the formation of homogeneous gel. Thus, for chitosan–phosphate system, hydrophobic interaction plays a major role in the gelation while hydrogen bonding and electrostatic interaction also helps the gel formation. However, in our CS–TPP microgel system, the high speed centrifugation provides driving force to settle down CS–TPP particles in a crowded packing manner. The large centrifugal force (11,000 × *g* for CS–TPP microgels) can overcome the barrier of electrostatic repulsion between CS–TPP particles in suspension and stick them together. The centrifugal force provides strong interfacial tension (γ) between CS–TPP particles. Considering the basic Newton Force Law, the relationship between interfacial tension (γ) and the radius of particle (r) is established as follows:

$$\gamma = \frac{F_{cen}}{S} \sim \frac{ma}{4f\pi r^2} \sim r \tag{3.3}$$

where F_{cen} is the centrifugal force acting on particles, S is the interfacial area between particles, m is particle mass, a is the centrifugal acceleration of the particle, f is the fraction of surface in-contact between particles and r is the particle radius. Figure 3.7A displays the schematic diagram of interfacial tension between CS–TPP particles. Under the same centrifugal field, the interfacial tension between large particles tends to be larger than that between small particles. Higher interfacial tension (γ) between large particles results in a tighter particle packing, which is in agreement with the occurrence of large storage modulus (G') for microgels of large particles.

After centrifugation, the CS–TPP microgels were stabilized through particle–particle interaction which involved electrostatic repulsion and van der Waals interaction. For the established CS–TPP microgel, we proposed the following mechanism to explain the effect of particle sizes on interparticle interactions, as shown in Figure 3.7B, which displays the van der Waals potential and electrostatic potential of CS–TPP particles under different particle size conditions. Since the zeta-potentials of CS–TPP particles with different particle sizes showed negligible difference, the electrostatic interaction between CS–TPP particles was kept unchanged (d curve in Figure 3.7B). In CS–TPP microgel, the short particle distance greatly increased the van der Waals force among particles. For large particles, the contour of van der Waals potential is close to that of total energy potential, indicating the dominant contribution of van der Waals force. This energy potential analysis was also in agreement with the results from dynamic oscillatory shear analysis. Large particles interacted much stronger with each other, leading to tighter particle packing in microgels. Finally, research relevant to the use of scattering techniques (*224*) to illustrate the nature of microgels packaging (i.e., face-centered cubic or hexagonally close-packed structure) is still undergoing in our laboratory.

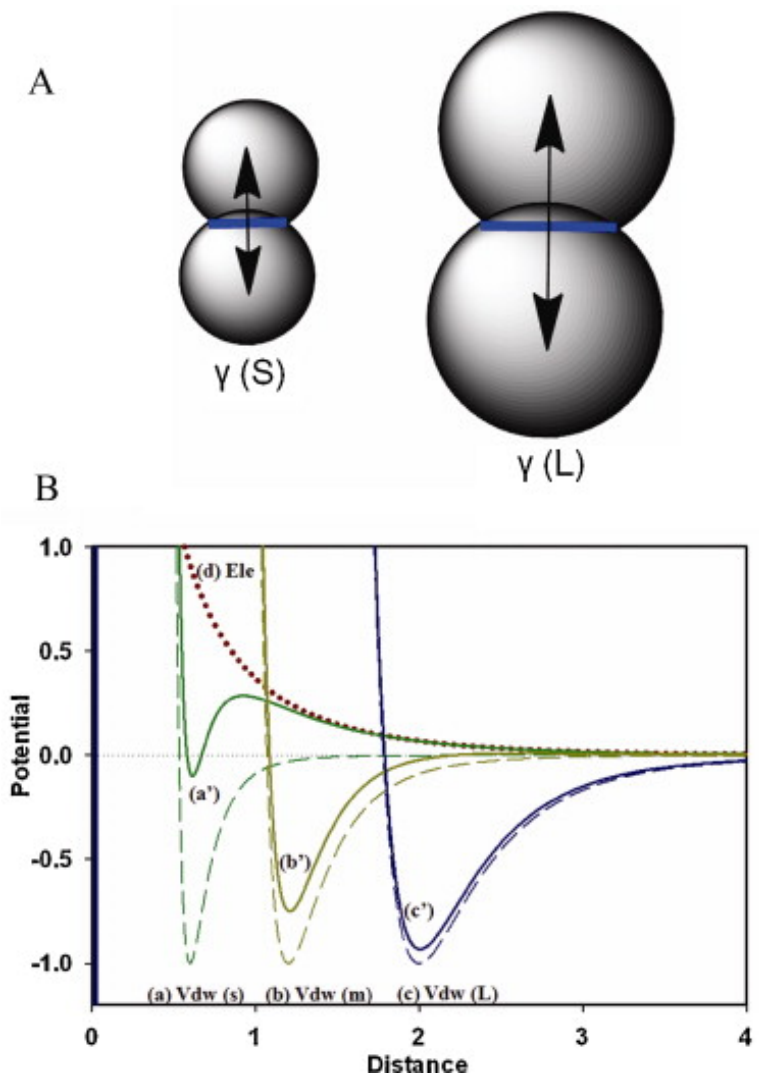

Figure 3.7 (A) Schematic diagrams of interfacial tension (γ) between CS–TPP particles with different sizes during centrifugation processing. (B) Inter-particle interaction potential profiles of chitosan–sodium tripolyphosphate (CS–TPP) microgels which include van der Waals potential for small-sized CS–TPP particles (a), medium-sized CS–TPP particles (b), and large-sized CS–TPP particles (c); as well as electrostatic potential (d), total potential of small-sized CS–TPP particles (a′), medium-sized CS–TPP particles (b′), and large-sized CS–TPP particles (c′).

3.5 Conclusion

CS–TPP particles with controlled particle sizes have been successfully prepared through the electrostatic interaction between amino groups of chitosan and phosphate groups of sodium tripolyphosphate. Different techniques including dynamic light scattering, atomic force microscopy, rheology, and Fourier transformed infrared spectroscopy were applied

to characterize the structure and rheological properties of CS–TPP particles. The CS/TPP mass ratio of 3.75 was found to be the optimum condition to achieve minimum particle sizes. Both chitosan concentration (10 mg/mL and 20 mg/mL) and sonication period (3–9 min, 3.75 W/mL energy output) were utilized to control the particle sizes of CS–TPP particles. Compared with pure chitosan solutions, the formation of CS–TPP particle suspensions decreased the solution viscosity. During centrifugation processing, strong centrifugal force overcame the barrier of electrostatic interaction between CS–TPP particles in suspension, after which CS–TPP microgels formed. Through the analysis of van der Waals attraction and electrostatic repulsion, and in combination with DLS and rheological measurements, we found that large CS–TPP particles tended to form tighter microgel than the small particles. Besides, water content analysis may suggest the pseudo-hard sphere nature of CS–TPP particles.

Chapter 4

Assembly of mPEG-*b*-PVL Block Copolymer and Star Polymer for Curcumin Encapsulation

4.1 Introduction

Many healthcare problems in the pharmaceutical, food and agricultural industries such as selective drug screening, improving active compounds' bioavailability, and efficient utilization of crop waste byproducts etc., still remain unsatisfactory. In the era of nanotechnology, nanoparticle platforms provide us with potential solutions to these critical problems. By manipulating formulations at nano- scale, we can design fresh functional food and drug ingredients with improved water solubility, thermal stability, and improved physiological performance (*225*). Thus, the rational design of nanoparticle with special structure at nano- scale is of importance to its macro- scale properties like encapsulation.

For targeting structural robustness and high loading capability of nanoparticles, various polymeric architectures have been established, including block copolymer micelles (*226*), a miktoarm terpolymer (*227-228*), hyperbranched polymers (*229*), and dendrimers (*230-231*). These polymer architectures all facilitate the delivery of active compounds to the human body. Previously, polyester miktoarm terpolymers provided us with a significantly low critical micelle concentration (CMC), and a high loading of paclitaxel with a narrow size distribution (*227*). Tested under the everted rat intestinal sac model, polyamidoamine

(PAMAM) dendrimer with 3~5 generations exhibited a more rapid serosal transfer rate than other synthetic and natural polymers, and displayed its potential as an oral drug delivery agent (*231*). Decorated with peripheral amino groups, PAMAM dendrimers improved the solubility of indomethacin by virtue of electrostatic interactions, and simultaneously targeted better skin permeation due to its affinity to the stratum corneum (*230*). However, regular polymer architectures still suffer from synthetic limitations (i.e. dendrimers (*232-233*)) and dynamic instability (i.e. micelles (*234*)). Based upon the large demand for easily synthesized, robust polymer architectures for nanomedicine, we are exploring the nanogel star polymer (unimolecular, globular, polymer architectures) as an alternative organic nanoparticle platform for potential biomedical applications.

We have leveraged an organocatalytic ring opening polymerization (OROP) approach to synthesize uniform nanogel star polymers with biodegradable compositions and tunable functionality (*59*). The method has been demonstrated to be a versatile synthetic route delivering effective functionalization, both internally and peripherally (*235*). The organocatalyst, an alternative to metal catalysts, can be applied to a rich variety of cyclic monomers (*236-237*). Comparing with the traditional organometallic compound catalyzed ROP (*238-239*), the current ROP is more environmentally friendly, and offers better product uniformity (*59*).

In this chapter, we exercise the OROP approach to nanogel star polymers. Simultaneously, we have studied both the solution structure and the nutraceutical encapsulation of the nanogel star polymer. The synchrotron small-angle X-ray scattering with its merit of intense photon source is utilized to probe the structures of the linear diblock copolymer and the nanogel star polymer in various solutions. The structures of

aggregates of the linear polymer, polymer micelles and nanogel star polymers in different solvents are elucidated and compared. Then the encapsulation of curcumin, a phytochemical with multiple functions but low water solubility (*240-243*), using the nanogel star polymer is investigated. The star polymer can efficiently enhance the water solubility of curcumin, and hence potentially improves its human bioavailability is also studied.

4.2 Experimental

4.2.1 Materials

1,5,7-triaza-bicyclo[4.4.0]dec-5-ene (TBD) was the organo-catalyst purified by a an earlier protocol (*46*). 5-5'-Bis(oxepanyl-2-one) (BOP), the crosslinking reagent (*244*), was synthesized by the exothermic reaction of the urea-hydrogen peroxide (Sigma-Aldrich) and 4,4'-bicyclohexanone (Tokyo Chemical Industry Co., Ltd) in formic acid. δ-valerolactone monomer (Sigma-Aldrich) was distilled under vacuum. Mono-methyl ether polyethylene glycol (PEG) 5000 g/mol (Fluka) was dried azeotropically from toluene prior to use. Dry toluene was degassed under vacuum with 5 freeze-thaw cycles. Anhydrous diethyl ether (Mallinckrodt Chemicals), anhydrous tetradhydrofuran (THF) (Sigma Aldrich), and acetone (J.T. Baker) were used without further purification. Curcumin, analytical standard grade, was purchased from Fluka.

4.2.2 Synthesis Method

The arm first route (*235*) was used for nanogel star polymer formation (Scheme 4.1). Initially, monomethylether-PEG-carbonate **1** (M_n 5000 g/mol, PDI 1.02, 0.83 g), a macroinitiator (MI) was dissolved in dry toluene (5 mL). Dry δ-valerolactone monomer **2** (M_n 100 g/mol, 0.65g) was then added into mPEG solution afterwards. 0.25 g 1,5,7-

triazabicyclo[4.4.0]dec-5-ene (TBD) **3** solution (0.32 g TBD dissolved in 16 g toluene) was added as an organo-catalyst. The ring-opening polymerization (ROP) was conducted in anhydrous environment at room temperature for 2 hours. The final mPEG-*b*-PVL block copolymers **4** were quenched by cold ethyl ether. Then, the synthesized mPEG-*b*-PVL were re-dissolved in dry toluene and served as macro-initiators for further reaction. The mPEG-*b*-PVLs were then crosslinked by 5-5'-Bis(oxepanyl-2-one) (BOP) **5**, a crosslinking agent for star formation **6**. The reaction for star polymer with an initial molar ratio of [MI]/ [BOP]/ [TBD] equal to 20/ 100~200/ 3 was conducted in anhydrous environment at 40 ^{o}C for successive 16 hours. The crude mixture was purified by dissolving it in methanol and gradually lowering the solvent quality through adding ethyl ether to fractionate the star polymer product by size sequentially. After synthesis, 10 mg of the wet powder (diblock copolymer or star polymer product) was then dissolved in 4 mL HPLC grade tetrahydrofuran (THF) and filtered by 0.2 μm PTFE microfilter for further GPC analysis. Another 10 mg of the wet powder was dissolved in 0.5 mL $CDCl_3$ for ^{1}H NMR analysis. Both synthesized block copolymer and star polymers display narrow polydispersity (M_w/M_n < 1.10 for block copolymer and <1.20 for star polymer).

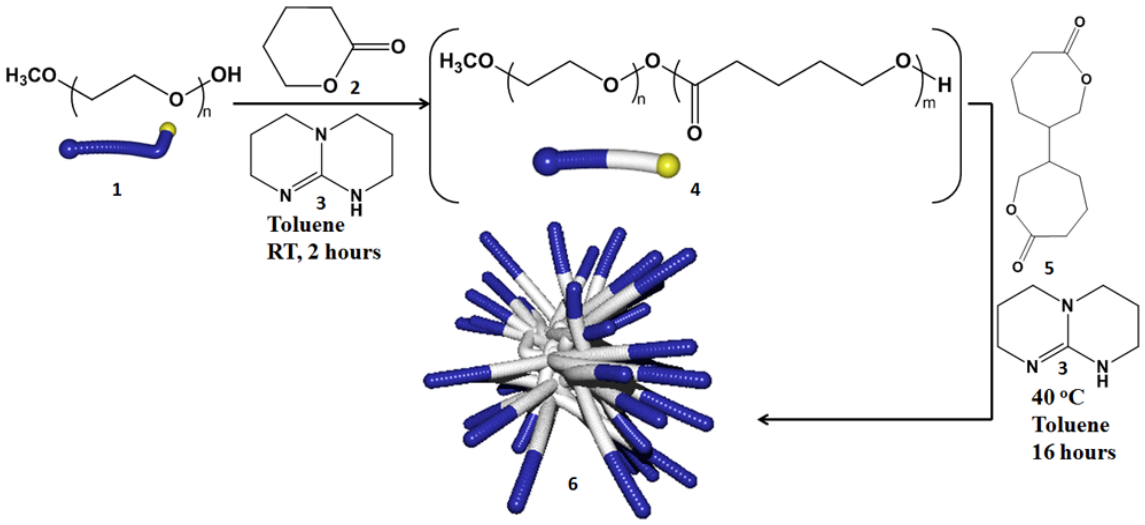

Scheme 4.1: Synthesis of mPEG-*b*-PVL star polymer by organocatalytic ring opening polymerization (OROP) method.

4.2.3 Physical Characterization

NMR spectra were obtained by a Bruker Avance 2000 (^{1}H NMR at 400 MHz). Gel permeation chromatography (GPC) was performed in THF using Waters chromatograph equipped with four 5 μm Waters columns (300×7.7mm) connected in series with an increasing pore size (10, 100, 1000, 105 and 106 Å), a Waters 410 differential refractometer, a 996 photodiode array detector and calibrated with polystyrene standards (750 to 2×106 g/mol). Static light scattering (SLS) and Dynamic light scattering (DLS) experiments of the freshly-prepared star polymers in THF were performed on DAWN® HELEOS™ II 18-angle light scattering detector equipped with WyattQELS™ on-line quasi elastic light scattering parts and Optilab DSP refractive index detector. The combined SLS and DLS system was connected to the same GPC machine. A separate DLS experiment of star polymer in aqueous solution was performed on DynaPro NanoStar dynamic light scattering instrument. Thus, the hydrodynamic radius (R_h) in THF and water, number-average molecular weight (M_n), weight-average molecular

weight (M_w), and polydispersity (PDI) of star polymers can be determined from CONTIN method of DLS and Zimm plot of SLS. Meanwhile, surface morphology of star polymer was collected by using a commercial Nanoscope IIIa Multi-Mode AFM (Veeco Instruments, CA) equipped with J scanner, which was operated in tapping mode using silicon nitride cantilever. Both height image and phase image were collected simultaneously using a set point ratio of ~0.9 for measurements at room temperature. In addition, the critical micelle concentration (CMC) of mPEG-*b*-PVL in aqueous solution was determined by steady-state fluorescence measurement. The detailed protocol can be found in the supplementary information.

4.2.4 Small-angle X-ray scattering measurement

SAXS profiles were collected by using the 18ID undulator beamline of the Biophysics Collaborative Access Team at the Advanced Photon Source, Argonne National Laboratory (*245*). The sample-to-detector distance was set at 2.3 meter to cover a Q range of 0.006-0.37 $Å^{-1}$. The experimental set-up also includes a 2 m sample-to-detector-length camera and another 0.3 m sample-to-detector-length camera with the high-sensitivity CCD detector. A flow cell of 1.5 mm diameter capillary equipped with a brass block (thermostatted with a water bath) was utilized to hold samples. In order to minimize the radiation damage, a MICROLAB 500 Hamilton pump was applied to load samples to the flow cell at a constant rate (10 mL/s). The X-ray wavelength was 1.033 Å and a short exposure period of 1 s was used to acquire the scattering data. The whole experiment was kept at room temperature. The initially-obtained 2D SAXS images were converted to 1D I(Q) versus Q curve by circular averaging. Fifteen curves were collected for each sample

and their averaged curves were utilized for further analysis. The final SAXS profiles were gained after subtracting the solvent background.

4.2.5 Curcumin-Star Polymer Occlusion Complex

Figure 4.1A displays curcumin solutions under different conditions. Clearly, curcumin is soluble in acetone but non-soluble in water. With star polymers, curcumin can be dispersed into water, which displays a yellowish color. To prepare curcumin-star polymer occlusion complex, specific amounts of curcumin and star polymer powder were weighed according to different initial [curcumin]/[star polymer] mass ratio. 0.1~0.2 g acetone was added to dissolve curcumin and star powder. After fully dissolution of powder mixture in acetone, 1~2 mL of Millipore water was added into curcumin-star mixture dropwisely. The curcumin-star polymer occlusion complex will form after 5-hour vacuum line to remove acetone.

The curcumin loading is monitored by UV-Vis spectroscopy method. Equal volume of acetone was added into curcumin-star polymer occlusion complex solution to release the curcumin entrapped in the PVL hydrophobic core. The UV-Vis absorbance at wavelength 419 nm was measured by using Agilent 8453 UV-Visible Value System equipped with HP 89090a Peltier temperature controller. A calibration curve of curcumin absorbance$_{\lambda=419nm}$ in acetone was established to obtain the molar absorptivity of curcumin in acetone prior to curcumin quantification. Figure 4.1B shows the typical UV-Vis spectra of curcumin-star polymer occlusion complex in water, curcumin in water after filter, and curcumin in acetone. The spectrum of curcumin-star polymer occlusion in water was almost overlapped with that of curcumin in acetone, with only a slight bathochromic shift (Figure 4.1B). This implied the sterically encumbered curcumin in a largely non-

aggregated state within the aqueous occlusion complex. The encapsulation efficiency (EE) and loading capacity (LC) of curcumin in star polymer were calculated from the following equations:

$$EE\ (\%) = \frac{\text{Amount of loaded curcumin in moles}}{\text{Amount of initial curcumin added in moles}} \times 100 \tag{4.1}$$

$$LC = \frac{\text{Amount of loaded curcumin in moles}}{\text{Amount of polymer in moles}} \tag{4.2}$$

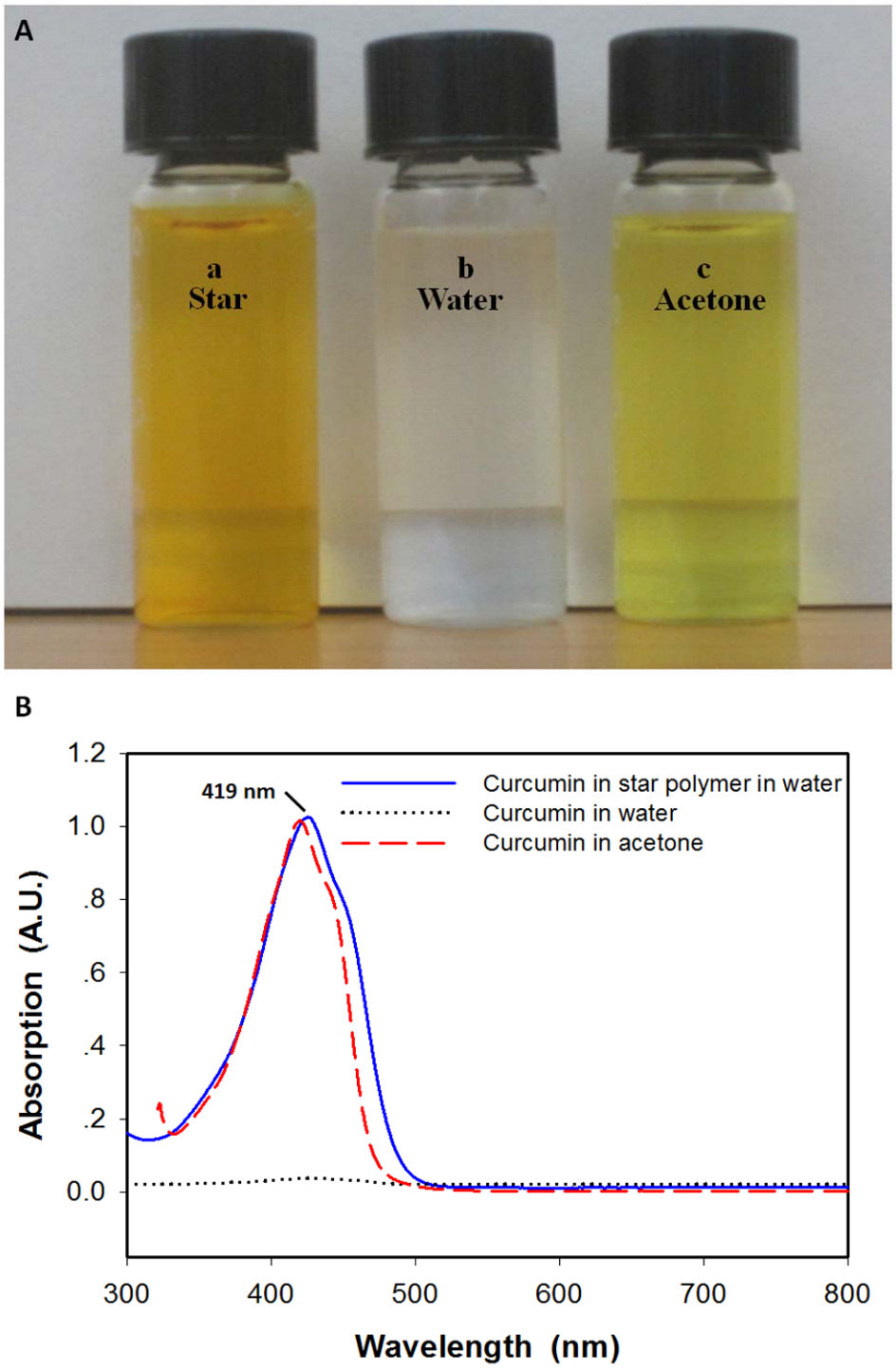

Figure 4.1: Encapsulation of curcumin by star polymer. Photo image of the solutions of curcumin-star in water, curcumin in water, and curcumin in acetone after filter through 0.2 μm PTFE microfilter (A), and their corresponding UV-Vis spectra (B).

4.2.6 SAXS Background

The scattering profile of colloidal particle in a liquid medium can be described by the following equation:

$$I(Q) = kN_p P(Q)S(Q) \tag{4.3}$$

where k is a constant containing information of scattering contrast between particle and solvent, N_p is the number of particles, P(Q) is the form factor of an individual particle, and S(Q) is the structure factor. P(Q) term provides us with the shape and size of individual particle, while S(Q) term gives information relevant to the interparticle distance.

For overall shape of particle or particle aggregate, different form factors such as solid sphere, core-shell sphere, cylinder, and core-shell cylinder can be applied to fit the SAXS profiles. The equations of those form factors can be found in the supporting information. For a comparative study, Guinier analysis at low Q region is also conducted for both compact sphere and cylinder.

For compact sphere:

$$In(I(Q)) = In(I_0) - \frac{Q^2 R_g^2}{3} \tag{4.4}$$

where R_g is the radius of gyration, and I_0 is the forward scattering.

For cylinder object:

$$In(Q * I(Q)) = In(\pi * I_0) - \frac{Q^2 R_c^2}{2} \tag{4.5}$$

where R_c is the cross-section radius of gyration, and I_0 is the forward scattering. The Guinier fitting is valid for Q_{max}*R (R_c and R_g) < 1.5. The first and last few points from the fitted curves were changed by appropriate handlers.

For an object of agglomeration, the aggregation number in an individual particle is determined from the forward scattering I_0:

$$I_0 = \frac{c \times nN_A \times \Delta b^2}{M} \tag{4.6}$$

where I_0 (cm^{-1}) is the forward scattering intensity, c (g/mL) is the concentration of polymer solution, M (g/mol) is the molecular weight of polymer, N_A is the Avogadro number, and Δb (cm) is the scattering length difference of one polymer relative to the solvent:

$$\Delta b = [\frac{\sum_i b_{iPEO}}{V_{PEO}} * \varphi_{PEO} + \frac{\sum_i b_{iPVL}}{V_{PVL}} * (1 - \varphi_{PEO}) - \frac{\sum_i b_{iH_2O}}{V_{H_2O}}] * V_{star} \tag{4.7}$$

where b_{iPEO} is the scattering length of element *i* in the PEO block, b_{iPVL} is the scattering length of element *i* in the PVL block, b_{iH2O} is the scattering length of element *i* in one water molecule, V_{PEO} is the volume of individual PEO block, V_{PVL} is the volume of individual PVL block, V_{H2O} is the volume of one water molecule, V_{star} is the volume of individual star polymer, and φ_{PEO} is the mole fraction of PEO in the diblock copolymer. The scattering length densities of PEO ($\frac{\sum_i b_{iPEO}}{V_{PEO}}$), PVL ($\frac{\sum_i b_{iPVL}}{V_{PVL}}$) , and water ($\frac{\sum_i b_{iH_2O}}{V_{H_2O}}$) are calculated to be 11.1×10^{10} cm^{-2}, 1.05×10^{10} cm^{-2}, and 9.4×10^{10} cm^{-2}, respectively. The scattering length density of water is identical with the reported value (*246*), indicating the validation of calculation.

4.3 Results and discussion

4.3.1 Basic Characterization

GPC and ^{1}H NMR were used for analysis of the mPEG-*b*-PVL copolymer, the crude nanogel star polymer and the purified nanogel star polymer. Figure 4.2A shows the GPC trace of the mPEG-*b*-PVL copolymer, crude star polymer and star polymer after purification. Under the analysis conditions the retention time of mPEG-*b*-PVL copolymer is 33.4 min. For the crude nanogel star collected right after synthesis, we observed two peaks at 29.5 min and 33.4 min, indicating the presence of the mPEG-*b*-PVL star polymer and residual mPEG-*b*-PVL linear copolymer. After a one-step purification, the residual mPEG-*b*-PVL copolymers were removed which was verified by the disappearance of residual mPEG-*b*-PVL copolymer peak in the purified star polymer. Figure 4.2B displays the ^{1}H NMR spectra of mPEG-*b*-PVL copolymer and the mPEG-*b*-PVL star polymer. The peaks at 1.68 ppm (4H, CO-CH_2-*CH_2*-*CH_2*-CH_2-O), 2.36 ppm (2H, CO-*CH_2*-CH_2-CH_2-CH_2-O), and 4.09 ppm (2H, CO-CH_2-CH_2–CH_2-*CH_2*-O) are attributed to the PVL block. The other two peaks at 3.39 ppm (3H, *CH_3*-O) and 3.66 ppm (4H, O-*CH_2*-*CH_2*-O) belong to the mPEG block. The polymer composition (i.e. block lengths) was determined from integration of characteristic peaks at 4.09 ppm (PVL) and 3.66 ppm (mPEG). The star polymer contains more VL monomers than the copolymer suggests that the presence of BOP can promote the ROP and introduce more PVL into the star polymer. From block lengths, we determined that the composition of mPEG-*b*-PVL copolymer was 5 kD_a mPEG (macroinitiator) and 3 kD_a PVL.

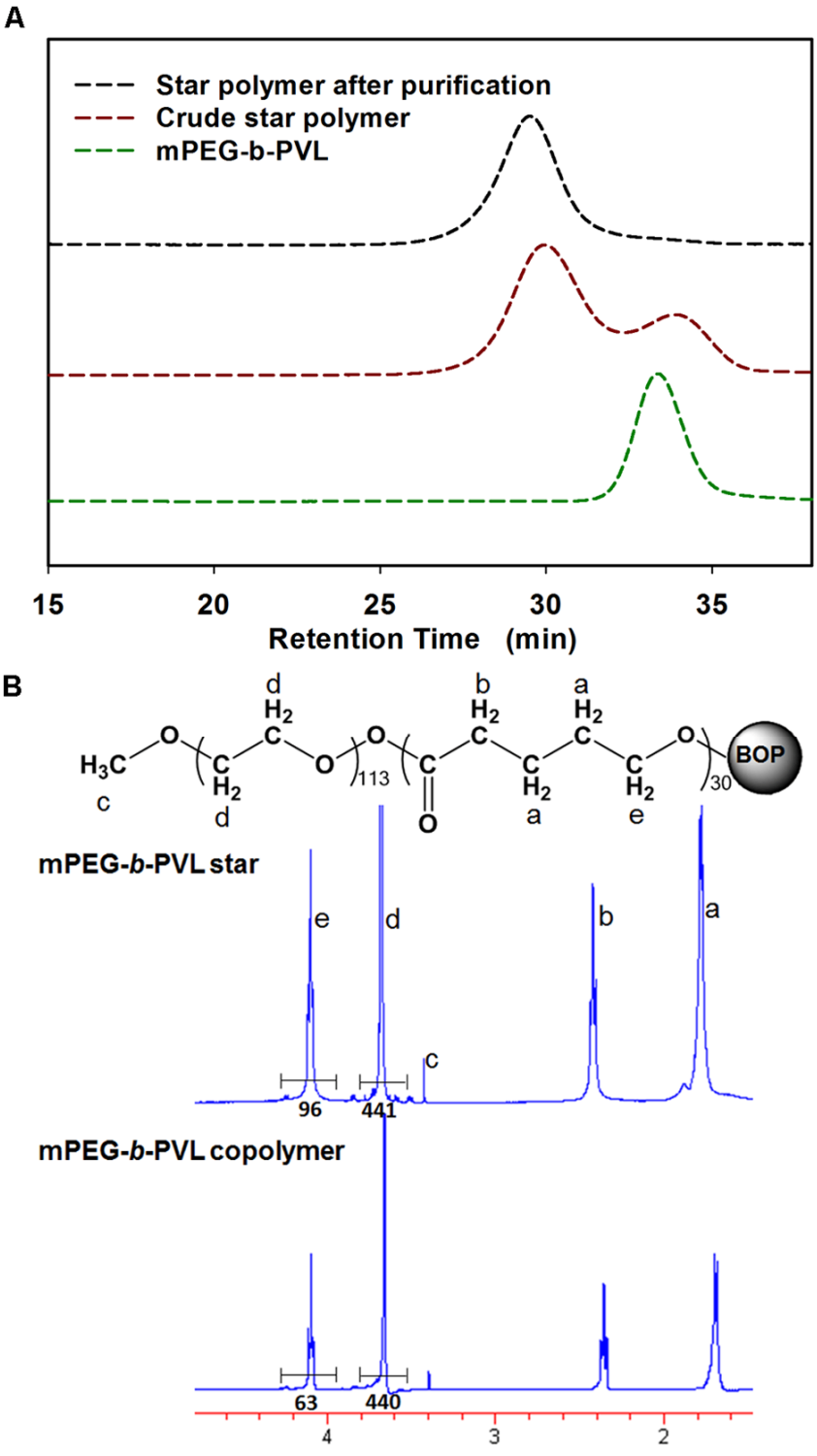

Figure 4.2: Synthesis trace of star polymer. (A) Gel permeation chromatography diagram of mPEG-*b*-PVL arm, star crude and star after purification; (B) ^{1}H NMR spectra of mPEG-*b*-PVL copolymer and star polymer 1.

Static light scattering (SLS) was utilized to determine the number-averaged molecular weight (M_n) and polydispersity (PDI) of the mPEG-*b*-PVL copolymer and the nanogel star polymers, while dynamic light scattering (DLS) was used to calculate the hydrodynamic radius (R_h) of the star polymers in THF and water. Table 4.1 summarizes the molecular characterization of mPEG-*b*-PVL, the nanogel star polymer 1, and the nanogel star polymer 2. The nanogel star polymer 1 (M_n=221 kD_a) was used in SAXS experiments for more structural details, and the nanogel star polymer 2 (M_n =1423 kD_a) was utilized in nutraceutical encapsulation studies. Based on the BOP content and the molecular weights of the mPEG-*b*-PVL copolymer and the star polymers, we determined that the nanogel star polymers 1 and 2 contained 22 and 142 diblock copolymer arms per nanogel star polymer, separately. The R_h of star polymer 2 in THF was 25.5 nm, almost double size of the nanogel star polymer 1 (Table 4.1). All the three synthesized polymers displayed a high uniformity in molecular weight with PDI less than 1.20. The surface morphology of star polymer 1 was captured by tapping mode-atomic force microscopy (Figure 4.3A). Section analysis embedded in the software Nanoscope 3.0 was utilized to determine the individual particle size of the nanogel star polymer 1 (Figure 4.3B). The height of a typical star polymer particle is ~7 nm which is considerably smaller than the R_h (13.2 nm) measured in THF solution (Table 4.1). It indicates the star polymer can be stably dispersed in THF with a swollen conformation while in a collapse conformation on the solid surface upon drying.

Table 4.1: Molecular characteristics of mPEG-*b*-PVL, star polymer 1, and star polymer 2

	Diblock copolymers/star[a]	M_n[b], kD_a	PDI[b]	R_h in THF[c], nm
mPEG-*b*-PVL	-	8	1.03	-
Star polymer 1	22	221	1.10	13.2
Star polymer 2	142	1423	1.20	25.5

[a] Calculated from the integration of characteristic signals in ^{1}H NMR spectra. [b] Determined by SLS measurements. [c] Obtained by DLS measurements.

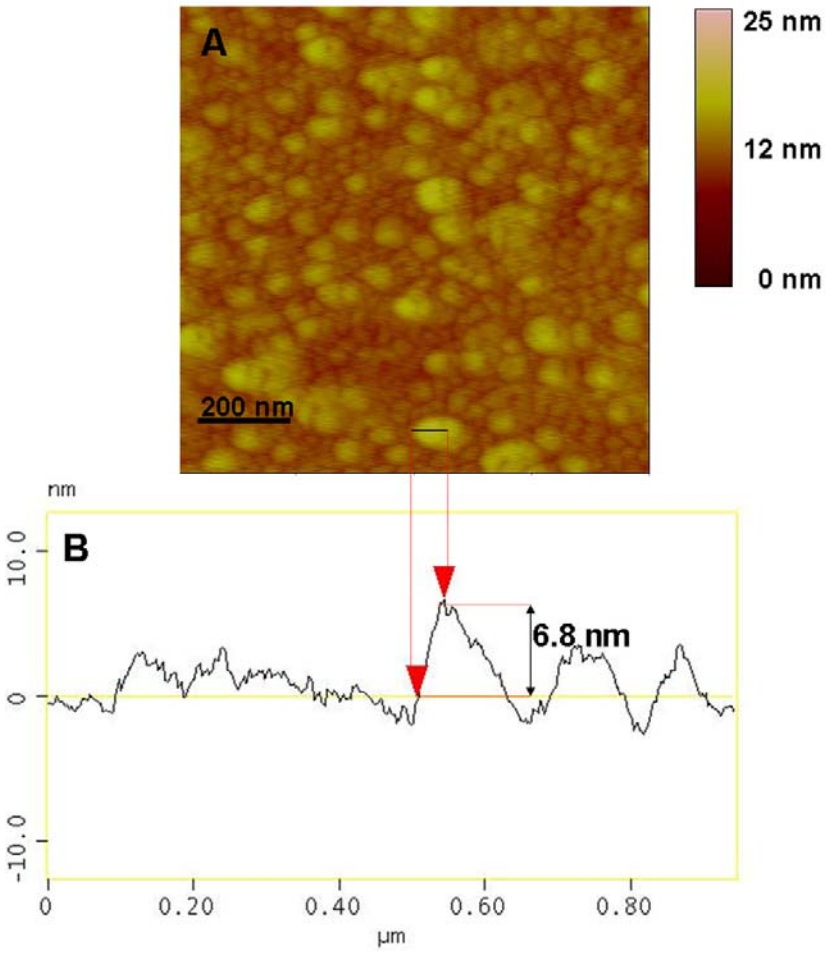

Figure 4.3: Surface morphology of star polymer. (A) Tapping-mode AFM height image of mPEG-*b*-PVL star polymer deposited on the mica surface; (B) Section analysis of single mPEG-*b*-PVL star polymer.

4.3.2 Structure analysis

4.3.2.1 Structure in THF

Though THF is a good solvent for both the hydrophobic PVL and the hydrophilic mPEG blocks, the solution behaviors of the mPEG-*b*-PVL based block copolymer and nanogel star polymer are still very different. Representative solution SAXS profiles of the block copolymer and the nanogel star polymer in THF are shown in Figure 4.4A. The scattering profile of mPEG-*b*-PVL block copolymer in THF followed a power law $Q^{-5/3}$ in both intermediate and high Q regions. However, the scattering profile of mPEG-*b*-PVL star polymer followed a power law $Q^{-2.7}$ in the same high Q region. These scaling features suggested that the diblock copolymer in THF behaved like a random coil (*247-248*), whereas the nanogel star polymer in THF behaved more like a hairy rather than a surface-smooth particle which has typical Porod scaling of Q^{-4} (*248-250*). Furthermore, the scattering profile of diblock copolymer in THF can be well fitted by the Debye function (*250-251*), which was used to depict a wormlike chain conformation. This suggests a random coil structure for the mPEG-*b*-PVL copolymer in THF. From the fitting, the R_g of the mPEG-*b*-PVL copolymer was determined to be ~4.5 nm. The inset of Figure 4A displays the Holtzer plot of star polymer in THF. The size of star polymer in THF was ~9 nm, which was determined from the crossover of two tangent lines initialized from the peak and the large Q region in the Holtzer plot. Thus, the bulk density of star polymer is calculated to be ~2.8 fold that of diblock copolymer based on those polymer dimensions.

Contrary to a random coil structure of the copolymer, the structure of the mPEG-*b*-PVL star polymer is more compact and denser in THF. The Kratky plot (*252*) shown in Figure 4B was used to identify whether the polymer aggregates had a compact core. We

observed a curve with an initial exponential increase and a subsequent plateau for the diblock copolymer in THF, which reflected a typical unfolded and loose polymeric random coil in a non-selective solvent. On the contrary, a sharp peak at Q=0.022 Å^{-1} followed by a continuous decay was observed for the nanogel star polymer in THF. According to the real-reciprocal law of $d = 2\pi/Q$, this sharp peak corresponds to a 28.6 nm which is attributed to the average separation of star polymer in THF. The average separation of star polymer was given by $d \sim (\frac{3M_w}{4\pi CN_A})^{1/3}$. Similar observations in the comparison of complex unimolecular polymer architectures such as poly(propyleneimine) dendrimers (*253*), polyisoprene (PI) and polybutadiene (PB) star polymers (*254*) in comparison with their linear polymers have also been reported.

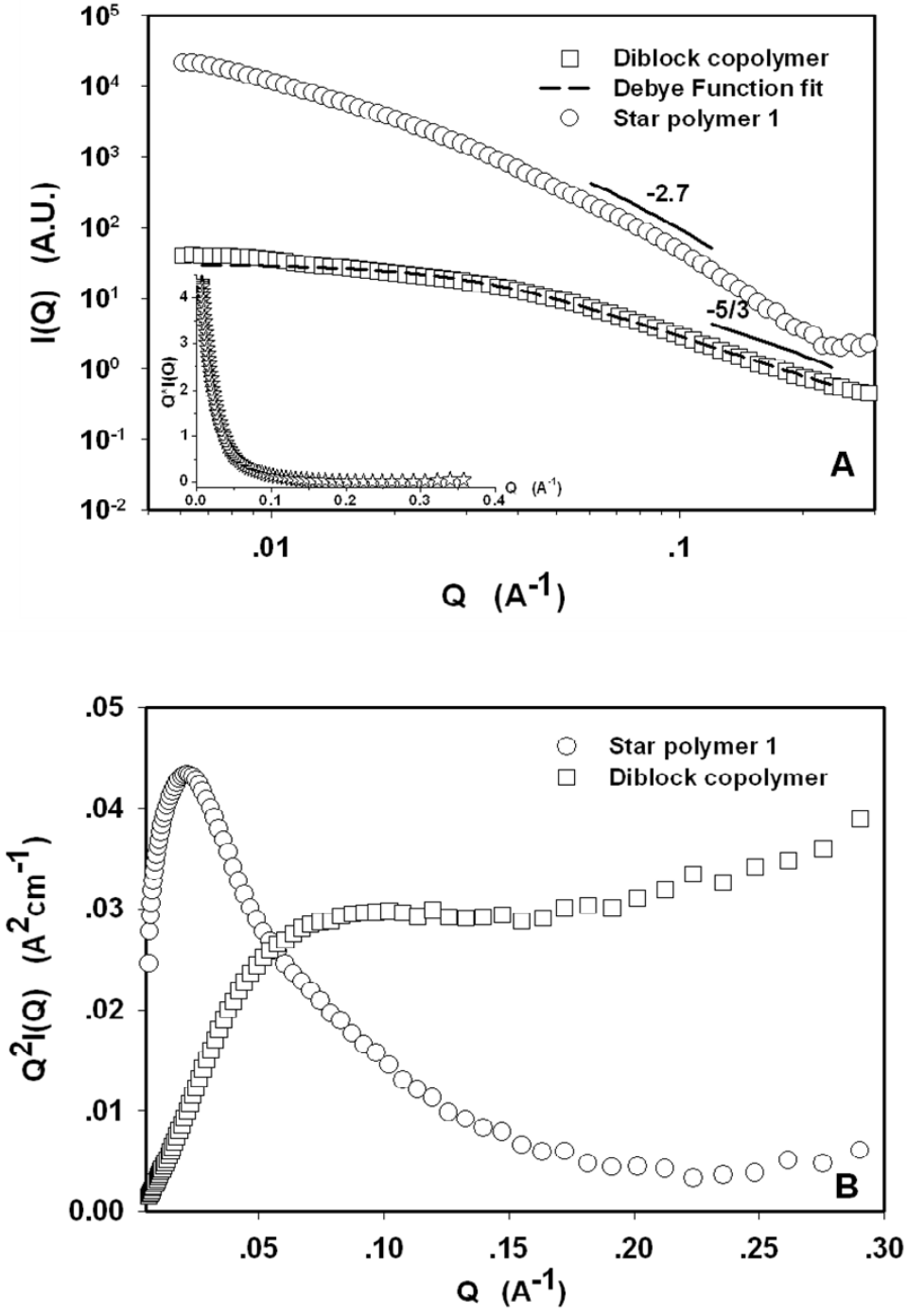

Figure 4.4: SAXS analysis of the mPEG-*b*-PVL copolymer and the nanogel star polymer 1 in non-selective solvent (THF), including (A) SAXS profiles with Gaussian chain fitting and (B) Kratky plots (concentration, 11.7 mg/mL) of the mPEG-*b*-PVL copolymer in THF and the mPEG-*b*-PVL star polymer (concentration, 3.3 mg/mL) in THF. The SAXS profile of the mPEG-*b*-PVL copolymer in THF is best-fit by the Debye function. The intermediate and high Q regions for the nanogel star polymer in THF and the high Q region for the diblock copolymer are also fit by a power law. The inset is the Holtzer plot of mPEG-*b*-PVL star polymer (concentration, 3.3 mg/mL) in THF.

4.3.2.2 Structure in water

For drug or nutraceutical delivery, water is usually the transporting medium. The mPEG-*b*-PVL copolymer tends to self-assemble into micellar structures due to the solvent block selectivity (PEG vs. PVL). The SAXS profiles of mPEG-*b*-PVL copolymers in water are presented in Figure 4.5A. In the low Q region, a plateau was observed, suggesting no large-scale aggregation. Since diblock copolymer in selective solvent typically can self-assemble into solid spherical or core-shell spherical-like micelle, both a solid sphere form factor and a core-shell sphere form factor were utilized to fit the SAXS profiles from the mPEG-*b*-PVL copolymer in aqueous solutions (Figure 4.5A). Meanwhile, Guinier analysis was performed to fit the linear region at low Q region (Figure 4.5C). The mentioned approaches (i.e. a spherical form factor and the Guinier analysis) for fitting over different Q regions might result in some deviations. However, we did not observe large deviation in the fits regardless of the approach. From these fittings, we determined the size of the individual mPEG-*b*-PVL micelle in water was 9~10 nm (Table 4.2), which was 2 times R_g of mPEG-*b*-PVL copolymer in THF (~4.5 nm), indicating a micelle structure composed of numerous diblock copolymers. The fitting from core-shell spherical model suggested the dimension of a single micelle was 12~13 nm (Table 4.2). The dimension of the copolymer micelle characterized either in solid-sphere or core-shell like is from 9 to 13nm, which is a few nm larger than other commercial micelle-forming materials such as Pluronic P105 (*255*). This can be rationalized by the molecular weight and chemical structure differences between mPEG-*b*-PVL (8 kD_a) and Pluronic 105 (6.5 kD_a). The experimental concentration for an 8 kD_a mPEG-*b*-PVL polymer in water was well beyond the critical aggregation concentration (CAC) (0.015 mg/mL in Figure S4.1).

Table 4.2: Dimensions of mPEG-*b*-PVL micelle in water fitted from the solid sphere form factor, shell-core sphere form factor, and Guinier analysis

***C*, mg/mL**	**Solid sphere**	**Shell-core sphere**		**Guinier**
	***r*, Å**	**r_{core} , Å**	**r_{shell} , Å**	**R_g, Å**
1.82	108±0.0	51±11	66±27	102±0.4
2.90	97±0.0	65±29	70±42	85±0.2
6.39	91±0.0	63±0.1	65±0.1	77±0.1

The SAXS profiles for the mPEG-*b*-PVL nanogel star polymer aqueous solutions were shown in Figure 4.5B. Unlike the polymer micelles, the nanogel star polymer scattering intensity can be fitted by a Q^{-1} power law in the low Q region, indicating of a rod-like aggregate (*248*). We then employed both a cylinderical and a core-shell cylinderical form factors to fit the SAXS data of star polymer in water, which can adequately describe the scattering profile (Figure 4.5B). Meanwhile, a modified Guinier analysis for rod-like objects was applied in the low Q range (Figure 4.5D). In consensus of the three different fittings, a dimension of 6 nm × 50 nm (cross-section radii × length) with a 3:4 core-to-shell ratio of a core-shell cylinder is the best description for the self-assembly of the star polymer in water (see detailed values in Table 4.3). The calculated core-to-shell ratio (3:4) is somewhat larger than the molecular weight ratio of PVL block to PEG block (3:5) in the polymer. This can be rationalized by the larger length of δ-valerolactone block relative to the ethylene glycol block. From the forward scattering I_0 determined from the modified Guinier analysis for rod-like objects (Figure 4.5E), the aggregation number n_{agg} of the nanogel star polymer aggregate is around 4. In other words, each cylindrical aggregate incorporated ~4 single star polymer molecules. Besides, given by the R_g of star

polymer (~7 nm) (Figure 4.5D) and dimension of star polymer aggregate (~6 nm × 50 nm) (Table 4.3), the volume of individual star polymer is determined to be 1436.8 nm^3, and the cylinder is 5654.9 nm^3. Clearly, the polymer volumes also verify the aggregation number of 4, which agrees with the aggregation number through Guinier analysis as well (Table 4.3).

Table 4.3: Aggregate dimensions of star polymer 1 (M_n=221 kD_a) in water fitted from the form factor fitting of cylinder and shell-core circular cylinder, and Guinier analysis

C,	**Cylinder**			**Shell-core circular cylinder**				**Guinier**
g/L	***r*, Å**	***L*, Å**	n_{agg}	r_{core} **, Å**	r_{shell} **, Å**	***L*, Å**	n_{agg}	n_{agg}
1.52	56.5±0.1	504.8±4.1	4.5±0.0	31.9±1.9	34.6±1.5	473.3±3.4	3.6±0.0	4.0±0.0
3.26	57.9±0.0	531.2±2.6	4.6±0.0	30.8±0.4	40.6±0.3	473.7±1.9	3.3±0.0	4.6±0.0
5.26	56.6±0.0	383.8±1.1	3.4±0.0	29.2±0.3	40.6±0.2	345.4±0.9	3.0±0.0	3.8±0.0

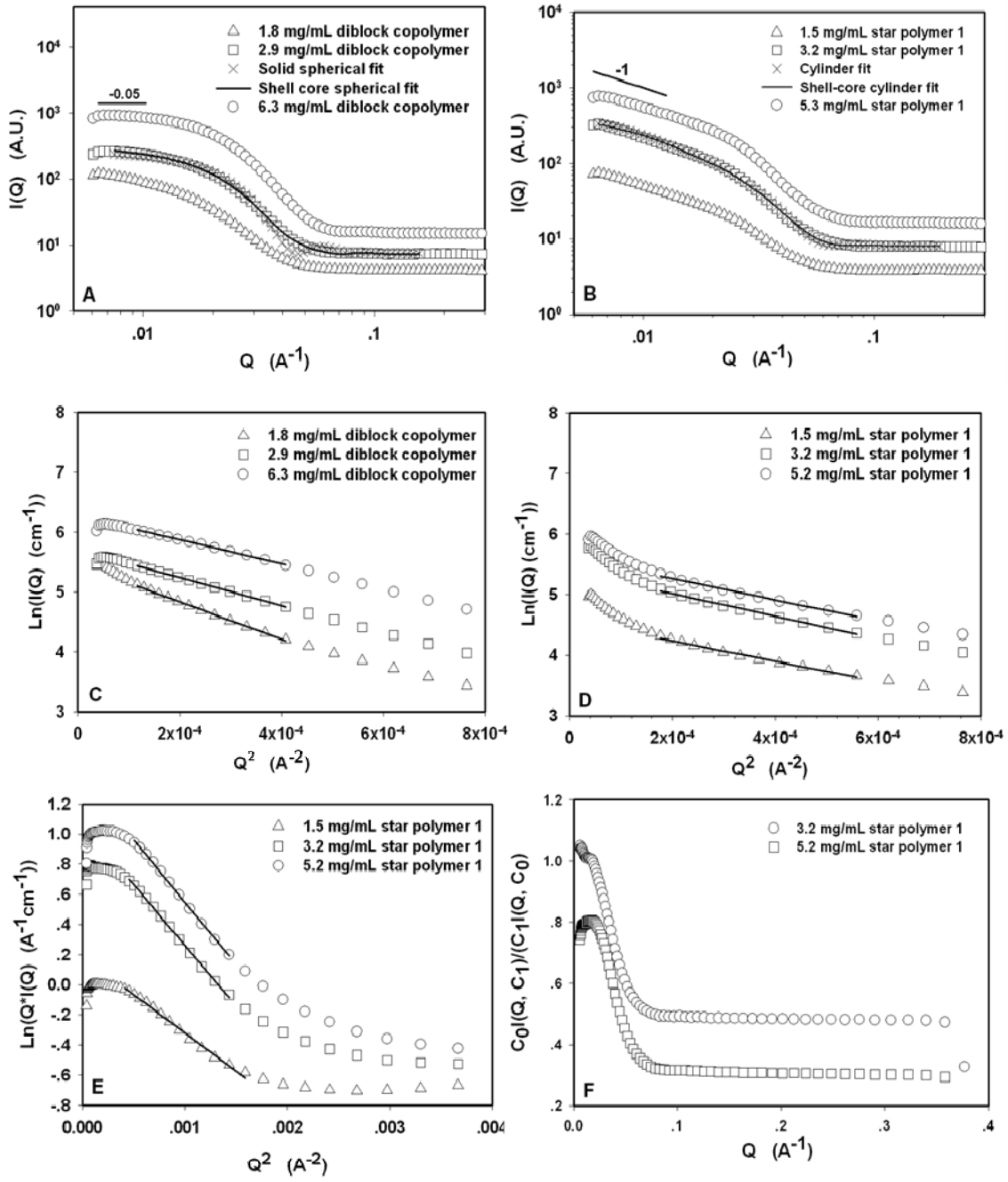

Figure 4.5: SAXS analysis of the mPEG-*b*-PVL micelle and the nanogel star polymer in a block selective solvent (water), including (A) SAXS profiles fit with a spherical model; (C) classical Guinier plot of the mPEG-*b*-PVL copolymer in water at various concentrations (1.82 mg/mL~6.3 mg/mL); (B) SAXS profiles fitted using a cylindrical model with cylinder-related fitting; (D) modified and (E) classical Guinier plot of the mPEG-*b*-PVL star polymer in water at various concentrations (1.52 mg/mL~5.26 mg/mL); and (F) effective structure factor of the mPEG-*b*-PVL star polymer in water at concentrations of 3.26 mg/mL and 5.26 mg/mL. The SAXS profile of the mPEG-*b*-PVL copolymer in water is best-fit by either a solid sphere form factor or a core-shell sphere form factor, while the SAXS profile of the mPEG-*b*-PVL star polymer is best-fit by either a cylinder form factor or a core-shell cylinder form factor. The Guinier fittings for a compact sphere and rod are performed at low Q region with $Q^*R_g < 1.5$.

From scattering analysis above, we suggest that each aggregate contains ~4 single star polymers. Since individual nanogel star polymer approximates a unimolecular sphere, the formation of aggregates in solution requires packing those spheres although some molecular distortion is likely. The overall shape of aggregate largely depends on how the building blocks are arranged spatially. Theoretically speaking, four spherical particles can possibly pack into various types of higher-order structures including tetrahedron, square, L shape, and linear rod. However, the star particles should naturally pack into large agglomerates based on the polymers' overlap convenience and volume saving. Packing of star particles in a line to form rod can be achieved more easily than other geometries through polymer overlapping. Thus, taking spatial arrangements into consideration, a rod is likely of highest stability among those possible higher-order structures, which is consistent with the scattering results. It has been reported that the non-ionic surfactant (i.e. poly(oxyethylene) dodecyl ether) also assembles into a wormlike structure (rod shape) under suitable conditions of concentration and temperature (*256-257*), since many factors (i.e. solvent, concentration and etc.) can affect the stability of the wormlike configuration. Moitzi et al. reported a concentration-dependent sphere-to-rod transition by observing the slope change in the small-angle neutron scattering profiles of poly(oxyethylene) cholesteryl ether in the low Q region (*256*). Compared with the transient and unstable wormlike structures observed for poly(oxyethylene) cholesteryl ether micelles, the rod-shaped aggregation of nanogel star polymers is concentration-independent over the Q range studied which can also be verified by concentration-independent effective structure (Figure 4.5F), indicating a more robust higher-order structure.

4.3.3 Curcumin-star polymer occlusion complex

Prior to the study of the curcumin loading performance through either the nanogel star polymers or the copolymer micelles, the hydrodynamic radii of both the micelles and the star polymers in aqueous solutions were collected by DLS. Their size response to environmental changes is critical to their biomedical applications. Table 4.4 shows the R_h of both the mPEG-*b*-PVL micelle and the nanogel star polymer 2 at varying temperatures and pHs. We see that the size of the micelles and the star polymer were negligibly affected by pH. The R_h of mPEG-*b*-PVL nanogel star polymer 2 (~37 nm) also changed little with temperature (between 25 - 37 ºC). In contrast, the R_h of micelle changed by ~7 nm over the same temperature range. This size fluctuation is probably due to the structural looseness and dynamic reorganization of the micelle. The stability of star polymer structure in response to environmental changes, arising from the covalent crosslinking, will ensure a consistent performance for cargo delivery. In contrast, the demonstrated size changes of micellar structures hightlights its temperature sensitivity, a feature which is undoubtedly due to the temperature-dependent hydrophobic interactions in the micelle core (*258*). From SAXS and DLS measurements, we observe a discrepancy between the measurement of R_g from SAXS and R_h from DLS for the micelle which has been reported previously for gold nanocrystals (*259*), zirconia nanoparticles (*260*), and polystyrene-block-poly(ethy1ene oxide) diblock copolymers (*261*). Here we observed that R_h for the mPEG-*b*-PVL micelle in water at room temperature (~20 nm) was twice as large as the calculated R_g (10 nm) from DLS. DLS quantifies the size by measuring the diffusion of solvated micelle (polymer plus associated solvent), while SAXS measures the electron contrast between the solvent and the polymer. In addition, since the predicted

ratio ($R_g/R_{h)}$ for spherical particle is < 0.775 (*262*), the measured value of R_g/R_h (0.5) is consistent with the spherical shape of mPEG-*b*-PVL micelle.

Table 4.4: Hydrodynamic radius (R_h) of mPEG-*b*-PVL micelle and mPEG-*b*-PVL star polymer 2 (M_n=1423 kD_a) at 1 mg/mL concentration in aqueous medium

Experimental condition	**mPEG-*b*-PVL micelle, nm**	**mPEG-*b*-PVL star polymer 2, nm**
pH 7.4, 25 ^oC	20.5±0.3	36.7±0.5
pH 7.4, 37 ^oC	27.3±0.5	35.5±0.5
pH 2.0, 25 ^oC	20.7±0.5	38.8±0.3
pH 2.0, 37 ^oC	27.9±0.2	37.1±0.4

To demonstrate the nutraceutical encapsulation, we used the star polymer 2 (M_n=1423 kD_a) to encapsulate curcumin. Although we have chosen to study curcumin, other hydrophobic nutraceuticals such as β-carotene could also be targets. Figure 4.6A graphically shows both the encapsulation efficiency and loading capacity of curcumin by the mPEG-*b*-PVL star polymer 2 under different initial [curcumin]/[star polymer] mass ratios (initial C/S mass ratio). The loading capacity increased from 170 curcumin molecules per star polymer molecule to 240 curcumin molecules per star polymer as the initial C/S mass ratio increased from 0.06 to 0.1. Beyond this, the loading capacity reached a plateau, and further increases in the initial C/S mass ratio did not affect loading capacity once the initial C/S mass ratio reaches 0.1. This suggests that the maximum loading of the nanogel star polymer 2 is around 240 curcumin molecules per star polymer molecule and that the hydrophobic portion of the star polymer (PVL core) becomes saturated by curcumin at this point. The encapsulation efficiency of star polymer increased from less than 20% to 75% as the initial C/S molar ratio decreased from 0.4 to 0.06. Knowing the loading capacity of star polymer facilitates the effective utilization of

raw materials, which can lead to even higher encapsulation efficiencies. The water solubility of curcumin reached 0.8 mg/mL at an initial C/S mass ratio of 0.1. For further solubility improvement, we made another curcumin-star complex sample maintaining this initial C/S mass ratio but at higher polymer concentration. We found that the water solubility of curcumin increased to 1.4 mg/mL simply by increasing the amount of star polymer in the solution.

For comparison, the curcumin loading capability and encapsulation efficiency of the mPEG-*b*-PVL micelle are shown in Figure 4.6B. The maximum loading capability of this block copolymer micelle was determined to be ~1.5 curcumin molecules per block copolymer molecule. If we calculate the loading/arm in the star polymer, we find ~1.7 curcumin molecules per block copolymer arm for the star polymer 2, somewhat higher than that of the micelle. The higher loading capability of mPEG-*b*-PVL star polymer is attributed to its longer PVL block length in the core region (Figure 4.2B), which attracts more curcumin molecules through hydrophobic interaction and the large number of arms. For encapsulation efficiency, none of the curcumin-micelle samples surpassed 40%, which was much lower than measured for the star polymer (Figure 4.6B). This combined with the dynamic behavior of micelles suggest that the nanogel star is preferred for curcumin encapsulation over a micellar species of similar composition.

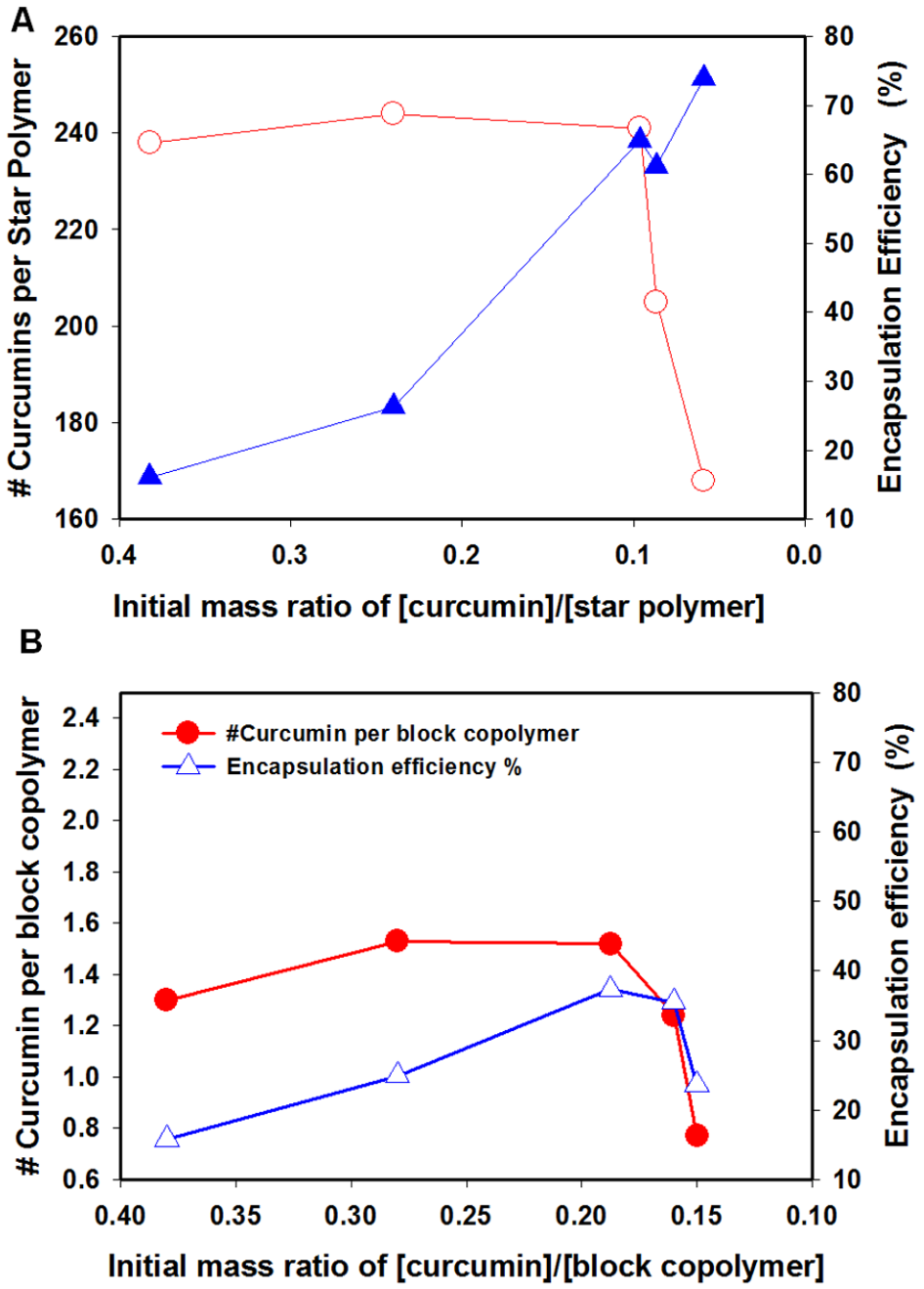

Figure 4.6: Loading capacity and encapsulation efficiency of (A) mPEG-*b*-PVL star polymer and (B) mPEG-*b*-PVL block copolymer for curcumin under different initial mass ratio of [curcumin]/[star polymer].

Historically, various amphiphilic carriers including dairy protein (*263*), lipid nanoparticles (*264*), and surfactants (*265-266*) have been reported to load curcumin cargos as well. Among these reported curcumin carriers, a poly(ethylene oxide)-*b*-poly(ε-

caprolactone) (PEG-*b*-PCL) micelle (*267*) has a similar chemical structure to mPEG-*b*-PVL. It was reported that the optimal encapsulation efficiency and loading capacity of the PEO-*b*-PCL (alternatively noted as PEG-*b*-PCL) micelles containing a hydrophobic region larger than 3 kD_a (i.e. the length of the PVL block in the nanogel stars) were 31.0% and 4.7 mol curcumin/mol polymer for PEO_{5000}-*b*-PCL_{24500}. The encapsulation efficiency of nanogel star polymer performs better than that of PEO_{5000}-*b*-PCL_{24500} micelle, however, the curcumin loading level per diblock copolymer is not, which is presumably due to the higher molecular weight of PCL block. The highest curcumin's water solubility achieved using PEO_{5000}-*b*-PCL_{24500} was 0.628 mg/L. Unlike the dynamic micellar structures, star polymers leverage the molecular stability through covalent bonding in the star polymers to improve both the loading capacity and efficiency. Hence, in comparison with both current and earlier polymer micelle studies, the nanogel star polymer architecture improves the encapsulation capability of the constituent diblock units, further expanding their functional limits.

4.3.4 Cytotoxicity Study

The nanoparticle platforms of diblock copolymer and nanogel star polymer synthesized through OROP approach has the potentials for biomedical and food applications. Those nanoparticle platforms should be biodegradable, biocompatible, and do not have adverse effects. To demonstrate the cytotoxicity of synthesized polymers, the biocompatibility of the synthesized polymers, diblock copolymer and nanogel star polymer, was examined with MTT assay on HepG2 cells to determine its cytotoxicity (*268-269*). No significant cytotoxicity was observed for either mPEG-*b*-PVL block copolymer or nanogel star polymer under the experimental conditions as shown in the Supplemental Information

(Figure S4.2). In addition to the biocompatibility status of mPEG-*b*-PVL copolymer, the nanogel core derived from the bis-ε-caprolactone type (*270*) crosslinker BOP also contributes to its biocompatibility.

4.4 Conclusions

In summary, mPEG-*b*-PVL diblock copolymers and the corresponding nanogel star polymers with high uniformity were synthesized using organocatalytic ring opening polymerization (OROP). Their solution behavior was investigated by synchrotron small-angle x-ray scattering (SAXS). In THF, the mPEG-*b*-PVL copolymer behaved as a typical loose random coil, while the mPEG-*b*-PVL star polymer 1 (M_n=221 kD_a) remained a robust, compact object. In water, the mPEG-*b*-PVL copolymers assembled into spherical micelles (9~10 nm). However, the mPEG-*b*-PVL nanogel star polymers aggregated into cylindrically-shaped aggregates (6 nm ×50 nm, radius x length). It is estimated that each aggregate contained ~ 4 individual star polymer molecules. The structural differences between the diblock copolymer and star polymer resulted in the distinct solution behavior. For nutraceutical encapsulation, we utilized the mPEG-*b*-PVL star polymer 2 (M_n=1423 kD_a) for curcumin encapsulation. We determined that each star polymer could load up to 240 curcumin molecules. Using the nanogel star for encapsulation, the water solubility of curcumin can reach 1.4 mg/mL which is a functional improvement over the constituent diblock copolymers. Finally, the biocompatibility of the mPEG-*b*-PVL copolymer and the nanogel star polymers was confirmed by cytotoxicity study.

Chapter 5

Structure and Physical Properties of Zein/Pluronic F127 Composite Films

5.1 Introduction

Nowadays, majority of packaging materials are petroleum-based polymers at the expense of sustainability and environmental protection (*271*). In order to alleviate the environmental pressure caused by petroleum-derived materials, researchers are actively exploring substitutes of those environment-unfriendly polymers from renewable resources such as polysaccharides, proteins, and microbial-fermented polymers (*272*). The investigation of those biopolymers matches the trend of novel material development, which is marked with the key words "functional", "environment-friendly", and "green chemistry" (*273-275*).

Among natural biopolymers, corn protein zein is a film-forming material which can potentially be utilized for packaging applications if its natural brittleness can be improved. In addition, zein also displays other advantageous physical properties including toughness, hydrophobicity, and resistance to microbial (*276*). Unlike globular protein, zein has different solution behaviors which have been investigated by several groups (*277-279*). Early, Tatham et al. determined that the radius of gyration (R_g) of zein in 70% (v/v) aqueous methanol solution was 4.4 nm with radius of gyration of cross-section (R_c)

of 0.25 nm (*279*). Later on, Matsushima et al. broke down the di-sulfide bond between Z19 and Z22 in α-zein mixture by β-mercatopethanol. From their small-angle X-ray scattering (SAXS) results, they established a tetramer model for α-zein Z22, which consisted of 10 anti-parallel helices with a reasonable axial ratio of 6:1 (*278*). This zein model was later supported by Momany et al (*280*). Very recently, by analyzing the concentration-dependent R_g obtained from SAXS and apparent viscosities data from rheological measurements, Li et al. observed two distinct scaling regions of zein in acetic acid under the same critical concentration (*277*). In addition, our recent study indicated that the different solvents (ethanol/water mixtures of different ratios versus acetic acid) could have significant impact on the surface morphology of zein films (*281*).

Although we are getting a clearer picture of zein's solution behavior, its natural brittleness still limits its further industrial applications as biodegradable packaging materials or edible films. The conventional approaches to improve the flexibility of zein include either chemical modification (*282*) or the formation of composite films through the addition of low molecular weight plasticizers (*283-284*). Compared with chemical modification approach, the formation of biopolymer composite films is an economical and convenient method for optimizing the overall performance of biopolymer product with the combined advantages of each component involved. Since most polymers cannot form completely compatible blends (*285*), the challenge for preparing biopolymer composite films largely depends on the selection of polymer components. Previously, different small molecules (e.g. sugars (*286*), polyethylene glycol 300 (*284*) and fatty acids (*287*)) and different synthetic polymers (e.g. polyvinylpyrrolidone (*288*), nylon-6 (*289*), and polyvinyl alcohol (*290*)) have been used to improve the mechanical properties

of zein. Ghanbarzadeh et al. compared the softening effect of different sugars such as fructose, galactose, and glucose on zein films. Their tensile test results showed fairly large Young's modulus and small elongation at break, indicating relatively small plasticizing effect of sugar (*286*). Santosa and Padua utilized oleic acid and linoleic acid as plasticizers to soften zein film (*287*). Those fatty acids-plasticized zein films also required additional re-plasticization process, which was time-consuming. Selling et al. pioneered the formation of zein composites with synthetic polymers such as PVP (*288*) and nylon-6 (*289*). The very first trial was zein/PVP composite film (*288*). From their report, the addition of 55 kD_a PVP into zein film enhanced the tensile strength of zein film by 24% (*288*). However, the elongation at break of zein/PVP blend film displayed no significant improvement compared with pure zein film. In another report, Selling et al. blended zein with 2% to 8% nylon-6 and found that the tensile strength of zein film was improved by 33%, and the solvent resistance of zein films to 90% ethanol/water was also found better (*289*). However, the elongation at break of zein/nylon-6 films was still on the same order of magnitude as the pure zein film, indicating no significant improvement in flexibility. Several mechanical tests were accomplished with the aid of combined plasticizers like tri(ethylene glycol) (*289*) and air moisture (*288*), because tri(ethylene glycol) and water could effectively interact with zein (*291*), and further alleviate zein's natural brittleness or low flexibility. In addition, few formulations have been investigated clearly from the viewpoints of both macro- property level and micro- structure level.

In this chapter, we aim to improve the flexibility of zein film and simultaneously understand the structure-property relationship behind it. We prepare zein/Pluronic F127 composite films to optimize the mechanical properties of the resulted zein films, and then

systematically investigate the microstructures of zein/F127 composite films under different F127 loadings. As a blending component, Pluronic F127 is an amphiphilic surfactant with a chemical composition of poly(ethylene oxide)$_{98}$-poly(propylene oxide)$_{67}$-poly(ethylene oxide)$_{98}$ (PEO_{98}-PPO_{67}- PEO_{98}). It has been widely studied for its solution behavior (*292-293*), unique polymorphism (*294*), sol-gel transition (*295*), and applications in drug delivery (*296*). Pluronic F127 not only shows biocompatibility itself (*297*), but also helps improve functionalities of other biomaterials like myoglobin (*298*). In liquid, Pluronic F127 exhibits an excellent capability as a stabilizing agent for drug delivery (*299*); while in solid, it serves as a structure-directing agent for silica film with controlled 3-dimensional porous structure (*300-301*). Because of its biocompatibility, predictable structures in both solid and liquid, and low glass transition temperature, Pluronic F127 was selected as a plasticizer and film-forming enhancer to form composite films with zein. The interaction, miscibility, structure, surface hydrophobicity and surface morphology of the zein/F127 composites were investigated by a combination of Fourier transform infrared spectroscopy (FTIR), differential scanning calorimetry (DSC), small-angle X-ray scattering (SAXS) and atomic force microscopy (AFM). The thermal and mechanical properties as well as the microstructures of zein/F127 composite films have been systematically studied. The structure-property relationship of zein/F127 composite films at different F127 loadings was established, which can benefit the future design of other protein-based biomaterials.

5.2 Materials and Methods

5.2.1 Materials

Zein powder containing ~95% α-zein was purchased from Wako Corporation. Pluronic® F127 NF Prill Poloxamer 407 was a gift obtained from BASF Corporation. Acetic acid (glacial, ACS grade) was purchased from Fisher Chemical. All of the reagents were used as received.

5.2.2 Preparation of zein/F127 composite films

The stock solutions of zein and F127 were prepared in pure acetic acid at the concentration of 100 mg/mL. After full dissolution of zein and F127 in acetic acid, the stock solutions of zein and F127 were filtered through 0.45 μm polytetrafluoroethylene (PTFE) filters to remove impurities. F127 solution was added into zein solution dropwisely to achieve F127 loadings ranging from 0% to 100%. Films with 0% and 100% F127 loading refer to pure zein and pure F127 samples, respectively. Then zein/F127 liquid mixtures were poured into highly flat Teflon Petri dishes. After staying at room temperature for 2 h to avoid film surface defects arising from fast solvent evaporation, those Petri dishes were placed in 50 °C oven overnight, and then dried in 40 °C vacuum oven for another 24 h. The transparency of final zein/F127 composite films was dependent upon F127 loading. When F127 loading reached 75%, the film became opaque due to the formation of F127 crystals.

5.2.3 Surface morphology analyses

Surface morphological images of zein/F127 composite films were collected using a commercial Nanoscope IIIa Multi-Mode AFM (Veeco Instruments, CA) equipped with a J scanner, which was operated in tapping mode using a silicon cantilever. Both height and

phase images were collected simultaneously using a set point ratio of ~0.9 for measurements at room temperature. At least 10 local spots on each film sample were imaged with the scan size of 10 μm× 10 μm. Thus, the AFM results can represent the overall surface morphology. The root-mean-square (RMS) surface roughness of each zein/F127 composite film was calculated using Nanoscope software 5.30.

5.2.4 Thermal analyses

Thermal properties of the dried zein/F127 composite films were determined by a differential scanning calorimetry (DSC) 823E thermal analyzer (Model 823, Mettler Toledo Instruments, OH). The films were cut into small pieces prior to experiments. DSC thermograms were collected by a two-cycle mode with 5~8 mg samples at the scan rate of 10 °C/min and compressed nitrogen purge of 60 mL/min. For the first cycle, the samples were heated from 25 °C to 200 °C to remove the thermal history and then cooled from 200 °C to -100 °C. The 2nd cycle scanning started from -100 °C to 200 °C at the same scanning rate. For each zein/F127 composite film, the melting temperature (T_m) of F127 was obtained as the peak temperature, while the glass transition temperature (T_g) of zein was the mid-point between the onset temperatures during 2nd cycle scanning. Also, the T_m of pure F127 and the T_g of pure zein were used as references after the DSC analyses of pure F127 film and pure zein film. Besides, the enthalpy of crystalline melting (ΔH) was calculated using the area under curve of the melting peak, and then normalized by the weight fraction of PEO blocks in the composite films.

5.2.5 Mechanical properties

Tensile test was performed for zein/F127 composite films. The elastic modulus, tensile strength and elongation at break of the films were measured by *TA.XT2i* Texture

Analyzer (Texture Technologies Corporation, Scarsdale, New York) according to EN ISO 527-3: 1995 E at a speed of 5.0 mm/min. The films were carefully cut into rectangular shape with a dimension of 1.0 mm×60.0 mm. The film thicknesses were between 0.3 mm and 0.4 mm. The initial gap was set at 25.0 mm. The film samples were subject to tensile test right after vacuum annealing. All the measurements were replicated at least three times for each sample.

5.2.6 ATR-FTIR spectroscopy

The attenuated total reflectance Fourier-transform infrared (ATR-FTIR) spectra of film surfaces were collected under ambient condition by utilizing a Thermal Nicolet Nexus 670 FT-IR spectrometer (Thermo Fisher Scientific Inc., Waltham, MA) equipped with a Smart MIRacle™ horizontal attenuated total reflectance Ge crystal accessory. Each spectrum was averaged over 512 scans with 4 cm^{-1} resolution.

5.2.7 Small-angle and wide-angle X-ray scattering

Small-angle and wide-angle X-ray scattering data were collected at the 18-ID beamline of BIO-CAT, at the Advanced Photon Sources, Argonne National Laboratory, Illinois, USA. The film samples with surfaces perpendicular to X-ray beam were directly positioned in the optical path of X-ray beam. For SAXS, sample-detector distance was fixed at 0.826 m, which was utilized to cover a scattering vector Q range of 0.01-0.35 $Å^{-1}$. For WAXS, the sample-to-detector distance is set at 180 mm, which corresponds to a Q range of 0.08-2.5 $Å^{-1}$. A Mar165 CCD was installed lateral to the X-ray beam. The X-ray wavelength was 1.033 Å and the energy of X-ray was 12 keV. A single exposure of 1 sec was used to obtain the scattering data. The background for films was air at room temperature. Three structural parameters of Pluronic F127 including PEO volume fraction in block

copolymer φ_{PEO}, chain length in liquid γ_v, and order-to-disorder transition temperature T_{ODT} were calculated to be 66%, 295 and 169 ºC, respectively (*302*). Therefore, Pluronic F127 should form order structure at room temperature.

The crystalline phases in the composite films were determined from the relative positions of the SAXS peaks. For lamellar structures, the peak positions should obey the relationship of 1:2:3:4 etc. The structure parameter *d* (average long periodicity) was obtained from the position (q^*) of the first (and the most intense) diffraction peak. The equation of average long periodicity *d* is shown as follows.

$$d = \frac{2\pi}{q^*} \tag{5.1}$$

In the lamellar phase, the average long periodicity *d* is quantified from the inverse film area (*A*) per volume (*V*) ratio. This *A*/*V* ratio of the local copolymer film is given by equation 5.2 (*303-304*). Assuming a clear interface between hydrophilic PEO and hydrophobic PPO, we calculate the interfacial area α_p, the effective area per PEO block at the interface between polar and apolar domains by equation 5.3.

$$A/V = 2\varphi_p\alpha_p / V_p \tag{5.2}$$

$$\alpha_p = \frac{V_p}{d\varphi_p} \tag{5.3}$$

where φ_p is the polymer volume fraction, α_p is the effective interfacial area per PEO block, and V_p (≈19933.6 Å^3) is the estimated volume of one F127 polymer molecule based on the calculation method of one Pluronic P105 volume (*305*).

5.2.8 Statistical analysis

SigmaPlot 11.0 software with SigmaStat integration (Systat Software) was used to perform all the statistical analysis. One-Way Analysis of Variance (ANOVA) tests were

followed by Holm–Sidak method, with the overall significance level set at 0.05. Non-normal raw data were first transformed to meet the requirement of ANOVA analysis.

5.3 Results and Discussion

5.3.1 Surface morphology

The surface morphologies of zein/F127 composite films were collected using tapping mode atomic force microscopy (AFM) and typical morphologies at different F127 loadings were presented in Figure 5.1. At low F127 loadings (Figures 5.1A to 5.1D), the film surfaces were flat and featureless. These flat surfaces are consistent with our previous observation where flat zein thin films were achieved by spin-cast on silicon wafer (*281*). At high F127 loadings (50%~100%), large amount of lamellae crystals were observed (Figures 5.1E to 5.1H). Interestingly, edge-on or branch-like lamellae crystals were found in the zein/F127 composite film with 50% F127 loading (Figures 5.1E and 5.1G). For comparison, 100% F127 crystalline pellet is also shown in Figure 5.1. It is clear that flat-on lamellae crystals are spread all over the pellet surface in Figures 5.1F and 5.1H. The difference of geometries between flat-on and edge-on lamellae lies in the crystal orientation. The crystal growth that follows a *c*-axis orientation generates flat-on lamellae, while crystals oriented in *a*-*b* plane have edge-on lamellae. The basic structures of flat-on and edge-on lamellaes are the same but just one is tilted 90º from another. Growth of lamellae crystals in different environments results in the observation of different surface morphologies. Without any external restriction, semicrystalline F127 can naturally stretch into flat-on lamellae, which is in agreement with the mean-field prediction of F127 melt at room temperature (Figures 5.1F and 5.1H) (*306-308*). As a blending partner, the amorphous zein not only occupies certain amount of space in the

bulk film, but also interacts with F127 through a couple of possible interactions (i.e., hydrogen bonding and hydrophobic interaction). Under such circumstance, the growth of F127 lamellae crystals is restricted by amorphous zein's geometry and its interaction with zein in the bulk film. Therefore, the confinement of amorphous zein shapes polyether chains to fold into branch-like geometry (Figures 5.1E and 5.1G). The details of F127 crystals confined by zein will be discussed in more details later on.

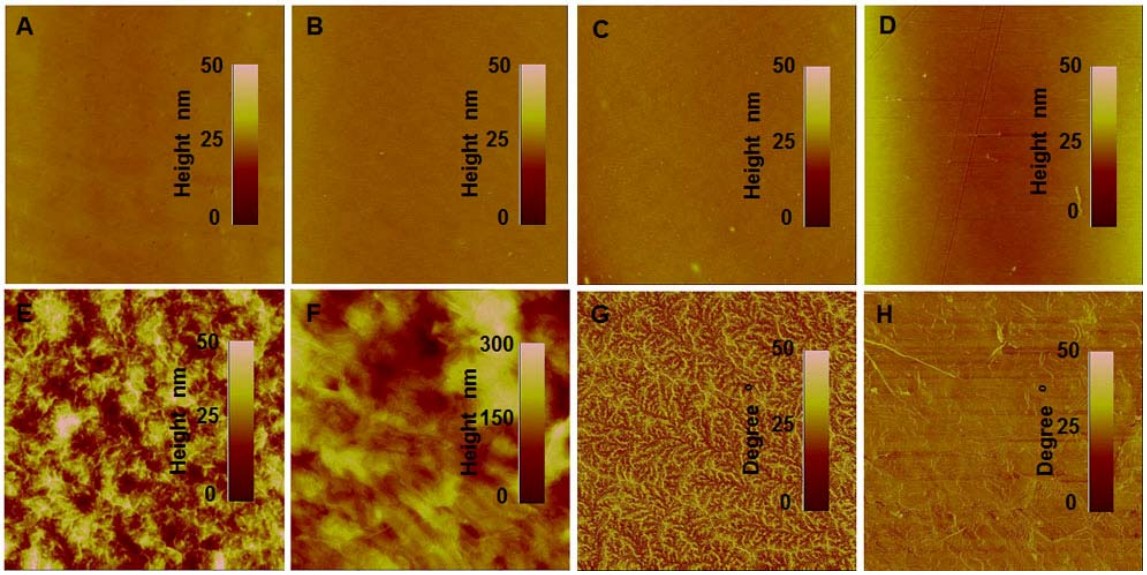

Figure 5.1: Tapping mode atomic force microscopy (TPAFM) images of zein/F127 composite films with different F127 loadings. Height images: (A) 0% F127, (B) 10% F127, (C) 20% F127, (D) 35% F127, (E) 50% F127, and (F) 100% F127; and phase images: (G) 50% F127, and (H) 100% F127. The scan size is fixed at 10 μm×10 μm.

The RMS surface roughness of the zein/F127 composite films was shown in Figure 5.2. With the increase of F127 loading from 0% to 75%, the averaged root-mean-square (RMS) roughness of zein films increased from 2 nm to 12 nm, indicating the surface roughening induced by F127 crystals. The roughness of pure F127 crystal pellet with a high value of 77.7 nm was shown as a reference value in Figure 5.2. Our results suggested that the film surfaces at high F127 loadings were very likely covered by

crystalline PEO blocks of F127. Such spatial distribution of F127 in the bulk film, in which each component tends to stay in the bottom or upper space, may be driven by gravity, surface tension and other molecular interactions (i.e., hydrogen bonding and hydrophobic interaction). Since the bulk density of zein is estimated to be higher than 1.36 g/mL (*309*) and the density of F127 is 1.05 g/mL, gravity exerts more impact on zein than F127. Hence, it is not unexpected to observe the F127-covered film surface due to the gravity role during solvent evaporation. Besides, due to hydrophilicity and self-crystallization, PEO block has lower miscibility than PPO to zein, thus it tends to segregate from the hydrophobic regions of zein and PPO, and then enriches in film surface. The segregation of PEO blocks onto the air/solid interface is also due to the difference of surface tension between zein, PPO and PEO ($\gamma_{PEO} > \gamma_{PPO}$ and γ_{zein}). Similar phenomenon of block segregation was also observed in the poly(styrene)-*b*-poly(methyl methacrylate) (PS-*b*-PMMA) film as well (*310*).

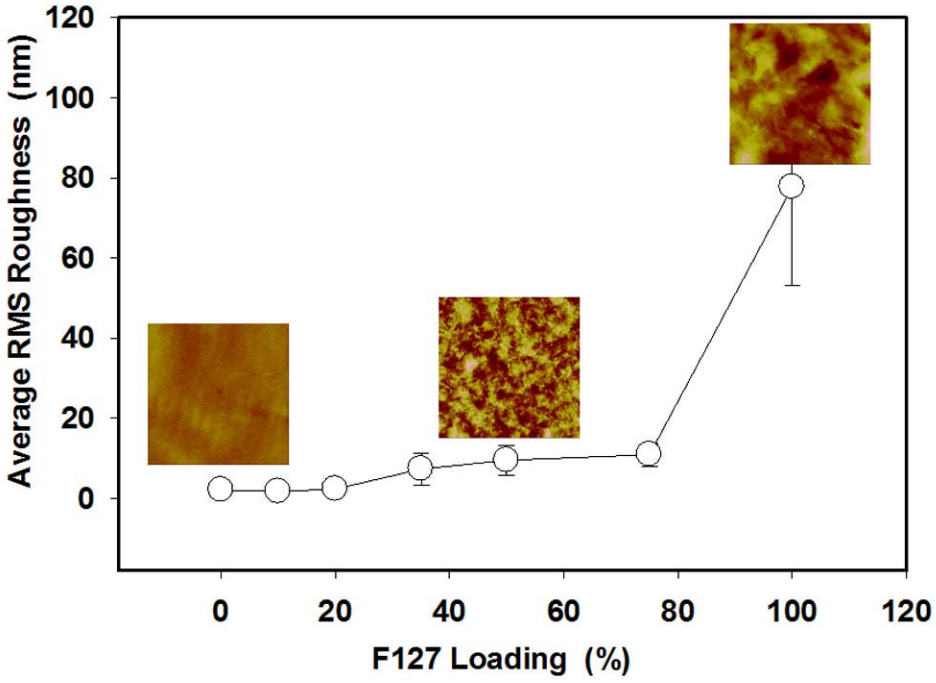

Figure 5.2: The plot of averaged root-mean-square (RMS) roughness of zein/F127 composite film surfaces versus F127 loadings. The insets are tapping mode atomic force microscopy height images of zein/F127 composite films with F127 loadings of 0%, 50%, and 100%, respectively.

5.3.2 Thermal analyses

Most zein composite films with low F127 loadings are transparent (see Figure S5.1 in supplementary information), suggesting that zein and F127 have certain degree of miscibility. Such miscibility is probably attributed to the hydrogen bonding and hydrophobic interaction between PPO block in F127 and hydrophobic residues in zein (*277*). The partial miscibility of PPO block and zein may confine the crystallization of PEO block in F127, causing a shift in melting temperature (T_m) and glass transition temperature (T_g). We then utilized differential scanning calorimeter (DSC) to detect such changes from the T_m of pure F127 (~56 ºC) and the T_g of pure zein (~97 ^oC) (Table 5.1). Figure 5.3A shows the DSC thermograms of zein/F127 composite films with different F127 loadings. For comparison, the DSC thermogram of pure F127 was listed in Figure

S5.2 of supplementary information. The T_m of the composite film was depressed when F127 loading decreased. Besides, the change of T_g in the composite film was also affected by the F127 loading. Since T_g change was less observable than T_m in the same plot, we re-plotted the typical glass transition curves of zein/F127 composite films for clearer observation (Figure 5.3B). With an increase of F127 loading, the decrease of T_g also suggested the partial miscibility between zein and F127 (Figure 5.3B). In addition, the melting enthalpy (ΔH) is relevant to crystallinity. Figure 5.3C shows the impact of F127 loading on the melting enthalpy. The non-linear decrease of ΔH with F127 loading indicated the existence of different crystal growth stages at different F127 loadings.

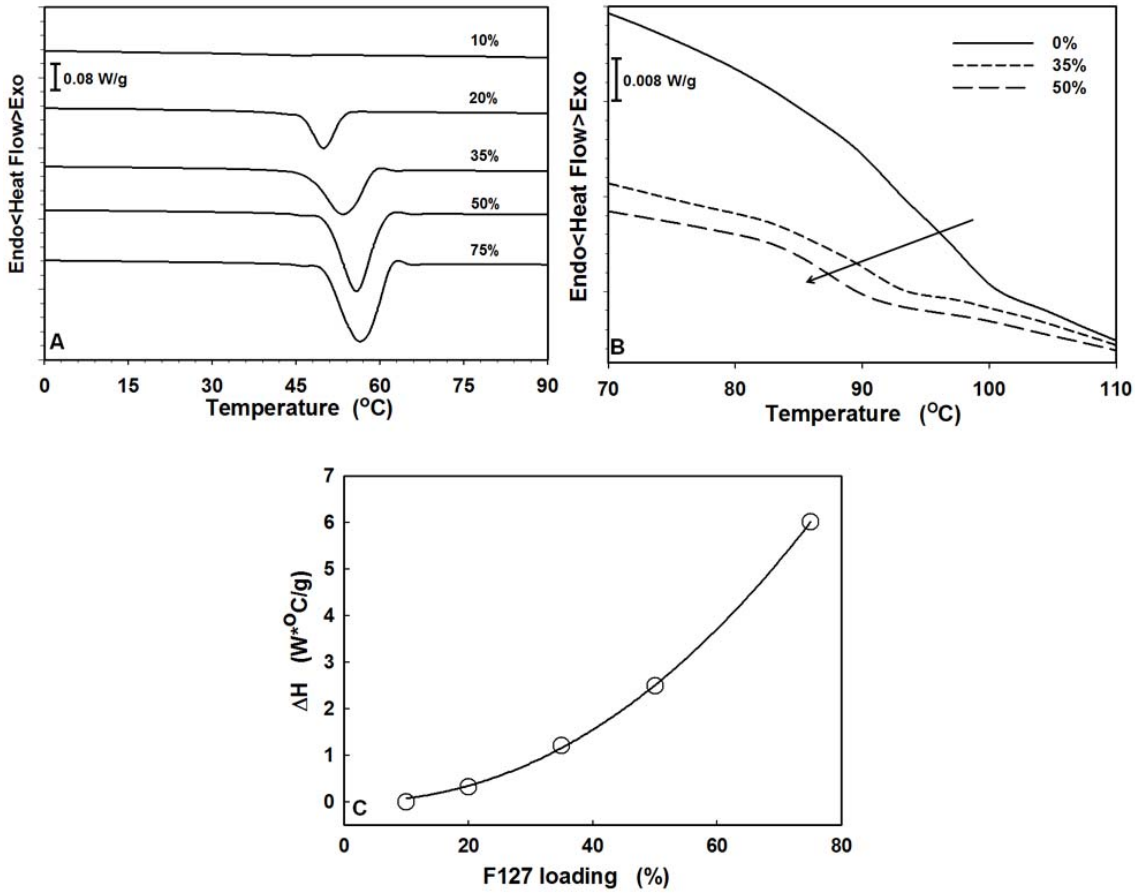

Figure 5.3: (A) Melting temperature (T_m) alternation of zein/F127 composite films with different F127 loadings (10%~75%); (B) Glass transition temperature (T_g) change of zein/F127 composite films with different F127 loadings (0%, 35%, and 50%); and (C) the plot of the crystalline melting enthalpy (ΔH) versus F127 loading. The solid line in (C) was used to guide the eyes.

Table 5.1 listed the detailed thermal properties of zein/F127 composite films with different F127 loadings. The T_g of pure zein film was 97 °C which was in agreement with the previous thermal results (*282*). With an increase of F127 loading from 0% to 35%, the T_g of zein dropped from 97.0 ºC to 88.4 ºC. In addition, the T_g of zein/F127 composite film with 35% F127 was significantly lower than that of pure zein film. The T_m values of the composite films decreased from 55.2 ºC to 47.6 ºC when F127 loading decreased from 75% to 20%. Such changes of T_g and T_m resulted from the miscibility of PPO block

and zein that suppressed the space for the crystallization of PEO block, which further caused the decrease of crystal size and introduced imperfections in crystal structure.

Table 5.1: Thermal properties of zein/F127 composite films

F127 Loading (%)	T_g (^oC)	T_m (^oC)
0	97.1±1.6	NA[a)]
10	95.5±0.7	NA[a)]
20	90.9±0.8*	47.6±3.0
35	88.4±0.9*	53.4±0.1
50	84.9±3.3*	51.5±5.9
75	NA[b)]	55.2±1.8
100	NA[b)]	56±0.0

[a)] T_m is not observable on the endothermal curve due to the amorphous structure; [b)] T_g is not observable on the endothermal curve due to the large melting peak of F127 and low amount of glassy zein.
* Denotes significant difference from the pure zein film.

5.3.3 Mechanical properties

Tensile test was conducted to determine the mechanical properties of zein/F127 composite films. Figure 5.4 exhibits the stress-strain curves of zein/F127 composite films with different F127 loadings. The elongation at break of the zein/F127 composite films was enhanced more than 8-folds (from less than 10% to more than 82%) when F127 increased from 10% to 35%. However, further increase of F127 loading to 50% brought deleterious impact on the elongation of the film. The tensile strength, elongation at break, and elastic modulus of these films were presented in Table 5.2. The variation of three parameters is likely due to the difference in film thickness. It can be seen that the loading

of F127 has significant impact on the mechanical properties of zein/F127 composite films. Among those films, the film with 35% F127 exhibited the lowest values of tensile strength (9.2 MPa), elastic modulus (163 MPa), and simultaneously showed the highest elongation at break (92.0%). The values of tensile strength, elastic modulus, and elongation at break of zein/F127 composite film with 35% F127 were significantly different from those of zein/F127 composite film with 10% F127. The decreases of tensile strength and elastic modulus verified the plasticizing effect of F127 on the composite film. Hence, 35% F127 loading reaches the maximum plasticizing effect of F127 due to its interaction with zein in amorphous region. At high F127 loading, the crystalline nature of F127 dominated the plasticizing effect of F127, causing the increased brittleness of the composite films.

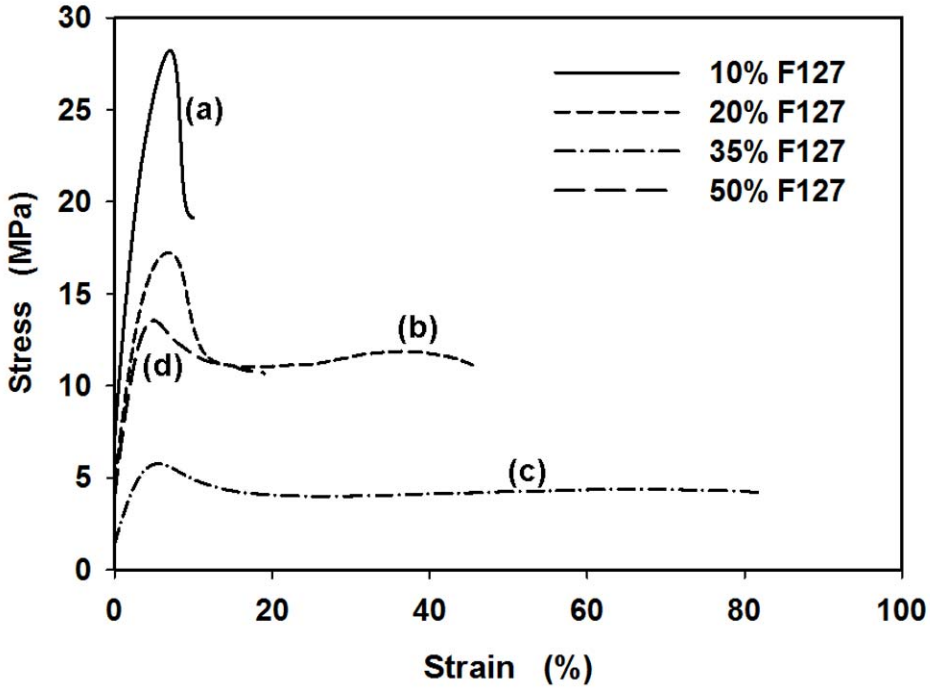

Figure 5.4: Tensile stress-strain curves of zein/F127 composite films with F127 loadings of (a) 10%, (b) 20%, (c) 35%, and (d) 50%.

Conventionally, different plasticizers such as glycerol, sugars, and fatty acids have been employed to improve the mechanical properties of zein films. Comparing our films with those reported plasticized films (*284, 287, 311*), remarkable advantages can be seen. Those fatty acid or sugar-plasticized zein films are either less effective or tedious in sample preparation. In contrast, Pluronic F127 surfactant exhibited a better plasticizing effect with convenient preparation. The mechanical test here suggests that at proper loading level, F127 can effectively reduce the brittleness of zein film due to the partial miscibility of zein and F127 at amorphous region, which also ensures the integrity of zein's structure as well.

Table 5.2: Mechanical properties of zein/F127 composite films

F127 Loading (%)	Tensile Strength (MPa)	Elongation at Break (%)	Elastic Modulus (MPa)
10	29.1±2.0	16.0±2.7	468.1±22.4
20	20.1±1.6*	45.0±14.9*	291.8±33.3*
35	9.2±1.4*	92.0±9.6*	163.0±26.7*
50	17.0±1.6*	16.0±3.3	258.0±16.8*

* Denotes significant difference from the zein/F127 composite film with 10% F127 loading.

5.3.4 Molecular interaction in zein/F127 composite films

Figure 5.5A shows the ATR-FTIR spectra (4000~600 cm^{-1}) from the surface of zein/F127 composite films with different F127 loadings. The characteristic peaks of F127 located at 1342 cm^{-1} (-CH_2 wag), 1279 cm^{-1} (-CH_2 twist), 1104 cm^{-1} (C-O-C stretching) and 962 cm^{-1} (-CH_2 rock) were in agreement with previous results (*312*). The two peaks located at 1649 cm^{-1} and 1536 cm^{-1} corresponded to amide I band and amide II band of zein (*218*). The absorption peaks at 3000~2880 cm^{-1} (C-H stretching) were sensitive to the F127 chain. With the increase of F127 loading, 2959 cm^{-1} peak (C-H asymmetric stretching vibration of -CH_3) disappeared and 2883 cm^{-1} peak (symmetric stretching vibration of -CH_2) grew gradually, which were probably attributed to the segregation of PEO blocks (-O-CH_2CH_2) on the composite film surface, because ATR-FITR majorly scanned the film surface. When F127 increased from 0% to 35%, strong increase of the broad peak at 3292 cm^{-1} was found due to the increased amount of hydroxyl groups (-OH) in the zein/F127 composite films. Additionally, this broad peak shifted to a lower

wavenumber, indicating that the addition of F127 led to different patterns of hydrogen bonding.

To further investigate hydrogen bonding in the zein/F127 composite films, the Fourier deconvolution plots of –OH and -NH_2 band were shown in Figure 5B for pure zein film and in Figure 5C for composite film with 35% F127 loading. Four peaks at 3345, 3291, 3189, and 3057 cm^{-1} were assigned to the stretching of –OH in intramolecular and intermolecular hydrogen bonding, –NH_2 in hydrogen binding and the stretching of -C-H. The area ratios of those four bands for pure zein film (0% F127 loading) were 43.8:23.2:12.0:21.0, indicating a large contribution from intramolecular hydrogen bonding. From 35% F127 composite film, these corresponding peaks shifted to 3383, 3290, 3191, and 3068 cm^{-1}, respectively, and the ratios changed to 30.4:32.2:10.0:27.4. It suggested that intermolecular hydrogen bonding between F127 and zein dominated the intramolecular hydrogen bonding of zein.

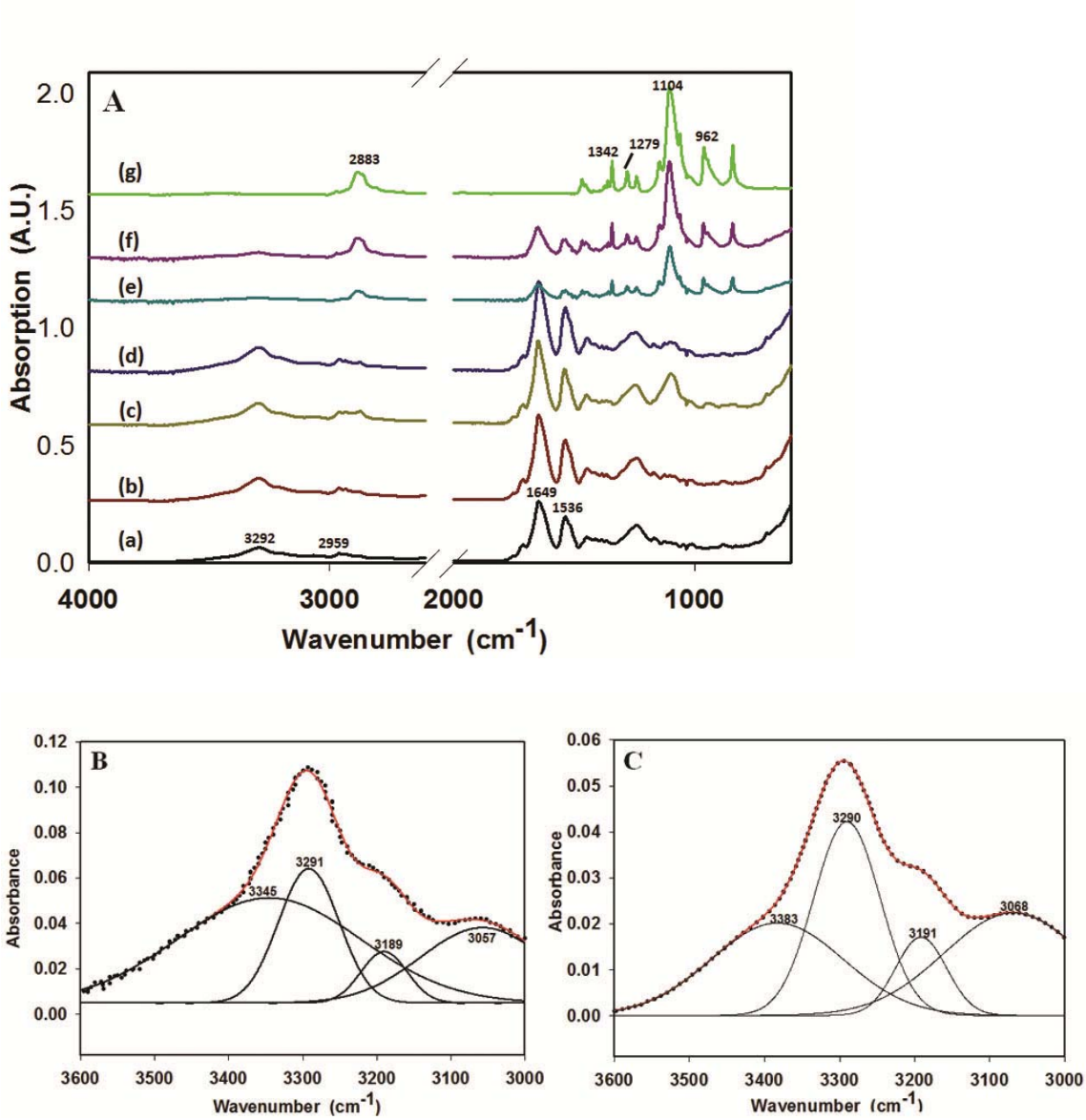

Figure 5.5: (A) Fourier transform infrared spectra of zein/F127 composite films with F127 loadings of (a) 0%, (b) 10%, (c) 20%, (d) 35%, (e) 50%, (f) 75%, (g) 100% within the wavenumber range of 4000~600 cm^{-1}; Best fit curves for the self-deconvoluted FTIR spectra using nonlinear regression analyses: (B) The overlapped –OH, $–NH_2$, and CH stretching bands (3600~3000 cm^{-1}) in pure zein film (0% F127 loading), and (C) zein/F127 blend film (35% F127 loading). The hydrogen bonding band was fitted with Gaussian functions using peak positions obtained from second derivative analysis.

Table 5.3 summarized the contribution from these four typical interactions in the zein/F127 composite films. The F127 loading had little impact on the contribution of hydrogen bonded $–NH_2$ and -CH stretching components. Clearly, by increasing F127 loading from 0% to 10%, 20%, and 35%, the component of intramolecular hydrogen

bond bonded –OH decreased, while intermolecular hydrogen bond bonded –OH contributed more to the hydrogen bonding profile. Also, compared with pure zein film, zein/F127 composite films with low F127 loadings (10%-35%) display significant differences of intramolecular hydrogen bond and intermolecular hydrogen bond. This phenomenon indicates that intermolecular hydrogen bond greatly contributes to the miscibility of zein and F127 in low F127 loading composite films.

Table 5.3: Hydrogen bonding profiles of zein/F127 composite films with low F127 loadings

F127 Loading (%)	$N_{intra\text{-}OH}$ (%)	$N_{inter\text{-}OH}$ (%)	N_{NH2} (%)	N_{CH} (%)
0	43.8±0.1	23.3±0.1	12.0±0.1	21.0±0.1
10	32.0±0.1*	32.2±0.1*	9.8±0.1	26.0±0.1
20	36.3±0.1*	30.4±0.1*	9.6±0.1	23.6±0.1
35	30.4±0.1*	32.2±0.1*	10.0±0.1	27.4±0.1

* Denotes significant difference from pure zein film.

5.3.5 Microstructure in zein/F127 composite films

Since Pluronic F127 can self-assemble to form order structure, we applied small and wide angle X-ray scattering to study the microstructure of the composite films. Figure 5.6A presented the small-angle X-ray scattering (SAXS) profile of pure F127, which has two clearly observable Bragg's peaks with the peak position (q*) ratio of 1:2 in q-space. The first two peaks corresponded to the first-order and second-order lamellar structures in the film. Such ordered structure is consistent with the AFM images shown in Figures 5.1F and 5.1H.

In terms of the microstructure of composite films, low F127 loadings (0~35%) are not enough to form highly ordered crystals in the zein-confined amorphous region, which is also reflected by tapping mode AFM images (Figures 5.1A~5.1D). It is worth mentioning that a peak located at q=0.6 $Å^{-1}$ is observed for zein films with 0~20% F127 loadings, which corresponds to the intermolecular distance within zein (~10.5 Å). High F127 loadings (50%~75%) can result in the formation of highly ordered crystalline phase in the composite films. In Figure 5.6A, composite film with 75% F127 loading displays two similar lamellar peaks as pure F127 pellet. Different from pure F127 pellet, the two peaks shifted to larger q region indicating the formation of smaller crystals. Simultaneously, there is another shoulder peak located at q=0.42 $Å^{-1}$ which may be due to other subtle metastable lamellar structure. For the film with 50% F127 loading, the first-order peak continued to shift to larger q region and the second-order peak became less obvious, suggesting that the periodicity of lamellar order structure became less clear. The films with low F127 loadings (10~35%) displays even weaker first-order peak which continued to shift to a larger q region.

Further application of wide-angle X-ray scattering (WAXS) to probe the structural change at crystallite level was shown in Figure 5.6B. The peak at q=0.6 $Å^{-1}$ from the composite films of 20% and 50% F127 loadings overlaps with the peak observed in the SAXS profiles of zein films with 0~20% F127 loadings (Figure 5.6A), suggesting the intermolecular size of zein. From the composite film containing 50% F127, two sharp peaks at 1.36 $Å^{-1}$ and 1.64 $Å^{-1}$ clearly indicate the formation of PEO crystals. While for the composite film containing 20% F127, only an amorphous halo was observed, suggesting a less ordered structure. Small amount of PEO crystallites can serve as nuclei

for further crystallization. Similar WAXS profiles in consideration of the crystallization of PEO confined in the self–assembled nanoconfined lamellaes of PEO-*b*-PS copolymers have also been reported (*313*).

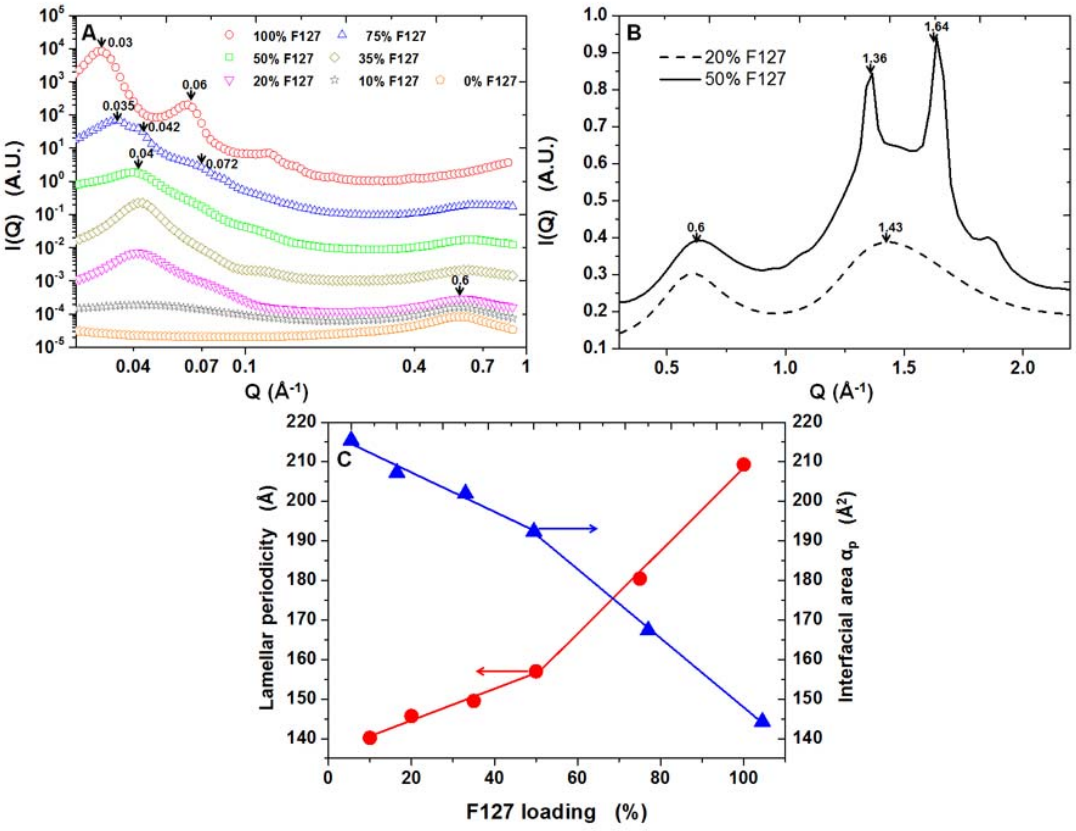

Figure 5.6: (A) Small-angle X-ray scattering (SAXS) profiles of zein/F127 composite films with different F127 loadings (10%~100%); (B) wide-angle X-ray scattering (WAXS) profiles of zein/F127 composite films with F127 loadings of 20% (dash line) and 50% (solid line); (C) the plots of averaged long periodicity *d* (solid circles) and polar-apolar interfacial area α_p (solid triangles) versus F127 loading for the zein/F127 composite films

Based upon equations 5.1 and 5.2, two lamellae parameters including long average periodicity *d* (*d*-spacing) and polar-apolar interfacial area α_p have been extracted from SAXS profiles (Figure 5.6A). Figure 5.6C exhibits the average long periodicity and interfacial area of zein/F127 composite films with different F127 loadings. Two linear trends were observed in the plot of *d* versus F127 loading and α_p versus F127 loading. As

F127 increased from 10% to 50%, *d* increased from 140.1 Å to 157 Å while α_p decreased from 2145.5 $Å^2$ to 192.4 $Å^2$. At higher F127 loading (50%~100%), the increase of *d* and decrease of α_p followed a sharper trend, suggesting two possible crystal growth stages (crystallite formation and crystal growth). The increase of periodic spacing *d* suggested that more F127 is involved in the lamellae construction with the increase of F127 loading. More F127 chains folded into lamellar structures and less F127 stayed at the interface between polar and apolar domains. Thus, the interfacial area between amorphous region and crystalline region decreased.

5.3.6 Understanding structure-property relationship

To understand the role of F127 on the structure and properties of zein/F127 composite films, we have studied the mechanical properties and microstructure of the zein/F127 composite films at different F127 loadings. Both of them are tightly related to the crystallization of PEO under the confinement by PPO/zein aggregate domains. Besides, pure PEO (M_w=4250 D_a, the molecular weight almost equal to that of PEO portion in Pluronic F127) has been reported to have two types of crystals with different chain conformations (*314-317*). Hence, we discuss the microstructure of zein/F127 blend film and its impact on the film properties from two aspects: 1. Confinement of PEO crystals; and 2. Integral-folding (IF) PEO chain conformation. Prior to further discussion, two types of crystals with different chain conformations are shown in Figure 5.7A. They are extended chain IF(n=0) crystal and once-folded chain IF(n=1) crystal. The number n represents the PEO chain folding times. For low molecular weight PEO fraction (M_w=4250 D_a), the number n is either 1 or 0.(*318*) Also, based upon the previously-

mentioned characterization results, we propose a possible crystallization mechanism of F127 at different loadings (Figures 5.7B~5.7D).

At low F127 loadings (10%~35%), the PEO blocks form very limited quantities of small crystallites which are not enough for large crystal formation (Figure 5.7B). And this can be verified by TP-AFM height images (Figures 5.1A~5.1D) and low melting temperatures (Figure 5.3A). Meanwhile, the amorphous PPO blocks strongly interact with zein domain through hydrogen bonding, which is supported by FTIR analysis (Figures 5.5B and 5.5C), and hydrophobic interaction. Since the matrix is a zein domain-dominant space, randomly-distributed PEO crystallites cannot compete with the plasticizing effect provided by PPO-zein interaction. Hence, from macro length scale, we clearly observed the improved flexibility of zein film. Under such confinement of zein domain, PEO fractions of the tri-block copolymers occupied space-saving conformation, and eventually formed double-layer once-folded chain IF(n=1) crystals. This argument can be supported by the long average periodicity *d* (*d*-spacing) *(*Figure 6C) calculated from the SAXS profiles (Figure 5.6A). At low F127 loading like 20%, the *d*-spacing is 145 Å which is almost identical to the fold length of IF(n=1) crystals (slightly higher than 137 Å) (*317*), illustrating that the majority of PEO crystallites is chain folded IF(n=1) crystal. Since the melting temperature of IF(n=1) crystals is reported to be lower than that of extended chain IF(n=0) crystals (*314-315, 317*), the low melting temperature (47.6 ^{o}C) observed from DSC thermogram (Figure 5.3A and Table 5.2) also give support to the dominance of IF(n=1) crystals at low F127 loadings.

At relatively high F127 loading like 50%, the amount of PEO crystallites is enough to form higher-order or larger crystals (Figure 5.7C). However, different from pure F127's

flat-on lamellae which grow in *c* orientation without confinement (Figure 5.7D), F127 chains are confined to grow in *a*-*b* plane into branch-like large crystals. The inter-space among branches is fulfilled with zein domains. Those zein domains still interact with amorphous PPO segments along the branch contour. At this time, the brittleness caused by large amounts of branch-like crystals surpasses the plasticizing effect of F127, resulting in the shrunk elongation of film at macro scale. Meanwhile, with an increased amount of F127 in the film matrix, larger space occupied by F127 results in an increasing portion of extended chain IF(n=0) crystals. The *d*-spacing of zein film at 50% F127 is 157 Å (Figure 5.6C), which is between the fold length of IF(n=1) crystals (137 Å) and that of IF(n=0) crystals (274 Å). But that value of *d*-spacing is still close to the fold length of IF(n=1) crystal, suggesting the majority of once-folded chain IF(n=1) crystals.

As a reference, 100% F127 pellet is also studied along with other zein blend films. Its brittleness comes from the formation of large crystals, also called "flat-on" lamellae, which grows in *c* orientation without confinement (Figure 5.7D). Its typical surface morphology can be viewed from TP-AFM images (Figures 5.1F and 5.1H). Without zein confinement, the majority of PEO chains are associated with each other in a more extended manner, and form extended chain IF(n=0) crystals. However, the *d*-spacing of 100% F127 pellet is 209 Å, still lower than the chain length of PEO (M_w=4250 D_a) (269 Å). This phenomenon is probably relevant to the kinetic pathway which refers to crystallization temperature and crystallization period. Since lower or higher crystallization temperature can lead to shorter or longer fold length of crystals, the current processing temperature itself limits the growth of IF(n=0) crystals during solvent casting.

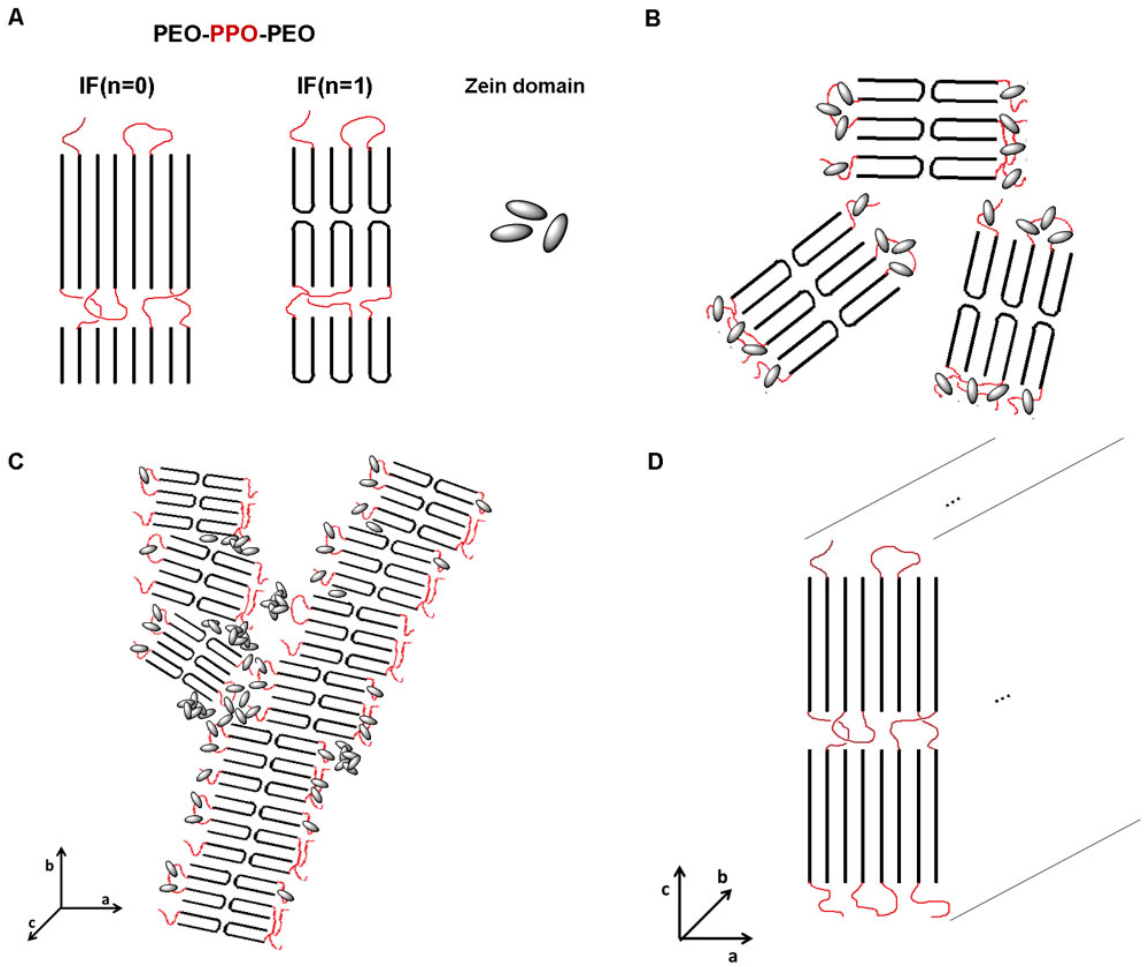

Figure 5.7: Mechanism of F127 crystallization in the zein/F127 composite films with different F127 loadings: (A) IF(n=0) and IF(n=1) crystal structures of PEO-PPO-PEO proposed by Zhang et al. (*318*), and zein domain in films; (B) crystallite formed at 20% F127; (C) branch-like (edge-on) lamellae formed at 50% F127 with eye perspective perpendicular (*c* axis) to the *a*-*b* plane; and (D) flat-on lamellae formed at 100% F127 with eye perspective perpendicular to the *a*-*c* plane. *a*-*b* plane is the film surface while *c* coordinate is perpendicular to the film surface.

In summary, adding F127 into zein film can efficiently overcome the brittleness and broaden the application of zein products. Different F127 loadings have a large impact upon the physical properties of the composite films, which arise from a competition between crystallization and plasticization of F127. At low F127 loading (35%), the plasticizing effect due to the interaction between PPO segments and zein domain is dominant over crystallization. The flexibility of zein film has been improved by more

than 8 folds while the surface flatness and hydrophobicity can still be maintained. The limited amount of crystals is majorly composed of once-folded chain (IF=1) PEO crystals. At high F127 loading (50% and above), the F127 crystallization results in a large quantity of lamellar structure which surpasses the plasticizing effect. Compared to the highly ordered flat-on lamellar structure in pure F127 film, the crystallization of F127 under the confinement of zein leads to less ordered branch-like lamellar structure. Large quantity of crystals is a mixture of once-folded chain (IF=1) and extended chain (IF=0) PEO crystals, and the portion of extended chain (IF=0) PEO crystals increases with F127 loading. Based upon the established structure-property relationship, we suggest that the optimized condition for zein/F127 composite film is with 35% F127 loading, which has significantly improved the mechanical properties of zein films and broadened the applications of zein as a novel biomaterial.

Chapter 6

Development of Highly-aligned Curcumin-loaded Zein Fibers

6.1 Introduction

Nutraceutical delivery systems are benefiting the healthcare of the human body through different channels, among which transdermal administration becomes emerging (*319*). Compared with conventional oral administration, transdermal delivery enjoys several advantages (*320*), including reduced first-pass drug degradation, fewer adverse effects after uptake, and convenience to carry. From the viewpoint of material construction, the design of porous material for a transdermal patch is of importance to its overall performance and functionality. Appropriate processing will help produce stable material, leading to the further innovation for transdermal patches.

Electrospinning is a straightforward method to generate non-woven fibrous mats from polymer solutions. To initiate electrospinning, an external electric field is applied to a polymer solution which results in the formation of a Taylor cone (*84*) at the end of the solution. As the applied voltage surpasses a critical level, usually on the order of several kilovolts, a polymer jet will be emitted from the Taylor cone. Through jet whipping and solvent evaporation, the polymer fibers will be deposited onto the metal-covered (i.e., Al) grounded collector. Compared with other fiberization techniques such as wet spinning (*321*), extrusion spinning (*322*), and melt blowing (*323-325*), electrospinning is more

environment-friendly which does not require large quantity of organic solvent, high temperature, or high pressure. Besides, this technique provides us with a one-step process to fabricate fibers with a wide range of sizes from 10 nm to 100 μm. More importantly, this technique is extremely versatile, which facilitates the production of fibers from materials ranging from synthetic polymers, natural polymers, composites, to ceramics (*82*). With such an advanced technology, electrospun fibers can conveniently match different applications such as superhydrophobic materials (*326*), electronic devices (*327*), energy storage (*328*), tissue engineering (*329*), filtration (*142*), and drug delivery (*330*). Currently, electrospinning enables us to fabricate porous fiber mats which can eventually serve as transdermal patches with biological functionalities.

Fiber alignment and compound encapsulation are two ways to functionalize the electrospun fiber mat. Fiber alignment means that the majority of polymer fibers are collected in uniaxial direction. Two collecting techniques including gap technique (*151, 331-332*) and rotational object technique (*94, 164, 333-336*) have been proven to generate highly-aligned fibers. Compared with randomly-orientated fibers, fibers with specific alignment are able to mimic the extracellular matrix (ECM) architecture (*337*), provide high surface-to-volume ratio for cell attachment (*338*), and significantly enhance skin cell migration (*339*). Hence, the highly-aligned fibrous mat will endow transdermal patches with better affinity to human skin.

On the other hand, compound encapsulation greatly expands the functional possibility of fibrous mats. High porosity and high surface-to-volume ratio facilitate the encapsulation and release of the functional component. Various functional components such as nutraceuticals (*146, 340-341*), drugs (*330, 342-344*), proteins (*345-346*), enzymes (*347*),

and DNA (*348*) have been demonstrated to be loaded into electrospun fibers. Those as-spun fibers serve as multifunctional platforms to maintain the bioactivity of human β-nerve growth factor (NGF) (*345*), maximize the enzymatic activity of immobilized α-chymotrypsin in aqueous and organic media (*347*), stimulate cellular transfection and eventually encode the protein β-galactosidase by sustainable release of DNA (*348*), and even combine biochemical, topographical superiorities for tissue regeneration (*153-154*). The multiple advantages brought by fiber alignment and compound encapsulation pave the way for the fabrication of functional fibrous devices.

In this chapter, we aim at making full use of agro-waste material and combine it with electrospinning to fabricate porous fibril material for supporting transdermal patches. The major material used was zein, a storage protein extracted from corn kernels. Not only being widely available in nature, zein is but also among a few electrospinnable biopolymers which offer strong processing capability and economic superiority. So far, several trials have been made to process zein electrospun fibers and compound-loaded zein fibers (*340, 349-352*). However, the multi-functionality exploration for zein fibrous material has been scarcely reported preciously. We try to demonstrate the feasibility of both nutraceutical encapsulation and fiber alignment for zein-based electrospun fibers. Such exploration will largely expand the potential applications of zein-based fibrous material for functional transdermal patch.

Dual functionalities, which include nutraceutical encapsulation and controllable alignment, were tested in zein fibrous mats. For nutraceutical encapsulation, curcumin, a multi-functional phytochemical (*240, 353-355*), was utilized to be loaded into the zein fibrous mat. The experimental loading of curcumin in zein fibrous mats gives the answer

of “how much curcumin we can precisely put in each fibrous mat”. For controllable alignment, a home-made wired drum collector is leveraged for achieving highly-aligned zein fibers. The progress of this research will benefit the biomaterial innovation and health care eventually.

6.2 Experimental

6.2.1 Materials

Zein and poly(ε-caprolactone) (PCL, M_n=80 kD_a) were purchased from Sigma-Aldrich. Curcumin (85% pure, with 11% of demethoxycurcumin and 4% of bisdemethoxycurcumin as impurities) was a gift from Sabinsa Corporation (Piscataway, NJ) and used without further purification. Solvents including N,N-dimethylformamide (DMF) and tetrahydrofuran (THF) (anhydrous, ≥99.9%) were also purchased from Sigma-Alrich.

6.2.2 Solution preparation and characterization

For randomly-oriented fibers, zein and curcumin were dissolved in DMF at concentrations of 40 w/v% to 55 w/v% for zein and 0.1 w/v% to 7 w/v% for curcumin. For aligned fibers, both zein and poly(caprolactone) were dissolved in DMF/THF (1:1, v/v) solvent at 10 w/v%. Afterwards, those two stock solutions were mixed together to form zein/poly(caprolactone) (3:7, v/v) mixed solution in the same solvent. Since zein solutions can have an aging effect (*356*), the zein and zein-curcumin solutions were subject to electrospinning process right after full dissolution.

The viscosity measurements were performed by using a strain-controlled ARES Rheometer (TA Instruments, New Castle, DE). The apparent viscosities (η) of zein and zein-curcumin solutions were determined in static mode with a fixture of cone and plate

(diameter 50 mm, 0.04 rad). The zero shear viscosity (η0), the viscosity at vanishing shear rate was determined by extrapolating the Newtonian plateau to zero shear rate.

6.2.3 Electrospinning of zein fiber

A home-made electrospinning facility was used to generate randomly-oriented and aligned zein-based fibers. Schematic diagram 6.1 displays the construction of this single fluid electrospinning facility which is composed of a syringe pump (New Era Pump Systems Inc., NY, USA), a high voltage supply (0~30 kV), and a grounded collector. Two fiber collectors, aluminum foil and home-made copper wire-framed drum (Figure S1), were utilized to collect randomly-oriented fibers and aligned fibers, respectively. The wired drum collector is composed of two circular non-conducting disks 9.5 cm in diameter with notches placed 4 cm apart around the circumference and a 1.2 cm diameter hole cut in the center, one metal rod mounting two disks at the ends, and copper wires stretched between the slots on the edge of the disks.

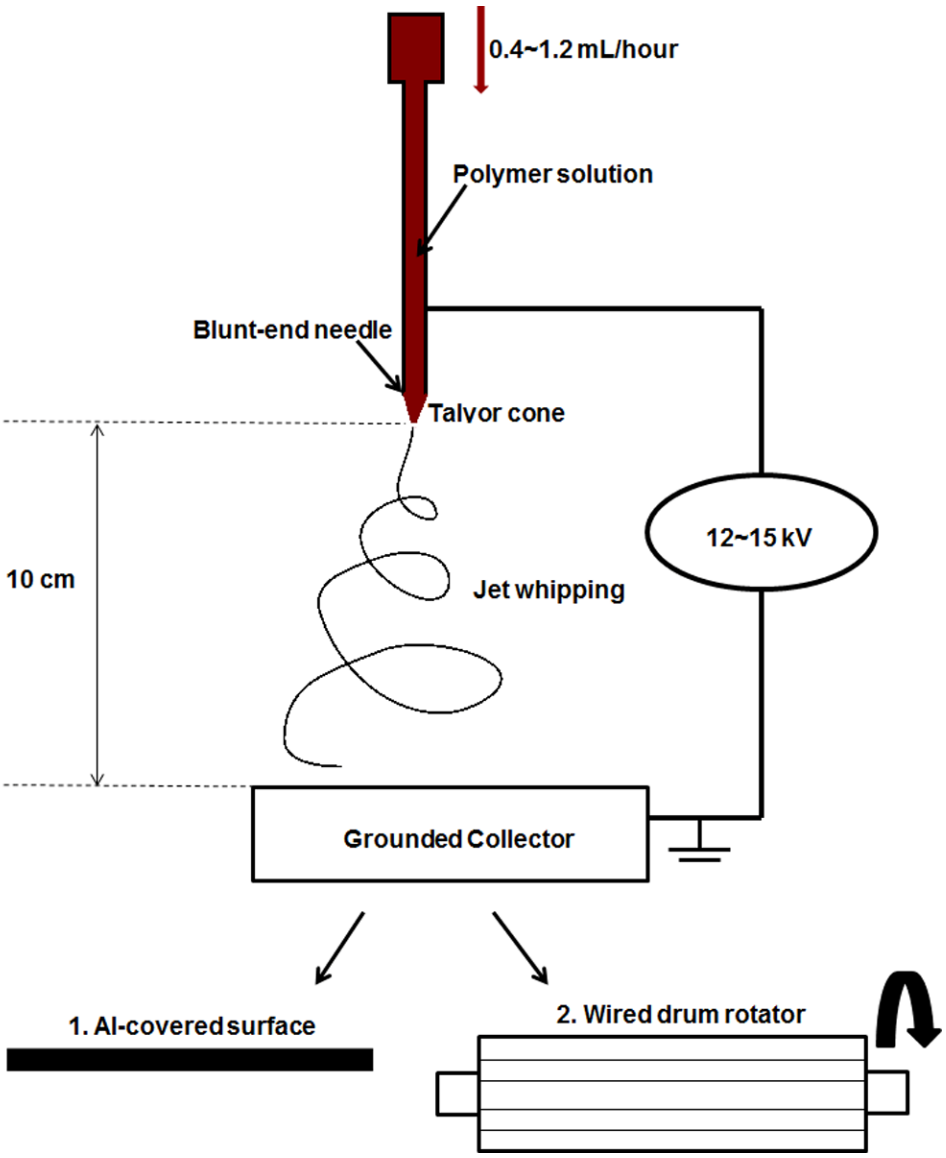

Schematic diagram 6.1: Electrospinning facility equipped with the fiber collectors of aluminum foil and wired drum rotator.

During electrospinning, a 3 mL plastic syringe filled with biopolymer solution was mounted onto the syringe pump. A positive electrode was clamped onto the blunt-end syringe tip (O.D. 0.7 mm), while the fiber collectors were grounded. The processing parameters of electrospinning were set at 12 to 15 kV for voltage, 10 cm for tip-to-collector distance, and 0.4 to 1.2 mL/hour for feeding rate.

6.2.4 Curcumin loading determination

The experimental loadings of curcumin in zein fibrous mats were determined by UV-Vis measurement. Basically, certain quantities (0.01 g to 0.04 g) of curcumin-loaded zein mats were dissolved in 10 mL of acetone. After 3-day release of curcumin from zein mat under vortex, the concentration of curcumin in acetone was quantified by monitoring the UV absorbance at wavelength 419 nm. The molar absorptivity of curcumin at wavelength 419 nm in acetone was measured prior to loading quantification.

6.2.5 Surface morphology

The fluorescence micrographs were recorded with a Nikon TE-2000-U inverted fluorescence microscope equipped with a CCD camera (Retiga EXi, Q-Imaging). Images were taken both under bright field and at the same region under a blue bandpass filter to observe the fluorescence signals emitting from curcumin compound (excitation: 488±10 nm and emission: 520±30 nm). All images were processed by C-Imaging software (SimplePCI, Compix Inc.).

To magnify the observation, surface morphologies of curcumin-loaded or unloaded zein electrospun fibers were also collected by a commercial Nanoscope IIIa Multimode AFM (Veeco Instruments, CA) equipped with a J scanner, which was operated in tapping mode using a phosphorus (n) doped silicon cantilever. Height images, phase images, and amplitude images were collected simultaneously by using a set point ratio of ~0.9 for measurements at room temperature. All the images were subjected to post-processes of first-order plane-fitting and flattening. At least 10 local spots on each sample were imaged with the scanning sizes of 50 μm× 50 μm. Thus, the AFM results can represent the overall surface morphology.

The degree of alignment was quantified by analyzing the TP-AFM height images of aligned fibers with Image J software installed with the Oval Profile plug-in. First, fast Fourier transform (FFT) was performed on the AFM height images, which converted the real space images to the reciprocal patterns, known as the scattering pattern. Then, radial sum mode in the Oval Profile plug-in of Image J was applied to those FFT output images. Oval Profile was then used to sum the pixel intensities along a circle for each one-degree sector, resulting in a graph of pixel intensities across 360^{o}. Afterwards, the plots of pixel intensity versus degree of angle were generated, which corresponded to the FFT output images. The baseline of the plot was also corrected. For further evaluation, only 180^{o} (0^{o} to 180^{o}) were necessary because the scattering pattern from FFT was always point symmetric). A similar process was systematically described in the previous literature (*152*).

6.2.6 In vitro cytotoxicity

Human hepatocellular carcinoma cell line HepG2 was obtained from American Type Culture Collection (HB-8065, Manassas, VA) and were cultured in minimum essential medium (Invitrogen, Carlsbad, CA) containing 10% foetal bovine serum (Invitrogen, Carlsbad, CA), 100 units/mL penicillin (Invitrogen, Carlsbad, CA) and 100 μg/mL streptomycin (Invitrogen, Carlsbad, CA). Cells were maintained in incubators at 37 ^{o}C under 95% relative humidity and 5% CO_2.

Zein and curcumin-zein fiber mats were disinfected at 40 ^{o}C environment. For fiber mats, the wells in each plate were divided into groups for corresponding samples. The first group was blank zein fiber group (6 wells for each), only 0.1 mg zein fiber mat and 20 μL of PBS (pH 7.4) were added. The second group was curcumin-loaded zein fiber groups (6

wells for each curcumin content), about 0.1 mg curcumin-zein fiber mat and 20 μL of PBS (pH 7.4) were added to each well. The curcumin contents of the zein fiber mats were obtained from UV-Vis measurement. For cell culture, HepG2 cells were seeded in 96-well microtiter plates at a density of 10,000 cells per well in a final volume of 100 μL medium. After 24 h, the cells were treated with a medium containing zein fiber mats or curcumin-zein fiber mats. After a certain period of time (6, 12, 24, 48, and 72 hour), cell culture media were aspirated and cells were incubated with 100 μL MTT solution (0.5 mg/mL in RPMI 1640 medium) for 2 h at 37 ^{o}C. Subsequently, MTT solution was carefully aspirated and the formazan crystals formed were dissolved in 100 μL DMSO per well. Light absorbance at 560 nm and 670 nm was recorded with Absorbance Microplate Reader (Molecular Devices, Sunnyvale, CA). Relative cell viability was expressed as A560–A670 normalized to that of the untreated wells. Data is presented as mean ± standard deviation with eight-well repeats.

6.3 Results and discussion

6.3.1 Solution characterization

Solution viscosity is of priority and can be regarded as a prerequisite for fiber formation, because the viscosity of polymer solution can affect polymer entanglement and further fiber formation. Figure 6.1 displays the apparent viscosities of zein and zein-curcumin in DMF at concentrations from 40 w/v% to 55 w/v%. At low concentrations (40 w/v% and 45 w/v%), the apparent viscosities of zein and zein-curcumin solutions were below 1 Pa*S. As zein concentration surpassed 50 w/v%, the solution viscosity became beyond 1 Pa*S. As reported previously (*350*), this viscosity may serve as a critical value for fiber formation, below or above which the morphology of electrospun fibers has a dramatic

difference. In addition, adding 0.5 w/v% curcumin into zein solution lead to the viscosity increase which suggests that there maybe exist interactions between curcumin and zein. And the interaction between curcumin and zein will be discussed in detail in the latter section.

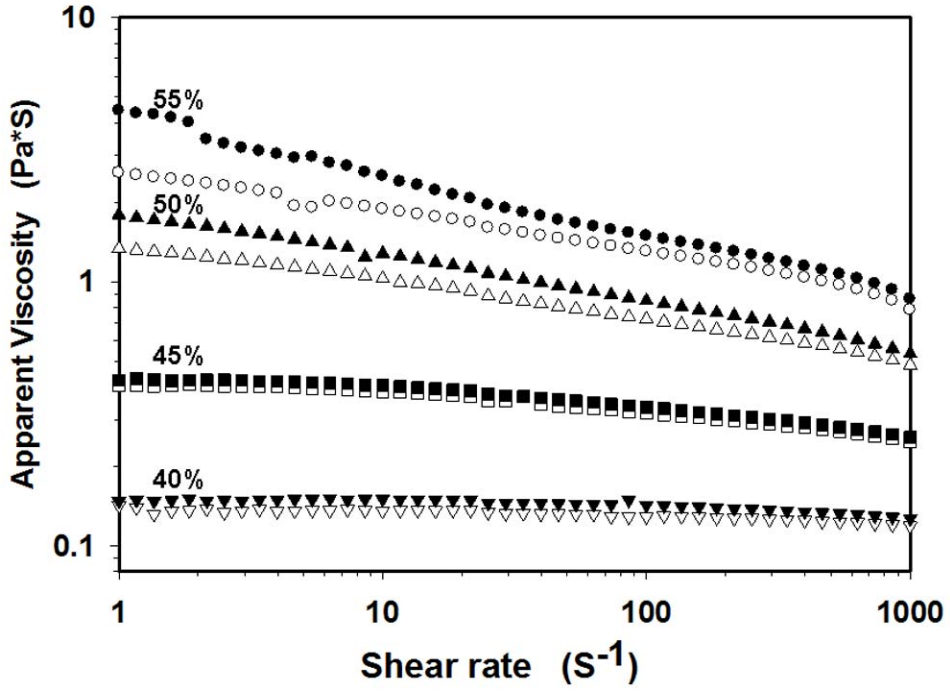

Figure 6.1: Apparent viscosity of zein fluids and curcumin-zein complex fluids under concentrations from 40 w/v% to 55 w/v%. The curves of unfilled symbols represent pure zein solutions at different concentrations. The curves of solid symbols represent zein solutions with the addition of 5 w/v% curcumin.

6.3.2 Curcumin distribution and loading

Fluorescence imaging is utilized to observe the curcumin distribution in the zein electrospun matrixes. The fluorescence emission comes from the curcumin compound which has intrinsic fluorescence properties (*357*). Figure 6.2 displays the fluorescence images (10×) of curcumin-zein matrixes deposited on the glass slides. At a first glance, curcumin were homogeneously distributed in all the zein fiber samples. Then, concentration-dependent morphology was clearly observed. At the lowest zein

concentration (40 w/v%), only curcumin-loaded beads formed. In other words, zein formed micro-sized beads to encapsulate curcumin at 40 w/v%. From FFT, no specific orientation and only spherical halo was observed. As zein concentration reached 50%, the thin zein fibers came out to connect zein beads which scattered around. Its FFT image displayed less halos but increased amount of white lines scattering in almost all directions. At even higher concentrations (50 w/v% and 55 w/v%), curcumin-loaded zein fibers were clearly observed. Random orientation with no circular halo was shown in the FFT images. This group of fluorescence images positively verifies the successful encapsulation of curcumin in zein fibers.

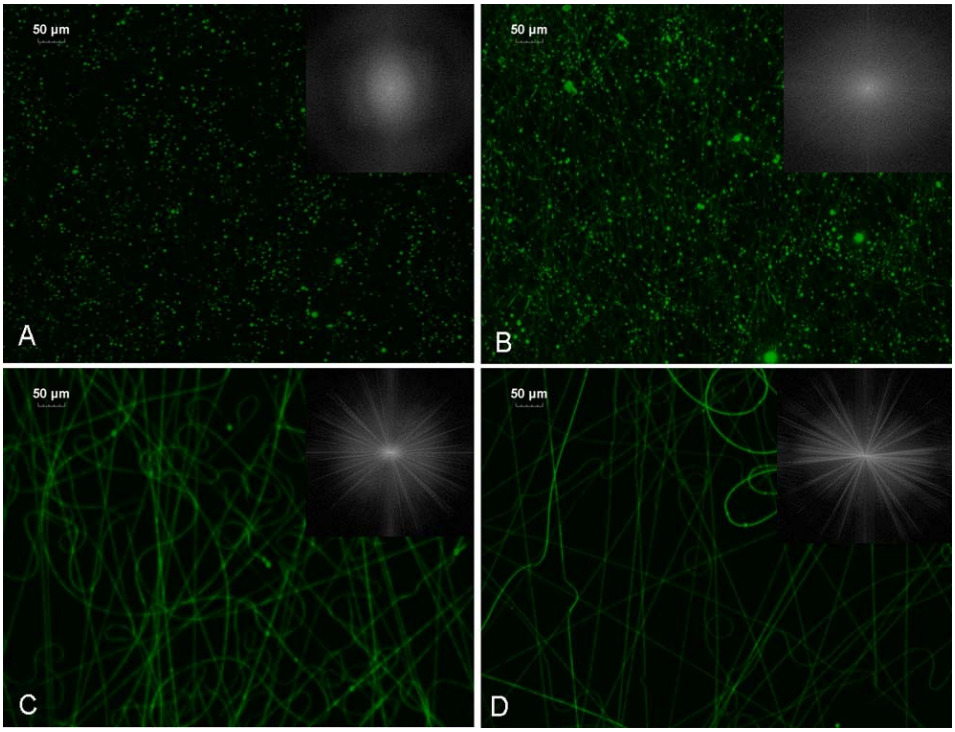

Figure 6.2: Fluorescence images (10×) of curcumin-loaded zein fibers electrospun under solution concentrations from 40 w/v% to 55 w/v%. The insets are the fast Fourier transform (FFT) output images of the fluorescence images.

To precisely quantify the curcumin loading in zein fibrous mats, UV-Vis measurement has been adopted. The definition of curcumin loading in zein fibrous mat here is the mass

of curcumin per mass of curcumin-loaded zein fiber mat. Figure 6.3 exhibits the quantification of curcumin loading in zein fibrous mats. In addition to the loading curves, we also present the photos of curcumin-loaded zein mats (first row) and the fluorescence images (10×) of upper layers of curcumin-loaded zein fibers (second row). From those photos, a gradual yellowish increase in appearance was observed when more curcumin was added into zein mat. For fluorescence imaging, the same exposure time were used for all curcumin-loaded zein fiber samples. Thus, we excluded the impact of light source upon observation, and the major difference lies in curcumin quantity. At low curcumin loadings (Sample A-C), majority of curcumin were homogeneously distributed along the fibers. As curcumin loading increased (Sample D-F), more curcumin was entrapped in the inter-spatial regions among fibers.

Underneath the photos and fluorescence images, we present the curcumin loading curves (Figure 6.3). Zein solution of 50 w/v% was spun into bead-free fibers, and hence we fixed that concentration for the fabrication of curcumin-loaded zein fibrous mats. The theoretical loadings of curcumin-loaded zein fibrous mats were calculated based on the initial [curcumin]/[zein] mass ratios, while the experimental loadings were determined from UV-Vis measurement. Within the current range of initial [curcumin]/[zein] mass ratios, we could maximize the curcumin loading to 12%. And the experimental loadings differed more pronouncedly from the theoretical loadings as the initial [curcumin]/[zein] mass ratio increased. This phenomenon is due to the impact of curcumin on the stability of the zein jet. As the zein jet becomes less stable due to the charge difference between curcumin and zein, only partial portion of curcumin-zein mixtures formed fibers. The deviation between theoretical and experimental loadings was also found in the protein-

polymer electrospun fibrous mat (*345*). When the initial [curcumin]/[zein] mass ratio reached 0.2, the curcumin yield in the fiber mat turned out to be 73%.

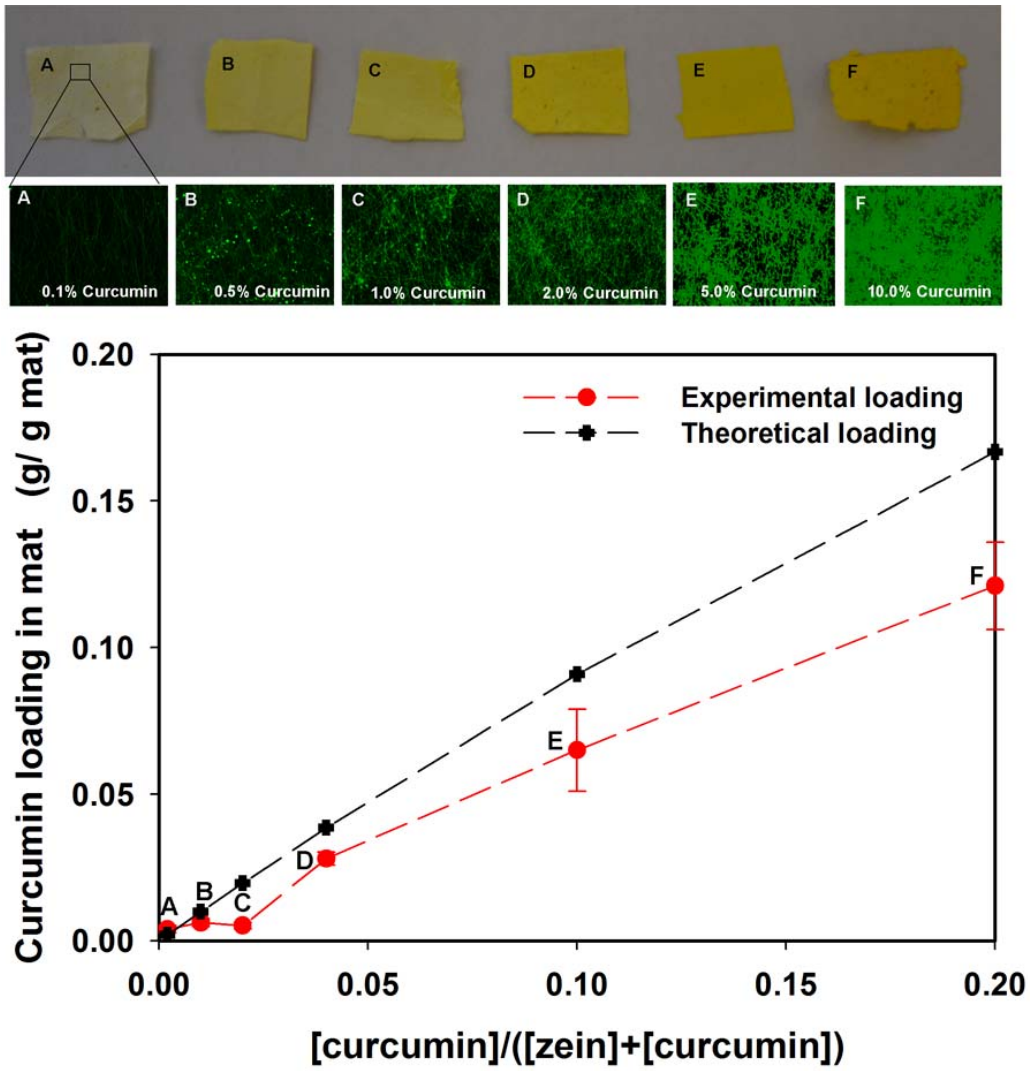

Figure 6.3: Curcumin loadings in zein fiber mats electrospun at 50 w/v%. The plot of curcumin loading in zein mat as a function of initial [curcumin]/[zein] mass ratio. The insets are the corresponding photos (first row) and fluorescence images (second row) of zein mats loaded with different quantities of curcumin.

6.3.3 Morphology of electrospun mat

For local morphology at a size of 50 μm× 50 μm, atomic force microscopy in tapping mode was utilized for imaging curcumin-loaded/unloaded zein fibers. Figure 6.4(A, C, F)

displays the surface morphologies of zein fibers electrospun at different concentrations. The zein fiber displayed a concentration-dependent behavior, which was commonly observed in fibers electrospun from synthetic or natural polymers like polyvinyl alcohol (*97, 358*) and dextran (*359*). Within the range of experimental concentrations, we observed a bead-to-fiber transition (*98*). At 40 w/v%, only irregularly-shaped beads formed while very thin fibers could be ambiguously observed between beads (Figure 6.4A). This was because most zein molecules contribute to the formation of beads rather than that of fibers at 40 w/v%. As concentration increased to 50 w/v%, thicker and beadless fibers occurred (Figure 6.4C). Continuous increase of zein concentration to 55 w/v% resulted in even thicker fibers (Figure 6.4F). Figure 6.4(D, G) shows the 0.5 w/v% curcumin-loaded zein fibers. It is clear that adding 0.5 w/v% curcumin in zein solution does not affect the overall shape of fibers. Different from neat zein fibers (Figure 6.4C and 6.4F), curcumin-loaded zein fibers were thinner (Figure 6.4D and Figure 6.4G) and occasionally with spindle-shaped beads along fibers (Figure 6.4D).

Section analysis embedded in the software Nanoscope 5.3 was utilized to calculate the fiber thickness (*218*). Since the tip itself occupies a width on the horizontal perspective, vertical distance between the bottom baseline and upper edge of individual fiber was determined to be the fiber thickness. Figure 6.4(B, E, H) show the fiber thickness distributions of curcumin-unloaded/loaded zein fibers electrospun at concentrations from 40 w/v% to 55 w/v%. At 40 w/v%, the distribution of fiber thickness ranged from 5 nm to 85 nm (Figure 6.4B), and the average fiber thickness was 37 nm. The formation of thin fibers was because large portion of zein contributed to the formation of beads. Thus, the quantity of zein molecules for fiber formation was very limited. As zein concentration

reached 50 w/v%, the averaged fiber thickness and size distribution increased to 187 nm and 90 nm to 330 nm, respectively (Figure 6.4E). Further increase of zein concentration to 55 w/v% resulted in even larger values of averaged fiber thickness and size distribution, 410 nm and 270 nm to 700 nm, respectively (Figure 6.4H). When 0.5 w/v% curcumin was added into zein, the fiber thickness distribution shifted to 30 nm to 300 nm for 50 w/v% and 150 nm to 360 nm for 55 w/v%. Besides, the average fiber thickness was lowered to 118 nm for 50 w/v% and 272 nm for 55 w/v%, respectively. The fiber thinning caused by curcumin was probably due to the interaction between zein and curcumin which affects the zein molecular entanglement and further undermines the fiber formation.

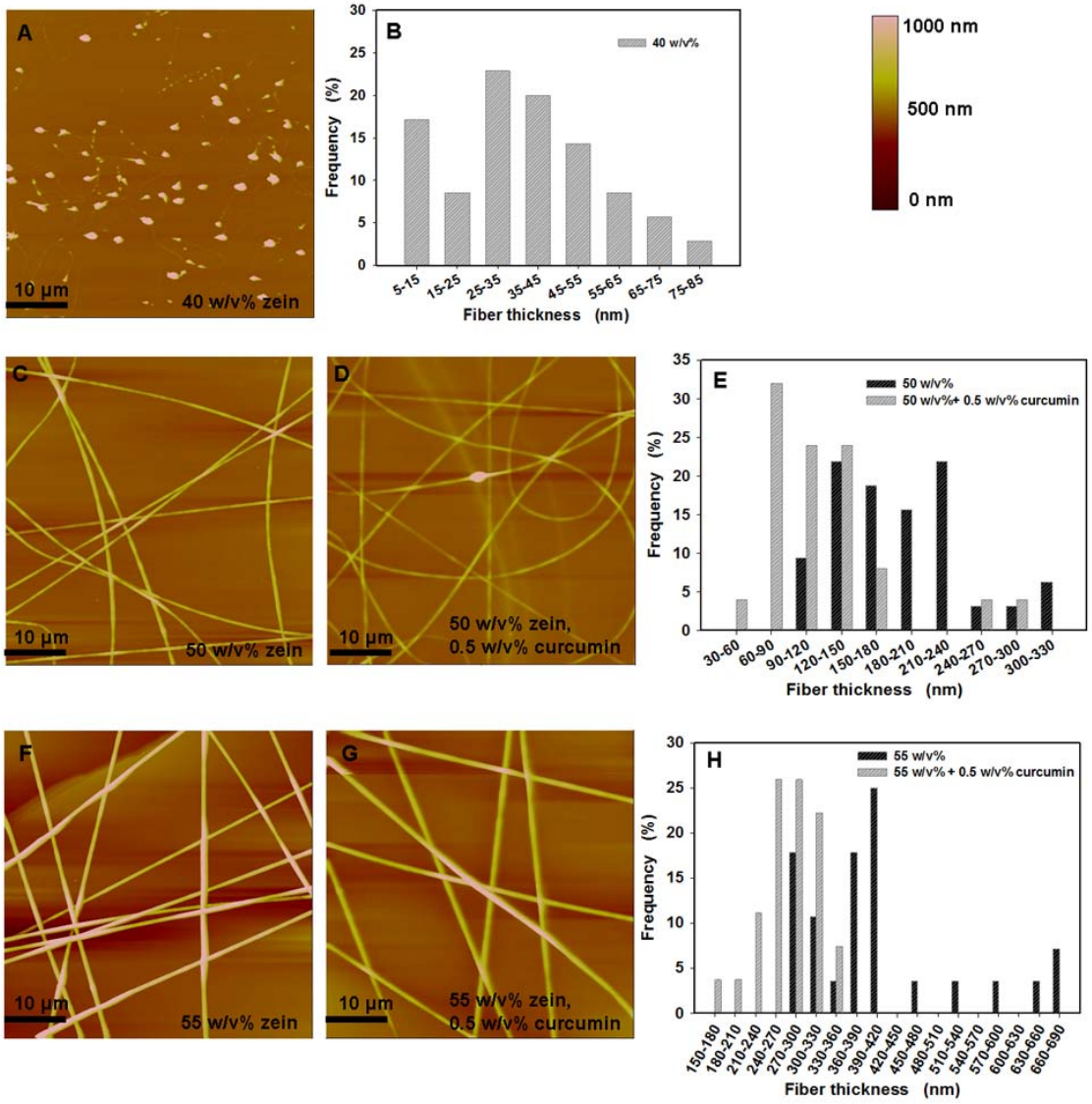

Figure 6.4: Tapping mode AFM height images of (A), (C), (F) zein fibers and (D), (G) curcumin-loaded zein fibers electrospun at concentrations from 40 w/v% to 55 w/v%; Fiber thickness distribution of (B) zein fibers electrospun at 40 w/v%, (E) curcumin-loaded/unloaded zein fibers electrospun at 50 w/v%, and (H) curcumin-loaded/unloaded zein fibers electrospun at 55 w/v%.

6.3.4 Fiber alignment

For fiber alignment, poly(caprolactone) (PCL, M_n=80 kD_a) was blended with zein to enhance the material flexibility which is important in the fiber alignment. We make use of drum rotation to control the degree of fiber alignment. Figure 6.5(A-D) display the TP-AFM height images of zein/PCL electrospun fibers collected at rotational rates from 0

RPM to 850 RPM. If the drum was kept static without motion, the formed fibers showed no difference with those collected on the aluminum foil (Figure 6.5A). Those fibers were thick and distributed in a dense pattern. When wired drum rotated at low rate (130 RPM), the fibers still displayed morphology without any specific orientation (Figure 6.5B). Meanwhile, fiber loops were observed due to the bending instability during electrospinning. When the rotational rate increased to 580 RPM, two major directions of fiber alignments were found, indicating a certain degree of fiber alignment (Figure 6.5C). Once rotational rate reached 850 RPM, high degree of fiber alignment was achieved, shown in Figure 6.5D.

After collecting TP-AFM images, we performed fast Fourier transform (FFT) analysis of those images to quantify the fiber alignment. The FFT output images corresponding to the AFM images are shown in Figure 6.5(E-H). As rotational rate increased, the white lines scattered in a narrower range of angles. Compared with the fibers electrospun at 0 RPM (Figure 6.5E), the fibers electrospun at 850 RPM displayed a more specifically-oriented scattering pattern (Figure 6.5H). To get a clearer quantification of fiber alignment, the radial summation of FFT output images was conducted. The plots of pixel intensity versus degree of angle are shown in Figure 6.5(I-L). According to the literature (*152*), the degree of fiber alignment can be reported by the height, shape, and the distribution of the peaks generated by FFT analysis (Figure 6.5E-H). Broader distribution of the peaks from FFT analysis means less degree of fiber alignment for the mats. For an individual peak, the sharper the peak, the more accurately the fibers are aligned uniaxially. At 0 RPM, there was a total of 11 peaks distributed along the angle range of 0^o to 180^o, indicating a random orientation of fibers (Figure 6.5I). As the drum rotational

rate increased, the peak number decreased to 8 at 130 RPM (Figure 6.5J), 5 at 580 RPM (Figure 6.5K), and 1 at 850 RPM (Figure 6.5L). This observation illustrated that increasing rotational rate promoted the degree of fiber alignment. At the highest rotational rate (850 RPM), only one sharp peak was centered at 180°, indicating an occurrence of highly aligned fibers.

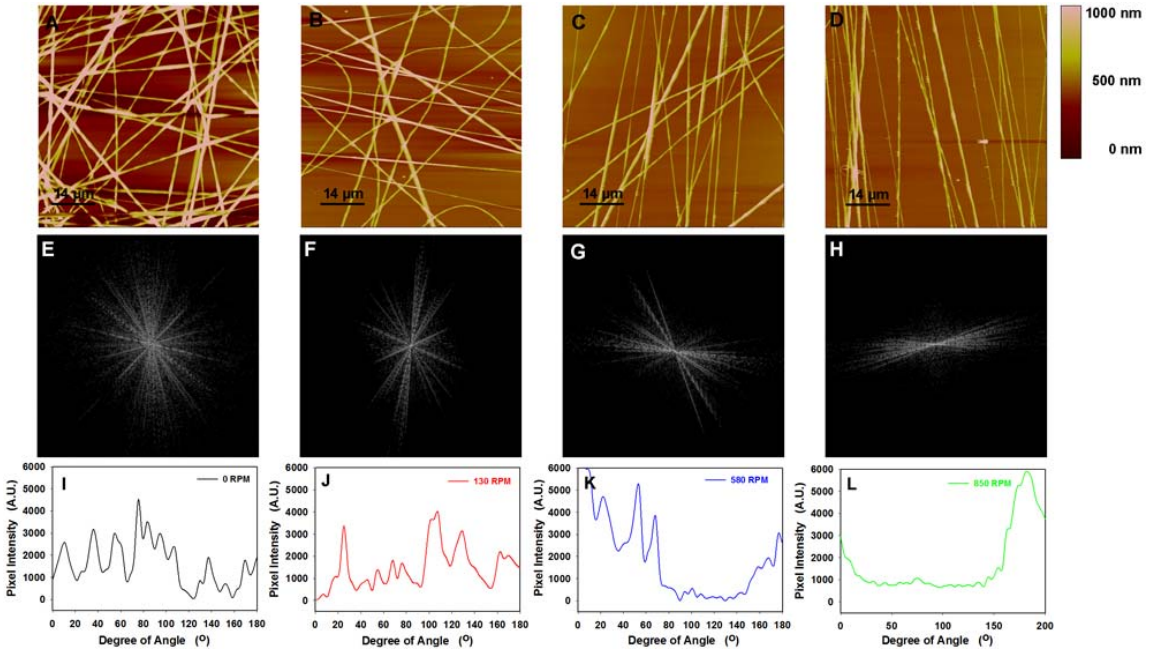

Figure 6.5: Tapping mode AFM images of zein/poly(caprolactone) (3:7 w/w) aligned fibers deposited by wired drum rotator operated at rotational rate of (A) 0 RPM, (B) 130 RPM, (C) 580 RPM, and (D) 850 RPM; Corresponding fast Fourier transform (FFT) output images (E~H); And normalized pixel intensity versus degree of angle plots (I~L). Note that the peaks generated by radial summation in the oval profile plug-in of Image-J containing information of fiber alignment.

6.3.5 *In vitro* anti-cancer activity

The cancer cell responses of zein fiber mats with different curcumin loadings are displayed in Figure 6.6. Blank fiber mats (circle) did not exhibit any cytotoxicity to the HepG2 cells up to 72 hours. By contrast, all the curcumin-loaded zein fiber mats show a polynomial decay of cell viability with cell culture time. The inverse second order polynomial ($y = y_0 + \frac{a}{x} + \frac{b}{x^2}$) was used to fit the cell response curves of curcumin-loaded

zein fiber mats. For instance, the cell viability of 12% curcumin-loaded zein fiber mats followed a sharp decay within the initial 12 hours, while cell viability decay of 2.8% curcumin-loaded zein fiber mats (triangle) was much more flattened. Besides, in the cases of 2.8% (triangle), 6.5% (inversed triangle), and 12% (star) curcumin loaded-zein fiber mats, cell growth inhibition percentages of 90.7%, 96.3%, and 96.8% were achieved after 72 h incubation, respectively. Compared with the zein fiber mat of low curcumin loading (2.8%), the zein fiber mats of high curcumin loadings (6.5% and 12%) have a quicker lethal effect to cancer cells. The release of curcumin from zein fiber matrix is facilitated by the porous structure, and eventually curcumin-zein fiber mats display a curcumin loading-dependent anti-cancer activity towards cancer cells.

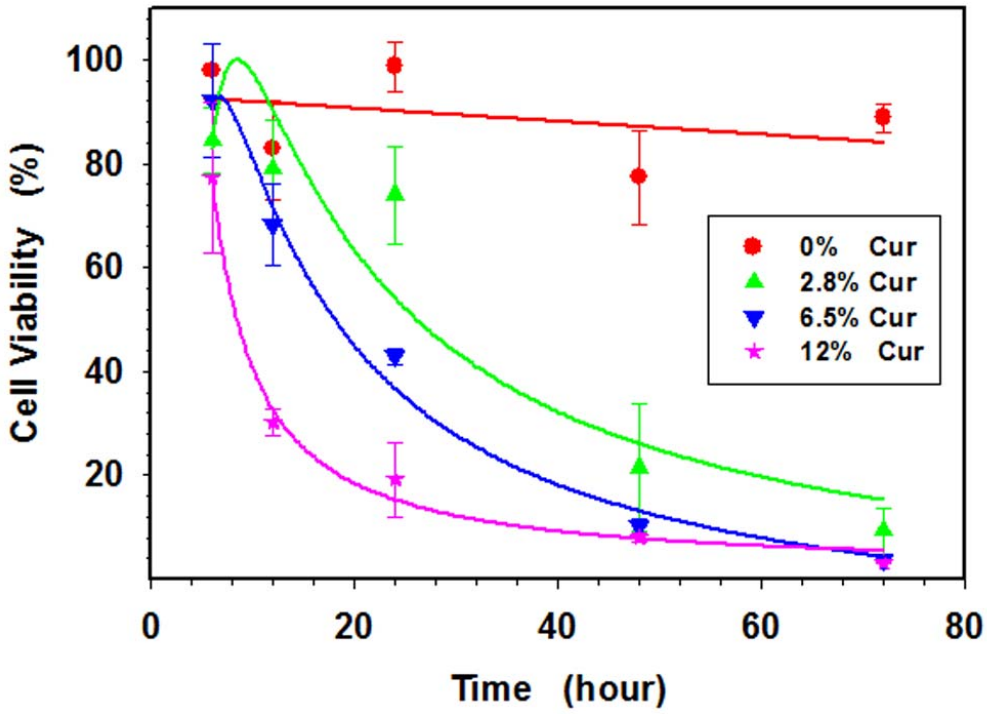

Figure 6.6: Cytotoxicity of the blank zein and curcumin-loaded zein fiber mats to the HepG2 cells. Curcumin content in the fibers with respect to zein: 0% (pure zein), 2.8%, 6.5%, and 12%.

6.3.6 Impact of curcumin on zein solution an fiber

In rheological measurement, we observed an apparent viscosity increase after adding 0.5 w/v% curcumin into zein solutions, which was likely due to the interaction between zein and curcumin. Since zein is majorly composed of hydrophobic residues (i.e. proline) (*277*) and the solvent DMF serves as hydrogen bond acceptor (HBA) (*360*) with the highest HBA basicity among most common organic solvent (~0.71) (*361-362*), it is reasonably speculated that the hydrophobic interaction dominates the binding between zein and curcumin in DMF. Besides, we found that the viscosity increase induced by curcumin occurred more significantly at higher zein concentration, especially at 55 w/v% (Figure 6.1). A more pronounced viscosity enhancement at high zein concentration is due to different binding profiles. At low protein concentration (40 w/v%), curcumin binds to

zein through the limited amount of binding sites. As the concentration increases to high values (55 w/v%), more binding sites of protein become available for curcumin. Under such circumstance, curcumin acts as a multidentate ligand and bridge zein molecules or zein/curcumin complexes. Thus, zein dimmers, trimmers or multi-mers are likely to form from the linkage of several curcumin-enriched zein. Because of curcumin's bridging, the molecular network within zein solution becomes denser and interrelated, which results in the higher viscosity.

In fiber formation, when curcumin is added into zein, curcumin does not affect the fiber formation (Figure 4D, 4G). Our finding is similar to curcumin-loaded poly(ε-caprolactone)-poly(ethylene glycol)-poly(ε-caprolactone) fibrous mat and curcumin-loaded cellulose acetate fibrous mat (*146, 363*). Meanwhile, compared with the neat zein fibers, curcumin-loaded zein fibers display a fiber thinning behavior. After adding 0.5 w/v% curcumin, the size distribution of zein fibers electrospun from 50 w/v% zein shifted from 90 nm-330 nm to 30 nm-300 nm, while the fibers from 55 w/v% zein even switched from 270 nm-690 nm to 150 nm-360 nm. The maintenance of fiber morphology lies in the molecular interaction between zein and curcumin, especially hydrophobic interaction. Thus, the interaction between zein and curcumin influences the zein-zein interaction or zein molecule entanglement, which further results in the phenomenon of fiber thinning.

6.3.7 Mechanism of Fiber Alignment by Drum Rotator

Although zein is an electrospinnable biopolymer, its natural brittleness is still a concern for mechanical processing. Therefore, we blend polycaprolactone (PCL, M_n=80 kD_a) with zein to enhance its flexibility during electrospinning process. We investigated the impact

of drum rotational rate on fiber alignment by using zein/PCL blend fibers. We found that the variation of rotational rate resulted in different fiber alignments. The driving force of fiber alignment lies in the stretching and pulling force exerted by the rotational drum.

To clearly state the mechanism, we define two parameters here, including fiber production velocity (v_f) and collector surface velocity (v_c). The fiber production velocity (v_f) is the speed of fiber electrospun from zein solution, which is quantified by the equation 6.1 $v_f=10000Q/(36\pi r_j^2)$ (m/s), where Q is the feeding rate of polymer solution (mL/hour), and r_j is the radius of polymer jet (μm). The terminal radius of the polymer jet is estimated based upon the equation 6.2 $\log(2r_j)=0.639\times\log(Q/I)-3.904$, where Q/I is the inverse of volume charge density (*364*). I/Q, volume charge density, is in the range of 100 C/m^3 to 150 C/m^3 by using the established relationship between I/Q and flow rate of poly(caprolactone) solution (*364*). On the other hand, the collector surface velocity (v_c) is the speed rate on the surface of the rotational drum which is calculated by the equation 6.3 $v_c=RPM\times\pi\times D_c/6000$ (m/s), where RPM is directly read by tachometer and D_c is the cross-section diameter of the drum rotator (cm). The v_c/v_f is used to illustrate the fiber alignment under different rotational rates. When v_c/v_f is 0, the wired drum stays stationary. Under such circumstance, the driving force for fiber alignment provided by the gap between copper wires is very limited. The fiber deposition of wired drum is similar to that of aluminum foil. As v_c/v_f becomes >0, drum starts rotation at low rate which exerts a pulling force on fibers which is too low to stretch and pull electrospun fibers in uniaxial direction. As v_c/v_f gradually increases (>0.5), fiber straightening is expected to start. Partial fibers align well in uniaxial direction, however, a large quantity of the fibers on the upmost surface are still in a multi-aligned pattern. This is due to the

strong electrostatic interaction between deposited fibers and undeposited fibers. When an undeposited fiber comes close to the fiber on the collector, the electrostatic repulsion between them will influence its conformation after deposition. As collecting period goes, more charged fibers are accumulated on the collector which results in a broad distribution of positive charges on the collector surface. Thus, it is more difficult to continuously maintain the coming fibers to align in uniaxial direction. The loss of fiber alignment for thick fiber mats after long time collection (i.e. 2.5 h) has also been reported previously (*94*). When v_c/v_f is close to 1, the fibers become straight and well-done alignment of fibers can be observed. However, some reported that too speedy rotation resulted in the fiber break (*365*). Kiselev et al. also stated that the best alignment of electrospun fibers occurred when the speed of rotational object matched that of fiber production (*365*). Others suggested the existence of an optimized rotational rate for fiber alignment (*335*). In our experiment, the drum rotation condition for the highest fiber alignment is still within the limit of fiber stretching, and the rotation rate at 850 RPM which allows v_c/v_f close to 1 is the optimized rate.

In addition to rotational stretching, the gaps between copper wires play a partial role in fiber stretching and alignment. As early reported by Li et al. (*151*), two sets of electrostatic forces occur during fiber deposition on the gap between two conductive electrodes. The first set of electrostatic force followed the direction of the electric field and stretched the fiber towards two electrodes. The second set of force occurred between the un-deposited fibers and two electrodes. According to the Coulomb law ($F \sim r^{-2}$), the strongest interaction between charged fibers and two electrodes occurred at the ends of the fibers which are closest to the electrodes. It is also worth noting that the stretching

force of drum rotation at high rate (850 RPM) is much stronger than electrostatic pulling force between un-deposited fibers and two electrodes. Hence, the alignment of zein/PCL electrospun fibers is dominated by the mechanical stretching of drum rotation.

The fiber stretching can be evidenced by the phenomenon of fiber thinning. Figure 6.7 shows the fiber thickness (D) and root-mean-square (RMS) roughness of fibers as a function of v_c/v_f ratio. The fiber thickness and RMS roughness were quantified by the section analysis and roughness analysis embedded in the software Nanoscope 5.30, respectively. We observed a plateau of fiber thickness at low v_c/v_f ratios, which indicated that low rotational rate provides insufficient force to stretch and elongate fibers. Once v_c/v_f reached ~0.1, a power-law decay of fiber thickness dependent on v_c/v_f was clearly observed, which was termed "fiber thinning". The inset AFM height images further verified this phenomenon. Also, the experimental fiber thickness obeys a rule of $D\sim(v_f/v_c)^{0.48}$. As comparison, the theoretic prediction of fiber thickness based upon the mass balance is shown in the equation 6.4 $D = 2\sqrt{\frac{Av_f C\rho_{sol}}{\pi v_c \rho_f}}$ (*365*), where A is the cross-sectional area of the needle, v_f is the fiber production velocity, v_c is the collector surface velocity, C the polymer weight fraction in the solution, ρ_{sol} is the solution density, and ρ_f is the density of the dry fiber. Clearly, the experimental fiber thickness rule of $D\sim v_f/v_c^{0.48}$ is in consistence with the theoretical prediction. In addition, the RMS roughness of fiber surface displays a similar trend as fiber thickness, which is composed of plateau region and inversed polynomial region as well. The decrease of the overall surface roughness is related to the shrinkage of fiber thickness.

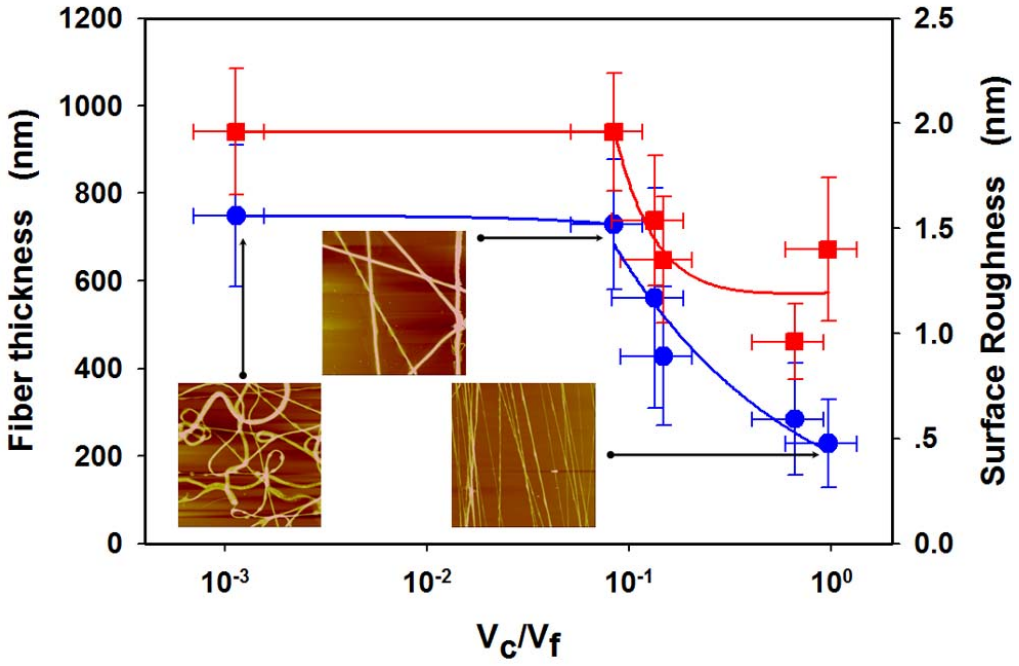

Figure 6.7: Fiber thickness (solid circle) and root-mean-square (RMS) roughness (solid square) of zein/poly(caprolactone) (3:7 w/w) aligned fibers as a function of v_c/v_f ratio. The insets are representative 50 μm×50 μm AFM height images of zein/PCL fibers electrospun at different v_c/v_f. The plot of fiber thickness~v_c/v_f is fitted by power-law equation $y=bx^a$, and the plot of RMS roughness~v_c/v_f is fitted by inverse second order polynomial equation: $y = a + \frac{b}{x} + \frac{c}{x^2}$.

In summary, we fabricated curcumin-loaded zein fibrous mats by using single fluid electrospinning process. Zein concentration is of importance to its fiber formation. We find that 50 w/v% is a critical concentration for bead-to-fiber transition, beyond which beadless fibers can be obtained. Based on that critical concentration, we further fabricated curcumin-loaded zein fibrous mats. Within the experimental condition, we can achieve 12% curcumin loading per zein mat. The fluorescence images show that curcumin can be well-dispersed into zein beads at low concentration and zein fibers at high concentration. With a home-made copper wired drum, we control the degree of zein fiber alignment, and the highly-aligned zein fibers can be processed at 850 RPM. The “fiber thinning”

phenomenon during fiber alignment is observed, which is due to the fiber stretching by rotational drum. The fiber thickness upon drum rotation can be well predicted based on the mass balance. In addition, the curcumin-loaded zein fiber mats exhibit a curcumin loading-dependent *in vitro* anti-cancer activity.

Chapter 7

Future work

This dissertation majorly unveils a scientific corner of three approaches for biopolymer platform fabrication, which are small molecule crosslinking, organocatalytic ring-opening polymerization (OROP), and electrospinning. Future work of each approach is going on continuously. For small molecule crosslinking (Chapter 3), development of novel crosslinkers and combination with other fabrications such as microfluidics (*366*) or electrospraying (*367*) can be taken into consideration. Novel crosslinkers are not limited to small molecules such as glutaraldehyde and sodium tripolyphosphate. Other resources such as natural peptides hydrolyzed from protein can also be utilized as crosslinker. For instance, caseinophosphopeptide, prepared by the tryptic digestion of bovine casein proteins can interact with other positively-charged biopolymers (i.e. chitosan). Hence, natural charged materials like caseinophosphopeptide can be used as next-generation biopolymer crosslinker. Compared with conventional glutaraldehyde, those natural materials are safer to use since many of them are in "GRAS" status. On the other hand, novel advanced technologies can also be combined with small molecular crosslinking to formulate well-controlled and cost-effective particulate carriers. Recently, Yang et al. demonstrated that they were able to manufacture chitosan-tripolyphosphate emulsion

droplets with a high throughput by using microfluidic chip (*368*). The fabricated chitosan emulsion droplets were proved to be promising agents for sustained nasal and gastrointestinal tract delivery with the potential for the enhancement of patient compliance and bacterial pathogenesis. Later, Aryia et al. succeeded to utilize electrospraying process to generate chitosan micro/nanoparticles which encapsulated ampicillin sodium, an antimicrobial drug (*369*). Through release kinetics study, it has been suggested that maintenance of antimicrobial activity and sustainable release can be achieved during and after electrospraying process.

In terms of organocatalytic ring-opening polymerization (OROP) (chapter 4), functionalization of cyclic monomers (*58, 61*) may be the trend for OROP approach. With functionalized cyclic monomers, we will be able to expand the macromolecular architectures of OROP. With a facile conjugate addition, extra thiol groups can be added to the monomer α,β-unsaturated valerolactone 5,6-dihydro-2*H*pyran-2-one, which can be further polymerized into polyesters functionalized either with benzyl mercaptans or oligoethylene glycol pendant groups (*58*). This simple strategy guides us to synthesize homopolymers or copolymers decorated with hydrophobic or hydrophilic functional groups.

In terms of electrospinning (chapter 6), investigation of *in vitro* release profile of active compound from electrospun fibrous mat and fabrication of micro-/nano- particulate platforms by using electrospraying technique should be put emphasis upon. *In vitro* release profile of active ingredients (i.e. drug and nutraceutical) can be traced by using Sotex UPS4 prototype dissolution tester equipped with semi-automatic sampling accessory. Similar investigation have been applied for studying the *in vitro* release profile

of ketoprofen from zein-polyvinylpyrrolidone fiber mat under different zein contents (*370*). The *in vitro* release data will be connected with the results of *in vivo* animal model to provide comprehensive understanding of sustainable compound release profiles under different conditions. In addition, electrospraying in cone-jet mode facilitates us to fabricate solid particle and particulate suspension in one-step process (*371*). Recently, Gomez-Estaca et al. demonstrated that electrospray curcumin-loaded zein particles were stable for over 3-month storage and the powder of curcumin-zein particles could be conventionally re-constituted into food matrix such as milk (*372*). To sum up, efforts will be put not only to fabricate novel biopolymer platforms but also to integrate those platforms into consumer goods in the future study of biopolymer fabrication.

Supplementary Information (SI) for Chapter 4

S4.1 Methods

S4.1.1 Critical micelle concentration determination

The critical micelle concentration (CMC) of 8 kD_a mPEG-*b*-PVL was determined by measuring the fluorescence emission spectra of pyrene in block copolymer solutions (0.001, 0.003, 0.005, 0.01, 0.05, 0.3, and 5 mg/mL). Prior to experiment, pyrene stock solution (1.0 mM) was prepared in methanol. Pyrene stock solution was added to glass tube, and methanol was removed by purging with nitrogen. Afterwards, mPEG-*b*-PVL solutions of different concentrations were transferred into each tube. 30-minute sonication was utilized to facilitate pyrene dissolution. Then, the fluorescence emission spectra of pyrene from 350 to 500 nm were obtained using Cary Eclipse fluorescence spectrophotometer (Varian Instruments, Walnut Creek, CA). The setting of fluorescence measurement includes excitation wavelength at 343 nm, excitation slit of 10 nm, and emission slit of 2.5 nm. The I_1/I_3 ratio was plotted versus the concentration of mPEG-*b*-PVL in semi-logarithmic coordinate system. A prominent change in the slope suggested the start of micellization.

S4.1.2 Form Factor equations

Different form factors are utilized to fit the SAXS profiles of mPEG-*b*-PVL copolymers and star polymers in water. The equations of solid sphere, core-shell sphere, cylinder, and core-shell cylinder are shown as follows:

For solid sphere:

$$I(Q) = [3b\frac{\sin(QR) - QR\cos(QR)}{(QR)^3}]^2 \quad \text{(S4.1)}$$

where *R* is the radius of the sphere, b is the scattering length contrast between particle and solvent.

For core-shell sphere:

$$I(Q) = NV_S^2 \left\{ (\rho_C - \rho_S) \frac{V_C}{V_S} \frac{3[\sin(QR_C) - QR_C \cos(QR_C)]}{(QR_C)^3} + (\rho_S - \rho_0) \frac{3[\sin(QR_S) - QR_S \cos(QR_S)]}{(QR_S)^3} \right\}$$

(S4.2)

where N is the aggregation number in a unit volume, V_S is the volume of an entire micelle, R_C is the outer radii of the core, R_S is the outer radii of the shell, ρ_S, ρ_C, and ρ_0 are the scattering length density of shell, core, and solvent, respectively.

For cylinder:

$$I(Q) = 16b^2 \int_0^1 \left(\frac{J_1(QR\sqrt{1-x^2}\,\sin(QLx/2)}{Q^2 R\sqrt{1-x^2}Lx} \right)^2 dx \qquad \text{(S4.3)}$$

where R is the cross-section radius, L is the rod length, b is the scattering length contrast, and J_1 is the first order of Bessel function.

For core-shell cylinder:

$$I(Q) = \int_0^1 (K_{cyl}(Q, \Delta b_{core-shell}, R, L, x) + K_{cyl}(Q, \Delta b_{shell-solvent}, R + \Delta R, L, x))^2 dx \qquad \text{(S4.4)}$$

$$\text{and } K_{cyl}(Q, \Delta b, R, L, x) = 2\Delta b \frac{J_1(QR\sqrt{1-x^2})}{QR\sqrt{1-x^2}} \frac{\sin(QLx/2)}{QLx/2} \qquad \text{(S4.5)}$$

where R is the core radius, ΔR is the shell thickness, L is the rod length, $\Delta b_{core\text{-}shell}$ is the scattering length contrast between cylinder core and cylinder shell, $\Delta b_{shell\text{-}solvent}$ is the scattering length contrast between cylinder shell and solvent.

S4.1.3 Cytotoxicity Test

Cell cytotoxicity was evaluated by 3-[4,5-dimethyl-thiazol-2-yl]-2,5-diphenyl tetrazolium bromide (MTT) assay as previous literature (*373*). Briefly, HepG2 cells were seeded in 96-well microtiter plates at a density of 10,000 cells per well in a final volume of 100 μL medium. After 24-hour incubation, the cells were treated with mPEG-b-PVL copolymers and its star polymers at various concentrations for another 24 hours. Then, cell culture media were aspirated after being incubated and 100 μL MTT solution (0.5 mg/mL in RPMI 1640 medium) was added to cells for 2-hour incubation at 37 °C. Subsequently, MTT solution was carefully aspirated and the formazan crystals formed were dissolved in 100 μL DMSO per well. Light absorbance at 560 and 670 nm was recorded with Absorbance Microplate Reader (Molecular Devices, Sunnyvale, CA). Relative cell viability was expressed as A560–A670 normalized to that of the untreated wells. Data were presented as mean ± standard deviation with six-well repeats.

S4.2 Results

Figure S4.1 displays the fluorescence measurement of pyrene in mPEG-*b*-PVL solutions. Figure S4.1A shows the typical fluorescence emission spectra of pyrene in mPEG-*b*-PVL solution at a concentration of 0.01 mg/mL. The intensity ratio of peak 1 and peak 3, I_1/I_3, is sensitive to the polarity of the microenvironment and has been frequently used as an indicator of a local environmental change. Therefore, the critical micelle concentration (CMC), which refers to the incept concentration of micelle formation by hydrophobic interaction, is determined from the abrupt change of I_1/I_3 value of pyrene in the presence of diblock copolymers. Figure S4.1B presents the change of I_1/I_3 as a function of diblock

copolymer concentrations. At low concentration, the values of I_1/I_3 were close to that of pyrene in water (*374*). As polymer concentration increased, a linear decrease of I_1/I_3 could be observed. Extracted from the intercept of two lines, the CMC of 8 kD_a mPEG-*b*-PVL was determined to be 0.015 mg/mL. This result was lower than the previous one of 8 kD_a mPEG-*b*-PVL (*375*). The CMC difference between the current 8 kD_a mPEG-*b*-PVL and previous one lies in the different lengths of PVL block. The previous 8 kD_a mPEG-*b*-PVL has 1.1 kD_a PVL block, while the current one has 3 kD_a PVL block. The increase of hydrophobic block results in stronger hydrophobic interaction. Under such circumstance, mPEG-*b*-PVL reasonably required much less concentration for micelle formation.

Figure S4.2 shows the cytotoxicity results of mPEG-*b*-PVL copolymers and star polymers. Within the experimental concentrations from 10^{-4} μg/mL to 10^{2} μg/mL, both mPEG-*b*-PVL copolymers and star polymers display high cell viability values, indicating the biocompatibility of the synthesized diblock copolymer and nanogel star polymer.

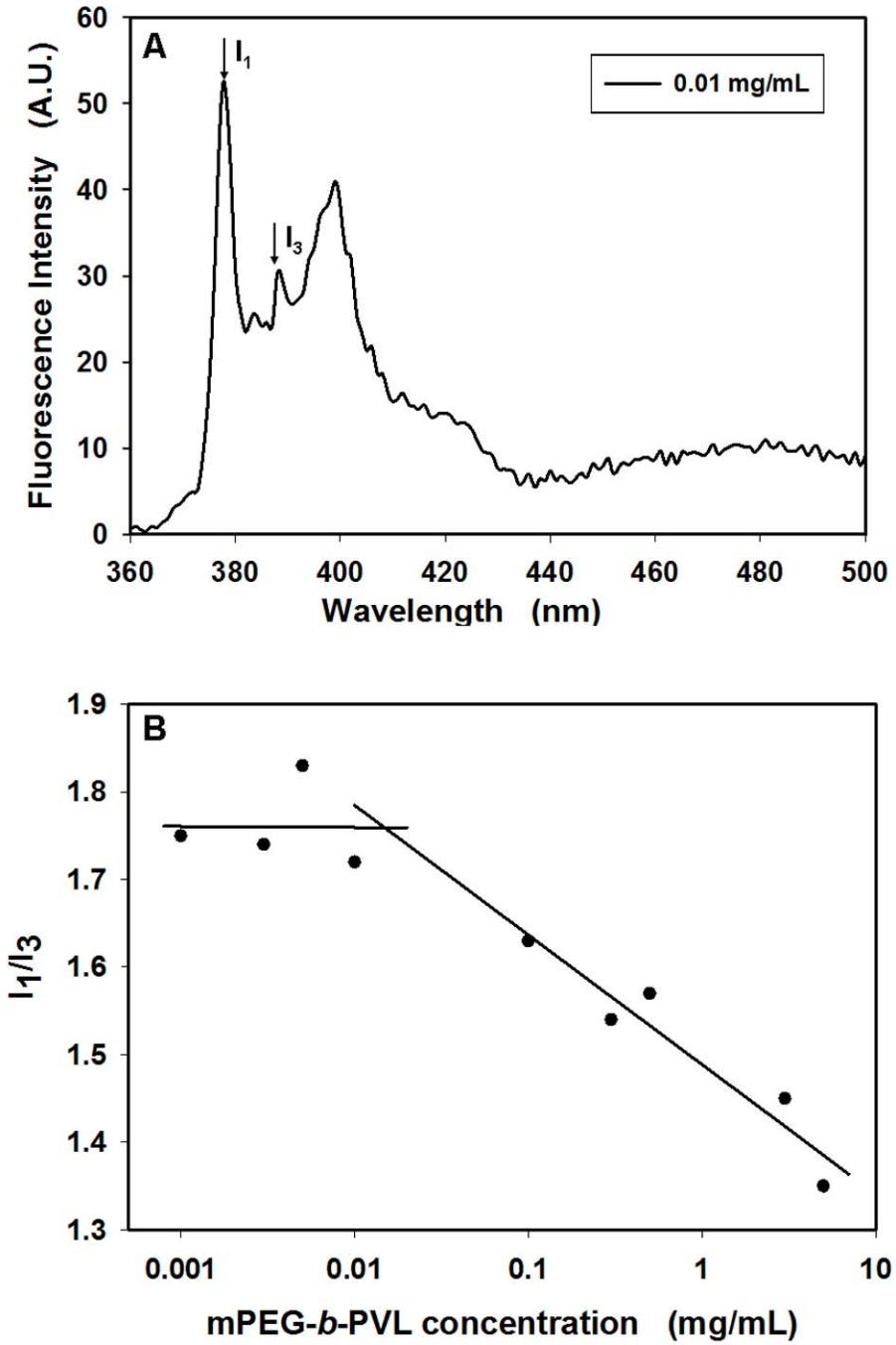

Figure S4.1: (A) Emission spectra of pyrene in mPEG-*b*-PVL solution with a concentration of 0.001 mg/mL. (B) Change of the intensity ratio (I_1/I_3) from excitation spectra of pyrene with various concentrations of mPEG-b-PVL.

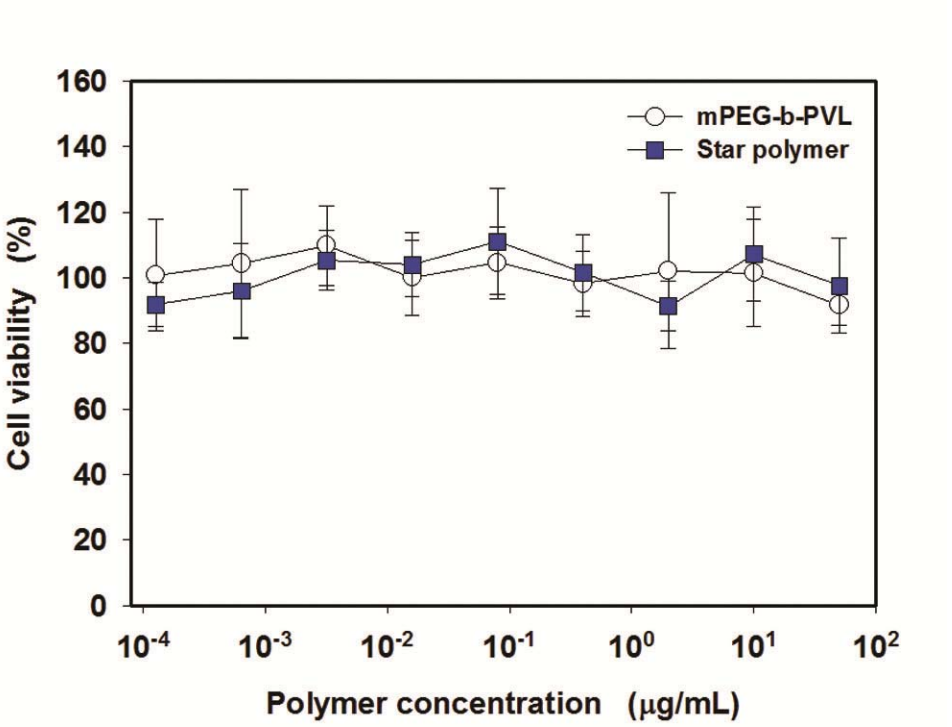

Figure S4.2: Cytotoxicity of mPEG-*b*-PVL copolymer and star polymer in HepG2 cells. Mean ± standard deviation (n =8).

Supplementary Information (SI) for Chapter 5

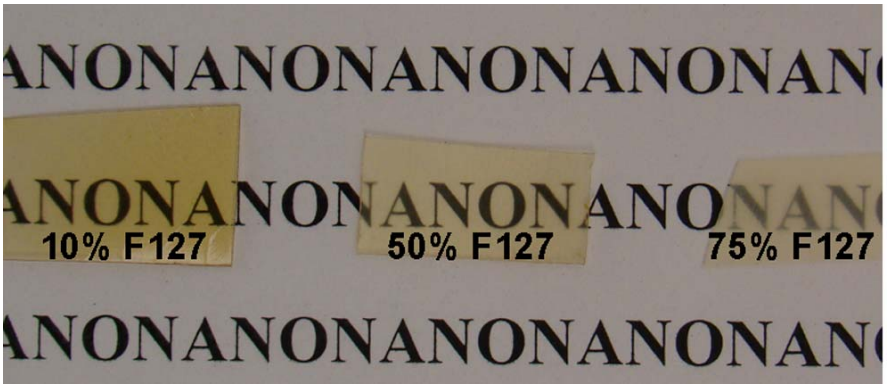

Figure S5.1: Photo image of zein/Pluronic F127 composite films containing 10%, 50%, and 75% of Pluronic F127.

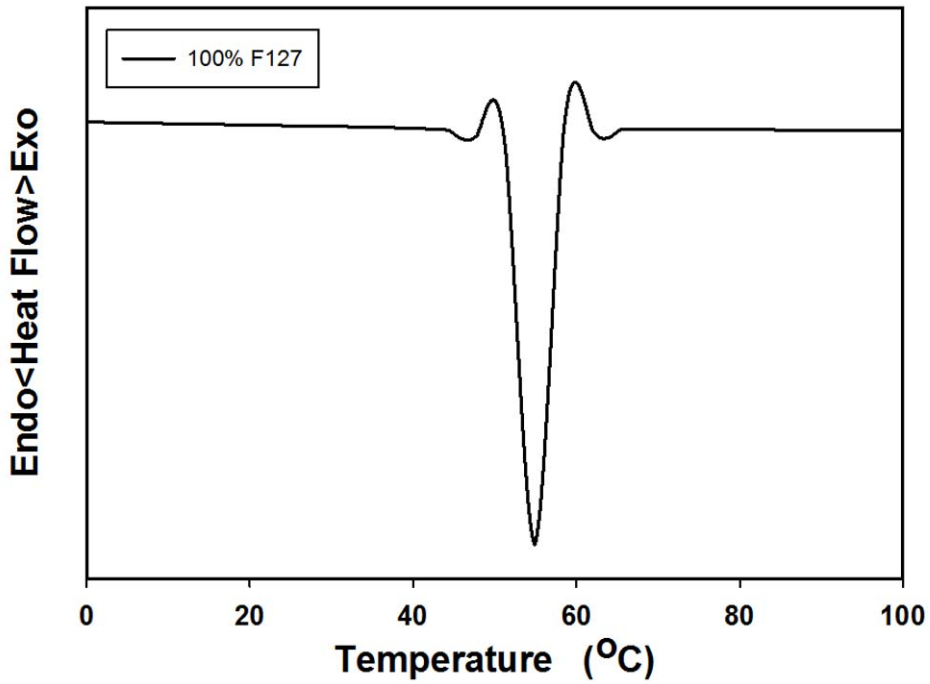

Figure S5.2: DSC thermogram of pure Pluronic F127 film (pellet).

Supplementary Information (SI) for Chapter 6

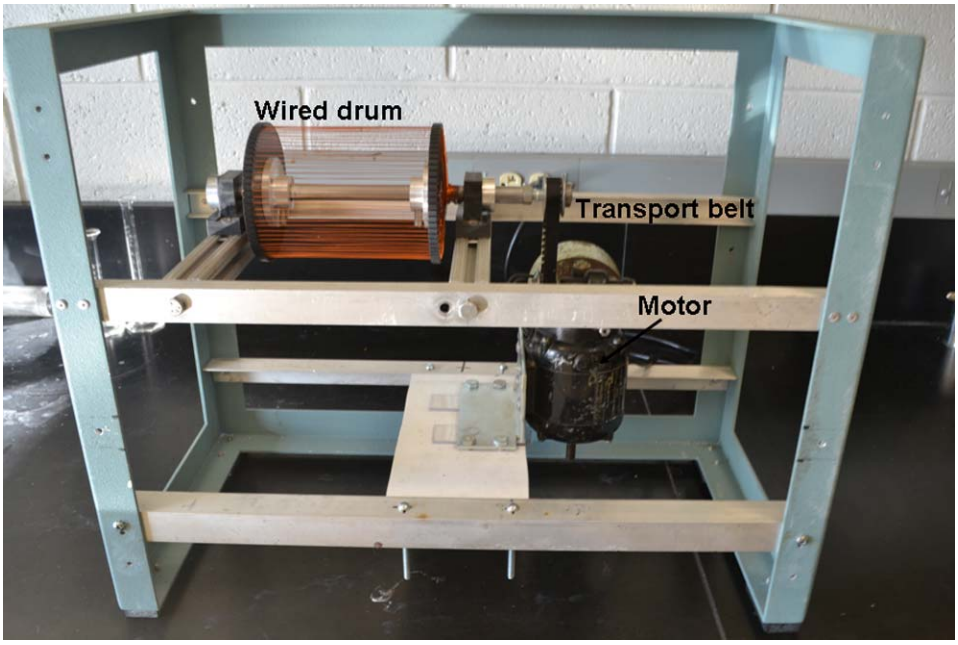

Figure S6.1: Photo of a home-made copper wire-framed drum fiber collector.

Bibliography

1. Orienti, I.; Aiedeh, K.; Gianasi, E.; Bertasi, V.; Zecchi, V. Indomethacin loaded chitosan microspheres. Correlation between the erosion process and release kinetics. *J. Microencapsul.* **1996,** 13, (4), 463-472.
2. Pujana, M. A.; Perez-Alvarez, L.; Iturbe, L. C. C.; Katime, I. Water dispersible pH-responsive chitosan nanogels modified with biocompatible crosslinking-agents. *Polymer* **2012,** 53, (15), 3107-3116.
3. Chen, T. Y.; Cao, Z.; Guo, X. L.; Nie, J. J.; Xu, J. T.; Fan, Z. Q.; Du, B. Y. Preparation and characterization of thermosensitive organic-inorganic hybrid microgels with functional Fe3O4 nanoparticles as crosslinker. *Polymer* **2011,** 52, (1), 172-179.
4. Lin, Y.; Zhang, L.; Yao, W.; Qian, H.; Ding, D.; Wu, W.; Jiang, X. Water-soluble chitosan-quantum dot hybrid nanospheres toward bioimaging and biolabeling. *ACS Appl. Mater. Inter.* **2011,** 3, (4), 995-1002.
5. Hardy, P. M.; Nicholls, A. C.; Rydon, H. N. The nature of glutaraldehyde in aqueous solution. *J. Chem. Soc. Chem. Comm.* **1969**, (10), 565-566.
6. Korn, A. H.; Feairheller, S. H.; Filachoine, E. M. Glutaraldehyde: Nature of the reagent. *J Mol. Biol.* **1972,** 65, (3), 525-529.
7. Whipple, E. B.; Ruta, M. Structure of aqueous glutaraldehyde. *J. Org. Chem.* **1974,** 39, (12), 1666-1668.
8. Pfister, S.; Meyer, P.; Steck, A.; Pfander, H. Isolation and structure elucidation of carotenoid−glycosyl esters in gardenia fruits (gardenia jasminoides ellis) and saffron (crocus sativus linne). *J. Agr. Food Chem.* **1996,** 44, (9), 2612-2615.

9. Choi, H.-J.; Park, Y. S.; Kim, M. G.; Kim, T. K.; Yoon, N. S.; Lim, Y. J. Isolation and characterization of the major colorant in Gardenia fruit. *Dyes Pigments* **2001,** 49, (1), 15-20.
10. Park, J.-E.; Lee, J.-Y.; Kim, H.-G.; Hahn, T.-R.; Paik, Y.-S. Isolation and characterization of water-soluble intermediates of blue pigments transformed from geniposide of gardenia jasminoides. *J. Agr. Food Chem.* **2002,** 50, (22), 6511-6514.
11. Mi, F.-L.; Sung, H.-W.; Shyu, S.-S. Synthesis and characterization of a novel chitosan-based network prepared using naturally occurring crosslinker. *J. Polym. Sci. Pol. Chem.* **2000,** 38, (15), 2804-2814.
12. Greenwood, N.; Earnshaw, A., *Chemistry of the Elements*. second ed.; Butterworth-Heinemann: 1997.
13. Schrödter, K.; Bettermann, G.; Staffel, T.; Wahl, F.; Klein, T.; Hofmann, T., Phosphoric Acid and Phosphates. In *Ullmann's Encyclopedia of Industrial Chemistry*, Wiley-VCH Verlag GmbH & Co. KGaA: 2000.
14. Varma, A. J.; Deshpande, S. V.; Kennedy, J. F. Metal complexation by chitosan and its derivatives: a review. *Carbohyd. Polym.* **2004,** 55, (1), 77-93.
15. Bailey, S. E.; Olin, T. J.; Bricka, R. M.; Adrian, D. D. A review of potentially low-cost sorbents for heavy metals. *Water Res.* **1999,** 33, (11), 2469-2479.
16. Ngah, W. S. W.; Endud, C. S.; Mayanar, R. Removal of copper(II) ions from aqueous solution onto chitosan and cross-linked chitosan beads. *React. Funct. Polym.* **2002,** 50, (2), 181-190.
17. Rorrer, G. L.; Hsien, T. Y.; Way, J. D. Synthesis of porous-magnetic chitosan beads for removal of cadmium ions from wastewater. *Ind. Eng. Chem. Res.* **1993,** 32, (9), 2170-2178.
18. Jameela, S. R.; Jayakrishnan, A. Glutaraldehyde crosslinked chitosan microspheres as a long-acting biodegradable drug delivery vehicle- Studies on the in-vitro release of mitoxantrone and in-vivo degradation of microspheres in rat muscle. *Biomaterials* **1995,** 16, (10), 769-775.
19. Nayak, U. Y.; Gopal, S.; Mutalik, S.; Ranjith, A. K.; Reddy, M. S.; Gupta, P.; Udupa, N. Glutaraldehyde cross-linked chitosan microspheres for controlled delivery of Zidovudine. *J. Microencapsul.* **2009,** 26, (3), 214-222.
20. Sung, H.-W.; Huang, R.-N.; Huang, L. L. H.; Tsai, C.-C. In vitro evaluation of cytotoxicity of a naturally occurring cross-linking reagent for biological tissue fixation. *J. Biomat. Sci-Polym. E.* **1999,** 10, (1), 63-78.
21. Mi, F.-L.; Sung, H.-W.; Shyu, S.-S. Release of indomethacin from a novel chitosan microsphere prepared by a naturally occurring crosslinker: Examination of crosslinking and polycation–anionic drug interaction. *J. Appl. Polym. Sci.* **2001,** 81, (7), 1700-1711.
22. Karnchanajindanun, J.; Srisa-ard, M.; Bairnark, Y. Genipin-cross-linked chitosan microspheres prepared by a water-in-oil emulsion solvent diffusion method for protein delivery. *Carbohyd. Polym.* **2011,** 85, (3), 674-680.
23. Yuan, Y.; Chesnutt, B. M.; Utturkar, G.; Haggard, W. O.; Yang, Y.; Ong, J. L.; Bumgardner, J. D. The effect of cross-linking of chitosan microspheres with genipin on protein release. *Carbohyd. Polym.* **2007,** 68, (3), 561-567.

24. Hussain, M. R.; Maji, T. K. Preparation of genipin cross-linked chitosan-gelatin microcapsules for encapsulation of Zanthoxylum limonella oil (ZLO) using salting-out method. *J. Microencapsul.* **2008,** 25, (6), 414-420.
25. Maji, T. K.; Hussain, M. R. Microencapsulation of zanthoxylum limonella oil (ZLO) in genipin crosslinked chitosan-gelatin complex for mosquito repellent application. *J. Appl. Polym. Sci.* **2009,** 111, (2), 779-785.
26. Chen, H.; Ouyang, W.; Lawuyi, B.; Prakash, S. Genipin cross-linked alginate-chitosan microcapsules: membrane characterization and optimization of cross-linking reaction. *Biomacromolecules* **2006,** 7, (7), 2091-2098.
27. Gan, Q.; Wang, T.; Cochrane, C.; McCarron, P. Modulation of surface charge, particle size and morphological properties of chitosan-TPP nanoparticles intended for gene delivery. *Collod. Surface B* **2005,** 44, (2-3), 65-73.
28. Hu, B.; Pan, C.; Sun, Y.; Hou, Z.; Ye, H.; Zeng, X. Optimization of fabrication parameters to produce chitosan−tripolyphosphate nanoparticles for delivery of tea catechins. *J. Agr. Food Chem.* **2008,** 56, (16), 7451-7458.
29. Li, J.; Huang, Q. R. Rheological properties of chitosan-tripolyphosphate complexes: From suspensions to microgels. *Carbohyd. Polym.* **2012,** 87, (2), 1670-1677.
30. Pan, Y.; Li, Y. J.; Zhao, H. Y.; Zheng, J. M.; Xu, H.; Wei, G.; Hao, J. S.; Cui, F. D. Bioadhesive polysaccharide in protein delivery system: chitosan nanoparticles improve the intestinal absorption of insulin in vivo. *Int. J. Pharm.* **2002,** 249, (1-2), 139-147.
31. Wu, Y.; Yang, W.; Wang, C.; Hu, J.; Fu, S. Chitosan nanoparticles as a novel delivery system for ammonium glycyrrhizinate. *Int. J. Pharm.* **2005,** 295, (1–2), 235-245.
32. Zhang, H.; Oh, M.; Allen, C.; Kumacheva, E. Monodisperse chitosan nanoparticles for mucosal drug delivery. *Biomacromolecules* **2004,** 5, (6), 2461-2468.
33. Desai, M. P.; Labhasetwar, V.; Amidon, G. L.; Levy, R. J. Gastrointestinal uptake of biodegradable microparticles: Effect of particle size. *Pharm. Res.* **1996,** 13, (12), 1838-1845.
34. Song, C.; Labhasetwar, V.; Cui, X.; Underwood, T.; Levy, R. J. Arterial uptake of biodegradable nanoparticles for intravascular local drug delivery: Results with an acute dog model. *J. Control. Release* **1998,** 54, (2), 201-211.
35. Bauer, D.; Buchhammer, H.; Fuchs, A.; Jaeger, W.; Killmann, E.; Lunkwitz, K.; Rehmet, R.; Schwarz, S. Stability of colloidal silica, sikron and polystyrene latex influenced by the adsorption of polycations of different charge density. *Colloid Surface A* **1999,** 156, (1-3), 291-305.
36. Shu, X.; Zhu, K. J. A novel approach to prepare tripolyphosphate/chitosan complex beads for controlled release drug delivery. *Int. J. Pharm.* **2000,** 201, (1), 51-58.
37. Grenha, A.; Seijo, B.; Remunan-Lopez, C. Microencapsulated chitosan nanoparticles for lung protein delivery. *Eur. J. Pharm. Sci.* **2005,** 25, (4-5), 427-437.
38. Xu, Y.; Du, Y. Effect of molecular structure of chitosan on protein delivery properties of chitosan nanoparticles. *Int. J. Pharm.* **2003,** 250, (1), 215-226.
39. Mao, H. Q.; Roy, K.; Troung-Le, V. L.; Janes, K. A.; Lin, K. Y.; Wang, Y.; August, J. T.; Leong, K. W. Chitosan-DNA nanoparticles as gene carriers: synthesis, characterization and transfection efficiency. *J. Control. Release* **2001,** 70, (3), 399-421.
40. Katas, H.; Alpar, H. O. Development and characterisation of chitosan nanoparticles for siRNA delivery. *J. Control. Release* **2006,** 115, (2), 216-225.

41. Silva, C. A.; Nobre, T. M.; Pavinatto, F. J.; Oliveira, O. N. Interaction of chitosan and mucin in a biomembrane model environment. *J. Colloid Interface Sci.* **2012,** 376, 289-295.
42. Fang, N.; Chan, V. Interaction of liposome with immobilized chitosan during main phase transition. *Biomacromolecules* **2003,** 4, (3), 581-588.
43. Pavinatto, F. J.; Caseli, L.; Pavinatto, A.; dos Santos, D. S.; Nobre, T. M.; Zaniquelli, M. E. D.; Silva, H. S.; Miranda, P. B.; de Oliveira, O. N. Probing chitosan and phospholipid interactions using langmuir and langmuir−blodgett films as cell membrane models. *Langmuir* **2007,** 23, (14), 7666-7671.
44. Sogias, I. A.; Williams, A. C.; Khutoryanskiy, V. V. Why is Chitosan Mucoadhesive? *Biomacromolecules* **2008,** 9, (7), 1837-1842.
45. Chen, L. Y.; Subirade, M. Chitosan/beta-lactoglobulin core-shell nanoparticles as nutraceutical carriers. *Biomaterials* **2005,** 26, (30), 6041-6053.
46. Pratt, R. C.; Lohmeijer, B. G. G.; Long, D. A.; Waymouth, R. M.; Hedrick, J. L. Triazabicyclodecene: A simple bifunctional organocatalyst for acyl transfer and ring-opening polymerization of cyclic esters. *J. Am. Chem. Soc.* **2006,** 128, (14), 4556-4557.
47. Kiesewetter, M. K.; Scholten, M. D.; Kirn, N.; Weber, R. L.; Hedrick, J. L.; Waymouth, R. M. Cyclic guanidine organic catalysts: What is magic about triazabicyclodecene? *J. Org. Chem.* **2009,** 74, (24), 9490-9496.
48. Coles, M. P. Bicyclic-guanidines, -guanidinates and -guanidinium salts: wide ranging applications from a simple family of molecules. *Chem. Commun.* **2009**, (25), 3659-3676.
49. Kaljurand, I.; Kütt, A.; Sooväli, L.; Rodima, T.; Mäemets, V.; Leito, I.; Koppel, I. A. Extension of the self-consistent spectrophotometric basicity scale in acetonitrile to a full Span of 28 pKa units: Unification of different basicity scales. *J. Org. Chem.* **2005,** 70, (3), 1019-1028.
50. Simoni, D.; Rossi, M.; Rondanin, R.; Mazzali, A.; Baruchello, R.; Malagutti, C.; Roberti, M.; Invidiata, F. P. Strong bicyclic guanidine base-promoted Wittig and Horner−Wadsworth−Emmons reactions. *Org. Lett.* **2000,** 2, (24), 3765-3768.
51. Simoni, D.; Rondanin, R.; Morini, M.; Baruchello, R.; Invidiata, F. P. 1,5,7-Triazabicyclo[4.4.0]dec-1-ene (TBD), 7-methyl-TBD (MTBD) and the polymer-supported TBD (P-TBD): three efficient catalysts for the nitroaldol (Henry) reaction and for the addition of dialkyl phosphites to unsaturated systems. *Tetrahedron Lett.* **2000,** 41, (10), 1607-1610.
52. Ye, W.; Xu, J.; Tan, C.-T.; Tan, C.-H. 1,5,7-Triazabicyclo[4.4.0]dec-5-ene (TBD) catalyzed Michael reactions. *Tetrahedron Lett.* **2005,** 46, (40), 6875-6878.
53. Corey, E. J.; Grogan, M. J. Enantioselective synthesis of α-amino nitriles from N-benzhydryl Imines and HCN with a chiral bicyclic guanidine as catalyst. *Organic Lett.* **1999,** 1, (1), 157-160.
54. Schuchardt, U.; Vargas, R. M.; Gelbard, G. Alkylguanidines as catalysts for the transesterification of rapeseed oil. *J. Mol. Catal. A: Chem.* **1995,** 99, (2), 65-70.
55. Lohmeijer, B. G. G.; Pratt, R. C.; Leibfarth, F.; Logan, J. W.; Long, D. A.; Dove, A. P.; Nederberg, F.; Choi, J.; Wade, C.; Waymouth, R. M.; Hedrick, J. L. Guanidine and Amidine Organocatalysts for Ring-Opening Polymerization of Cyclic Esters. *Macromolecules* **2006,** 39, (25), 8574-8583.

56. Chuma, A.; Horn, H. W.; Swope, W. C.; Pratt, R. C.; Zhang, L.; Lohmeijer, B. G. G.; Wade, C. G.; Waymouth, R. M.; Hedrick, J. L.; Rice, J. E. The reaction mechanism for the organocatalytic ring-opening polymerization of l-Lactide using a guanidine-based catalyst: Hydrogen-bonded or covalently bound? *J. Am. Chem. Soc.* **2008,** 130, (21), 6749-6754.
57. Dove, A. P.; Pratt, R. C.; Lohmeijer, B. G. G.; Waymouth, R. M.; Hedrick, J. L. Thiourea-based bifunctional organocatalysis: Supramolecular recognition for living polymerization. *J. Am. Chem. Soc.* **2005,** 127, (40), 13798-13799.
58. Kim, H.; Olsson, J. V.; Hedrick, J. L.; Waymouth, R. M. Facile synthesis of functionalized lactones and organocatalytic ring-opening polymerization. *ACS Macro Lett.* **2012,** 1, (7), 845-847.
59. Appel, E. A.; Lee, V. Y.; Nguyen, T. T.; McNeil, M.; Nederberg, F.; Hedrick, J. L.; Swope, W. C.; Rice, J. E.; Miller, R. D.; Sly, J. Toward biodegradable nanogel star polymers via organocatalytic ROP. *Chem. Commun.* **2012,** 48, (49), 6163-6165.
60. Zhang, K.; Tew, G. N. Cyclic brush polymers by combining ring-expansion metathesis polymerization and the "grafting from" technique. *Acs Macro Lett.* **2012,** 1, (5), 574-579.
61. Fukushima, K.; Pratt, R. C.; Nederberg, F.; Tan, J. P. K.; Yang, Y. Y.; Waymouth, R. M.; Hedrick, J. L. Organocatalytic Approach to Amphiphilic Comb-Block Copolymers Capable of Stereocomplexation and Self-Assembly. *Biomacromolecules* **2008,** 9, (11), 3051-3056.
62. Nederberg, F.; Trang, V.; Pratt, R. C.; Mason, A. F.; Frank, C. W.; Waymouth, R. M.; Hedrick, J. L. New Ground for Organic Catalysis: A Ring-Opening Polymerization Approach to Hydrogels. *Biomacromolecules* **2007,** 8, (11), 3294-3297.
63. Coady, D. J.; Engler, A. C.; Yang, Y. Y.; Hedrick, J. L. Facile routes to star polymers via an organocatalytic approach. *Polym. Chem.* **2011,** 2, (11), 2619-2626.
64. Wang, J. S.; Matyjaszewski, K. Controlled living radical polymerization- Halogen atom-transfer radical polymerization promoated by a Cu(I) Cu(II) redox process. *Macromolecules* **1995,** 28, (23), 7901-7910.
65. Chiefari, J.; Chong, Y. K.; Ercole, F.; Krstina, J.; Jeffery, J.; Le, T. P. T.; Mayadunne, R. T. A.; Meijs, G. F.; Moad, C. L.; Moad, G.; Rizzardo, E.; Thang, S. H. Living free-radical polymerization by reversible addition-fragmentation chain transfer: The RAFT process. *Macromolecules* **1998,** 31, (16), 5559-5562.
66. Uyama, H.; Kobayashi, S. Enzymatic ring-opening polymerization of lactones catalyzed by lipase. *Chem. Lett.* **1993,** 22, (7), 1149-1150.
67. Uyama, H.; Takeya, K.; Hoshi, N.; Kobayashi, S. Lipase-catalyzed ring-opening polymerization of 12-dodecanolide. *Macromolecules* **1995,** 28, (21), 7046-7050.
68. Schwach, G.; Coudane, J.; Engel, R.; Vert, M. More about the polymerization of lactides in the presence of stannous octoate. *J. Polym. Sci. Pol. Chem.* **1997,** 35, (16), 3431-3440.
69. Rafler, G.; Dahlmann, J. Biodegradable polymers. 6. Polymerization of epsilon-caprolactone. *Acta Polym.* **1992,** 43, (2), 91-95.
70. Stjerndahl, A.; Wistrand, A. F.; Albertsson, A.-C. Industrial Utilization of Tin-Initiated Resorbable Polymers: Synthesis on a Large Scale with a Low Amount of Initiator Residue. *Biomacromolecules* **2007,** 8, (3), 937-940.

71. Schappacher, M.; Le Hellaye, M.; Bareille, R.; Durrieu, M.-C.; Guillaume, S. M. Comparative in vitro cytotoxicit toward human osteoprogenitor cells of polycaprolactones synthesized from various metallic initiators. *Macromol. Biosci.* **2010,** 10, (1), 60-67.
72. Schwach, G.; Coudane, J.; Engel, R.; Vert, M. Influence of polymerization conditions on the hydrolytic degradation of poly(dl-lactide) polymerized in the presence of stannous octoate or zinc-metal. *Biomaterials* **2002,** 23, (4), 993-1002.
73. Gilbert, W., *De Magnete, Magneticisque Corporibus, et de Magno Magnete Tellure (On the Magnet and Magnetic Bodies, and on That Great Magnet the Earth)*. London: Peter Short, 1628.
74. Boys, C. V. On the production, properties, and some suggested uses of the finest threads. *P. Phys. Soc. Lond.* **1887,** 9, (1), 8.
75. Cooley, J. F. Improved methods of and apparatus for electrically separating the relatively volatile liquid component from the component of relatively fixed substances of composite fluids. Patent GB 06385, 1900.
76. Morton, W. J. Method of dispersing fluids. U.S. patent No. 705,691, 1902.
77. Formhals, A. Process and apparatus for preparing artificial threads. U.S. Patent No. 1,975,504, 1934.
78. Formhals, A. Method and apparatus for spinning. U.S. Patent No. 2,349,950, 1944.
79. Taylor, G. Disintegration of water drops in an electric field. *P. Roy. Soc. Lond. A Mat.* **1964,** 280, (1382), 383-397.
80. Taylor, G. Electrically driven jets. *P. Roy. Soc. Lond. A Mat.* **1969,** 313, (1515), 453-475.
81. Fridrikh, S. V.; Yu, J. H.; Brenner, M. P.; Rutledge, G. C. Controlling the fiber diameter during electrospinning. *Phys. Rev. Lett.* **2003,** 90, (14), 144502.
82. Li, D.; Xia, Y. Electrospinning of nanofibers: Reinventing the wheel? *Adv. Mater.* **2004,** 16, (14), 1151-1170.
83. Reneker, D. H.; Yarin, A. L. Electrospinning jets and polymer nanofibers. *Polymer* **2008,** 49, (10), 2387-2425.
84. Yarin, A. L.; Koombhongse, S.; Reneker, D. H. Taylor cone and jetting from liquid droplets in electrospinning of nanofibers. *J. Appl. Phys.* **2001,** 90, (9), 4836-4846.
85. Greiner, A.; Wendorff, J. H. Electrospinning: A fascinating method for the preparation of ultrathin fibers. *Angew. Chem. Int. Edit.* **2007,** 46, (30), 5670-5703.
86. Eda, G.; Liu, J.; Shivkumar, S. Solvent effects on jet evolution during electrospinning of semi-dilute polystyrene solutions. *Eur. Polym. J.* **2007,** 43, (4), 1154-1167.
87. Mestel, A. J. The electrohydrodynamic cone-jet at high reynolds number. *J. Aerosol. Sci.* **1994,** 25, (6), 1037-1047.
88. Reneker, D. H.; Yarin, A. L.; Fong, H.; Koombhongse, S. Bending instability of electrically charged liquid jets of polymer solutions in electrospinning. *J. Appl. Phys.* **2000,** 87, (9), 4531-4547.
89. Shin, Y. M.; Hohman, M. M.; Brenner, M. P.; Rutledge, G. C. Experimental characterization of electrospinning: the electrically forced jet and instabilities. *Polymer* **2001,** 42, (25), 09955-09967.
90. Feng, J. J. The stretching of an electrified non-Newtonian jet: A model for electrospinning. *Phys. Fluids* **2002,** 14, (11), 3912-3926.

91. Wang, C.; Cheng, Y. W.; Hsu, C. H.; Chien, H. S.; Tsou, S. Y. How to manipulate the electrospinning jet with controlled properties to obtain uniform fibers with the smallest diameter?-a brief discussion of solution electrospinning process. *J. Polym. Res.* **2011,** 18, (1), 111-123.
92. Sun, Z.; Zussman, E.; Yarin, A. L.; Wendorff, J. H.; Greiner, A. Compound core–shell polymer nanofibers by co-electrospinning. *Adv. Mater.* **2003,** 15, (22), 1929-1932.
93. Kong, L.; Ziegler, G. R. Role of molecular entanglements in starch fiber formation by electrospinning. *Biomacromolecules* **2012,** 13, (8), 2247-2253.
94. Katta, P.; Alessandro, M.; Ramsier, R. D.; Chase, G. G. Continuous electrospinning of aligned polymer nanofibers onto a wire drum collector. *Nano Lett.* **2004,** 4, (11), 2215-2218.
95. Shenoy, S. L.; Bates, W. D.; Frisch, H. L.; Wnek, G. E. Role of chain entanglements on fiber formation during electrospinning of polymer solutions: good solvent, non-specific polymer–polymer interaction limit. *Polymer* **2005,** 46, (10), 3372-3384.
96. Munir, M. M.; Suryamas, A. B.; Iskandar, F.; Okuyama, K. Scaling law on particle-to-fiber formation during electrospinning. *Polymer* **2009,** 50, (20), 4935-4943.
97. Tao, J.; Shivkumar, S. Molecular weight dependent structural regimes during the electrospinning of PVA. *Mater. Lett.* **2007,** 61, (11–12), 2325-2328.
98. Eda, G.; Shivkumar, S. Bead-to-fiber transition in electrospun polystyrene. *J. Appl. Polym. Sci.* **2007,** 106, (1), 475-487.
99. McKee, M. G.; Wilkes, G. L.; Colby, R. H.; Long, T. E. Correlations of solution rheology with electrospun fiber formation of linear and branched polyesters. *Macromolecules* **2004,** 37, (5), 1760-1767.
100. McKee, M. G.; Hunley, M. T.; Layman, J. M.; Long, T. E. Solution rheological behavior and electrospinning of cationic polyelectrolytes. *Macromolecules* **2006,** 39, (2), 575-583.
101. de Gennes, P. G., *Scaling Concepts in Polymer Physics*. Cornell University Press: Ithaca, NY, 1979.
102. Colby, R. H.; Fetters, L. J.; Funk, W. G.; Graessley, W. W. Effects of concentration and thermodynamic interaction on the viscoelastic properties of polymer solutions. *Macromolecules* **1991,** 24, (13), 3873-3882.
103. Ohkawa, K.; Cha, D.; Kim, H.; Nishida, A.; Yamamoto, H. Electrospinning of chitosan. *Macromol. Rapid Comm.* **2004,** 25, (18), 1600-1605.
104. Ohkawa, K.; Minato, K.-I.; Kumagai, G.; Hayashi, S.; Yamamoto, H. Chitosan nanofiber. *Biomacromolecules* **2006,** 7, (11), 3291-3294.
105. Schiffman, J. D.; Schauer, C. L. One-step electrospinning of cross-linked chitosan fibers. *Biomacromolecules* **2007,** 8, (9), 2665-2667.
106. Sangsanoh, P.; Supaphol, P. Stability improvement of electrospun chitosan nanofibrous membranes in neutral or weak basic aqueous solutions. *Biomacromolecules* **2006,** 7, (10), 2710-2714.
107. Schiffman, J. D.; Schauer, C. L. Cross-linking chitosan nanofibers. *Biomacromolecules* **2006,** 8, (2), 594-601.
108. Subbiah, T.; Bhat, G. S.; Tock, R. W.; Parameswaran, S.; Ramkumar, S. S. Electrospinning of nanofibers. *J. Appl. Polym. Sci.* **2005,** 96, (2), 557-569.

109. Angammana, C. J.; Jayaram, S. H. Investigation of the optimum electric field for a stable electrospinning process. *IEEE T. Ind. Appl.* **2012,** 48, (2), 808-815.
110. Sill, T. J.; von Recum, H. A. Electrospinning: Applications in drug delivery and tissue engineering. *Biomaterials* **2008,** 29, (13), 1989-2006.
111. Deitzel, J. M.; Kleinmeyer, J.; Harris, D.; Beck Tan, N. C. The effect of processing variables on the morphology of electrospun nanofibers and textiles. *Polymer* **2001,** 42, (1), 261-272.
112. Ki, C. S.; Baek, D. H.; Gang, K. D.; Lee, K. H.; Um, I. C.; Park, Y. H. Characterization of gelatin nanofiber prepared from gelatin–formic acid solution. *Polymer* **2005,** 46, (14), 5094-5102.
113. Yang, Y.; Jia, Z.; Liu, J.; Li, Q.; Hou, L.; Wang, L.; Guan, Z. Effect of electric field distribution uniformity on electrospinning. *J. Appl. Phys.* **2008,** 103, (10), 104307.
114. Zhuo, H.; Hu, J.; Chen, S.; Yeung, L. Preparation of polyurethane nanofibers by electrospinning. *J. Appl. Polym. Sci.* **2008,** 109, (1), 406-411.
115. Tong, H. W.; Wang, M. Negative voltage electrospinning of fibrous nanocomposite scaffolds for bone tissue engineering. *J. Aust. Ceram. Soc.* **2012,** 48, (1), 38-43.
116. Lvov, Y.; Ariga, K.; Ichinose, I.; Kunitake, T. Assembly of multicomponent protein films by means of electrostatic layer-by-layer adsorption. *J. Am. Chem. Soc.* **1995,** 117, (22), 6117-6123.
117. Lvov, Y.; Decher, G.; Mohwald, H. Assembly, structural characterization, and thermal behavior of layer-by-layer deposited ultrathin films of poly(vinyl sulfate) and poly(allylamine). *Langmuir* **1993,** 9, (2), 481-486.
118. Cui, W. G.; Li, X. H.; Zhou, S. B.; Weng, J. Investigation on process parameters of electrospinning system through orthogonal experimental design. *J. Appl. Polym. Sci.* **2007,** 103, (5), 3105-3112.
119. Kidoaki, S.; Kwon, K.; Matsuda, T. Structural features and mechanical properties of in situ-bonded meshes of segmented polyurethane electrospun from mixed solvents. *J. Biomed. Mater. Res. Part B* **2006,** 76B, (1), 219-229.
120. Li, D.; Xia, Y. Fabrication of titania nanofibers by electrospinning. *Nano Lett.* **2003,** 3, (4), 555-560.
121. Megelski, S.; Stephens, J. S.; Chase, D. B.; Rabolt, J. F. Micro- and nanostructured surface morphology on electrospun polymer fibers. *Macromolecules* **2002,** 35, (22), 8456-8466.
122. Tan, S. H.; Inai, R.; Kotaki, M.; Ramakrishna, S. Systematic parameter study for ultra-fine fiber fabrication via electrospinning process. *Polymer* **2005,** 46, (16), 6128-6134.
123. Wang, C.; Hsu, C. H.; Lin, J. H. Scaling laws in electrospinning of polystyrene solutions. *Macromolecules* **2006,** 39, (22), 7662-7672.
124. Zong, X.; Kim, K.; Fang, D.; Ran, S.; Hsiao, B. S.; Chu, B. Structure and process relationship of electrospun bioabsorbable nanofiber membranes. *Polymer* **2002,** 43, (16), 4403-4412.
125. Jiang, H. L.; Hu, Y. Q.; Zhao, P. C.; Li, Y.; Zhu, K. J. Modulation of protein release from biodegradable core-shell structured fibers prepared by coaxial electrospinning. *J. Biomed. Mater. Res. Part B* **2006,** 79B, (1), 50-57.

126. Jiang, H. L.; Zhao, P. C.; Zhu, K. J. Fabrication and characterization of zein-based nanofibrous scaffolds by an electrospinning method. *Macromol. Biosci.* **2007,** 7, (4), 517-525.
127. Zhao, P.; Jiang, H.; Pan, H.; Zhu, K.; Chen, W. Biodegradable fibrous scaffolds composed of gelatin coated poly(ϵ-caprolactone) prepared by coaxial electrospinning. *J. Biomed. Mater. Res. A* **2007,** 83A, (2), 372-382.
128. Moghe, A. K.; Gupta, B. S. Co-axial electrospinning for nanofiber structures: Preparation and applications. *Polym. Rev.* **2008,** 48, (2), 353-377.
129. Zhang, Y. Z.; Wang, X.; Feng, Y.; Li, J.; Lim, C. T.; Ramakrishna, S. Coaxial electrospinning of (fluorescein isothiocyanate-conjugated bovine serum albumin)-encapsulated poly(ε-caprolactone) nanofibers for sustained release. *Biomacromolecules* **2006,** 7, (4), 1049-1057.
130. López-Rubio, A.; Sanchez, E.; Sanz, Y.; Lagaron, J. M. Encapsulation of living bifidobacteria in ultrathin PVOH electrospun fibers. *Biomacromolecules* **2009,** 10, (10), 2823-2829.
131. Dalton, P. D.; Grafahrend, D.; Klinkhammer, K.; Klee, D.; Moller, M. Electrospinning of polymer melts: Phenomenological observations. *Polymer* **2007,** 48, (23), 6823-6833.
132. Dalton, P. D.; Lleixà Calvet, J.; Mourran, A.; Klee, D.; Möller, M. Melt electrospinning of poly-(ethylene glycol-block-ϵ-caprolactone). *Biotechnol. J.* **2006,** 1, (9), 998-1006.
133. Wang, C.; Chien, H. S.; Hsu, C. H.; Wang, Y. C.; Wang, C. T.; Lu, H. A. Electrospinning of polyacrylonitrile solutions at elevated temperatures. *Macromolecules* **2007,** 40, (22), 7973-7983.
134. Simonet, M.; Schneider, O. D.; Neuenschwander, P.; Stark, W. J. Ultraporous 3D polymer meshes by low-temperature electrospinning: Use of ice crystals as a removable void template. *Polm. Eng. Sci.* **2007,** 47, (12), 2020-2026.
135. Kanjanapongkul, K.; Wongsasulak, S.; Yoovidhya, T. Investigation and prevention of clogging during electrospinning of zein solution. *J. Appl. Polym. Sci.* **2010,** 118, (3), 1821-1829.
136. Kanjanapongkul, K.; Wongsasulak, S.; Yoovidhya, T. Prediction of clogging time during electrospinning of zein solution: Scaling analysis and experimental verification. *Chem. Eng. Sci.* **2010,** 65, (18), 5217-5225.
137. Li, Y.; Lim, L. T.; Kakuda, Y. Electrospun zein fibers as carriers to stabilize (-)-epigallocatechin gallate. *J. Food Sci.* **2009,** 74, (3), C233-C240.
138. Yoshimoto, H.; Shin, Y. M.; Terai, H.; Vacanti, J. P. A biodegradable nanofiber scaffold by electrospinning and its potential for bone tissue engineering. *Biomaterials* **2003,** 24, (12), 2077-2082.
139. Gopal, R.; Kaur, S.; Ma, Z. W.; Chan, C.; Ramakrishna, S.; Matsuura, T. Electrospun nanofibrous filtration membrane. *J. Membr. Sci.* **2006,** 281, (1-2), 581-586.
140. Yoon, J.; Kim, J.-M. Fabrication of conjugated polymer supramolecules in electrospun micro/nanofibers. *Macromol. Chem. Physic.* **2008,** 209, (21), 2194-2203.
141. Katti, D. S.; Robinson, K. W.; Ko, F. K.; Laurencin, C. T. Bioresorbable nanofiber-based systems for wound healing and drug delivery: Optimization of fabrication parameters. *J. Biomed. Mater. Res. Part B* **2004,** 70B, (2), 286-296.

142. Veleirinho, B.; Lopes-da-Silva, J. A. Application of electrospun poly(ethylene terephthalate) nanofiber mat to apple juice clarification. *Process Biochem.* **2009,** 44, (3), 353-356.
143. Stevens, M. M.; George, J. H. Exploring and engineering the cell surface interface. *Science* **2005,** 310, (5751), 1135-1138.
144. Zhang, Y. Z.; Wang, X.; Feng, Y.; Li, J.; Lim, C. T.; Ramakrishna, S. Coaxial electrospinning of (fluorescein isothiocyanate-conjugated bovine serum albumin)-encapsulated poly(epsilon-caprolactone) nanofibers for sustained release. *Biomacromolecules* **2006,** 7, (4), 1049-1057.
145. Zeng, J.; Yang, L. X.; Liang, Q. Z.; Zhang, X. F.; Guan, H. L.; Xu, X. L.; Chen, X. S.; Jing, X. B. Influence of the drug compatibility with polymer solution on the release kinetics of electrospun fiber formulation. *J. Control. Release* **2005,** 105, (1-2), 43-51.
146. Guo, G.; Fu, S.; Zhou, L.; Liang, H.; Fan, M.; Luo, F.; Qian, Z.; Wei, Y. Preparation of curcumin loaded poly([varepsilon]-caprolactone)-poly(ethylene glycol)-poly([varepsilon]-caprolactone) nanofibers and their in vitro antitumor activity against Glioma 9L cells. *Nanoscale* **2011,** 3, (9), 3825-3832.
147. Kurban, Z.; Lovell, A.; Bennington, S. M.; Jenkins, D. W. K.; Ryan, K. R.; Jones, M. O.; Skipper, N. T.; David, W. I. F. A solution selection model for coaxial electrospinning and its application to nanostructured hydrogen storage materials. *J. Phys. Chem. C* **2010,** 114, (49), 21201-21213.
148. Han, D.; Steckl, A. J. Superhydrophobic and oleophobic fibers by coaxial electrospinning. *Langmuir* **2009,** 25, (16), 9454-9462.
149. Jiang, H. L.; Hu, Y. Q.; Li, Y.; Zhao, P. C.; Zhu, K. J.; Chen, W. L. A facile technique to prepare biodegradable coaxial electrospun nanofibers for controlled release of bioactive agents. *J. Control. Release* **2005,** 108, (2-3), 237-243.
150. Huang, H.-H.; He, C.-L.; Wang, H.-S.; Mo, X.-M. Preparation of core-shell biodegradable microfibers for long-term drug delivery. *J. Biomed. Mater. Res. A* **2009,** 90A, (4), 1243-1251.
151. Li, D.; Wang, Y.; Xia, Y. Electrospinning of polymeric and ceramic nanofibers as uniaxially aligned arrays. *Nano Lett.* **2003,** 3, (8), 1167-1171.
152. Ayres, C.; Bowlin, G. L.; Henderson, S. C.; Taylor, L.; Shultz, J.; Alexander, J.; Telemeco, T. A.; Simpson, D. G. Modulation of anisotropy in electrospun tissue-engineering scaffolds: Analysis of fiber alignment by the fast Fourier transform. *Biomaterials* **2006,** 27, (32), 5524-5534.
153. Chew, S. Y.; Mi, R.; Hoke, A.; Leong, K. W. Aligned protein–polymer composite fibers enhance nerve regeneration: A potential tissue-engineering platform. *Adv. Funct. Mater.* **2007,** 17, (8), 1288-1296.
154. Wittmer, C. R.; Claudepierre, T.; Reber, M.; Wiedemann, P.; Garlick, J. A.; Kaplan, D.; Egles, C. Multifunctionalized Electrospun Silk Fibers Promote Axon Regeneration in the Central Nervous System. *Adv. Funct. Mater.* **2011,** 21, (22), 4232-4242.
155. Yang, F.; Murugan, R.; Wang, S.; Ramakrishna, S. Electrospinning of nano/micro scale poly(L-lactic acid) aligned fibers and their potential in neural tissue engineering. *Biomaterials* **2005,** 26, (15), 2603-2610.

156. Cipitria, A.; Skelton, A.; Dargaville, T. R.; Dalton, P. D.; Hutmacher, D. W. Design, fabrication and characterization of PCL electrospun scaffolds-a review. *J. Mater. Chem.* **2011,** 21, (26), 9419-9453.
157. Anderson, J. M.; Shive, M. S. Biodegradation and biocompatibility of PLA and PLGA microspheres. *Adv. Drug Deliv. Rev.* **1997,** 28, (1), 5-24.
158. Xie, J.; MacEwan, M. R.; Li, X.; Sakiyama-Elbert, S. E.; Xia, Y. Neurite Outgrowth on Nanofiber Scaffolds with Different Orders, Structures, and Surface Properties. *ACS Nano* **2009,** 3, (5), 1151-1159.
159. Bashur, C. A.; Dahlgren, L. A.; Goldstein, A. S. Effect of fiber diameter and orientation on fibroblast morphology and proliferation on electrospun poly(d,l-lactic-co-glycolic acid) meshes. *Biomaterials* **2006,** 27, (33), 5681-5688.
160. Zhang, X.; Baughman, C. B.; Kaplan, D. L. In vitro evaluation of electrospun silk fibroin scaffolds for vascular cell growth. *Biomaterials* **2008,** 29, (14), 2217-2227.
161. Zong, X.; Bien, H.; Chung, C.-Y.; Yin, L.; Fang, D.; Hsiao, B. S.; Chu, B.; Entcheva, E. Electrospun fine-textured scaffolds for heart tissue constructs. *Biomaterials* **2005,** 26, (26), 5330-5338.
162. Choi, J. S.; Lee, S. J.; Christ, G. J.; Atala, A.; Yoo, J. J. The influence of electrospun aligned poly(ε-caprolactone)/collagen nanofiber meshes on the formation of self-aligned skeletal muscle myotubes. *Biomaterials* **2008,** 29, (19), 2899-2906.
163. Chew, S. Y.; Mi, R.; Hoke, A.; Leong, K. W. The effect of the alignment of electrospun fibrous scaffolds on Schwann cell maturation. *Biomaterials* **2008,** 29, (6), 653-661.
164. Liu, Y.; Ji, Y.; Ghosh, K.; Clark, R. A. F.; Huang, L.; Rafailovichz, M. H. Effects of fiber orientation and diameter on the behavior of human dermal fibroblasts on electrospun PMMA scaffolds. *J. Biomed. Mater. Res. Part A* **2009,** 90A, (4), 1092-1106.
165. Xie, J.; Li, X.; Lipner, J.; Manning, C. N.; Schwartz, A. G.; Thomopoulos, S.; Xia, Y. "Aligned-to-random" nanofiber scaffolds for mimicking the structure of the tendon-to-bone insertion site. *Nanoscale* **2010,** 2, (6), 923-926.
166. Li, X.; Xie, J.; Lipner, J.; Yuan, X.; Thomopoulos, S.; Xia, Y. Nanofiber scaffolds with gradations in mineral content for mimicking the tendon-to-bone insertion site. *Nano Lett.* **2009,** 9, (7), 2763-2768.
167. Liu, W.; Yeh, Y.-C.; Lipner, J.; Xie, J.; Sung, H.-W.; Thomopoulos, S.; Xia, Y. Enhancing the Stiffness of Electrospun Nanofiber Scaffolds with a Controlled Surface Coating and Mineralization. *Langmuir* **2011,** 27, (15), 9088-9093.
168. Choi, S. W.; Zhang, Y.; Yeh, Y. C.; Wooten, A. L.; Xia, Y. N. Biodegradable porous beads and their potential applications in regenerative medicine. *J. Mater. Chem.* **2012,** 22, (23), 11442-11451.
169. Klossner, R. R.; Queen, H. A.; Coughlin, A. J.; Krause, W. E. Correlation of chitosan's rheological properties and its ability to electrospin. *Biomacromolecules* **2008,** 9, (10), 2947-2953.
170. Sollich, P.; Lequeux, F.; Hébraud, P.; Cates, M. E. Rheology of soft glassy materials. *Phys. Rev. Lett.* **1997,** 78, (10), 2020-2023.
171. Domagata, J.; Sady, M.; Grega, T.; Bonczar, G. Rheological properties and texture of yoghurts when oat-maltodextrin is used as a fat substitute. *Int. J. Food Prop.* **2006,** 9, (1), 1-11.

172. Sittikijyothin, W.; Torres, D.; Goncalves, M. P. Modelling the rheological behaviour of galactomannan aqueous solutions. *Carbohyd. Polym.* **2005,** 59, (3), 339-350.
173. Hyun, Y. H.; Lim, S. T.; Choi, H. J.; Jhon, M. S. Rheology of poly(ethylene oxide)/organoclay nanocomposites. *Macromolecules* **2001,** 34, (23), 8084-8093.
174. Ramaswamy, H. S.; Basak, S. Rheology of stirred yogurts. *J. Texture Stud.* **1991,** 22, (2), 231-241.
175. Ketz, R. J.; Prudhomme, R. K.; Graessley, W. W. Rheology of concentrated microgel solutions. *Rheol. Acta.* **1988,** 27, (5), 531-539.
176. Wang, X.; Lee, J.; Wang, Y.-W.; Huang, Q. Composition and rheological properties of β-Lactoglobulin/pectin coacervates: Effects of salt concentration and initial protein/polysaccharide ratio. *Biomacromolecules* **2007,** 8, (3), 992-997.
177. Liang, S.; Liu, L.; Huang, Q.; Yam, K. L. Unique rheological behavior of chitosan-modified nanoclay at highly hydrated state. *J. Phys. Chem B* **2009,** 113, (17), 5823-5828.
178. Kavanagh, G. M.; Ross-Murphy, S. B. Rheological characterisation of polymer gels. *Prog. Polym. Sci.* **1998,** 23, (3), 533-562.
179. Pipe, C. J.; Majmudar, T. S.; McKinley, G. H. High shear rate viscometry. *Rheol. Acta.* **2008,** 47, (5-6), 621-642.
180. Hong, D. W.; Liu, T. H.; Chu, I. M. Encapsulation of curcumin by methoxy poly(ethylene glycol-b-aromatic anhydride) micelles. *J. Appl. Polym. Sci.* **2011,** 122, (2), 898-907.
181. Shi, K.; Kokini, J. L.; Huang, Q. Engineering zein films with controlled surface morphology and hydrophilicity. *J. Agr. Food Chem.* **2009,** 57, (6), 2186-2192.
182. Hou, Y.; Cao, M.; Deng, M.; Wang, Y. Highly-ordered selective self-assembly of a trimeric cationic surfactant on a mica surface. *Langmuir* **2008,** 24, (19), 10572-10574.
183. Wang, X.; Wang, Y.-W.; Ruengruglikit, C.; Huang, Q. Effects of salt concentration on formation and dissociation of β-Lactoglobulin/pectin complexes. *J. Agr. Food Chem.* **2007,** 55, (25), 10432-10436.
184. Musevic, I.; Slak, G.; Blinc, R. Temperature controlled microstage for an atomic force microscope. *Rev. Sci. Instrum.* **1996,** 67, (7), 2554-2556.
185. Schönherr, H.; Frank, C. W. Ultrathin films of poly(ethylene oxides) on oxidized silicon. 2. *In situ* study of crystallization and melting by hot stage AFM. *Macromolecules* **2003,** 36, (4), 1199-1208.
186. Liu, G.; Li, J.; Shi, K.; Wang, S.; Chen, J. W.; Liu, Y.; Huang, Q. R. Composition, scecondary structure, and self-assembly of oat protein isolate. *J. Agr. Food Chem.* **2009,** 57, (11), 4552-4558.
187. Li, J.; Huang, Q. R. Structure study of Oat Protein Isolate in aqueous medium via synchrotron small angle X-ray scattering. *J. Agr. Food Chem.* **2013,** to be submitted.
188. Fishman, M. L.; Cooke, P. H. The structure of high-methoxyl sugar acid gels of citrus pectin as determined by AFM. *Carbohyd. Res.* **2009,** 344, (14), 1792-1797.
189. Mezzenga, R.; Schurtenberger, P.; Burbidge, A.; Michel, M. Understanding foods as soft materials. *Nat Mater* **2005,** 4, (10), 729-740.
190. Coppens, P.; Penner-Hahn, J. Introduction: X-rays in chemistry. *Chem. Rev.* **2001,** 101, (6), 1567-1568.

191. Beaucage, G.; Rane, S.; Sukumaran, S.; Satkowski, M. M.; Schechtman, L. A.; Doi, Y. Persistence length of isotactic poly(hydroxy butyrate). *Macromolecules* **1997,** 30, (14), 4158-4162.
192. Bras, W.; Ryan, A. J. Sample environments and techniques combined with small angle X-ray scattering. *Adv. Colloid Interface Sci.* **1998,** 75, (1), 1-43.
193. Roe, R. J., *Methods of X-ray and Neutron Scattering in Polymer Science*. Oxford University Press, USA: 2000.
194. Svergun, D. I.; Koch, M. H. J. Small-angle scattering studies of biological macromolecules in solution. *Rep. Prog. Phys.* **2003,** 66, (10), 1735-1782.
195. Yi, H. M.; Wu, L. Q.; Bentley, W. E.; Ghodssi, R.; Rubloff, G. W.; Culver, J. N.; Payne, G. F. Biofabrication with chitosan. *Biomacromolecules* **2005,** 6, (6), 2881-2894.
196. Espinosa-Andrews, H.; Baez-Gonzalez, J. G.; Cruz-Sosa, F.; Vernon-Carter, E. J. Gum Arabic-chitosan complex coacervation. *Biomacromolecules* **2007,** 8, (4), 1313-1318.
197. Luo, K.; Yin, J. B.; Song, Z. J.; Cui, L.; Cao, B.; Chen, X. S. Biodegradable interpolyelectrolyte complexes based on methoxy poly(ethylene glycol)-b-poly(alpha,L-glutamic acid) and chitosan. *Biomacromolecules* **2008,** 9, (10), 2653-2661.
198. Zhang, M. G.; Smith, A.; Gorski, W. Carbon nanotube-chitosan system for electrochemical sensing based on dehydrogenase enzymes. *Anal. Chem.* **2004,** 76, (17), 5045-5050.
199. Skotak, M.; Leonov, A. P.; Larsen, G.; Noriega, S.; Subramanian, A. Biocompatible and biodegradable ultrafine fibrillar scaffold materials for tissue engineering by facile grafting of L-lactide onto chitosan. *Biomacromolecules* **2008,** 9, (7), 1902-1908.
200. Han, E.; Shan, D.; Xue, H. G.; Cosnier, S. Hybrid material based on chitosan and layered double hydroxides: Characterization and application to the design of amperometric phenol biosensor. *Biomacromolecules* **2007,** 8, (3), 971-975.
201. Zhang, H.; Mardyani, S.; Chan, W. C. W.; Kumacheva, E. Design of biocompatible chitosan microgels for targeted pH-mediated intracellular release of cancer therapeutics. *Biomacromolecules* **2006,** 7, (5), 1568-1572.
202. Zhang, Y. Z.; Su, B.; Ramakrishna, S.; Lim, C. T. Chitosan nanofibers from an easily electrospinnable UHMWPEO-doped chitosan solution system. *Biomacromolecules* **2008,** 9, (1), 136-141.
203. Janes, K. A.; Calvo, P.; Alonso, M. J. Polysaccharide colloidal particles as delivery systems for macromolecules. *Adv. Drug Deliv. Rev.* **2001,** 47, (1), 83-97.
204. Pillai, O.; Panchagnula, R. Polymers in drug delivery. *Curr. Opin. Chem. Biol.* **2001,** 5, (4), 447-451.
205. Jang, K. I.; Lee, H. G. Stability of chitosan nanoparticles for l-ascorbic acid during heat treatment in aqueous solution. *J. Agr. Food Chem.* **2008,** 56, (6), 1936-1941.
206. Richardson, S. C. W.; Kolbe, H. J. V.; Duncan, R. Potential of low molecular mass chitosan as a DNA delivery system: biocompatibility, body distribution and ability to complex and protect DNA. *Int. J. Pharm.* **1999,** 178, (2), 231-243.
207. Liu, C. G.; Desai, K. G. H.; Chen, X. G.; Park, H. J. Preparation and characterization of nanoparticles containing trypsin based on hydrophobically modified chitosan. *J. Agric. Food Chem.* **2005,** 53, (5), 1728-1733.

208. Yao, Z.; Zhang, C.; Ping, Q. N.; Yu, L. L. L. A series of novel chitosan derivatives: Synthesis, characterization and micellar solubilization of paclitaxel. *Carbohyd. Polym.* **2007,** 68, (4), 781-792.
209. Huang, Y. P.; Yu, H. L.; Guo, L. A.; Huang, Q. R. Structure and self-assembly properties of a new chitosan-based amphiphile. *J. Phys. Chem B* **2010,** 114, (23), 7719-7726.
210. Carvalho, E.; Mateus, N.; Plet, B.; Pianet, I.; Dufourc, E.; De Freitas, V. Influence of wine pectic polysaccharides on the interactions between condensed tannins and salivary proteins. *J. Agric. Food Chem.* **2006,** 54, (23), 8936-8944.
211. Weinbreck, F.; Tromp, R. H.; de Kruif, C. G. Composition and structure of whey protein/gum arabic coacervates. *Biomacromolecules* **2004,** 5, (4), 1437-1445.
212. Gan, Q.; Wang, T. Chitosan nanoparticle as protein delivery carrier - Systematic examination of fabrication conditions for efficient loading and release. *Colloid Surf. B-Biointerfaces* **2007,** 59, (1), 24-34.
213. Ko, J. A.; Park, H. J.; Hwang, S. J.; Park, J. B.; Lee, J. S. Preparation and characterization of chitosan microparticles intended for controlled drug delivery. *Int. J. Pharm.* **2002,** 249, (1-2), 165-174.
214. Stepanek, P., Data analysis in dynamic light scattering In *Dynamic Light Scattering: The Method and Some Applications*, Brown, W., Ed. Oxford University Press: Oxford, 1993; pp 177-241.
215. Wang, X. Y.; Jiang, Y.; Wang, Y. W.; Huang, M. T.; Ho, C. T.; Huang, Q. R. Enhancing anti-inflammation activity of curcumin through O/W nanoemulsions. *Food Chem.* **2008,** 108, (2), 419-424.
216. Li, Y.; Lee, J.; Lal, J.; An, L.; Huang, Q. Effects of pH on the interactions and conformation of bovine serum albumin: Comparison between chemical force microscopy and small-angle neutron scattering. *J. Phys. Chem B* **2008,** 112, (12), 3797-3806.
217. Niebuhr, M.; Koch, M. H. J. Effects of urea and trimethylamine-N-oxide (TMAO) on the interactions of lysozyme in solution. *Biophys. J.* **2005,** 89, (3), 1978-1983.
218. Liu, G.; Li, J.; Shi, K.; Wang, S.; Chen, J.; Liu, Y.; Huang, Q. Composition, secondary structure, and self-assembly of oat protein isolate. *J. Agr. Food Chem.* **2009,** 57, (11), 4552-4558.
219. Calvo, P.; RemunanLopez, C.; VilaJato, J. L.; Alonso, M. J. Novel hydrophilic chitosan-polyethylene oxide nanoparticles as protein carriers. *J. Appl. Polym. Sci.* **1997,** 63, (1), 125-132.
220. Calvo, P.; RemunanLopez, C.; VilaJato, J. L.; Alonso, M. J. Chitosan and chitosan ethylene oxide propylene oxide block copolymer nanoparticles as novel carriers for proteins and vaccines. *Pharm. Res.* **1997,** 14, (10), 1431-1436.
221. Ta, H. T.; Han, H.; Larson, I.; Dass, C. R.; Dunstan, D. E. Chitosan-dibasic orthophosphate hydrogel: A potential drug delivery system. *Int. J. Pharm.* **2009,** 371, (1-2), 134-141.
222. Chenite, A.; Buschmann, M.; Wang, D.; Chaput, C.; Kandani, N. Rheological characterisation of thermogelling chitosan/glycerol-phosphate solutions. *Carbohyd. Polym.* **2001,** 46, (1), 39-47.
223. Chenite, A.; Chaput, C.; Wang, D.; Combes, C.; Buschmann, M. D.; Hoemann, C. D.; Leroux, J. C.; Atkinson, B. L.; Binette, F.; Selmani, A. Novel injectable neutral

solutions of chitosan form biodegradable gels in situ. *Biomaterials* **2000,** 21, (21), 2155-2161.
224. Higgins, J. S.; Benoît, H., *Polymers and neutron scattering*. Corr. ed.; Oxford University Press: Oxford, 1996; p xix, 436 p.
225. Huang, Q. R.; Yu, H. L.; Ru, Q. M. Bioavailability and Delivery of Nutraceuticals Using Nanotechnology. *J. Food Sci.* **2010,** 75, (1), 50-57.
226. Kataoka, K.; Harada, A.; Nagasaki, Y. Block copolymer micelles for drug delivery: design, characterization and biological significance. *Adv. Drug Deliv. Rev.* **2001,** 47, (1), 113-131.
227. Nederberg, F.; Appel, E.; Tan, J. P. K.; Kim, S. H.; Fukushima, K.; Sly, J.; Miller, R. D.; Waymouth, R. M.; Yang, Y. Y.; Hedrick, J. L. Simple Approach to Stabilized Micelles Employing Miktoarm Terpolymers and Stereocomplexes with Application in Paclitaxel Delivery. *Biomacromolecules* **2009,** 10, (6), 1460-1468.
228. Yuan, Y. Y.; Wang, Y. C.; Du, J. Z.; Wang, J. Synthesis of Amphiphilic ABC 3-Miktoarm Star Terpolymer by Combination of Ring-Opening Polymerization and "Click" Chemistry. *Macromolecules* **2008,** 41, (22), 8620-8625.
229. Uhrich, K. Hyperbranched polymers for drug delivery. *Trends Polym. Sci.* **1997,** 5, (12), 388-393.
230. Chauhan, A. S.; Sridevi, S.; Chalasani, K. B.; Jain, A. K.; Jain, S. K.; Jain, N. K.; Diwan, P. V. Dendrimer-mediated transdermal delivery: enhanced bioavailability of indomethacin. *J. Control. Release* **2003,** 90, (3), 335-343.
231. Wiwattanapatapee, R.; Carreno-Gomez, B.; Malik, N.; Duncan, R. Anionic PAMAM dendrimers rapidly cross adult rat intestine in vitro: A potential oral delivery system? *Pharm. Res.* **2000,** 17, (8), 991-998.
232. Astruc, D.; Boisselier, E.; Ornelas, C. t. Dendrimers designed for functions: From physical, photophysical, and supramolecular properties to applications in sensing, catalysis, molecular electronics, photonics, and nanomedicine. *Chem. Rev.* **2010,** 110, (4), 1857-1959.
233. Tomalia, D. A. Birth of a new macromolecular architecture: dendrimers as quantized building blocks for nanoscale synthetic polymer chemistry. *Prog. Polym. Sci.* **2005,** 30, (3–4), 294-324.
234. Bae, Y. H.; Yin, H. Stability issues of polymeric micelles. *J. Control. Release* **2008,** 131, (1), 2-4.
235. Lee, V. Y.; Havenstrite, K.; Tjio, M.; McNeil, M.; Blau, H. M.; Miller, R. D.; Sly, J. Nanogel star polymer architectures: A nanoparticle platform for modular programmable macromolecular self-assembly, intercellular transport, and dual-mode cargo delivery. *Adv. Mater.* **2011,** 23, (39), 4509-4515.
236. Kamber, N. E.; Jeong, W.; Waymouth, R. M.; Pratt, R. C.; Lohmeijer, B. G. G.; Hedrick, J. L. Organocatalytic ring-opening polymerization. *Chem. Rev.* **2007,** 107, (12), 5813-5840.
237. Kiesewetter, M. K.; Shin, E. J.; Hedrick, J. L.; Waymouth, R. M. Organocatalysis: Opportunities and challenges for polymer synthesis. *Macromolecules* **2010,** 43, (5), 2093-2107.
238. Albertsson, A.-C.; Varma, I. K. Recent developments in ring opening polymerization of lactones for biomedical applications. *Biomacromolecules* **2003,** 4, (6), 1466-1486.

239. Varma, I. K.; Albertsson, A.-C.; Rajkhowa, R.; Srivastava, R. K. Enzyme catalyzed synthesis of polyesters. *Prog. Polym. Sci.* **2005,** 30, (10), 949-981.
240. Agarwal, R.; Goel, S. K.; Behari, J. R. Detoxification and antioxidant effects of curcumin in rats experimentally exposed to mercury. *J. Appl. Toxicol.* **2010,** 30, (5), 457-468.
241. Bisht, K.; Choi, W. H.; Park, S. Y.; Chung, M. K.; Koh, W. S. Curcumin enhances non-inflammatory phagocytic activity of RAW264.7 cells. *Biochem. Biophys. Res. Commun.* **2009,** 379, (2), 632-636.
242. Ono, K.; Naiki, H.; Yamada, M. The development of preventives and therapeutics for Alzheimer's disease that inhibit the formation of beta-amyloid fibrils (fA beta), as well as destabilize preformed fA beta. *Curr. Pharm. Design* **2006,** 12, (33), 4357-4375.
243. Yu, S. W.; Shen, G. X.; Khor, T. O.; Kim, J. H.; Kong, A. N. T. Curcumin inhibits Akt/mammalian target of rapamycin signaling through protein phosphatase-dependent mechanism. *Mol. Cancer Ther.* **2008,** 7, (9), 2609-2620.
244. Nijenhuis, A. J.; Grijpma, D. W.; Pennings, A. J. Crosslinked poly(l-lactide) and poly(ϵ-caprolactone). *Polymer* **1996,** 37, (13), 2783-2791.
245. Fischetti, R.; Stepanov, S.; Rosenbaum, G.; Barrea, R.; Black, E.; Gore, D.; Heurich, R.; Kondrashkina, E.; Kropf, A. J.; Wang, S.; Zhang, K.; Irving, T. C.; Bunker, G. B. The BioCAT undulator beamline 18ID: a facility for biological non-crystalline diffraction and X-ray absorption spectroscopy at the Advanced Photon Source. *J. Synchrotron Radiat.* **2004,** 11, (5), 399-405.
246. Orthaber, D.; Bergmann, A.; Glatter, O. SAXS experiments on absolute scale with Kratky systems using water as a secondary standard. *J. Appl. Crystallogr.* **2000,** 33, (2), 218-225.
247. Jin, S.; Higashihara, T.; Jin, K. S.; Yoon, J.; Rho, Y.; Ahn, B.; Kim, J.; Hirao, A.; Ree, M. Synchrotron X-ray Scattering Characterization of the Molecular Structures of Star Polystyrenes with Varying Numbers of Arms. *J. Phys. Chem. B* **2010,** 114, (19), 6247-6257.
248. Roe, R.-J., *Methods of X-ray and neutron scattering in polymer science*. Oxford, University Press: New York, 2000.
249. Bale, H. D.; Schmidt, P. W. Small-Angle X-Ray-Scattering Investigation of Submicroscopic Porosity with Fractal Properties. *Phys. Rev. Lett.* **1984,** 53, (6), 596-599.
250. Higgins, J. S.; Benoit, H. C., *Polymers and neutron scattering*. Clarendon Press: Oxford, 2009.
251. Debye, P. The Intrinsic Viscosity of Polymer Solutions. *J. Chem. Phys.* **1946,** 14, (10), 636-639.
252. Glatter, O.; Kratky, O., *Small angle X-ray scattering*. Academic Press: New York, 1982.
253. Scherrenberg, R.; Coussens, B.; van Vliet, P.; Edouard, G.; Brackman, J.; de Brabander, E.; Mortensen, K. The Molecular Characteristics of Poly(propyleneimine) Dendrimers As Studied with Small-Angle Neutron Scattering, Viscosimetry, and Molecular Dynamics. *Macromolecules* **1998,** 31, (2), 456-461.
254. Willner, L.; Jucknischke, O.; Richter, D.; Roovers, J.; Zhou, L. L.; Toporowski, P. M.; Fetters, L. J.; Huang, J. S.; Lin, M. Y.; Hadjichristidis, N. Structural Investigation of Star Polymers in Solution by Small-Angle Neutron Scattering. *Macromolecules* **1994,** 27, (14), 3821-3829.

255. Alexandridis, P.; Yang, L. SANS Investigation of Polyether Block Copolymer Micelle Structure in Mixed Solvents of Water and Formamide, Ethanol, or Glycerol. *Macromolecules* **2000,** 33, (15), 5574-5587.
256. Moitzi, C.; Freiberger, N.; Glatter, O. Viscoelastic Wormlike Micellar Solutions Made from Nonionic Surfactants: Structural Investigations by SANS and DLS. *J. Phys. Chem. B* **2005,** 109, (33), 16161-16168.
257. Varade, D.; Rodríguez-Abreu, C.; Shrestha, L. K.; Aramaki, K. Wormlike Micelles in Mixed Surfactant Systems: Effect of Cosolvents. *J. Phys. Chem. B* **2007,** 111, (35), 10438-10447.
258. Shimizu, S.; Chan, H. S. Temperature dependence of hydrophobic interactions: A mean force perspective, effects of water density, and nonadditivity of thermodynamic signatures. *J. Chem. Phys.* **2000,** 113, (11), 4683-4700.
259. Connolly, S.; Rao, S. N.; Fitzmaurice, D. Characterization of Protein Aggregated Gold Nanocrystals. *J. Phys. Chem. B* **2000,** 104, (19), 4765-4776.
260. Pabisch, S.; Feichtenschlager, B.; Kickelbick, G.; Peterlik, H. Effect of interparticle interactions on size determination of zirconia and silica based systems – A comparison of SAXS, DLS, BET, XRD and TEM. *Chem. Phys. Lett.* **2012,** 521, (0), 91-97.
261. Jada, A.; Hurtrez, G.; Siffert, B.; Riess, G. Structure of polystyrene-block-poly(ethylene oxide) diblock copolymer micelles in water. *Macromol. Chem. Phys.* **1996,** 197, (11), 3697-3710.
262. Antonietti, M.; Heinz, S.; Schmidt, M.; Rosenauer, C. Determination of the Micelle Architecture of Polystyrene/Poly(4-vinylpyridine) Block Copolymers in Dilute Solution. *Macromolecules* **1994,** 27, (12), 3276-3281.
263. Sahu, A.; Kasoju, N.; Bora, U. Fluorescence Study of the Curcumin-Casein Micelle Complexation and Its Application as a Drug Nanocarrier to Cancer Cells. *Biomacromolecules* **2008,** 9, (10), 2905-2912.
264. Sou, K.; Inenaga, S.; Takeoka, S.; Tsuchida, E. Loading of curcumin into macrophages using lipid-based nanoparticles. *Int. J. Pharm.* **2008,** 352, (1-2), 287-293.
265. Lapenna, S.; Bilia, A. R.; Morris, G. A.; Nilsson, M. Novel Artemisinin and Curcumin Micellar Formulations: Drug Solubility Studies by NMR Spectroscopy. *J. Pharm. Sci.* **2009,** 98, (10), 3666-3675.
266. Sahu, A.; Bora, U.; Kasoju, N.; Goswami, P. Synthesis of novel biodegradable and self-assembling methoxy poly(ethylene glycol)-palmitate nanocarrier for curcumin delivery to cancer cells. *Acta Biomater.* **2008,** 4, (6), 1752-1761.
267. Ma, Z. S.; Haddadi, A.; Molavi, O.; Lavasanifar, A.; Lai, R.; Samuel, J. Micelles of poly(ethylene oxide)-b-poly(epsilon-caprolactone) as vehicles for the solubilization, stabilization, and controlled delivery of curcumin. *J. Biomed. Mater. Res. Part A* **2008,** 86A, (2), 300-310.
268. Huang, Y.; Yu, H.; Guo, L.; Huang, Q. Structure and self-assembly properties of a new chitosan-based amphiphile. *J. Phys. Chem. B* **2010,** 114, (23), 7719-7726.
269. Yu, H. L.; Huang, Q. R. Enhanced in vitro anti-cancer activity of curcumin encapsulated in hydrophobically modified starch. *Food Chem.* **2010,** 119, (2), 669-674.
270. Palmgren, R.; Karlsson, S.; Albertsson, A.-C. Synthesis of degradable crosslinked polymers based on 1,5-dioxepan-2-one and crosslinker of bis-ϵ-caprolactone type. *J. Polym. Sci., Part A: Polym. Chem.* **1997,** 35, (9), 1635-1649.

271. Harding, K. G.; Dennis, J. S.; von Blottnitz, H.; Harrison, S. T. L. Environmental analysis of plastic production processes: Comparing petroleum-based polypropylene and polyethylene with biologically-based poly-beta-hydroxybutyric acid using life cycle analysis. *J. Biotechnol.* **2007,** 130, (1), 57-66.
272. Yu, L.; Dean, K.; Li, L. Polymer blends and composites from renewable resources. *Prog. Polym. Sci.* **2006,** 31, (6), 576-602.
273. Andersson, C.; Jarnstrom, L.; Fogden, A.; Mira, I.; Voit, W.; Zywicki, S.; Bartkowiak, A. Preparation and Incorporation of Microcapsules in Functional Coatings for Self-healing of Packaging Board. *Packag. Technol. Sci.* **2009,** 22, (5), 275-291.
274. Lankey, R. L.; Anastas, P. T. Life-cycle approaches for assessing green chemistry technologies. *Ind. Eng. Chem. Res.* **2002,** 41, (18), 4498-4502.
275. Liu, J.; Tolvgard, A.; Malmodin, J.; Lai, Z. H. A reliable and environmentally friendly packaging technology - Flip-chip joining using anisotropically conductive adhesive. *IEEE Trans. Compon. Packaging Technol.* **1999,** 22, (2), 186-190.
276. Shukla, R.; Cheryan, M. Zein: the industrial protein from corn. *Ind. Crop. Prod.* **2001,** 13, (3), 171-192.
277. Li, Y.; Xia, Q.; Shi, K.; Huang, Q. Scaling behaviors of α-zein in acetic acid solutions. *J. Phys. Chem B* **2011,** 115, (32), 9695-9702.
278. Matsushima, N.; Danno, G.; Takezawa, H.; Izumi, Y. Three-dimensional structure of maize alpha-zein proteins studied by small-angle X-ray scattering. *Biochim. Biophys. Acta-Protein Struct. Molec. Enzym.* **1997,** 1339, (1), 14-22.
279. Tatham, A. S.; Field, J. M.; Morris, V. J.; Ianson, K. J.; Cardle, L.; Dufton, M. J.; Shewry, P. R. Solution conformational analysis of the alpha-zein proteins of maize. *J. Biol. Chem.* **1993,** 268, (35), 26253-26259.
280. Momany, F. A.; Sessa, D. J.; Lawton, J. W.; Selling, G. W.; Hamaker, S. A. H.; Willett, J. L. Structural characterization of alpha-zein. *J. Agric. Food Chem.* **2006,** 54, (2), 543-547.
281. Shi, K.; Kokini, J. L.; Huang, Q. Engineering Zein Films with Controlled Surface Morphology and Hydrophilicity. *J. Agric. Food Chem.* **2009,** 57, (6), 2186-2192.
282. Shi, K.; Huang, Y. P.; Yu, H. L.; Lee, T. C.; Huang, Q. R. Reducing the Brittleness of Zein Films through Chemical Modification. *J. Agric. Food Chem.* **2011,** 59, (1), 56-61.
283. Lawton, J. W. Zein: A history of processing and use. *Cereal Chem.* **2002,** 79, (1), 1-18.
284. Lawton, J. W. Plasticizers for zein: Their effect on tensile properties and water absorption of zein films. *Cereal Chem.* **2004,** 81, (1), 1-5.
285. Paul, D. R.; Barlow, J. W.; Keskkula, H., Encyclopedia of polymer science and engineering. In Mark, H. F., Ed. Wiley: New York, 1985; Vol. 12.
286. Ghanbarzadeh, B.; Musavi, M.; Oromiehie, A. R.; Rezayi, K.; Rad, E. R.; Milani, J. Effect of plasticizing sugars on water vapor permeability, surface energy and microstructure properties of zein films. *LWT-Food Sci. Technol.* **2007,** 40, (7), 1191-1197.
287. Santosa, F. X. B.; Padua, G. W. Tensile properties and water absorption of zein sheets plasticized with oleic and linoleic acids. *J. Agric. Food Chem.* **1999,** 47, (5), 2070-2074.
288. Woods, K.; Selling, G.; Cooke, P. Compatible Blends of Zein and Polyvinylpyrrolidone. *J. Polym. Environ.* **2009,** 17, (2), 115-122.

289. Selling, G.; Biswas, A. Blends of Zein and Nylon-6. *J. Polym. Environ.* **2012,** 20, (3), 631-637.
290. Senna, M. M.; Salmieri, S.; El-Naggar, A. W.; Safrany, A.; Lacroix, M. Improving the Compatibility of Zein/Poly(vinyl alcohol) Blends by Gamma Irradiation and Graft Copolymerization of Acrylic Acid. *J. Agric. Food Chem.* **2010,** 58, (7), 4470-4476.
291. Selling, G. W.; Sessa, D. J.; Palmquist, D. E. Effect of water and tri(ethylene) glycol on the rheological properties of zein. *Polymer* **2004,** 45, (12), 4249-4255.
292. Bohorquez, M.; Koch, C.; Trygstad, T.; Pandit, N. A study of the temperature-dependent micellization of pluronic F127. *J. Colloid Interface Sci.* **1999,** 216, (1), 34-40.
293. Desai, P. R.; Jain, N. J.; Sharma, R. K.; Bahadur, P. Effect of additives on the micellization of PEO/PPO/PEO block copolymer F127 in aqueous solution. *Colloid Surf. A-Physicochem. Eng. Asp.* **2001,** 178, (1-3), 57-69.
294. Ivanova, R.; Lindman, B.; Alexandridis, P. Evolution in structural polymorphism of pluronic F127 poly(ethylene oxide)-poly(propylene oxide) block copolymer in ternary systems with water and pharmaceutically acceptable organic solvents: From "glycols" to "oils". *Langmuir* **2000,** 16, (23), 9058-9069.
295. Li, Y. Q.; Shi, T. F.; Sun, Z. Y.; An, L. J.; Huang, Q. R. Investigation of sol-gel transition in Pluronic F127/D2O solutions using a combination of small-angle neutron scattering and Monte Carlo simulation. *J. Phys. Chem. B* **2006,** 110, (51), 26424-26429.
296. Desai, S. D.; Blanchard, J. In vitro evaluation of pluronic F127-based controlled-release ocular delivery systems for pilocarpine. *J. Pharm. Sci.* **1998,** 87, (2), 226-230.
297. Mao, C.; Liang, C. X.; Mao, Y. Q.; Li, L.; Hou, X. M.; Shen, J. Modification of polyethylene with Pluronics F127 for improvement of blood compatibility. *Colloid Surf. B-Biointerfaces* **2009,** 74, (1), 362-365.
298. Xie, Y.; Hu, N. F.; Liu, H. Y. Bioelectrocatalytic reactivity of myoglobin in layer-by-layer films assembled with triblock copolymer Pluronic F127. *J. Electroanal. Chem.* **2009,** 630, (1-2), 63-68.
299. Wei, Z.; Hao, J. G.; Yuan, S.; Li, Y. J.; Juan, W.; Sha, X. Y.; Fang, X. L. Paclitaxel-loaded Pluronic P123/F127 mixed polymeric micelles: Formulation, optimization and in vitro characterization. *Int. J. Pharm.* **2009,** 376, (1-2), 176-185.
300. Naik, S. P.; Yamakita, S.; Ogura, M.; Okubo, T. Studies on mesoporous silica films synthesized using F127, a triblock co-polymer. *Micropor. Mesopor. Mat.* **2004,** 75, (1-2), 51-59.
301. Naik, S. P.; Yamakita, S.; Sasaki, Y.; Ogura, M.; Okubo, T. Synthesis of mesoporous silica thin film with three-dimensional accessible pore structure. *Chem. Lett.* **2004,** 33, (9), 1078-1079.
302. Fairclough, J. P. A.; Yu, G.-E.; Mai, S.-M.; Crothers, M.; Mortensen, K.; Ryan, A. J.; Booth; Colin First observation of an ordered microphase in melts of poly(oxyethylene)-poly(oxypropylene) block copolymers. *Phys. Chem. Chem. Phys.* **2000,** 2, (7), 1503-1507.
303. Alexandridis, P. Structural Polymorphism of Poly(ethylene oxide)−Poly(propylene oxide) Block Copolymers in Nonaqueous Polar Solvents. *Macromolecules* **1998,** 31, (20), 6935-6942.
304. Alexandridis, P.; Zhou, D.; Khan, A. Lyotropic Liquid Crystallinity in Amphiphilic Block Copolymers: Temperature Effects on Phase Behavior and Structure

for Poly(ethylene oxide)-b-poly(propylene oxide)-b-poly(ethylene oxide) Copolymers of Different Composition. *Langmuir* **1996,** 12, (11), 2690-2700.
305. Alexandridis, P. Structural polymorphism of poly(ethylene oxide)-poly(propylene oxide) block copolymers in nonaqueous polar solvents. *Macromolecules* **1998,** 31, (20), 6935-6942.
306. Matsen, M. W.; Thompson, R. B. Equilibrium behavior of symmetric ABA triblock copolymer melts. *J. Chem. Phys.* **1999,** 111, (15), 7139-7146.
307. Mayes, A. M.; Delacruz, M. O. Microphase separation in multiblock copolymer melts. *J. Chem. Phys.* **1989,** 91, (11), 7228-7235.
308. Mayes, A. M.; Delacruz, M. O. Concentration fluctuation effects on disorder-order transitions in block copolymer melts. *J. Chem. Phys.* **1991,** 95, (6), 4670-4677.
309. Fischer, H.; Polikarpov, I.; Craievich, A. F. Average protein density is a molecular-weight-dependent function. *Protein Sci.* **2004,** 13, (10), 2825-2828.
310. Johnson, W. C.; Wang, J.; Chen, Z. Surface structures and properties of polystyrene/poly(methyl methacrylate) blends and copolymers. *J. Phys. Chem B* **2005,** 109, (13), 6280-6286.
311. Ghanbarzadeh, B.; Oromiehie, A. R.; Musavi, M.; D-Jomeh, Z. E.; Rad, E. R.; Milani, W. Effect of plasticizing sugars on rheological and thermal properties of zein resins and mechanical properties of zein films. *Food Res. Int.* **2006,** 39, (8), 882-890.
312. Su, Y. L.; Wang, J.; Liu, H. Z. FTIR spectroscopic investigation of effects of temperature and concentration on PEO-PPO-PEO block copolymer properties in aqueous solutions. *Macromolecules* **2002,** 35, (16), 6426-6431.
313. Zhu, L.; Calhoun, B. H.; Ge, Q.; Quirk, R. P.; Cheng, S. Z. D.; Thomas, E. L.; Hsiao, B. S.; Yeh, F.; Liu, L.; Lotz, B. Initial-Stage Growth Controlled Crystal Orientations in Nanoconfined Lamellae of a Self-Assembled Crystalline−Amorphous Diblock Copolymer. *Macromolecules* **2001,** 34, (5), 1244-1251.
314. Chen, E. Q.; Jing, A. J.; Weng, X.; Huang, P.; Lee, S. W.; Cheng, S. Z. D.; Hsiao, B. S.; Yeh, F. J. In situ observation of low molecular weight poly(ethylene oxide) crystal melting, recrystallization. *Polymer* **2003,** 44, (19), 6051-6058.
315. Cheng, S. Z. D.; Chen, J.; Barley, J. S.; Zhang, A.; Habenschuss, A.; Zschack, P. R. Isothermal thickening and thinning processes in low molecular-weight poly(ethylene oxide) fractions crystallized from the melt. 3. Molecular weight dependence. *Macromolecules* **1992,** 25, (5), 1453-1460.
316. Cheng, S. Z. D.; Wu, S. S.; Chen, J.; Zhuo, Q.; Quirk, R. P.; von Meerwall, E. D.; Hsiao, B. S.; Habenschuss, A.; Zschack, P. R. Isothermal thickening and thinning processes in low-molecular-weight poly(ethylene oxide) fractions crystallized from the melt. 4. End-group dependence. *Macromolecules* **1993,** 26, (19), 5105-5117.
317. Cheng, S. Z. D.; Zhang, A.; Barley, J. S.; Chen, J.; Habenschuss, A.; Zschack, P. R. Isothermal thickening and thinning processes in low-molecular-weight poly(ethylene oxide) fractions. 1. From nonintegral-folding to integral-folding chain crystal transitions. *Macromolecules* **1991,** 24, (13), 3937-3944.
318. Zhang, F.; Stühn, B. Crystallization and melting behavior of low molar weight PEO–PPO–PEO triblock copolymers. *Colloid Polym. Sci.* **2007,** 285, (4), 371-379.
319. Barry, B. W. Novel mechanisms and devices to enable successful transdermal drug delivery. *Eur. J. Pharm. Sci.* **2001,** 14, (2), 101-114.

320. Prausnitz, M. R.; Mitragotri, S.; Langer, R. Current status and future potential of transdermal drug delivery. *Nat Rev Drug Discov* **2004,** 3, (2), 115-124.
321. Liivak, O.; Blye, A.; Shah, N.; Jelinski, L. W. A microfabricated wet-spinning apparatus To spin fibers of silk proteins. Structure−property correlations. *Macromolecules* **1998,** 31, (9), 2947-2951.
322. Sharpe, I. D.; Ismail, A. F.; Shilton, S. J. A study of extrusion shear and forced convection residence time in the spinning of polysulfone hollow fiber membranes for gas separation. *Sep. Purif. Technol.* **1999,** 17, (2), 101-109.
323. Begenir, A.; Michielsen, S.; Pourdeyhimi, B. Melt-blowing thermoplastic polyurethane and polyether-block-amide elastomers: Effect of processing conditions and crystallization on web properties. *Polym. Eng. Sci.* **2009,** 49, (7), 1340-1349.
324. Lee, Y. E.; Wadsworth, L. C. Fiber and web formation of melt-blown thermoplastic polyurethane polymers. *J. Appl. Polym. Sci.* **2007,** 105, (6), 3724-3727.
325. Lewandowski, Z.; Ziabicki, A.; Jarecki, L. The nonwovens formation in the melt-blown process. *Fibres Text. East. Eur.* **2007,** 15, (5-6), 77-81.
326. Ma, M.; Hill, R. M.; Lowery, J. L.; Fridrikh, S. V.; Rutledge, G. C. Electrospun poly(styrene-block-dimethylsiloxane) block copolymer fibers exhibiting superhydrophobicity. *Langmuir* **2005,** 21, (12), 5549-5554.
327. Zhang, Y.; Rutledge, G. C. Electrical conductivity of electrospun polyaniline and polyaniline-blend fibers and mats. *Macromolecules* **2012,** 45, (10), 4238-4246.
328. Kim, C.; Yang, K. S.; Kojima, M.; Yoshida, K.; Kim, Y. J.; Kim, Y. A.; Endo, M. Fabrication of electrospinning-derived carbon nanofiber webs for the anode material of lithium-ion secondary batteries. *Adv. Funct. Mater.* **2006,** 16, (18), 2393-2397.
329. Bhattarai, S. R.; Bhattarai, N.; Yi, H. K.; Hwang, P. H.; Cha, D. I.; Kim, H. Y. Novel biodegradable electrospun membrane: scaffold for tissue engineering. *Biomaterials* **2004,** 25, (13), 2595-2602.
330. Zeng, J.; Xu, X.; Chen, X.; Liang, Q.; Bian, X.; Yang, L.; Jing, X. Biodegradable electrospun fibers for drug delivery. *J. Control. Release* **2003,** 92, (3), 227-231.
331. Liu, L. H.; Dzenis, Y. A. Analysis of the effects of the residual charge and gap size on electrospun nanofiber alignment in a gap method. *Nanotechnology* **2008,** 19, (35).
332. Park, S. H.; Yang, D. Y. Fabrication of Aligned Electrospun Nanofibers by Inclined Gap Method. *J. Appl. Polym. Sci.* **2011,** 120, (3), 1800-1807.
333. Doshi, J.; Reneker, D. H. Electrospinning process and applications of electrospun fibers. *J. Electrostat.* **1995,** 35, (2–3), 151-160.
334. He, C. L.; Huang, Z. M.; Han, X. J. Fabrication of drug-loaded electrospun aligned fibrous threads for suture applications. *J. Biomed. Mater. Res. Part A* **2009,** 89A, (1), 80-95.
335. Mathew, G.; Hong, J. P.; Rhee, J. M.; Leo, D. J.; Nah, C. Preparation and anisotropic mechanical behavior of highly-oriented electrospun poly(butylene terephthalate) fibers. *J. Appl. Polym. Sci.* **2006,** 101, (3), 2017-2021.
336. Zussman, E.; Theron, A.; Yarin, A. L. Formation of nanofiber crossbars in electrospinning. *Appl. Phys. Lett.* **2003,** 82, (6), 973-975.
337. Mo, X. M.; Xu, C. Y.; Kotaki, M.; Ramakrishna, S. Electrospun P(LLA-CL) nanofiber: a biomimetic extracellular matrix for smooth muscle cell and endothelial cell proliferation. *Biomaterials* **2004,** 25, (10), 1883-1890.

338. Mottaghitalab, F.; Farokhi, M.; Mottaghitalab, V.; Ziabari, M.; Divsalar, A.; Shokrgozar, M. A. Enhancement of neural cell lines proliferation using nano-structured chitosan/poly(vinyl alcohol) scaffolds conjugated with nerve growth factor. *Carbohyd. Polym.* **2011,** 86, (2), 526-535.
339. Patel, S.; Kurpinski, K.; Quigley, R.; Gao, H.; Hsiao, B. S.; Poo, M.-M.; Li, S. Bioactive Nanofibers: Synergistic Effects of Nanotopography and Chemical Signaling on Cell Guidance. *Nano Lett.* **2007,** 7, (7), 2122-2128.
340. Li, Y.; Lim, L. T.; Kakuda, Y. Electrospun zein fibers as carriers to stabilize (−)-epigallocatechin gallate. *J. Food Sci.* **2009,** 74, (3), C233-C240.
341. Taepaiboon, P.; Rungsardthong, U.; Supaphol, P. Vitamin-loaded electrospun cellulose acetate nanofiber mats as transdermal and dermal therapeutic agents of vitamin A acid and vitamin E. *Eur. J. Pharm. Biopharm.* **2007,** 67, (2), 387-397.
342. Verreck, G.; Chun, I.; Rosenblatt, J.; Peeters, J.; Dijck, A. V.; Mensch, J.; Noppe, M.; Brewster, M. E. Incorporation of drugs in an amorphous state into electrospun nanofibers composed of a water-insoluble, nonbiodegradable polymer. *J. Control. Release* **2003,** 92, (3), 349-360.
343. Cui, W.; Li, X.; Zhu, X.; Yu, G.; Zhou, S.; Weng, J. Investigation of Drug Release and Matrix Degradation of Electrospun Poly(dl-lactide) Fibers with Paracetanol Inoculation. *Biomacromolecules* **2006,** 7, (5), 1623-1629.
344. Kenawy, E.-R.; Bowlin, G. L.; Mansfield, K.; Layman, J.; Simpson, D. G.; Sanders, E. H.; Wnek, G. E. Release of tetracycline hydrochloride from electrospun poly(ethylene-co-vinylacetate), poly(lactic acid), and a blend. *J. Control. Release* **2002,** 81, (1–2), 57-64.
345. Chew, S. Y.; Wen, J.; Yim, E. K. F.; Leong, K. W. Sustained release of proteins from electrospun biodegradable fibers. *Biomacromolecules* **2005,** 6, (4), 2017-2024.
346. Kim, T. G.; Lee, D. S.; Park, T. G. Controlled protein release from electrospun biodegradable fiber mesh composed of poly(ε-caprolactone) and poly(ethylene oxide). *Int. J. Pharm.* **2007,** 338, (1–2), 276-283.
347. Jia, H.; Zhu, G.; Vugrinovich, B.; Kataphinan, W.; Reneker, D. H.; Wang, P. Enzyme-Carrying Polymeric Nanofibers Prepared via Electrospinning for Use as Unique Biocatalysts. *Biotechnol. Progr.* **2002,** 18, (5), 1027-1032.
348. Luu, Y. K.; Kim, K.; Hsiao, B. S.; Chu, B.; Hadjiargyrou, M. Development of a nanostructured DNA delivery scaffold via electrospinning of PLGA and PLA–PEG block copolymers. *J. Control. Release* **2003,** 89, (2), 341-353.
349. Fernandez, A.; Torres-Giner, S.; Lagaron, J. M. Novel route to stabilization of bioactive antioxidants by encapsulation in electrospun fibers of zein prolamine. *Food Hydrocolloid* **2009,** 23, (5), 1427-1432.
350. Jiang, H.; Zhao, P.; Zhu, K. Fabrication and Characterization of Zein-Based Nanofibrous Scaffolds by an Electrospinning Method. *Macromol. Biosci.* **2007,** 7, (4), 517-525.
351. Selling, G. W.; Biswas, A.; Patel, A.; Walls, D. J.; Dunlap, C.; Wei, Y. Impact of solvent on electrospinning of zein and analysis of resulting fibers. *Macromol. Chem. Physic.* **2007,** 208, (9), 1002-1010.
352. Yao, C.; Li, X.; Song, T. Electrospinning and crosslinking of zein nanofiber mats. *J. Appl. Polym. Sci.* **2007,** 103, (1), 380-385.

353. Bisht, K.; Choi, W. H.; Park, S. Y.; Chung, M. K.; Koh, W. S. Curcumin enhances non-inflammatory phagocytic activity of RAW264.7 cells. *Biochem. Bioph. Res. Co.* **2009,** 379, (2), 632-636.
354. Ono, K.; Naiki, H.; Yamada, M. The development of preventives and therapeutics for Alzheimers disease that inhibit the formation of β-Amyloid Fibrils (fAβ), as Well as Destabilize Preformed fAβ. *Curr. Pharm. Design* **2006,** 12, (33), 4357-4375.
355. Yu, S.; Shen, G.; Khor, T. O.; Kim, J.-H.; Kong, A.-N. T. Curcumin inhibits Akt/mammalian target of rapamycin signaling through protein phosphatase-dependent mechanism. *Mol. Cancer Ther.* **2008,** 7, (9), 2609-2620.
356. Selling, G. W.; Lawton, J.; Bean, S.; Dunlap, C.; Sessa, D. J.; Willett, J. L.; Byars, J. Rheological studies utilizing various lots of zein in N,N-dimethylformamide solutions. *J. Agr. Food Chem.* **2005,** 53, (23), 9050-9055.
357. Sahu, A.; Kasoju, N.; Bora, U. Fluorescence study of the curcumin−casein micelle complexation and its application as a drug nanocarrier to cancer cells. *Biomacromolecules* **2008,** 9, (10), 2905-2912.
358. Koski, A.; Yim, K.; Shivkumar, S. Effect of molecular weight on fibrous PVA produced by electrospinning. *Mater. Lett.* **2004,** 58, (3–4), 493-497.
359. Jiang, H.; Fang, D.; Hsiao, B. S.; Chu, B.; Chen, W. Optimization and characterization of dextran membranes prepared by electrospinning. *Biomacromolecules* **2004,** 5, (2), 326-333.
360. Le Bourvellec, C.; Renard, C. Interactions between polyphenols and macromolecules: Quantification methods and mechanisms. *Cr. Rev. Food Sci.* **2012,** 52, (1-3), 213-248.
361. Kamlet, M. J.; Abboud, J. L. M.; Abraham, M. H.; Taft, R. W. Linear solvation energy relationships. 23. A comprehensive collection of the solvatochromic parameters, .pi.*, .alpha., and .beta., and some methods for simplifying the generalized solvatochromic equation. *J. Org. Chem.* **1983,** 48, (17), 2877-2887.
362. Kamlet, M. J.; Taft, R. W. The solvatochromic comparison method. I. The .beta.-scale of solvent hydrogen-bond acceptor (HBA) basicities. *J. Am. Chem. Soc.* **1976,** 98, (2), 377-383.
363. Suwantong, O.; Opanasopit, P.; Ruktanonchal, U.; Supaphol, P. Electrospun cellulose acetate fiber mats containing curcumin and release characteristic of the herbal substance. *Polymer* **2007,** 48, (26), 7546-7557.
364. Fridrikh, S. V.; Yu, J. H.; Brenner, M. P.; Rutledge, G. C. Controlling the fiber diameter during electrospinning. *Phys. Rev. Lett.* **2003,** 90, (14).
365. Kiselev, P.; Rosell-Llompart, J. Highly aligned electrospun nanofibers by elimination of the whipping motion. *J. Appl. Polym. Sci.* **2012,** 125, (3), 2433-2441.
366. Martynova, L.; Locascio, L. E.; Gaitan, M.; Kramer, G. W.; Christensen, R. G.; MacCrehan, W. A. Fabrication of plastic microfluid channels by imprinting methods. *Anal. Chem.* **1997,** 69, (23), 4783-4789.
367. Jaworek, A.; Sobczyk, A. T. Electrospraying route to nanotechnology: An overview. *J. Electrostat.* **2008,** 66, (3–4), 197-219.
368. Yang, C.-H.; Huang, K.-S.; Lin, P.-W.; Lin, Y.-C. Using a cross-flow microfluidic chip and external crosslinking reaction for monodisperse TPP-chitosan microparticles. *Sensor Actuat. B-Chem* **2007,** 124, (2), 510-516.

369. Arya, N.; Chakraborty, S.; Dube, N.; Katti, D. S. Electrospraying: A facile technique for synthesis of chitosan-based micro/nanospheres for drug delivery applications. *J. Biomed. Mater. Res. B* **2009,** 88B, (1), 17-31.
370. Nie, W.; Yu, D. G.; Branford-White, C.; Shen, X. X.; Zhu, L. M. Electrospun zein-PVP fibre composite and its potential medical application. *Mater. Res. Innov.* **2012,** 16, (1), 14-18.
371. Ganan-Calvo, A. M.; Davila, J.; Barrero, A. Current and droplet size in the electrospraying of liquids. Scaling laws. *J. Aerosol. Sci.* **1997,** 28, (2), 249-275.
372. Gomez-Estaca, J.; Balaguer, M. P.; Gavara, R.; Hernandez-Munoz, P. Formation of zein nanoparticles by electrohydrodynamic atomization: Effect of the main processing variables and suitability for encapsulating the food coloring and active ingredient curcumin. *Food Hydrocolloid* **2012,** 28, (1), 82-91.
373. Yu, H.; Huang, Q. Enhanced in vitro anti-cancer activity of curcumin encapsulated in hydrophobically modified starch. *Food Chem.* **2010,** 119, (2), 669-674.
374. Dong, D. C.; Winnik, M. A. The Py scale of solvent polarities. *Can. J. Chem.-Rev. Can. Chim.* **1984,** 62, (11), 2560-2565.
375. Lee, H.; Zeng, F. Q.; Dunne, M.; Allen, C. Methoxy poly(ethylene glycol)-block-poly(delta-valerolactone) copolymer micelles for formulation of hydrophobic drugs. *Biomacromolecules* **2005,** 6, (6), 3119-3128.

Curriculum Vitae

Ji Li

Education

09/2007 – 05/2013	Ph.D. Food Science Department, Rutgers, the State University of New Jersey Dissertation advisor: Qingrong Huang Dissertation topic: "Towards biopolymer platforms via small molecule crosslinking, organocatalytic ring-opening polymerization, and electrospinning"
09/2003 – 07/2007	B.S. Food Science Department, Shanghai Jiaotong University
09/2004 – 07/2007	B.A. English Department, Shanghai Jiaotong University

Publication

1. **Li, Ji**; Rong, P.; and Huang, Q. R. (2012) Characterization of food Materials in multi-Length scales using small-angle X-ray scattering and nuclear magnetic resonance: Principle and applications. In "Nanotechnology in the Food, Beverage and Nutraceutical Industries", Huang, Q. R. ed., Woodhead Publishing Limited, Chapter 6, 149-176.

2. Gang Liu, **Ji Li**, Ke Shi, Su Wang, Jiwang Chen, Ying Liu, Qingrong Huang. Composition, secondary structure, and self-assembly of oat protein isolates, *Journal of Agriculture and Food Chemistry*, **2009**, *57*, 4552–4558.

3. Francesco Donsi, Yu-wen Wang, **Ji Li**, Qingrong Huang. Preparation of submicron curcumin dispersions by high pressure homogenization, *Journal of Agriculture and Food Chemistry*, **2010**, 58, 2848-2853.

4. Bing Hu, Shushu Wang, **Ji Li**, Xiaoxiong Zeng, Qingrong Huang. Assembly of bioactive peptides and chitosan nanocomplexes, *Journal of Physical Chemistry B*, **2011**, 115, 7515-7523.

5. Hailong Yu, **Ji Li**, Ke Shi, Qingrong Huang. Elevated cellular antioxidant activity of curcuminoids encapsulated in modified epsilon polylysine micelles, *Food and Function*, **2011**, 2, 373-380.

6. **Ji Li** and Qingrong Huang, Rheological properties of chitosan-tripolyphosphate complexes: from suspensions to microgels, *Carbohydrate Polymers*, **2012**, 87, 1670-1677.

7. Fei Xu, **Ji Li**, Vikas Jain, Raymond S. Tu, Qingrong Huang, Vikas Nanda. Compositional control of higher order assembly using synthetic collagen peptides, *Journal of the American Chemical Society*, **2012**, 134, 47-50.

8. Yunqi Li, **Ji Li**, Qiuyang Xia, Boce Zhang, Qin Wang, Qingrong Huang. Understanding the dissolution of α-zein in aqueous ethanol and acetic acid solutions. *Journal of Physical Chemistry B,* **2012**, *116*, 12057–12064.

9. **Ji Li**, Yunqi Li, Tung-Ching Lee, Qingrong Huang. Controlling the flexibility of zein films through the competition of plasticizing effect and crystal formation of Pluronic F127. *Journal of Agricultural and Food Chemistry*, **2013**, 61, 1309-1318.

10. Nicolás I. Torres, Katia Sutyak Noll, Shiqi Xu, **Ji Li**, Qingrong Huang, Patrick J. Sinko, Mónica B. Wachsman, and Michael L. Chikindas. Safety, Formulation, and *in vitro* antiviral activity of the antimicrobial peptide subtilosin against herpes simplex virus type 1. *Probiotics and Antimicrobial Proteins*, **2013**, 5, 26-35.

11. **Ji Li**, Yunqi Li, Yu-wen Ting, and Qingrong Huang. Development of highly-aligned curcumin-loaded zein fibers. *Journal of Agricultural and Food Chemistry*, submitted.

12. **Ji Li**, Yunqi Li, Yu-wen Ting, Timothy Nguyen, Victor Lee, Teddie Magbitang, Robert Miller, Joseph Sly, and Qingrong Huang. Assembly of mPEG-*b*-PVL block copolymer and star polymer for curcumin encapsulation. *Biomacromolecules*, to be submitted.

13. **Ji Li** and Qingrong Huang. Structure study of oat protein isolate in aqueous medium via synchrotron small-angle X-ray scattering. *Journal of Agricultural and Food Chemistry*, to be submitted.

14. **Ji Li**, Zhenyu Lin, Yin Wang, and Qingrong Huang. Structure and luminescent properties of curcumin-loaded electrospun fiber mat. *Journal of Agricultural and Food Chemistry*, to be submitted.